Title

On the interactions of silver with DNA: from metal-mediated base pairings to fluorescent clusters

Permalink

https://escholarship.org/uc/item/1nw648db

Author

Swasey, Steven Michael

Publication Date

2017

Peer reviewed|Thesis/dissertation

UNIVERSITY OF CALIFORNIA

Santa Barbara

On the interactions of silver with DNA: from metal-mediated base pairings to fluorescent clusters

A dissertation submitted in partial satisfaction of the requirements for the degree Doctor of Philosophy in Chemistry

by

Steven M. Swasey

Committee in charge:

Professor Elisabeth Gwinn, Co-Chair

Professor Kevin Plaxco, Co-Chair

Professor Bernard Kirtman

Professor Songi Han

January 2018

The dissertation of Steven M. Swasey is approved.

Songi Han

Kevin Plaxco

Elisabeth Gwinn, Committee Co-Chair

Bernard Kirtman, Committee Co-Chair

December 2017

On the interactions of silver with DNA: from metal-mediated base pairings to fluorescent clusters

By

Steven M. Swasey

Acknowledgements

This thesis has come to fruition not only due to my labor, but due to the excellent work, advice and support from a multitude of amazing advisors, peers, friends and family. I would like to start by specifically thanking my primary graduate advisor, Beth Gwinn, for her unwavering support and help throughout my time here at UCSB. You have represented so many things I truly respect and aspire to be. I am very lucky to have been able to work with you!

I would like to thank all of our collaborators who have worked tirelessly and diligently to get to where we are today. To my first collaborators Christine Aikens and Natalia Karimova: thank you for making my first collaboration such an excellent one with your intricate circular dichroism calculations on twisted metal silver rods. To Olga Lopez-Acevedo, Leonardo Espinosa-Leal, Alexander Karpenko and Xi Chen: thank you for your patience in working with us and these very complicated systems – your calculations have provided pivotal insight! Thank you Xiaobing Zuo and Argonne National Labs for collaborating with us to attempt x-ray scattering experiments – although the experiments did not work out as intended the experience was valuable. To Valérie Gabelica and Frédéric Rosu: thank you for your invaluable expertise on ion mobility spectroscopy on DNA and your eagerness to work with us. Thank you Gary Ren for your help and impressive work with atomic force microscopy on DNA duplexes with silver.

I would like to thank Dani Schultz for showing me the ropes as a new grad student. I would also like to thank Stacy Copp for all of her helpful advice and discussions over the years. You have made being a grad student much more interesting and entertaining! Thank you to all the undergraduate student researchers I have had the pleasure of working with. Jackie Geler-Kremer, Alex Chiu, Alexis Faris and Hunter Nicholson – I know you will all be doing great things and you have helped me grow too.

I would like to thank my committee members Bernard Kirtman, Kevin Plaxco and Songi Han for their time and advice. I would like to thank all my previous advisers and mentors that have helped me in my life leading up to the graduate program at UCSB. Thank you to my undergraduate adviser, Andrew Terentis, for giving me a chance and guiding me through my early research career. Thank you Riaz Ahmad and Katie Cychosz for being great supervisors and helping me reach my full potential. Thank you Matthias Thommes for being such an important part of where I am today – your passion, intelligence, and understanding never cease to amaze me. I am very grateful for all of the help and opportunities you have afforded me.

I would like to thank the super crew at the UCSB facilities on campus. Thank you James Pavlovich and Rachel Behrens for all of your help with the mass spectrometer, advice and accommodating our negative ion mode needs. Thank you Nelly Traitcheva, Lior Dassau and Jennifer Smith for your awesome management of the Biological Nanostructures Lab and you eagerness to assist us. Thank you Alexander Mikhailovsky for being so helpful and giving the new circular dichrometer a home.

I would like to thank my family – for whose love and support has always been a beacon in this crazy world. Thank you to my siblings who are important friends today. Thank you to my grandparents who have been amazing and strong role models. Thank you to my many aunts, uncles and cousins who have fostered a great environment for me to grow up in. Most of all, thank you Mom and Dad for everything. There is no way I can thank you for everything you have afforded for me in life, but here is a start: thank you for your patience with me asking a million questions when I was growing up, your support for me to follow the path I want to in life, your devotion to your kids, your understanding and acceptance, your hard work, your friendship and your love.

Curriculum Vitae for

Steven Swasey

November 2017

EDUCATION

Ph.D. Candidate
University of California Santa Barbara Santa Barbara, CA 2012-present

B.S. in Chemistry
Florida Atlantic University Boca Raton, FL 2009

WORK EXPERIENCE

Laboratory Associate
Quantachrome Instruments Boynton Beach, FL 2010 – 2012

AWARDS AND HONORS

Nanomaterials Travel Award for Excellence in Nanoscience Research 2016
Norris Fellowship for Mentorship in Science 2014
Worster Fellowship for Undergraduate Student Mentorship 2014
Pegasus Gold Award for Academic Excellence 2005
Florida Academic Scholars Award for Academic Excellence and Community Service 2005

PUBLICATIONS

1) **S.M. Swasey**, F. Rosu, V. Gabelica, S. M. Copp and E. G. Gwinn. Structural insights into Ag^+-paired DNA from ion mobility mass spectrometry and fluorescence resonance energy transfer studies. *In preparation.*
2) **S.M. Swasey**, H. C. Nicholson, S. M. Copp, P. Bogdanov, A. Govorits and E. G. Gwinn. Low-cost adaptation of a visible wavelength fluorescence microplate reader for discovery of near-infrared fluorescent probes. *In preparation*.
3) S. A. Bogh, M. R. Carro-Temboury, C. Cerretani, **S. M. Swasey**, S. M. Copp, E. G. Gwinn, T. Vosch. Unusually large stokes shift for a near-infrared emitting DNA-stabilized silver nanocluster. *In review*.
4) S.M. Copp, D. Schultz, A. Faris, **S.M. Swasey**, and E.G. Gwinn. Cluster plasmonics:

Dielectric and shape effects on DNA-stabilized silver clusters. *Nano Lett.* **2016**, 16, 3594-3599.

5) **S.M. Swasey** and E.G. Gwinn**.** Silver-mediated base pairings: towards dynamic DNA nanostructures with enhanced chemical and thermal stability. *New J. Phys*. **2016**, 18, 045008.
6) S.M. Copp, A. Faris, **S.M. Swasey** and E.G. Gwinn. Heterogeneous Solvatochromism of Fluorescent DNA-Stabilized Silver Clusters Precludes Use of Simple Onsager-Based Stokes Shift Models. *J. Phys. Chem. Lett.* **2016**, 7, 698-703.
7) L.E. Leal, A. Karpenko, **S.M. Swasey**, E.G. Gwinn, V. Rojas-Carvellera, C. Rovira and O. Lopez-Acevedo. The Role of Hydrogen Bonds in the Stabilization of Silver-Mediated Cytosine Tetramers. *J. Phys. Chem. Lett.* **2015**, 6, 4061-4066.
8) **S.M. Swasey**, L.E. Leal, O. Lopez-Acevado, J. Pavlovich and E.G. Gwinn. Silver (I) as DNA Glue: Ag^+-mediated Guanine Pairing is revealed by relaxing Watson-Crick constraints. *Sci. Rep.* **2015**, 5, 10163.
9) E.G. Gwinn, D. Schultz, S.M. Copp and **S.M. Swasey**. DNA-Protected Silver Clusters for Nanophotonics. *Nanomaterials* **2015**, 5, 180-207.
10) S.M. Copp, D. Schultz, **S.M. Swasey** and E.G. Gwinn. Atomically Precise Arrays of Fluorescent Silver Clusters: A Modular Approach for Metal Cluster Photonics on DNA Nanostructures. *ACS Nano* **2015**, 9, 2303-2310.
11) S.M. Copp, D. Schultz, **S. M. Swasey**, J. Pavlovich, M. Debord, A. Chiu, K. Olsson and E.G. Gwinn. Magic Numbers in DNA-Stabilized Fluorescent Silver Clusters Lead to Magic Colors. *J. Phys. Chem. Lett.* **2014**, *5*, 959-963.
12) **S. M. Swasey**, N. Karimova, C. Aikens, D. Schultz, A. Simon and E.G. Gwinn. Chiral Electronic Transitions in Fluorescent Silver Clusters Stabilized by DNA. *ACS Nano.* **2014**, *8*, 6883-6892.
13) A. Dukhin, **S. M. Swasey** and M. Thommes, A method for pore size and porosity analysis of porous materials using electroacoustics and high frequency conductivity. *Colloids Surf. A* **2013**, *437*, 127-132.

Abstract

On the interactions of silver with DNA: from metal-mediated base pairings to fluorescent clusters

by

Steven M. Swasey

In this dissertation we focus on better understanding the interactions of silver with DNA, a topic with far reaching implications that range from the realization of more robust DNA nanotechnology, to silver clusters templated by DNA (Ag_N-DNA) that can serve as fluorophores and molecular sensors, to better understanding of biological interactions that could lead to development of new approaches to the treatment of diseases that exploit silver-nucleic acid interactions. One important aspect of the interaction of Ag^+ with DNA is that Ag^+ can specifically bind to DNA bases as opposed to the negatively charged phosphate backbone allowing for precise control on where the Ag^+ binds. For DNA nanotechnology this is ideal since DNA nanostructures require intricate designs with DNA strands self-assembling in a precise manner. Current DNA nanotechnology has harnessed the decades of research in canonical base pairing to realize 3D nanostructures, ranging from simple molecular machines to more complex and functional assemblies. Unfortunately, DNA nanotechnology is somewhat limited by DNA nanostructure stability as they are held together by weak hydrogen bonds and pi-stacking interactions. This is an issue which incorporation of strong Ag^+-mediated pairings

could help resolve. But in order to effectively use Ag^+ in DNA nanotechnology, many more details must be known about the interactions of Ag^+ with DNA.

DNA nanostructures are typically formed by combining many different single-stranded DNA strands which can then self-assemble into spatially arranged duplexes by canonical base pairing. As such, we begin by removing the canonical duplex constraints and first explore interactions of Ag^+ with single-stranded DNA. We test every combination of homobase strands of the four canonical bases adenine, cytosine, guanine and thymine with Ag^+ using electrospray ionization mass spectrometry (ESI-MS). Homobase Ag^+-paired strands of guanine and cytosine bases were detected. The emergence of C-Ag^+-C and G-Ag^+-G base pairs was evidenced both by the binding ratio of Ag^+ to DNA bases and the stability of Ag^+-mediated base pairs from theoretical calculations. These Ag^+-paired guanine and cytosine homobase strands were found to have exceptional thermal stability even at short, 6 base lengths. We also find these Ag^+-paired cytosine and guanine homobase strands form monodisperse products in certain solution conditions and have good stabilities in typical conditions used to form DNA nanostructures. Even heterobase strands which contain both cytosine and guanine bases can form Ag^+-paired strands, with increased Ag^+ incorporation associated with heterobase composition. These Ag^+-paired cytosine and guanine homobase pairs appear to have properties which would allow incorporation into DNA nanostructures with canonical base pairings.

We explore strand orientation in Ag^+-paired guanine and cytosine strands by using dye labelled strands and Förster resonance energy transfer (FRET) techniques. We find that both Ag^+-paired cytosine and guanine strands prefer a parallel strand orientation, which is a pivotal piece of knowledge to effectively incorporate Ag^+-mediated bases into DNA nanotechnology. We explore the shape of Ag^+-paired guanine and cytosine homobase strands of various lengths by ion-mobility spectrometry ESI-MS. In ion-mobility spectroscopy the gas-phase structures retain a memory of their solution phase structure, which can be a useful structural analysis tool. The Ag^+-paired guanine homobase strands appear to be elongated and linear in the akin to a canonically paired duplex, while the Ag^+-paired cytosine strands have a compact and extended form in the which depends on charge state.

Ag_N-DNA are an aspect of DNA nanotechnology which are particularly promising as emerging fluorophores. Ag_N-DNA have optical properties that differ depending on the sequence of the DNA template strand. Certain sequences template Ag_N-DNA with quantum yields which approach unity. Ag_N-DNA have also been discovered with wavelengths of emission ranging from the visible to near-infrared. We explore the structure of these Ag_N-DNA using high performance liquid chromatography (HPLC) to purify them and analyze them with circular dichroism (CD) spectroscopy. We find that agreement between experimental CD spectra and theoretical calculations of a slightly twisted silver wire suggest a chiral, rod-like shape for the cluster in the Ag_N-DNA. We additionally find that the CD signal of Ag_N-DNA suggest that Ag^+-mediated base pairs form an important foundation in the DNA secondary structure for the formation of Ag_N-DNA.

Table of Contents

Ackknowledgements......iv

Curriculum Vitae......vii

Abstract......ix

List of Figures......xv

List of Tables......xx

Chapter 1) Introduction 1

Chapter 2) Silver (I) as DNA glue: Ag^+-mediated guanine pairing revealed by re moving Watson-Crick constraints 12

2.1) Introduction 12

2.2) Results and Discussion 15

2.2.1) Detection of $(Ag^+)_N$-DNA products by ESI-MS 15

2.2.2) Thermal stability of silver mediated DNA homobase duplexes. 19

2.2.3) Quantum chemical calculations of binding strengths and geometries. 20

2.3) Conclusions 24

2.4) Methods 25

2.4.1) DNA preparation. 25

2.4.2) Mass spectrometry experiments. 25

2.4.3) Circular dichroism experiments. 25

Chapter 3) Silver-mediated base pairings: towards dynamic DNA nanostructures with enhanced chemical and thermal stability 27

3.1) Introduction 27

3.2) Results and Discussion 31

3.3) Towards Ag^+-stabilized DNA Nanotechnology 45

3.4) Conclusions 49

3.5) Methods 50

Chapter 4) Structural insights into Ag^+-paired DNA from fluorescence resonance energy transfer studies and ion mobility mass spectrometry 51

4.1) Introduction 51

4.2) Results and Discussion 54

4.2.1) Investigation of strand orientation in Ag^+-paired DNA by FRET 54

4.2.2) Sequential C-Ag^+C pairings prefer a parallel strand orientation 56

4.2.3) Sequential G-Ag^+-G pairings prefer a parallel strand orientation 60

4.2.4) Probing the shapes of $(G_N)_2(Ag^+)_N$ and $(C_N)_2(Ag^+)_N$ by ion mobility measurements 64

4.3) Conclusions 73

4.4) Methods 75

4.4.1) General FRET Experimental Methods: 75

4.4.2) Cytosine Ag^+-paired strands FRET experiments: 76

4.4.3) Guanine Ag^+-paired strands FRET experiments: 76

4.4.4) Ion-mobility experiments: 78

Chapter 5) Chiral Electronic Transitions in Fluorescent Silver Clusters Stabilized by DNA 79

5.1) Introduction 79

5.2) Results and Discussion 82

5.2.1) Reshaping of UV Circular Dichroism in Ag_N-DNA 82

5.2.2) Low Energy, Cluster-Dominated CD 86

5.2.3) Giant Anisotropies at Intermediate Energies 88

5.2.4) Fits to CD Spectra 89

5.2.5) Quantum chemical calculations 90

5.2.6) A Solvent-driven Conformational Shift 95

5.3) Conclusions 97

5.4) Methods 98

5.4.1) Synthesis and Purification of Ag_N-DNA 98

5.4.2) Optical Characterization 99

5.4.3) Calculation Techniques 100

Chapter 6) Concluding remarks 102

Appendix A) Supporting Information for Chapter 2 104

A.1) Experimental mass spectra 104

A.2) Computational details 111

A.2.1) Planarity of metal mediated homodimers 113

A.2.2) Metal bound to single bases 113

A.2.3) Metal mediated GC and AT dimers 114

A.2.4) The PAW method 117

A.2.5) Images of calculated ground state geometries 118

A.2.6) Initial configurations 124

Appendix B) Supporting Information for Chapter 3 127

B.1) Determining the number of Ag$^+$ cations in Ag$^+$-paired DNA from Electrospray-Ionization Mass Spectrometry (ESI-MS) 127
B.2) Mass spectra for centrally mutated Ag$^+$-paired strands 129
B.3) CD spectra for centrally mutated Ag$^+$-paired strands 131
B.4) Mass spectra for Ag$^+$-paired heterobase strands 132
B.5) Mass spectra for Ag$^+$-paired $T_2C_{20}T_2$ 133
B.6) CD spectra for T_2C20T_2 with and without $MgSO_4$ 135
B.7) Absorbance spectra of C20 and T2C20T2 with and without $MgSO_4$ and NaCl 136
Appendix C) Supporting Information for Chapter 4 137
C.1) FRET experiments 137
C.1.1) Experimental Design 137
C.1.2) Purification and mass spectral characterization 138
C.1.3) FRET efficiency calculation and spectral normalization 145
C.2) IMS-MS Experiments 147
C.2.1) Tabular CCS values 147
C.2.2) Representative mass spectra and CCS distributions 151
C.2.3) CD spectra for G-quadruplexes used in IMS 154
Appendix D) Supporting Information for Chapter 5 155
D.1) Ag_N-DNA Synthesis 155
D.2) Sample Purity Estimates 156
D.3) Quantum Chemical Calculations 157
D.4) Pure versus Impure Spectra 159
D.5) Gaussian Fits to CD Spectra 160
Appendix E) Ag$^+$ disrupts folding in a human telomeric G-quadruplex structure 162
E.1) Introduction 162
E.2) Results and Discussion 163
E.3) Conclusion 164
E.4) Methods 164
References 165

List of Figures

Figure 2.1) (a) Schematic of the homo-base strand types and combinations studied. Stars denote the detected Ag^+-paired strands. (b) Example of isotope peak envelope resolved in MS. 14

Figure 2.2) Effects of Ag^+ on solutions of mixed C_{11} and G_{11} (a)-(c), and solutions of mixed A_{11} and T_{11} (d)-(f), at 40 µM per strand.. 16

Figure 2.3) (a-l) Percentage of the total integrated counts (%IC) for each detected Ag^+-bearing DNA product plotted versus number of attached Ag^+ 17

Figure 2.4) Circular dichroism (CD) spectra of C_6 (a) and G_6 (b)..19

Figure 2.5) Calculated ground state geometries of Ag^+-mediated homobase pairs................20

Figure 3.1) a) Isotope peak envelope in a typical mass spectrum (red curve) for an Ag^+-DNA product at charge state z = -6, for a solution containing the strand $CG_3C_3G_2C_2G$ at 1 Ag^+/base.. 33

Figure 3.2) Distribution of the number of attached Ag^+ in paired strands formed by the strands a) C_{11}, b) C_5AC_5, c) C_5GC_5, d) C_5TC_5, e) G_{11}, f) G_5AG_5, g) G_5CG_5 and h) G_5TG_5. 36

Figure 3.3) Distribution of Ag^+ binding stoichiometry in Ag^+-paired strands of 12 base C,G strands, and corresponding CD spectra...38

Figure 3.4) HPLC chromatograms of Ag^+- $T_2C_{20}T_2$ solutions monitored at 260 nm for solutions prepared at 5 µM DNA and 1 Ag^+/base 41

Figure 3.5) CD spectra for solutions of strands a) C_{20} and b) G_{20} at 1 Ag^+ per base in varying concentrations of urea...43

Figure 3.6) CD spectra of C_{20} with a) NaCl and b) $MgSO_4$ and G_{20} in c) NaCl and d) $MgSO_4$ 45

Figure 3.7) CD spectra of varying lengths of a) G and b) C homobase oligonucleotides in 7.5 mM MOPS at 1 Ag^+ per base 47

Figure 3.8) (a) Simple 4-strand scheme for a robust structure that employs Ag^+-pairing to form a stable “frame” around a central, dynamic “picture” 48

Figure 4.1) (a) Schematic for the FRET experiment. (b) Unsmoothed emission spectra of $D_{3'C}$ DNA, without Ag^+ (dotted blue curve) and of the purified Ag^+-paired $A_{3'C}$-$D_{3'C}$ (solid blue curve) and $D_{5'C}$-$A_{3'C}$ (solid orange curve) 58

Figure 4.2) Unsmoothed emission spectra of $D_{3'G}$ bare DNA (dotted blue curve) and of the purified Ag^+-paired $A_{3'G}$-$D_{3'G}$ (solid blue curve), $(D_{5'G}$-$A_{3'G})_x$ (solid orange curve) and $(D_{5'G}$-$A_{3'G})_y$ (dotted orange curve) 62

Figure 4.3) Collision cross-sections (CCS) from IMS-MS of a) $(G_N)_2(Ag^+)_N$ for N=6-20, b) $(C_N)_2(Ag^+)_N$ for N=6-30, c) WC-paired duplexes $((CG)_N)_2$ for N=4-15 and d) G-quadruplexes $(TG_NT)_4$ for N=5,8 versus charge state (Z)........66

Figure 4.4) (a) Experimental CCS plotted versus the total number of bases in a product, N_{total}, at fixed charge to base ratios, Z/N_{total}. (a) $Z/N_{total} = 0.15$ and (b) $Z/N_{total} = -0.2$. Experimental CCS points are from linear interpolation of the measured CCS (Figure 4.3).........71

Figure 4.5) Peak widths of major features in CCS distributions at various charge states, Z, for a) $((CG)_7)_2$, $(C_{14})_2(Ag^+)_{14}$, $(G_{14})_2(Ag^+)_{14}$ and $(TG_5T)_4$ and b) $((CG)_9)_2$, $(C_{20})_2(Ag^+)_{20}$, $(G_{20})_2(Ag^+)_{20}$ and $(TG_8T)_4$........72

Figure 5.1) UV CD spectra for templates S1-S4 in (a) – (d), respectively.........83

Figure 5.2) CD (black) and absorption (blue) spectra of pure cluster solutions S1 (a), S2 (b), S3 (c) (aqueous solution) and S4 (d; 50% MeOH)..........86

Figure 5.3) Fits (red dashed curves) of experimental CD spectra (black curves) to the superposition of seven Gaussian peaks for S1 (a), S2 (b), S3 (c) (aqueous solution) and S4 (d) (50% MeOH).. 88

Figure 5.4) Calculated circular dichroism spectra (a) and optical absorption spectra (b) for neutral, filamentary Ag6 clusters shown at the top right. Calculations using the SAOP functional with TZP basis set........90

Figure 5.5) (a) CD and (b) absorbance spectra for the titration of sample S4 from 0-50% methanol by volume in 5% increments........95

Figure A.1) Full range mass spectra of solutions containing A_{11} and T_{11} with a) no Ag^+ and b) $0.5Ag^+$/base as well as G_{11} and C_{11} with c) no Ag^+ and d) 0.5 Ag^+/base 103

Figure A.2) Full range mass spectra of a) T_{11} b) A_{11} c) C_{11} and d) G_{11} at 80μM DNA concentration and 0.5 Ag^+/base ratio taken in ESI negative mode.........104

Figure A.3) Full range mass spectra of a) T_{11} b) A_{11} c) C_{11} and d) G_{11} at 80μM DNA concentration and 0.75 Ag^+/base ratio taken in ESI negative mode.........105

Figure A.4) Full range mass spectra of a) T_{11} b) A_{11} c) C_{11} and d) G_{11} at 80μM DNA concentration and 1 Ag^+/base ratio taken in ESI negative mode.........106

Figure A.5) Mass spectra of a) C_6, b)G_6, c) C_{20} and d) G_{20} at 80μM DNA concentration and 1 Ag^+/base ratio taken in ESI negative mode 107

Figure A.6) Mass spectra of a) C_6 and b) G_6 at strand concentrations used for circular dichroism experiments (17 μM) and 1 Ag^+/base ratio taken in ESI negative mode.............108

Figure A.7) Labels used in this work for the definition of the dihedral angles in the four DNA bases...117

Figure A.8) Representation of the optimized geometries for the A-Ag^+-A pairs (see Table A.2) obtained by means of Density Functional theory (DFT) at PBE+vdW level. 118

Figure A.9) Representation of the optimized geometries for the C-Ag^+-C pairs (see Table A.2) obtained by means of Density Functional theory (DFT) at PBE+vdW level. 119

Figure A.10) Representation of the optimized geometries for the G-Ag^+-G pairs (see Table A.2) obtained by means of Density Functional theory (DFT) at PBE+vdW level. 120

Figure A.11) Representation of the optimized geometries for the T-Ag^+-T pairs (see Table A.2) obtained by means of Density Functional theory (DFT) at PBE+vdW level. 120

Figure A.12) Representation of the optimized geometries for the A-Ag^+-T pairs (see Table A.2) obtained by means of Density Functional theory (DFT) at PBE+vdW level. 121

Figure A.13) Representation of the optimized geometries for the G-Ag^+-C pairs (see Table A.2) obtained by means of Density Functional theory (DFT) at PBE+vdW level. 122

Figure A.14) Representation of the optimized geometries for the deprotonated T*-Ag^+-A and G*-Ag^+-C pairs (see Table A.2) obtained by means of Density Functional theory (DFT) at PBE+vdW level. 122

Figure A.15) Schematic representation of the initial configurations used for the search algorithm in the case of the Ag^+ homo-duplex with Guanine. 124

Figure A.16) Example of a single force optimization leading to the bridged Guanine homo-duplex ground state. 125

Figure B.1) Mass spectra for solutions of 80 μM DNA, 880 μM $AgNO_3$ and 50 mM $NH_4C_2H_3O_2$ (pH = 7) injected into the mass spectrometer in negative ion mode for DNA strands a) C_{11}, b) C_5AC_5, c) C_5GC_5 and d) C_5TC_5.. 128

Figure B.2) Mass spectra for solutions of 80 μM DNA, 880 μM $AgNO_3$ and 50 mM $NH_4C_2H_3O_2$ (pH = 7) injected into the mass spectrometer in negative ion mode for DNA strands a) G_{11}, b) G_5AG_5, c) G_5GG_5 and d) G_5TG_5 129

Figure B.3) Circular dichroism spectra for solutions of 7.5 μM DNA, 82.5 μM $AgNO_3$ and 50 mM $NH_4C_2H_3O_2$ (pH = 7) for strands a) C_{11} (red curve), C_5AC_5 (teal curve), C_5GC_5 (green curve) and C_5TC_5 (purple curve) and b) G_{11} (red curve), G_5AG_5 (teal curve), G_5CG_5 (green curve) and G_5TG_5 (purple curve). 130

Figure B.4) Mass spectra for solutions of 80 μM DNA, 960 μM $AgNO_3$ and 10 mM $NH_4C_2H_3O_2$ (pH = 7) injected into the mass spectrometer in negative ion mode for DNA strands a) $G_4C_4G_4$, b) $C_4G_4C_4$ and c) $CG_3C_3G_2C_2G$. 131

Figure B.5) Mass spectra of the HPLC aliquots collected from the two dominant chromatogram peaks of a solution prepared at 5 μM $T_2C_{20}T_2$, 100 uM $AgNO_3$ and 10 mM $NH_4C_2H_3O_2$ pH = 7. 132

Figure B.6) Mass spectra of samples prepared by annealing strand $T_2C_{20}T_2$ with 1 Ag^+/base in a) 10 mM $C_2H_3O_2NH_4$, b) 500 mM $C_2H_3O_2NH_4$, c) 10mM $C_2H_3O_2NH_4$ and 10mM $MgSO_4$, d) 10mM $C_2H_3O_2NH_4$ and 30 mM $MgSO_4$ and e) 10mM $C_2H_3O_2NH_4$ and 60 mM $MgSO_4$. ...133

Figure B.7) CD spectra of solutions of 5 μM $T_2C_{20}T_2$ and 10 mM $NH_4C_2H_3O_2$ (pH = 7) in 0 mM (purple) and 60 mM (teal) $MgSO_4$ 134

Figure B.8) Absorbance spectra of solutions with a) 4 μM C_{20} and b) 5 μM $T_2C_{20}T_2$ in 10mM $NH_4C_2H_3O_2$ (pH = 7) at 1 Ag^+ per cytosine base, as used for CD experiments. 135

Figure C.1) Experimental absorbance (solid curves) and emission (dashed curves) spectra for donor dye Alexa 488 “d” (green curves) and acceptor dye Alexa 647 “a” (red curves) used in this study. 137

Figure C.2) HPLC chromatograms for sample C(3’-3’) (solutions containing strands $A_{3'C}$ and $D_{3'C}$ with Ag^+) for a) absorbance and b) emission. HPLC chromatograms for sample C(5’-3’) (solutions containing strands $A_{3'C}$ and $D_{5'C}$ with Ag^+) for c) absorbance and d) emission...139

Figure C.3) Mass spectra of the HPLC-isolated duplex solutions of a) $A_{3'C}$-$D_{3'C}$ and b) $D_{5'C}$-$A_{3'C}$ and c) $(D_{5'C}\text{-}A_{3'C})_y$....................140

Figure C.4) HPLC chromatograms for sample G(3’-3’) (solutions containing strands $A_{3'G}$ and $D_{3'G}$ with Ag^+) for a) absorbance and b) emission as well as for sample G(5’-3’) (solutions containing strands $A_{3'G}$ and $D_{5'G}$ with Ag^+) for c) absorbance and d) emission....................141

Figure C.5) Mass spectra of HPLC isolated solutions of a) $A_{3'G}$-$A_{3'G}$, b) $A_{3'G}$-$D_{3'G}$, c) $(D_{5'G}\text{-}A_{3'G})_1$ and d) $(D_{5'G}\text{-}A_{3'G})_2$....................143

Figure C.6) HPLC absorbance chromatograms monitored at 260 nm for strand $A_{3'G}$ at 2.5 μM with a) 10 mM NH_4OAc and b) 50 mM NH_4OAc and 37.5 μM $AgNO_3$ 144

Figure C.7) Representative mass spectra for solutions containing the DNA species explored in the IMS-MS studies in Chapter 4 150

Figure C.8) Representative CCS distributions for various charge states of a) $(G_{20})_2(Ag^+)_{20}$ and b) $(C_{20})_2(Ag^+)_{20}$. 151

Figure C.9) Representative CCS distributions for various charge states of a) $(CG_{11})_2$ and b) $(TG_8T)_4(NH_4^+)_7$. 152

Figure C.10) CD spectra for solutions of 80 µM DNA in 100 mM NH_4OAc pH = 7. The spectral signature is as expected for a parallel four-stranded G-quadruplex.[187] 153

Figure D.1) Purity estimates based on the overlaid 4.77 eV (260 nm) (dashed red) chromatograms, which peak when any DNA-containing species elutes from the column, and the chromatograms measured at the peak visible absorbance energy specific to each sample 155

Figure D.2) TDDFT A) optical absorption and B) circular dichroism spectra for Ag_n (n = 4, 6, 8, 10, 12) with 170° Ag-Ag-Ag bond angles and 10° Ag-Ag-Ag-Ag torsional angles.........157

Figure D.3) UV CD spectra of purified (A) and unpurified (B) solutions of S1 (teal), S2 (red), S3 (purple) and S4 (green). 158

Figure E.1) CD spectra for the titration of human telomeric sequence $(T_2AG_3)_6$ with $AgNO_3$. 162

List of Tables

Table 3.1) Strand names and corresponding sequences. 30

Table 5.1) Ag_N-DNA properties. (a) Aqueous visible fluorescence excitation maxima and emission maxima. (b) Numbers of neutral silver atoms (Ag^0) and numbers of silver cations (Ag^+) in the AgN-DNA templated by the indicated strand..81

Table 5.2) Experimental anisotropy values (g x 10_3) at energies of individual fitted Gaussian CD peaks (eV)..89

Table A.1) m/z values for highly abundant charge state products obtained from the mass spectra in Figures A.1-2 and the corresponding numbers of attached silver cations, N, rounded to an integer from the experimental value in parentheses..109

Table A.2) Summary of all structures including: structure label (str), binding energies obtained with PBE+vdW, dihedral angles and atom-metal-atom bond lengths and angles................113

Table A.3) Values of rcut (in Bohr) for the different atoms in the studied molecular structures of this work. The van der Waals radius is giving for comparison. 116

Table C.1) Tabular CCS values for WC-paired $((CG_N)_2)$ duplexes. 146

Table C.2) Tabular CCS values for $(TG_NT)_4$ G-quadruplexes. 147

Table C.3) Tabular CCS values for Ag^+-paired $(C_N)_2(Ag^+)_N$. 148

Table C.4) Tabular CCS values for Ag^+-paired $(G_N)_2(Ag^+)_N$. 149

Table D.1) Synthesis and Purification Parameters for Ag_N-DNA 154

Table D.2) Calculated Parameters of the Two Lowest CD Peaks.[a] Molar ellipticity deg·cm^2·$dmole^{-1}$; [b] rotatory strength 10^{-40} esu^2 ·cm^2; [c] oscillator strength............................156

Table D.3) Calculated Parameters of the Two Lowest CD Peaks for Silver Wires Ag_n (n = 4, 6, 8, 10, 12) with 170° Bond Angles and 10° Torsional Angles. [a] Molar ellipticity deg·cm^2·$dmole^{-1}$; [b] rotatory strength 10^{-40} esu^2 ·cm^2; [c] oscillator strength............................158

Table D.4) Table for the parameters of the Gaussian peaks fitted to the experimental CD spectra in Chapter 5, Figure 5.3. 160

Chapter 1) Introduction

Life as we know it cannot exist without a means to consistently retain and transfer encoded information about an organism's makeup. One of the vital molecules involved in this process is deoxyribonucleic acid (DNA). DNA encodes for proteins through patterns of the four canonical bases: guanine (G), cytosine (C), thymine (T) and adenine (A). DNA is a dynamic biological molecule capable of supercoiling or changing its compactness depending on the biological process, organizing into ordered chromosomal tertiary structures and altering chemical or secondary structure to regulate gene expression. Even with the strong focus on DNA research over the past century there is still so much to learn about this fascinating molecule. Due to its special properties, non-biological uses have recently started to emerge in the form of DNA nanotechnology.

The structure of B-form DNA (B-DNA) was originally discovered in 1953 by James Watson and Francis Crick and partly inspired by a crystal structure produced by Rosalind Franklin and Maurice Wilkins. This work was built on the knowledge provided by many scientists before that such as the first isolation of DNA by Friedrich Miescher in 1869, discovery of the general composition of DNA by Phoebus Levene in the early 1900's and the patterns of base composition in DNA by Erwin Chargaff in 1950. B-DNA consists of two DNA strands paired together forming a linear, right-handed double-helix. Each DNA strand consists of multiple nitrogenous bases connected by deoxyribose sugars and phosphate groups. DNA has a directionality and is typically written 5', the phosphoryl end, to 3', the hydroxyl end. Each strand in B-DNA is paired in an anti-parallel orientation where one strand's 5' end is paired with the other strand's 3' end. The overall double-helix form is stabilized primarily with hydrogen-bonded (H-bonded) base pairs from the canonical bases, forming G-C and A-T base pairs, and pi-stacking interactions between adjacent base pairs. The phosphate groups in DNA are negatively charged at physiological pH and can destabilize B-DNA as well as other forms of DNA if they are not properly screened by counterions, typically Na^+, K^+ and Mg^{2+}.[1]

The vast conformational landscape of DNA makes it an incredibly interesting and complex molecule. Aside from the canonical B-DNA duplex there are other forms which can be produced depending on strand sequence and solution conditions. Many of these forms are evidenced to have biological relevance and are still an active area of current research. A-form (A-DNA) and Z-form (Z-DNA) DNA are similar to B-DNA with two strands canonically paired in antiparallel orientation forming a linear double-helix, but differ in their relative orientation of base pairs. A-DNA is much more compacted relative to B-DNA and thought to be an intermediate when certain proteins bind to DNA.[2] Z-DNA is left-handed as opposed to the right-handed A-DNA and B-DNA, and is believed to form from induced stress on DNA during transcription.[3] Triplex DNA can form intermolecularly with one additional strand hybridizing to duplex DNA through non-canonical H-bonding to the bases, or intramolecularly where the single-stranded region of one strand in a duplex wraps back around the duplex to form a triplex region.[4] Triplex DNA has been suggested to play an important role in the regulation of gene expression.[5] G-Quadruplexes are formed from G-rich sequences, where four guanine bases H-bond into a planar G-tetrad which can stack successively.[6] G-quadruplexes have been hypothesized to form in telomeric regions of DNA which can affect telomerase activity and in other regions of DNA for gene expression regulation.[7,8] I-motifs form from C-rich sequences and consist of two duplexes with intercalating hemiprotonated cytosine base pairs.[9] Initially i-motif structures were thought only to form at low, non-physiological pH, however with the emergence of i-motif structures formed at neutral pH further research is required into the i-motif structure's possible biological relevance.[9]

Metal cations have varied interactions with DNA, which can be utilized in both biological DNA and DNA nanotechnology. One of the most well-known utilization of these interactions in biological DNA is with Pt^{2+}, where the platinum complex cis-platin serves as a potent anti-cancer drug by binding between guanine bases.[10,11] It is for this reason that many other kinds of metal complexes such as copper, zinc, silver and gold are currently being investigated as potential cancer drugs.[12] Silver complexes are of particular interest due to its potent antibacterial activity and low toxicity in humans.[13] Despite the growing evidence of many silver complexes having potent antitumor activity, very little is understood about their mechanism of action.[14–18]

The important properties of DNA for biological uses also makes it ideal as a structural material capable of self-assembly into various kinds of functional nanostructures. This field of DNA nanotechnology was pioneered by Ned Seeman, whose earliest work published in 1982 proposed the formation of 3D DNA lattices,[19] and in 1991 realized the formation of a 3D DNA cube.[20] DNA nanotechnology is of particular interest due to its myriad of potential applications such as using DNA nanostructures which can respond to stimulus for drug delivery,[21] DNA breadboards with the ability to specifically and uniformly distribute molecules on its surface with particular promise for light harvesting and general fluorophore studies,[22] DNA based probes and biosensors,[23] and functional DNA-based molecular machines.[24] Most DNA nanotechnology relies on Watson-Crick (WC) base pairing and pi-stacking interactions for few to hundreds of DNA strands to self-assemble into a nanostructure. While the emerging uses of DNA nanotechnology have been very promising, the field of DNA nanotechnology still faces issues such as nanostructure degradation from enzymatic interactions and long term stabilities at low concentrations.[25,26]

Metal-mediated base pairings are recent tools which have a myriad of potential uses in DNA nanotechnology, and may have to potential to reduce the issues of enzymatic degradation and general stability issues of DNA nanostructures. Much of the earlier work with metal-mediated base pairing focused on the metal-mediated pairing of artificial bases incorporated into DNA strands.[27,28] It was later discovered that mercury (II) could mediate thymine homobase pairs in DNA duplex with base mismatches.[29] More recently it was found that silver (I) can also mediate cytosine homobase pairs in a DNA duplex with base mismatches.[30,31] Metal-mediated base pairings in DNA have seen interesting applications for use in metal ion sensors,[32–34] DNA wires comprised of metal-mediated base pairs with increased conductivity for use in DNA based electronics,[35,36] and molecular switches where the activity of DNA nanostructures change based on the input of a metal cation and the resulting metal-mediated base pairs.[36–38]

Since Ag^+ has very low toxicity compared to Hg^{2+}, it is a promising subject for use in practical applications and further research in metal-mediated base pairings. Prior to the work done in this dissertation, most studies of Ag^+ with canonical bases have been confined to base mismatches in an otherwise WC paired duplex.[29–31,39] Previous work with guanine nucleotides and Ag^+ has suggested the possibility of an additional Ag^+-mediated base pairing in DNA,[40] making the exploration of Ag^+-mediated base pairings from single-stranded DNA an interesting avenue of investigation. The early chapters of this dissertation will focus on the interactions of Ag^+ with DNA, with the long-term aims of contributing to the development of more robust DNA nanotechnology utilizing Ag^+-mediated base pairings in conjunction with

WC base pairings. We hope this work will contribute to a better understanding of the interactions of Ag^+ with DNA towards the possibility of biomedical advances.

The interaction of DNA with metals provides a useful tool in DNA nanotechnology by using DNA as a nucleation site to form or extend metal nanoparticles.[41] This has resulted in the formation of conductive metal DNA wires,[42,43] sequence-dependent control of fine details in nanoparticle shape[44] and nanoparticles which conform to the shape of the DNA origami template.[45] A recent trend is to use DNA to template small fluorescent copper, silver and gold nanoclusters.[46] DNA templated silver clusters (Ag_N-DNA) are of particular prominence due to their desirable optical properties, which are coded by the DNA's sequence, including potentially high quantum yields and emission wavelengths spanning the visible into the near-infrared.[47] Ag_N-DNA's optical properties are sensitive to small changes in the DNA template's sequence where even a single base mutation can significantly change the wavelength of emission.[48]

Ag_N-DNA are formed by reducing a solution of DNA template strands and $AgNO_3$ with $NaBH_4$. Ag_N-DNA typically consist of 1-2 DNA strands and 10-30 silver atoms, of which some are neutral silver and some are cationic.[47] How the neutral and cationic silver interact, if at all, and where they are located on the DNA is not yet clear and remains an important question in understanding these promising fluorophores. There is growing evidence that the neutral cluster size is the property in Ag_N-DNA which is most closely correlated to Ag_N-DNA's wavelength of emission, with larger clusters resulting in a longer wavelength emission.[49,50] Additionally, Ag_N-DNA are suggested to have a unique rod-like shape.[49,51] Theoretical calculations for this rod-like shape are found to best describe the optical absorption spectra observed for purified solutions of Ag_N-DNA, and match much more closely with experimental

Ag_N-DNA data than calculations for globular clusters.[49] This theory is additionally supported by the existence of magic numbers in Ag_N-DNA, where certain sizes of clusters are more abundant due to the enhanced stability imparted by their electronic configurations.[51] The pattern of magic numbers for Ag_N-DNA theoretically matches with a non-globular, rod-like cluster.[51]

Ag_N-DNA are fluorophores with incredible potential. Currently many Ag_N-DNA have been found with good stability, high quantum yields and varied wavelengths of emission.[52] Most Ag_N-DNA have formed on DNA templates 10-30 bases in length, and even combining all current studies on Ag_N-DNA there has only been a tiny fraction of possible Ag_N-DNA with desirable properties discovered.[52] This is due to the vast sequence space that DNA has at these lengths, where the number of total number of sequences with N bases is 4^N. That is about 10^6 sequences at 10 base lengths and 10^{18} sequences at 30 base lengths. Most discovery of new Ag_N-DNA has relied on educated guessing to create the DNA template sequences, as there is currently no clear relationship between sequence and the type of Ag_N-DNA that is produced, if one is formed at all. Recent efforts in using machine learning to deconvolute the issue of DNA template sequence for forming "bright" Ag_N-DNA, Ag_N-DNA with high chemical and/or high quantum yields, have proven to be successful in addressing this issue.[53] Randomly generated 10 base long strands were used to synthesize Ag_N-DNA, and the strands which produced the brightest Ag_N-DNA (top 30% in integrated emission) were used as training data. Generating sequences predicted to form bright Ag_N-DNA from these machine learning techniques increased the overall brightness of formed Ag_N-DNA. The success rate increased from 30%, as defined by the training data, to 80%.[53] The last chapter in this dissertation will focus on trying to understand the finer details of the cluster structure in Ag_N-DNA and how the cationic silver is important to the formation of Ag_N-DNA. Typical chemical yields of Ag_N-DNA are low and their scalability remains a challenge.[47] We hope by better understanding the physical structure of Ag_N-DNA, we can integrate this understanding with machine learning techniques and achieve much higher yields of designed products.

In Chapter 2 of this dissertation we focus on elucidating binding mechanisms of Ag^+ with single-stranded DNA, a topic that had been largely unexplored in DNA composed of canonical bases. While a large amount of work has been done on metal-mediated base pairings with artificial bases,[54] DNA with canonical bases is currently ideal due to its commercially economical cost. We use 11 base long homopolymer strands of the four canonical bases A, C, G and T with Ag^+ to probe every possible Ag^+-mediated base pairing combination in tandem with electrospray-ionization mass spectrometry (ESI-MS). We find products in the mass spectra which consist of two DNA strands paired together by Ag^+ for two cytosine homobase strands, two guanine homobase strands and an adenine homobase strand with a thymine homobase strand. We find in addition to the previously known C-Ag^+-C base pairs a previously unknown G-Ag^+-G base pair in DNA from experimental Ag^+ to base binding ratios and theoretical evidence from calculations on Ag^+-mediated base pairs. We find the Ag^+-mediated homobase pairs are exceptionally thermally stable, with melting temperatures above 90ºC for 6 base long cytosine and guanine Ag^+-paired homobase strands. We also find evidence for A-Ag^+-T base pairs, albeit from products with lower abundances in mass spectra than products with C-Ag^+-C and G-Ag^+-G base pairs. The formation of G-Ag^+-G base pairs holds particular promise as an additional motif to use in DNA nanotechnology and may be an important avenue for further exploration in conjunction with biologically relevant G-quadruplexes.

In Chapter 3 we look at the potential of using Ag^+-mediated base pairings to form more robust Ag^+-mediated DNA nanotechnologies by exploring the properties of Ag^+-paired homobase cytosine and guanine strands of various lengths as well as Ag^+-paired mixed base strands. We find that Ag^+ can pair strands at a ratio of 1 Ag^+ per base pair from 2-20 bases long for cytosine homobase strands and from 6-20 bases long in guanine homobase strands using ESI-MS. With the correct ionic conditions these Ag^+-paired strands can form with a high degree of monodispersity as inferred from HPLC studies. Using CD spectroscopy we show that these Ag^+-paired strands can persist in high concentrations of Mg^{2+}, a common stabilizing ion used in the formation of DNA nanotechnology. Despite the strong precipitation reaction between Ag^+ and Cl^-, Ag^+-paired cytosine homobase strands persist even in 100 mM NaCl. We find a complex behavior in 11 base long Ag^+-paired strands composed of all guanine bases except for a centrally located single-point mutation. Apparently even one single-point mutation can lead to significant changes in the binding of Ag^+, causing most mutations to lead to an approximately 50% increase in the amount of bound Ag^+ at the same concentrations of Ag^+. More heterogeneous Ag^+-paired strands, with alternating runs of C and G bases, also show this trend of increased Ag^+ binding. Circular dichroism spectra (CD) which is very sensitive to secondary structure, does not show significant spectral differences between these Ag^+-paired heterogeneous base strands and Ag^+-paired cytosine and guanine homobase strands suggesting that the incorporation of the additional Ag^+ produces little change in secondary structure for these strands. Additional binding modes between base crossovers, which could produce local perturbations in structure rather than a different folded DNA form, is a possible explanation. Overall, long strings of Ag^+-paired cytosine bases seem most ideal in conditions with high chloride conditions, otherwise Ag^+-paired cytosine and guanine bases appear to be feasible for use in creating more robust DNA nanotechnology.

In Chapter 4 we elucidate structural information of Ag^+-paired cytosine and guanine homobase strands which is important for incorporation into DNA nanotechnology. Unfortunately, use of structurally sensitive techniques such as NMR and X-ray scattering is precluded by issues of aggregation, as mentioned in Chapter 3, at the high concentrations required by these techniques. As such, we first examine preferred strand orientation by using Förster energy resonance transfer (FRET). FRET is a process where one donor fluorophore non-radiatively transfers energy upon excitation to an acceptor fluorophore which can then either emit a photon or non-radiatively relax. This is particularly useful due to the strong distance dependent effect on the efficiency of FRET with chromophore separation, making it an extremely powerful tool in probing distances between dye-labelled sites on biological molecules. We harness this effect for use on Ag^+-paired strands with a 20 base long run of cytosine bases and a 15 base long run of guanine bases. For each experiment one strand was labelled with an acceptor dye on one end while two strands were labeled with a donor dye on opposite ends. We find that for both the Ag^+-paired strands with a long run of cytosine bases and a long run of guanine bases the preferred strand orientation is parallel. We further probe the general shape of Ag^+-paired homobase cytosine strands from 6-30 bases long and homobase guanine strands from 6-20 bases long by ion-mobility spectroscopy (IMS) ESI-MS. The data suggests that Ag^+-paired guanine strands have extended, linear shapes akin to a WC paired B-DNA duplex. The Ag^+-paired cytosine strands have more convoluted behavior with different trends at high and low magnitude charge states. At high magnitude charge states the Ag^+-paired cytosine strands seem to favor a more extended form, while at low magnitude charge states they seem to favor a more compact form. Even in their most compact forms the Ag^+-paired cytosine homobase strands still appear more expanded than G-quadruplexes with the same number of bases. Unfortunately, which charge state most faithfully reflects solution phase data is currently not clear. The additional details provided in this study of Ag^+-paired DNA structure will be useful to further the goal of creating more robust DNA technology with Ag^+-mediated base pairs.

In Chapter 5 we explore Ag_N-DNA silver cluster and DNA structure by using high performance liquid chromatography (HPLC) to isolate Ag_N-DNA with high purity and analyze them with CD spectroscopy. We use CD as a structural probe here since current Ag_N-DNA research is not at a point where upscaling to the concentrations required for more direct structural analysis techniques is feasible. While CD is sensitive to DNA secondary structure through relative orientations of the DNA bases, it is also a useful analytical tool to investigate chiral structures of other molecules. We find a strong CD signal in the visible to near-infrared spectral regions of Ag_N-DNA where there is no DNA absorbance, suggesting that the signal is coming from a chiral silver cluster. Comparison of the experimental CD shape and amplitude in these regions to theoretical calculations on chiral, neutral silver cluster wires finds good overall agreement, suggesting that the silver cluster is not only rod-like but also chiral. We additionally find similar spectral shapes between CD spectra of Ag_N-DNA and their corresponding template strands with unreduced Ag^+, suggesting that the secondary structure reorganization caused by Ag^+ is important to the formation of Ag_N-DNA. Finally, we discover an Ag_N-DNA that is very sensitive to its environment, displaying a reversible transition between a low and high fluorescence form depending on the solvent composition. This particular Ag_N-DNA is relatively unique in this behavior and could have promising sensor applications.

Chapter 2) Silver (I) as DNA glue: Ag^+-mediated guanine pairing revealed by re moving Watson-Crick constraints

Adapted with permission from: S. M. Swasey, L. E. Leal, O. Lopez-Acevedo, J. Pavlovich and E. G. Gwinn. Silver (I) as DNA glue: Ag^+-mediated guanine pairing revealed by removing Watson-Crick constraints. *Sci. Rep*. **2015**, 5, 10163.[55] *This work was published under the Creative Commons Attributions v4.0 International License.*

2.1) Introduction

The long-standing biochemical interest in metal-DNA interactions now extends into the field of DNA nanotechnology[56], where incorporation of strongly bound metal cations promises to realize more robust, diversely functional DNA-based materials.[54,57–59] This potential stimulated the recent development of artificial bases that form metal-mediated pairs bridged by Ag^+, Cu^{2+} and Hg^{2+}.[28,60–62] The identification of more diverse metal cation pairings of the natural bases could remove the need to incorporate expensive synthetic elements and amplify the impact of such metal-mediated pairings. Ag^+ is uniquely interesting because it exhibits unusually specific interactions with DNA, binding exclusively to natural bases rather than the negatively charged phosphate backbone (Hg^{2+} also associates exclusively with the bases, but is far more toxic).[59] The potential that Ag^+-DNA interactions hold for nanotechnology is already exemplified by the fluorescent, DNA-stabilized silver clusters[63,64] used recently in novel chemical and biochemical sensing schemes.[65] These nano-optical, DNA based materials are known to incorporate Ag^+ as well as neutral silver atoms,[49] indicating that Ag^+-DNA interactions are key to stabilizing the fluorescent clusters. In addition to the previously known bridging of cytosine (C) bases by Ag^+,[30,66] the formation of fluorescent silver clusters on homobase guanine (G) strands of DNA and RNA,[67] the Ag^+ induced dimerization of individual modified guanine bases in non-aqueous solution[68] and the Ag^+-mediated assembly of guanosine monophosphate[40] suggests that Ag^+ might also bridge G bases in DNA oligomers. In biochemistry, the strong interactions of G bases with Pt^{2+} are thought to be key to important chemotherapy drugs.[69,70] Thus the discovery of stable Ag^+-G binding might find use in treatment of disease associated with mutations. Ag^+-base interactions may also underlie the antimicrobial action of silver nanoparticles.[71] The known biochemical roles of metal cations suggest that a better understanding of how Ag^+ binds to the natural DNA bases could aid future development of disease therapeutics.

Despite this compelling potential, surprisingly little is known about how Ag^+ interacts with the natural bases when DNA is not conformationally constrained by the canonical Watson-Crick (WC) hydrogen bonding of adenine (A) to thymine (T) and C to G. Early studies of biological double-stranded (ds) DNA could not unravel the diversity of base-Ag^+ interactions due to the mixed A, C, G and T composition.[72–78] More recent studies of synthetic dsDNA used the insertion of single-base mismatches to examine which bases could be bridged by Ag^+, when subject to the conformational constraints of the WC-paired surroundings.[30,39,79] In addition to C-Ag^+-C, evidence for a C-Ag^+-A pair has been reported,[80] while the recent experimental literature is conflicting on the possibility of C-Ag^+-T pairing,[39,79] and mostly silent regarding Ag^+ interactions with G in DNA.[81] Prior computational studies of Ag^+-base interactions have been challenged by the plethora of possible binding geometries, especially for G,[82–86] and have focused largely on binding geometries compatible with WC-like structure.

Although many prior studies have focused on Ag^+ incorporation into a canonical dsDNA environment, there is no *a priori* reason to assume that base pairing by hydrogen bonding will persist in the presence of Ag^+. The dominant mode of binding must depend on the affinities and geometries of Ag^+-base interactions relative to WC pairing. Here we remove the constraint of WC pairing by focusing on homo-base deoxyoligonucleotides and mixtures of these A_N, C_N, G_N and T_N strands, for strand lengths N=6 to N=20 bases (Figure 2.1a), at neutral pH. We use relative abundances in electrospray ion mass spectrometry (ESI-MS) to determine the ordering of Ag^+ affinities to each homo-base strand. The competition of Ag^+-mediated base pairing with WC pairing is tested by studies of the mixed complementary strands. Through quantum chemical calculations that explore an unrestricted space of binding geometries, we find that the order of binding energies (BE) for the most stable Ag^+-bridged homobase complexes agree with abundance trends in ESI-MS data. Strikingly, experiments show that G_N strands form fully Ag^+-paired strands, G_N-$(Ag^+)_N$-G_N, that are more stable than the WC paired C_N-G_N duplex.

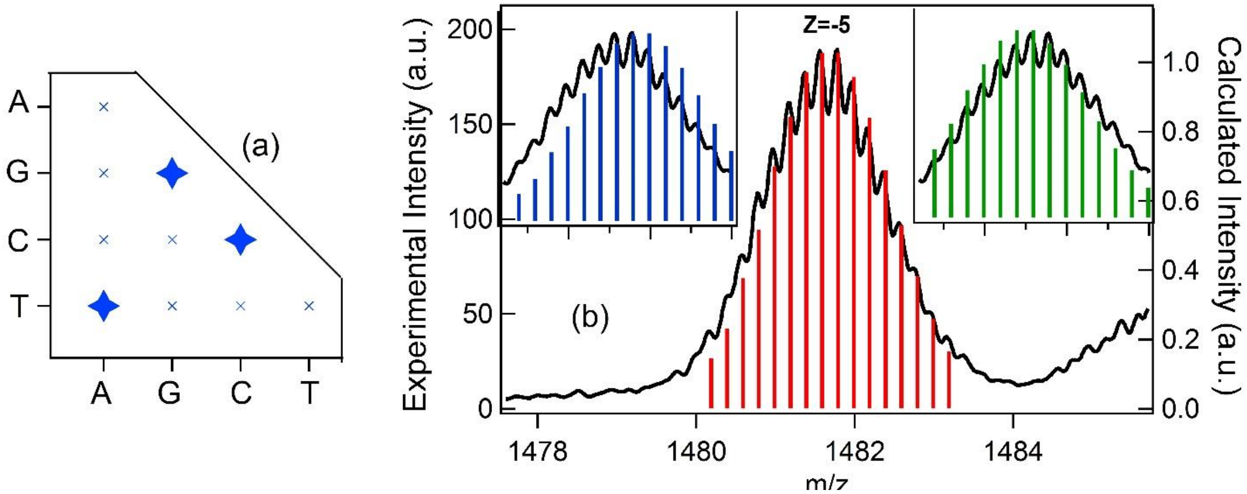

Figure 2.1) (a) Schematic of the homo-base strand types and combinations studied. Stars denote the detected Ag^+-paired strands. (b) Example of isotope peak envelope resolved in MS for C_{11}-$(Ag^+)_{11}$-C_{11}. Black lines: data. The total mass of the ionized species (m) is given by $m = m_{DNA} + m_{Ag}N_{Ag} - n_{pr,}$ where m_{DNA} is the mass of the unionized DNA strand, $m_{Ag}N_{Ag}$ is the mass of the total silver content, and n_{pr} is the number of protons removed by negative mode electrospray ionization. The charge state, z (negative) of the ionized species is $z = Q_{Ag}/e - n_{pr}$, where Q_{Ag} is the total charge associated with the silver content. Bars show the calculated isotope peak patterns for a net charge on the silver content of Q_{Ag} = +10e (blue), +12e (green)(insets) and +11e (red). The best fit at a charge of +11e confirms that all of the attached silver atoms are cations, Ag^+.

2.2) Results and Discussion

2.2.1) Detection of $(Ag^+)_N$-DNA products by ESI-MS

We use high-resolution, negative ion ESI-MS to determine the composition of complexes formed by Ag^+ attachment to the homo-base oligomers. ESI-MS is a powerful tool for detecting non-covalently bound molecules to DNA in solution[87] and for investigating solution binding stoichiometries to DNA.[88] Our use of high-resolution MS resolves the isotope peak envelopes (Figure 2.1b), which enables determination of absolute composition, not just the ratio of silver cations per base (stoichiometry). This is important for unambiguous determination of strand dimerization by Ag^+. By fitting the calculated isotope peak envelope to the MS data,[49,51,89] we find that all of the attached silver atoms are cationic (Ag^+), as expected.

To investigate the possible disruption of WC pairing by Ag^+, we combined C_{11} with G_{11}, and A_{11} with T_{11}, at 40 µM/strand in 10 mM ammonium acetate (pH 7). Mass spectra of the mixture of C_{11} and G_{11} strands (Figure 2.2a) show the expected peaks for the WC-paired C_{11}-G_{11} duplex, with additional peaks for the individual C_{11} and G_{11} strands (Appendix A.1). After addition of 0.5 Ag^+ per base, the C_{11}-G_{11} duplexes entirely vanish from the mass spectra (Figure 2.2b). New peaks appear for Ag^+-decorated strand monomers, C_{11}-$(Ag^+)_N$ and G_{11}-$(Ag^+)_N$; and for Ag^+-paired homobase strands, C_{11}-$(Ag^+)_N$-C_{11} and G_{11}-$(Ag^+)_N$-G_{11}. Strikingly, there were no detectable C_{11}-$(Ag^+)_N$-G_{11} *hetero*base Ag^+-paired strands or triplex products (Figure 2.2c). If present, such products are at too low concentration to produce detectable ion currents, while the Ag^+-paired homobase strands are present in concentrations that result in high ion currents. We infer that the binding of Ag^+ in G_{11} or C_{11} Ag^+-paired strands is more stable than canonical WC pairing of G_{11} to C_{11}, and also more stable than C_{11}-$(Ag^+)_N$-G_{11}

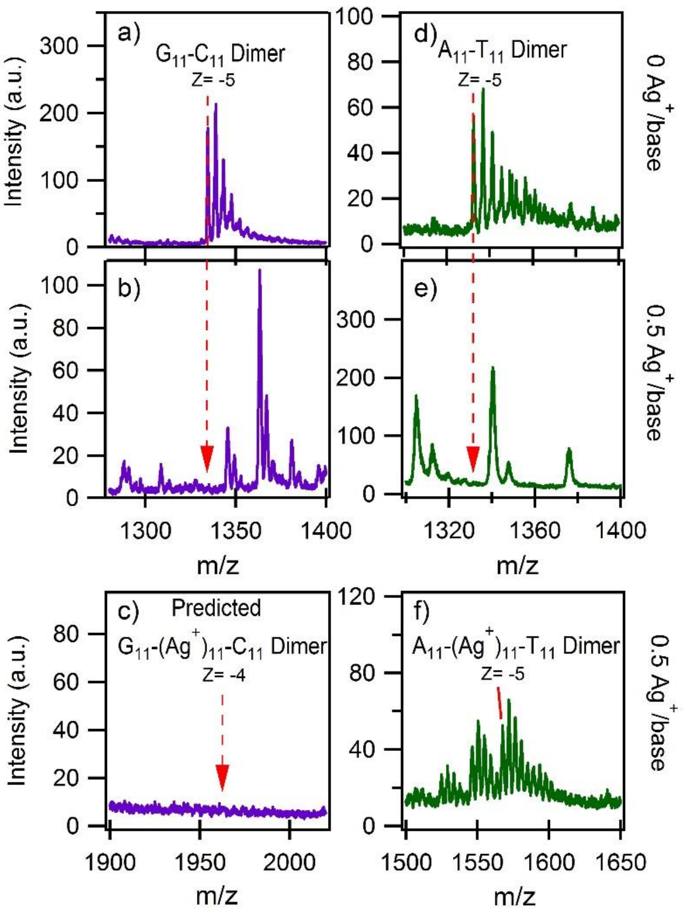

Figure 2.2) Effects of Ag^+ on solutions of mixed C_{11} and G_{11} (**a**)-(**c**), and solutions of mixed A_{11} and T_{11} (**d**)-(**f**), at 40 µM per strand. (**a**) Mass spectra (MS) of the C_{11}-G_{11} mixture at 0 Ag^+/base and (**b**) 0.5 Ag^+/base. Dashed line: m/z for the WC paired G_{11}-C_{11} duplex, present in the absence of Ag^+ (a) but undetectable after adding Ag^+ (b). The peak envelope to higher m/z in (a), (d) and (f) is attachment of Na^+ from residual salts. (**c**) No G_{11}-$(Ag^+)_N$-C_{11} products were detected, for N= 1-11, as exemplified by the absence of G_{11}-$(Ag^+)_{11}$-C_{11} (expected at dashed line). (**d**) MS of A_{11}-T_{11} mixture at 0 Ag^+/base and (**e**) 0.5 Ag^+/base. Dashed line: m/z for the WC paired product showing no detectable signal after adding Ag^+. (**f**) A_{11}-$(Ag^+)_N$-T_{11} products did form, exemplified by A_{11}-$(Ag^+)_{11}$-T_{11} (dashed line). Additional, unlabeled peaks in (b) and (e) are various $(Ag^+)_N$-DNA products (see Appendix A.1).

pairing. For A_{11}-T_{11} (Figure 2.2d), WC-paired strands were undetectable after addition of 0.5 Ag^+ per base (Figure 2.2e), but A_{11}-$(Ag^+)_N$-T_{11} products were detected (Figure 2.2f) as well as A_{11}-$(Ag^+)_N$. There were no detectable A_{11}-$(Ag^+)_N$-A_{11} or T_{11}-$(Ag^+)_N$-T_{11} products. Measurements on every strand combination (Figure 2.1a) found A_{11}-$(Ag^+)_N$-T_{11} as the only detectable Ag^+-paired heterobase product. Apparently the favored mode of attachment of Ag^+ to A_{11} is incompatible with Ag^+-paired homobase strand formation under these solution conditions. Other, less stable Ag^+-paired heterobase strands may exist but be reduced to undetectable levels by formation of C_{11}-$(Ag^+)_N$-C_{11}, G_{11}-$(Ag^+)_N$-G_{11} and A_{11}-$(Ag^+)_N$ instead.

To better understand the patterns of Ag^+ attachment, we investigated the products formed on all individual strands at Ag^+/base ratios of 0.5, 0.75 and 1.0. Figure 2.3a-l show the integrated counts (IC) measured for the highest abundance charge state, z_{max}, of the strand monomer (z_{max} = -3 or -4) and Ag^+-paired strand (z_{max} = -5 or -6) products. Figure 2.3m,n show full spectra for C_{11} and G_{11} at 1 Ag^+/base (Appendix A.2-A.4 show all other full spectra). The IC provide a semi-quantitative comparison of the relative abundances of Ag^+-DNA products (IC do not give quantitative product yields due to dependence of count rates on z and the possibility of unbinding events during ESI). The small shifts in Ag^+/strand stoichiometry from 0.75 to 1.0 Ag^+/base suggest that the silver binding to DNA is near saturation. For T_{11}

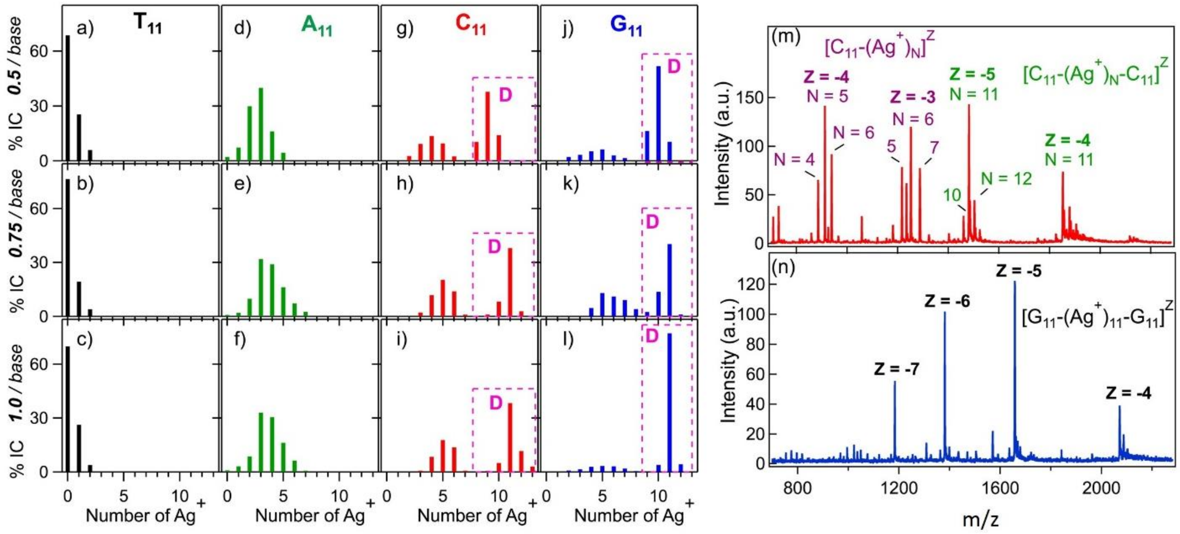

Figure 2.3) (**a-l**) Percentage of the total integrated counts (%IC) for each detected Ag^+-bearing DNA product plotted *versus* number of attached Ag^+. *Top, middle and bottom rows*: solutions with 0.5, 0.75 and 1 Ag^+/base. Product yields are qualitatively different depending on base type. The boxed peaks labeled "D" are Ag^+-paired strands, containing two copies of the strand. All other peaks correspond to strand monomers. Data are for the highest abundance charge state of each product. (**a-c**) T_{11} solutions exhibit the bare strand as the major product. (**d-f**) A_{11} shows a range of Ag^+ attachment to strand monomers and no Ag^+-paired strands. (**g-i**) C_{11} exhibits strand monomer and Ag^+-paired products. (**j-l**) G_{11} products are heavily biased to Ag^+-paired strands. The Ag^+-paired product with 11 bridging Ag^+, G_{11}-$(Ag^+)_{11}$-G_{11}, is the overwhelming majority product at 1 Ag^+/base (l). (**m,n**) Mass spectra of C_{11} and G_{11} solutions at 1 Ag^+/base, corresponding to % IC plots i) and l). Major peaks are labeled.

(Figure 2.3a-c), the dominant product at all Ag^+/base was the bare strand. A_{11} formed a wider range of strand monomer products, with A_{11}-$(Ag^+)_3$ dominant (Figure 2.3 d-f). It appears that A_{11} binds Ag^+ more stably than T_{11}, as expected at neutral pH.[90]

For C_{11} (Figure 2.3g-i,m), dominant products at the higher Ag^+ concentrations were C_{11}-$(Ag^+)_{11}$-C_{11}, corresponding to Ag^+ bridging each pair of C bases, and the strand monomer product $C_{11}(Ag^+)_5$. The presence of the Ag^+-paired C_{11} strands (dashed boxes labeled "D", Figure 2.3g-i) agrees with previous circular dichroism (CD) studies that suggested Ag^+-induced dimerization of a C_8 strand[91].

Mass spectra for G_{11} (Figure 2.3j-l, n) exhibit narrower product distributions than for C_{11}. The fully Ag^+-paired strand, G_{11}-$(Ag^+)_{11}$-G_{11}, dominates overwhelmingly at 1 Ag^+/base (Figure 2.3l, n). Small amounts of strand monomer G_{11}-$(Ag^+)_N$ products are still detectable, but in much reduced abundances relative to strand monomer Ag^+-C_{11} products. Results were similar for C_N and G_N strands with N = 6 and 20 (Appendix A.5).

The relative abundances in Figure 2.3 reflect the partitioning of Ag^+ between the solvent and the various Ag^+-DNA products. The hydrated state of the Ag^+ in solution is the same in all cases. If the hydrated Ag^+ has lower free energy than the Ag^+-DNA complexes, the bare DNA strand will be the major product. This is the case for T_{11}, for which the bare strand comprises ~70% of all products. For A_{11} the bare strand is still detectable, but as only 1-2% of all products. This indicates that the hydrated Ag^+ is no longer the thermodynamically favored state and consequently, that the complexes of Ag^+ with A_{11} have lower free energy than the complexes of Ag^+ with T_{11}. For C_{11} and G_{11}, the bare strand is undetectable, indicating a further lowering in free energy of the complexes of Ag^+ with C_{11} and G_{11}. The fully Ag^+-paired G_N-$(Ag^+)_N$-G_N product appears to be the most stable of all Ag^+-G_N complexes. The higher presence of Ag^+-

paired strands relative to monomer strand products for G_N than for C_N may indicate a reduced propensity for strand self-folding around Ag^+ for the larger G base. To our knowledge this is the first study to detect Ag^+-mediated pairing of guanine bases in DNA, a possibility that has not been investigated previously without the imposition of structural constraints from canonical WC pairing.

2.2.2) Thermal stability of silver mediated DNA homobase duplexes.

To investigate thermal stability we carried out circular dichroism (CD) studies of C_6 and G_6. The solutions contained 1 Ag^+/base (pH 7) at DNA concentrations of 17 µM. Ag^+-paired homobase products remain abundant at this concentration in mass spectra (Appendix A.6). In the absence of Ag^+, the C_6 solution (Figure 2.4a; black dashed line) shows the expected peak structure for predominantly unstructured cytosine oligonucleotides.[92,93] The peak structure of the G_6 solution (Figure 2.4b) indicates some presence of parallel G-quadruplex type structures.[94,95] With Ag^+, the CD spectra are dramatically altered by base-Ag^+ interactions (Figure 2.4). Remarkably, the Ag^+-imposed structure persists to the highest temperature we investigated, 90ºC (red curves). For comparison, t5he nearest-neighbor two-state model

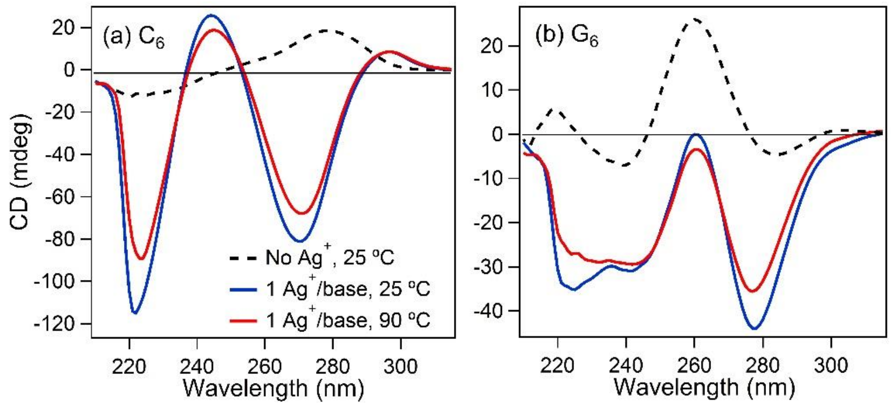

Figure 2.4) Circular dichroism (CD) spectra of C_6 (**a**) and G_6 (**b**). Dashed black lines: data for the bare strands at 25 ºC. Blue lines: with 1 Ag^+/base at 25 ºC. Red lines: with 1 Ag^+/base at 90 ºC. The restructuring of the CD spectra upon addition of Ag^+ reflects the reconfiguration of the DNA by incorporation of Ag^+. Persistence of the dichroic peaks to the highest temperature accessible experimentally shows that this structural change is thermally robust.

calculated melting temperature (mfold) for the C_6-G_6 duplex formed by canonical WC pairing is 16 ºC for the low ionic conditions in Figure 2.4. Apparently Ag^+-bridging of G to G and C to C bases is much more stable than canonical WC pairing. DNA nanotechnology is currently limited by the low thermal melting temperatures imposed by Watson-Crick pairing. This discovery of highly stable Ag^+-mediated pairing of G bases in DNA, in addition to the previously known C-Ag^+-C pairing, has promise to broaden the range of applications for DNA nanotechnology and may also impact development of disease therapeutics based on metal-DNA interactions.

2.2.3) Quantum chemical calculations of binding strengths and geometries.

For theoretical investigation of the geometries and stabilities of Ag^+-mediated base pairing, we consider two bases and a silver atom in vacuum with the charge of the entire system set to +1. To calculate the electronic ground state we used density functional theory with a real space basis and the projector-augmented wave method.[96] The exchange correlation functional PBE+TS09 was chosen to account for van der Waals dispersion inter-actions.[97,98] The grid spacing was 0.18 Å and the calculation was spin-polarized. Per atom, the electronic

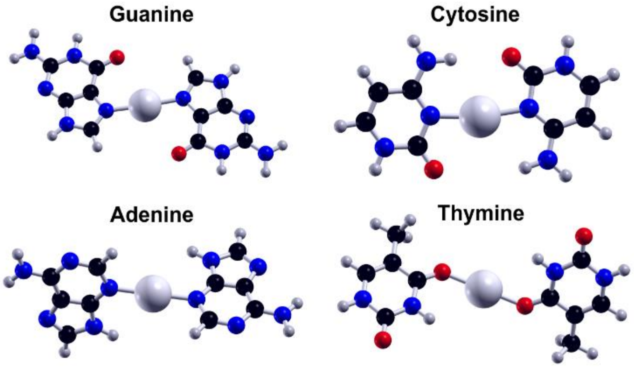

Figure 2.5) Calculated ground state geometries of Ag^+-mediated homobase pairs. Binding energies decrease in the order G>C>A>T (see text). G-Ag^+-G and C-Ag^+-C are planar, while A-Ag^+-A and T-Ag^+-T are non-planar.

configuration of the valence electrons are H($1s^1$), O($2s^22p^4$), C($2s^22p^2$), N($2s^22p^3$), Ag($4p^64d^{10}5s^1$), including a scalar relativistic correction and a frozen core. We also report CAM-B3LYP binding energies (BE) calculated with the Gaussian code[99] and a LANL2DZ/ECP basis set for the silver atom and 6-311+G(d,p) for the rest.

Starting from many initial geometries (Appendix A), a global search is performed *via* force optimization using the Hessian matrix (BFGS algorithm in ASE) until the residual force is below 0.02 eV/Å. To verify that the relative ordering of Ag^+-mediated BE is invariant with functional, CAM-B3LYP/6-311+G(d,p) was used. The same ordering as PBE+TS09 is obtained (Appendix A).

Figure 2.5 shows the calculated ground state geometries for the Ag^+-bridged bases. Bond lengths and dihedral angles are specified in Appendix A, along with the geometries of higher-lying structures. For homo-base pairs bridged by Ag^+, the calculated BE, defined as the sum of the energy of fragments minus the energy of the complex, are 129.7, 126.2, 111.9, and 91.5 kcal/mol for G-Ag^+-G, C-Ag^+-C, A-Ag^+-A and T-Ag^+-T, respectively. These BE are all higher than those for attachment of Ag^+ to the individual bases, calculated in prior work to be to be 77.08, 71.16, 60.30 and 51.19 kcal/mol for the most stable G-Ag^+, C-Ag^+, A-Ag^+ and T-Ag^+ complexes, respectively (in the most stable C-Ag^+ and G-Ag^+ configurations, the silver coordinates to two binding sites on one base[100]). With respect to prior work with PBE only functional, the BE is very close and ordering is the same. The pairing of bases by Ag^+ and the attachment of Ag^+ to individual bases show the same base-dependent ordering of BE, G ~ C > A > T.

In the absence of interfering steric factors, the higher BE for base-Ag^+-base pairing than for individual base-Ag^+ binding should result in higher yields of Ag^+-paired strands than strand monomer products with Ag^+. However, experimentally we observe Ag^+- paired homobase strands only for G_N and C_N (Figure 2.3; dashed boxes labeled "D"). The calculated ground state structures are consistent with this experimental observation. The bases in the G-Ag^+-G ground state are very nearly coplanar, with dihedral angle $\theta = 181.2^o$, and close to co-planar for C-Ag^+-C ($\theta = 171.9^o$), as required to permit base-stacking interactions in Ag^+-paired DNA strands containing multiple bases. In contrast, for A-Ag^+-A and T-Ag^+-T the ground state structures have highly non-coplanar bases with $\theta = 101.6^o$ and 140^o, respectively. Such a twisted geometry would disrupt base-stacking and sterically hinder the formation of Ag^+-paired homobase strands of A and of T bases, consistent with the absence of these products in data (Figure 2.3). We expect that the small (~ 10^o) calculated rotation of the base planes in C-Ag^+-C may account for the relatively high presence of strand monomer complexes, C_N-$(Ag^+)_m$, in Figure 2.3. Overall, the stoichiometric abundances of Ag^+ bound to bases in Figure 2.3 agree with the ordering of the calculated BE, G ~ C > A > T.

Our calculations find that in G-Ag^+-G, Ag^+ binds through the N7 atom of G, a site that does not engage in WC pairing (Figure 2.5; see Appendix A.7 for site numbering). This can account for the non-detection of G-Ag^+-G pairing in prior studies of single G base mismatches within otherwise WC-paired duplexes, in which the canonically-paired surroundings restricted presentation of the mismatch bases.[39] In C-Ag^+-C, we find that Ag^+ bridges the N3 atom of the C bases. This site also participates in WC pairing, consistent with the observation of Ag^+-pairing of C base mismatches in earlier work on WC duplexes.[39] For both G-Ag+-G and C-Ag+-C, hydrogen bonding helps stabilize the complexes. We note that G-Ag^+-C has a comparable predicted BE (Appendix A), with nearly co-planar bases. Presumably factors that are beyond the present calculations, specifically base stacking and solvation, cause the preferential formation of G_{11}-$(Ag^+)_{11}$-G_{11} and C_{11}-$(Ag^+)_{11}$-C_{11} rather than C_{11}-$(Ag^+)_{11}$-G_{11} (Figure 2.2).

Our calculations for binding energy (BE) contribute to the enthalpy only while unaccounted entropic costs of complex formation also contribute to relative solution abundances. For canonical WC duplexes, it is well-known that the entropic costs of duplex formation substantially compensate the enthalpic contributions to the free energy.[101,102] However, the free energy and the enthalpy correlate, as evidenced by higher melting temperatures for canonical G-C rich duplexes compared to A-T rich duplexes. Because the BE of the Ag^+-bridged bases are substantially higher than for canonical WC pairing (25.5 kcal/mol for G-C and 13.5 kcal-mol for A-T with PBE+TS09, respectively), we expect that the relative solution free energies of base-Ag^+-base products will have the same ordering as the calculated BE if the calculated ground state geometries are consistent with formation of helices and the hydration free energies of the Ag^+-paired strands are similar to each other (as is the case for canonical duplexes of varying composition).[103] For the homobase, Ag^+-paired strands, relative experimental abundances (G~C>A>T) are consistent with the ordering of the calculated BE. The narrower product distribution for G-Ag^+-G complexes (which are heavily dominated by G_{11}-$(Ag^+)_{11}$-G_{11}) than for C-Ag^+-C complexes may reflect greater solvent stabilization associated with the higher solvent accessible area for the larger G base, and greater stacking tendencies.

For the heterobase Ag^+-paired strands, the lowered symmetry in steric properties adds additional complexity. The data for mixed A_{11}-T_{11} (Figure 2.2 and Appendix A.1b) show T-Ag^+-A heterobase complexes but no T or A homobase duplexes. For T-Ag^+-T, this is consistent with the lower calculated BE (91.5 kcal/mol) than for T-Ag^+-A (102 kcal/mol); however for

A-Ag$^+$-A, the calculated BE (111.9 kcal/mol) is ~ 10 kcal/mol higher than for the hetero-base complex. We expect that the non-planar calculated structure of A-Ag$^+$-A (Appendix A) may be destabilizing relative to A-Ag$^+$-T when stacking and hydration are included, accounting for the absence of A-Ag$^+$-A in the data (A-Ag$^+$-T is also calculated to be non-planar, but given the small size of the T base there may still be A stacking). In the case of the mixed C_{11}-G_{11} (Figure 2.2), the predicted BE of G-Ag$^+$-C (130.95 kcal/mol) is similar to G-Ag$^+$-G (129.72 kcal/mol) and C-Ag$^+$-C (126.18 kcal/mol) but the heterobase complexes are not detectable in the data for mixed G_{11} and C_{11} strands. The differences in hydration and stacking free energies may be what is dictating the preferential formation of homobase complexes. We also note that previous experimental work has detected C-Ag$^+$-G pairings[81], but only within hydrogen-bonded triplexes stabilized by multiple inter-strand T-A-T triplet pairings, with facing C bases embedded in the T-rich regions and facing G bases in A-rich regions. The homobase oligomers studied here provide an entirely different context.

2.3) Conclusions

In conclusion, our experimental studies of homobase strands of DNA have identified an Ag$^+$-mediated pairing of guanine bases in homobase oligonucleotides. This discovery of the highly stable, silver-mediated pairing of G bases in DNA expands the diversity of known nontoxic metal-mediated interactions with natural DNA bases. Our complementary calculations do not constrain Ag$^+$ to attach at base sites that correspond to WC pairing. Instead the unrestricted binding configurations identify that the most stable Ag$^+$ attachment in G-Ag$^+$-G pairs is to base sites that do not engage in WC pairing. Our results suggest that in mixed base, double stranded DNA with long enough runs of consecutive C or G bases, addition of sufficient Ag$^+$ should reconfigure WC pairing to more stable Ag$^+$-mediated base pairing. This expansion of the known interactions between silver cations and DNA bases paves the way for more robust DNA nanotechnology and for potential applications in biomedical science.

2.4) Methods

2.4.1) DNA preparation.

DNA oligonucleotides were synthesized by Integrated DNA Technologies with standard desalting. We solvent-exchanged the strands to remove residual salts. All solutions used RNase/DNase-free distilled water (Life Technologies). $AgNO_3$ was analytical grade (Sigma-Aldrich). Before each analysis, strands with and without Ag^+ were annealed to 90°C for 5 minutes and allowed to cool to room temperature over 30 minutes.

2.4.2) Mass spectrometry experiments.

Samples for ESI-MS used 80 μM single-stranded DNA concentrations in 10 mM ammonium acetate buffer. Solutions of DNA with Ag^+ contained a ratio of 0.5, 0.75 or 1.0 $AgNO_3$ per base. The oligonucleotide solutions were injected into the MS (Waters QTOF2) at 10 μL/min in ESI negative mode with a 2 kV capillary voltage, 30 V cone voltage and 10 V collision energy. The signal was integrated over approximately 5 minutes.

2.4.3) Circular dichroism experiments.

Samples for CD experiments used 17 μM single-stranded DNA concentrations in 7.5 mM MOPS buffer (pH=7.0) containing approximately 2.5 mM Na^+. All measurements were collected on an Aviv 202 circular dichrometer. For the measurements at 90°C, the samples were heated at a rate of 3°C/min and allowed 10 minutes to equilibrate at 90°C before taking the full spectra. Blanks containing the appropriate concentration of buffer were collected before and after the samples, averaged and then subtracted from the sample spectra to correct for background signal.

Chapter 3) Silver-mediated base pairings: towards dynamic DNA nanostructures with enhanced chemical and thermal stability

Adapted with permission from: S. M. Swasey and E. G. Gwinn. Silver-mediated base pairings: towards dynamic DNA nanostructures with enhanced chemical and thermal stability. *New J. Phys.* **2016**, 18, 045008.[104]

3.1) Introduction

The thermal, chemical and mechanical fragility of DNA nanomaterials assembled by Watson-Crick (WC) pairing constrain how these structures can be functionalized and the settings in which they can be used. For example, WC-paired linker stability and charge repulsion limit the achievable packing densities of metal nanoparticles on DNA origami,[105,106] and the delicacy of tile-assembled DNA nanotubes leads to tube-opening ruptures in AFM imaging.[107,108] Chemical compatibility is another limiting factor: denaturing conditions are inhospitable to WC paired structures, while dilution on repeated operation limits the performance of dynamic DNA nanostructures that employ strand displacement reactions on toehold designs.[25,26] New approaches to DNA self-assembly and dynamic manipulation of DNA structures are needed to overcome these types of limitations.

Due to the special interactions of silver (I) cations with the nucleobases,[57–59,72,109] DNA assemblies that incorporate Ag^+ provide a possible route to more robust, self-assembled DNA materials that can survive in new settings. Silver is quite unusual amongst metal cations for its specific interaction with the nucleobases, rather than the sugar-phosphate backbone (Hg^{2+} also associates exclusively with the bases, but its toxicity makes it undesirable for general self-assembly schemes).[59,72] This special property of Ag^+ has already been exploited for metallization of DNA by chemical reduction after the addition of Ag^+ to DNA solutions.[110,111] As discussed in recent review articles[47,65] much of the current effort on metal-DNA assemblies is focused on fluorescent silver clusters whose colors are selected by the DNA oligomer template.[64,112,113] In such "Ag_N-DNA," roughly half the silver content is neutral, presumably forming the cluster core, with the remainder as cations (Ag^+) that may serve to attach the cluster core to the bases.[49,51] Thus base-Ag^+ interactions appear to be a key feature of fluorescent Ag_N-DNA and are likely to be generally important in other settings involving metallic silver in intimate contact with DNA.

Rather than as a step towards metallization, here we are primarily interested in the potential of Ag^+ for self-assembly of new, more robust types of DNA nanostructures. Ag^+ incorporation has already been used to increase the melting temperature of canonical duplexes with sparse insertions of C-C mismatches.[30,39] Ag^+ is also known to assemble Ag^+-paired homobase DNA *via* non-canonical, Ag^+-bridged pairings of guanine (G) or cytosine (C) bases.[91,114] Recent quantum chemical calculations found high binding energies for C-Ag^+-C and G-Ag^+-G pairs, roughly four times larger than for native C-G base pairs (see Chapter 2). These prior findings suggest that Ag^+-bridged pairings of the natural bases may provide a route to more robust DNA nanostructures, without the need for expensive artificial bases and/or backbone modifications.

Important unresolved issues for using Ag^+-mediated self-assembly in DNA nanotechnology include the types of base motifs suitable for such metal-mediated pairings and the length of Ag^+-paired regions needed for stability. Currently, only two motifs that form Ag^+-paired strands have been identified, specifically homobase runs of G bases as seen in Chapter 2 and homobase runs of C bases.[91] If this were the complete set of base motifs capable of forming Ag^+-mediated assemblies, it would not be possible to go beyond the simplest Ag^+-assembled structures. Thus the usefulness of Ag^+ in future DNA nanotechnology hinges on the yet-to-be established existence of sufficiently diverse base motifs for Ag^+-paired structural elements to enable low-error assembly at an interesting degree of structural complexity. Achieving sufficient yields of designed products will also require identification of solution conditions that realize planned Ag^+ strand pairings while suppressing undesired byproducts. Because combining Ag^+-mediated and WC pairings would maximize design flexibility, it is important to identify solution conditions compatible with sequential stages of Ag^+ assembly and WC assembly. In addition, Ag^+ pairings may permit DNA scaffolds to have spatial resolutions finer than the 10-15 base pair "sticky ends" currently used in dynamically responsive, WC paired DNA structures.[115] Thus it is important to determine whether Ag^+-paired motifs can remain robust at significantly fewer paired bases than required for stable WC pairings.

Here we select simple base motifs that enable a first study of these issues (Table 3.1). To explore the length of Ag^+-paired regions needed for stability, we study short strands of all C and all G bases. To examine the issue of motif diversity, we employ length 11 oligomers with a central heterobase within an all C or all G strand context. At the outset, it is unclear whether such heterobase crossovers will be destabilizing, by inhibiting Ag^+ incorporation; or stabilizing, by enhancing Ag^+ incorporation. This issue has not been explored previously in experiment or theory, and is not amenable to simple predictions due to the wide diversity of possible binding geometries as described in Chapter 2 and other works.[100] To determine whether stable Ag^+-paired strand formation can be preserved by short C and G repeat motifs, we study 12 base strands with a 4 base separation between two, non-adjacent base crossovers. To examine the effects of a higher crossover content, we study one exemplary strand with 5 heterobase crossovers. We use circular dichroism (CD) spectroscopy to probe for changes in Ag^+-paired structure relative to the homobase context. As a testbed for developing solution conditions that select for formation of Ag^+-paired structural motifs (in preference to strand monomer byproducts), we use 20-24 base strands that also enable tests of the structural stability of Ag^+-paired strands in the presence of additional salts required by DNA nanotechnology schemes such as origami. This is important for determining whether future self-assembly schemes could combine sequential Ag^+-mediated and Watson-Crick mediated stages. These longer strands additionally serve to probe the stability of Ag^+-mediated pairings in the presence of a chemical denaturant, urea, which has interesting potential for suppressing WC pairing during Ag^+-mediated assembly stages for future strand sets designed to form structures that incorporate both types of pairings.

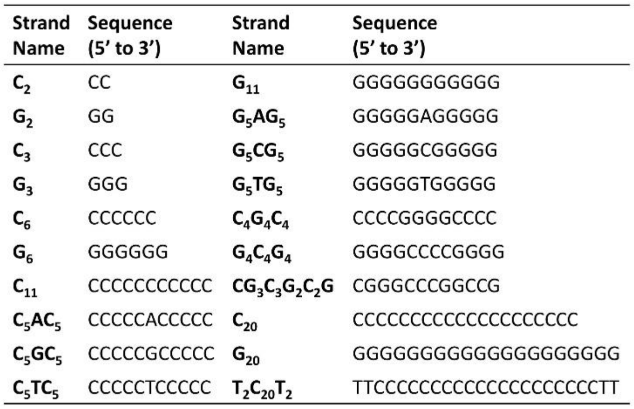

Strand Name	Sequence (5′ to 3′)	Strand Name	Sequence (5′ to 3′)
C_2	CC	**G_{11}**	GGGGGGGGGGG
G_2	GG	**G_5AG_5**	GGGGGAGGGGG
C_3	CCC	**G_5CG_5**	GGGGGCGGGGG
G_3	GGG	**G_5TG_5**	GGGGGTGGGGG
C_6	CCCCCC	**$C_4G_4C_4$**	CCCCGGGGCCCC
G_6	GGGGGG	**$G_4C_4G_4$**	GGGGCCCCGGGG
C_{11}	CCCCCCCCCCC	**$CG_3C_3G_2C_2G$**	CGGGCCCGGCCG
C_5AC_5	CCCCCACCCCC	**C_{20}**	CCCCCCCCCCCCCCCCCCCC
C_5GC_5	CCCCCGCCCCC	**G_{20}**	GGGGGGGGGGGGGGGGGGGG
C_5TC_5	CCCCCTCCCCC	**$T_2C_{20}T_2$**	TTCCCCCCCCCCCCCCCCCCCCTT

Table 3.1) Strand names and corresponding sequences.

Here we find that widely varying C- and G-rich base motifs can be paired by Ag^+. Under optimized solution conditions, Ag^+-mediated assembly results in paired DNA products with narrowly distributed numbers of attached Ag^+, indicating suitability as building blocks in more elaborate structures. CD spectroscopy suggests simple helical structures for both homobase and heterobase Ag^+-paired strands, although base mutations inserted between long homobase G runs may produce a different structure. For C-rich strands, high stability is exhibited in urea and with added salts, while G-rich sequences display more varied behaviors. We propose simple prototype assemblies to indicate how Ag^+ could be used in dynamic DNA structures that preserve strand content by combining both WC and Ag^+-mediated pairings.

3.2) Results and Discussion

Predictable formation of all but the simplest Ag^+-paired DNA structures will require diverse base motifs that produce well-defined Ag^+-mediated pairings. Therefore the distribution of Ag^+-bound products formed by multi-base motifs is a crucial issue. Here we use negative ion electrospray-ionization mass spectrometry (ESI-MS) to identify the composition of the Ag^+-DNA products that form on oligonucleotides with wide-ranging lengths and compositions (Table 3.1).

In ESI, non-equilibrium ionization processes involving a series of Coulomb explosions ultimately yield the desolvated ion that is detected in MS. In principle this can result in product distributions that differ from those in solution. However due to the gentleness and ease of ionizing DNA in negative ion mode, ESI-MS has long been used to detect delicate DNA bindings, including non-covalent attachment of molecules to DNA[87] and for investigation of binding stoichiometries to DNA.[116] Gas phase ESI-MS data for binding stoichiometry studies has also been experimentally shown to agree with high fidelity to solution phase data,[88] though some fragmentation of canonically paired DNA oligomers may occur depending on the instrumental conditions employed.[117,118] Due to the considerably higher strength of Ag^+-mediated pairings than Watson-Crick pairings (Chapter 2), we expect minimal fragmentation for these non-canonical, metal-bridged products and gas-phase distributions that are good approximations to solution phase abundances. The exceptions would be any oligonucleotides that produce products with high degrees of mass heterogeneity, for which widely varying ionization efficiencies can mask true abundances. In addition, sufficiently high mass Ag^+-DNA aggregates may not support high enough ionization rates to be detected within the range of instrument sensitivity.

The high resolution of the ESI-MS instrument used here generally produces mass accuracies comparable to or better than a third of a proton, or ~0.3% the mass of a silver atom, allowing facile differentiation of the number of Ag^+ bound to different Ag^+-DNA products. We note that mass accuracy differs slightly depending on charge state and quality of calibration over the relevant region of the m/z axis. Figure 3.1a shows a typical mass spectrum of Ag^+-DNA in this study. The overall peak width is set by the distribution of elemental isotope abundances in the DNA strands and silver as well as the charge state. These natural abundances are well characterized, enabling accurate prediction of the isotope peak envelope for any given product. In cases where the product counts are high enough, the individual isotope peak fingers are clearly resolved (Figure 3.1b).

Negative ion mode ESI produces deprotonated DNA gas phase ions. If no other ions are bound to the DNA, the negative charge state of the detected ion, z, is equal in magnitude to the number of deprotonated sites on the DNA. When there are additional positive charges embedded in the DNA, such as Ag^+, more deprotonated sites are required to achieve the same value of z. Therefore, the high mass accuracy of the ESI-MS instrument enables determination of the net positive charge associated with the total silver content through fits to the isotope peak envelope, which shifts by 1.007/z for each proton removed. [49,51,89] However if the heterogeneity of products is too high, fitting becomes infeasible due to overlapping signals. Our previous study of Ag^+-DNA solutions in Chapter 2 formed on homobase oligomers found that negative ion ESI left all of the silver content in cationic (Ag^+) form, a finding that carries over to the heterobase strands studied here. Previous studies found that Ag^+ causes self-assembly of C and G Ag^+-paired homobase strands (Chapter 2), but does not form A or T Ag^+-paired homobase strands. Because these studies did not investigate *mixed* base building blocks

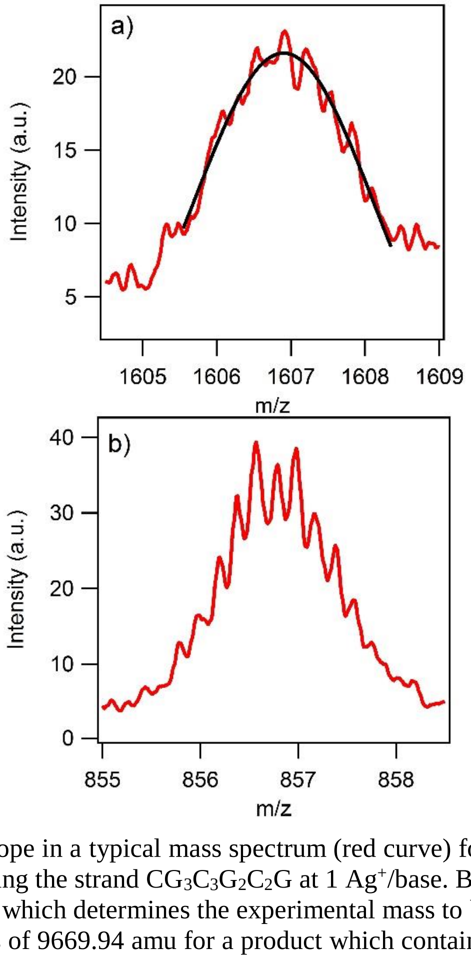

Figure 3.1) a) Isotope peak envelope in a typical mass spectrum (red curve) for an Ag^+-DNA product at charge state z = -6, for a solution containing the strand $CG_3C_3G_2C_2G$ at 1 Ag^+/base. Black curve: the Gaussian fit to the calculated isotope peak envelope, which determines the experimental mass to be 9669.59 amu, within a fraction of a proton to the theoretical mass of 9669.94 amu for a product which contains two DNA strands and 22 silver cations. b) With sufficient signal, individual isotope fingers are clearly resolved within the isotope peak envelope.

for Ag^+ assembly, it is currently unknown whether mixed base strands can form Ag^+-paired strands or whether mixed base composition perturbs the Ag^+-paired structure to the extent that it is no longer a well-defined building block. The ability to specifically control where the Ag^+-base pairs are formed is also an important aspect of designing more complex structures that can self-assemble in an organized manner. To investigate these issues, we explore the Ag^+-paired products produced by the assembly of DNA oligonucleotides with mixed base compositions using ESI-MS, at the same 1 Ag^+/base concentration ratio as used in the studies in Chapter 2. Strand monomer products are also detected (full mass spectra are shown in Appendix B), in most cases as minor products in comparison to Ag^+-paired strands. Because we show below that salt conditions in solution can be manipulated to eliminate these one-strand byproducts, here we focus on the Ag^+-paired products with Ag^+ bridging two strands.

We first examine the consequences of replacing the central bases in C_{11} and G_{11} strands with heterobase mutations. Due to the distinct silver binding sites and strengths on the different bases as seen in Chapter 2 and other works,[100] this heterobase inclusion could be destabilizing for Ag^+-mediated pairings (which we expect to reduce Ag^+ incorporation), or stabilizing (which we expect to increase Ag^+ incorporation). Figure 3.2 displays the distribution of the numbers of Ag^+ in Ag^+-paired products for C_{11} and G_{11}, together with their daughter strands containing central single base mutations (full mass spectra are displayed in Appendix B.1 and B.2). We use the integrated area of Ag^+-paired product peaks in the mass spectrum as a semi-quantitative measure of the relative abundances of each Ag^+-paired species. We find a narrow distribution of Ag^+ per paired strands for the C_{11} DNA strand (Figure 3.2a), with an abundance-weighted Ag^+ stoichiometry of 11.0 Ag^+ per paired strand. This binding stoichiometry corresponds to one Ag^+ atom bridging each C-Ag^+-C base pair, suggesting a simple helical structure, and agrees with the studies in Chapter 2. Upon mutation of the central cytosine to A and G bases (Figure 3.2b,c), the distribution of Ag^+-paired strand products becomes wider, but the abundance weighted Ag^+ stoichiometry is nearly unchanged (10.8 and 11.2 Ag^+ per paired strand, respectively). The wider distribution of products with more than 11 Ag^+ per paired strand likely corresponds to structural perturbations of the Ag^+-paired strand near the mutation site. The wider distribution could instead reflect formation of single-stranded overhangs in the presence of the central base mutations. However, we expect low yields of such products because quantum chemical calculations found 50-60 kcal/mole higher binding energies for Ag^+ that bridge between two bases, as G-Ag^+-G and C-Ag^+-C, than for Ag^+ bound to individual bases, as G-Ag^+ and C-Ag^+ (Chapter 2 and other works).[100]

Circular dichroism (CD) spectroscopy at UV wavelengths is quite sensitive to relative base orientations, and thus serves to probe structural similarity amongst strand assemblies with similar base compositions. The CD spectra for $C_5\mathbf{A}C_5$, $C_5\mathbf{G}C_5$ and $C_5\mathbf{T}C_5$ all closely resemble that for C_{11} (Appendix B.3a). Because Ag^+-paired strand products dominate the integrated intensities in the mass spectra (Appendix B.1), we expect the CD spectra to be dominated by the corresponding Ag^+-paired structures. We conclude that Ag^+-paired strands are similarly structured across C_{11} and all of the mutated C_{11} strands. Although the mass spectrum for $C_5\mathbf{G}C_5$ exhibits a higher degree of strand monomer products (Appendix B.1c), the CD is also similar to that for C_{11} with a reduced amplitude that is consistent with the same underlying Ag^+-paired structure diluted spectrally by the higher presence of strand monomer products. We also note that the T mutation increases the abundance weighted Ag^+ stoichiometry to 11.8 Ag^+ per paired strand (Figure 3.2d). This is significantly higher than the value of 10 Ag^+ per paired strand we had naively expected based on the low affinity of thymine homobase strands for Ag^+ (Chapter

2 and other works).[90] The incorporation of ~2 additional Ag$^+$ and the narrower Ag distribution for the T mutation of C_{11}, in comparison to the A and G mutations, suggests that the CTC motif is especially stabilized by additional Ag$^+$ incorporation and may be particularly useful for low-error assembly of Ag$^+$-mediated DNA nanostructures.

The central single base mutations in G_{11} strands introduce larger differences in Ag$^+$ distributions (Figure 3.2e-h). For G_{11}, Ag$^+$-paired products are narrowly distributed around an abundance-weighted Ag$^+$ per paired strand of 10.8 Ag$^+$, consistent with 1 Ag$^+$ bridging each base pair (Figure 3.2e), just as for the case of C_{11} (Figure 3.2a). However G_5**A**G_5, G_5**C**G_5 and

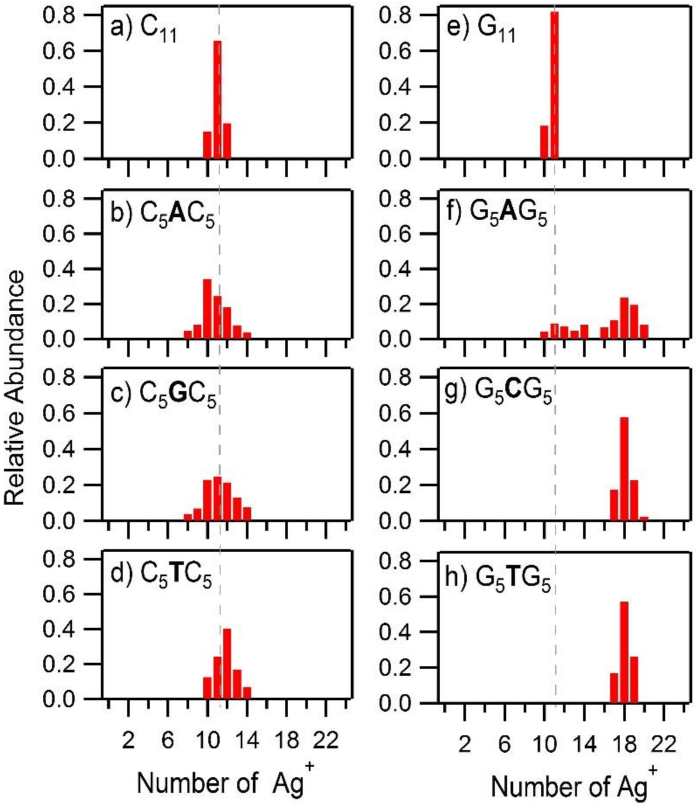

Figure 3.2) Distribution of the number of attached Ag$^+$ in paired strands formed by the strands a) C_{11}, b) C_5**A**C_5, c) C_5**G**C_5, d) C_5**T**C_5, e) G_{11}, f) G_5**A**G_5, g) G_5**C**G_5 and h) G_5**T**G_5 at 80 µM DNA and 1 Ag$^+$/base in 50 mM ammonium acetate. The relative abundances represent the integrated area of the Ag$^+$-paired product divided by the total integrated area of all Ag$^+$-paired products in the mass spectrum. The abundance-weighted Ag$^+$ per paired strand for a) C_{11} is 11.0 Ag$^+$ and e) G_{11} is 10.8, corresponding closely to 1.0 Ag$^+$ per base pair, as marked by the gray dashed line. b)-d) Single base mutations to the central base in C_{11} produce somewhat wider distributions that are only slightly shifted. f)-g) Single base mutations to the central base in G_{11} produce significantly higher incorporation of Ag$^+$.

G_5**T**G_5 exhibit significantly higher abundance-weighted Ag^+ per paired strand (16.2, 18.1 and 18.1 in Figure 3.2f-h, respectively, corresponding to 1.47, 1.65 and 1.65 Ag^+ per paired base). Because the full mass spectra are heavily dominated by Ag^+-paired products (Appendix B.2), the CD spectra should reflect the Ag^+-paired structure. The pronounced shift to higher Ag^+ content in strands with central base mutations (Figure 3.2f-h) is accompanied by small shifts in wavelengths of CD spectral features but more significant shifts in CD amplitudes (Appendix B.3b). Thus it is unclear whether the additional ~7 Ag^+ introduced by the mutations to G_{11} (Figure 3.2e-h) are held near the mutation, retaining an overall similar Ag^+-paired structure; or if the central base mutations produce a different type of structural motif.

To test whether shorter homobase C and G runs can be combined into larger motifs that preserve overall Ag^+-paired structure, we used the sequences $C_4G_4C_4$ and $G_4C_4G_4$. We selected these palindromic sequences because, although calculations suggest a *parallel* strand orientation for Ag^+ mediated pairings (Chapter 2), this has not been definitively established by published experimental results. In particular, if Ag^+ were to assemble paired strands in *anti*parallel orientation, then non-palindromic sequences would *not* be self-complementary for Ag^+-paired strand formation. We avoid this issue by using $C_4G_4C_4$ and $G_4C_4G_4$, which are complementary for Ag^+ pairing regardless of strand orientation (because Ag^+ preferentially pairs C to C and G to G, rather than C to G as seen in Chapter 2). The abundance weighted Ag^+ stoichiometry was 17.4 and 20.1 Ag^+ per paired strand, respectively (Figure 3.3a,b), corresponding to 1.45 and 1.68 Ag^+ per paired base, similar to the additional Ag^+ incorporated by single base mutations to G_{11}. Full mass spectra are shown in Appendix B.4a,b.

The CD spectra for these palindromic strands, $C_4G_4C_4$ and $G_4C_4G_4$, suggest that the Ag^+-paired structures are similar despite their quite different C, G content (Figure 3.3d). To represent the case of no structural perturbation from heterobase inclusion, we used CD spectra for Ag^+-assembled cytosine homobase strands and Ag^+-assembled guanine homobase strands. These exhibit almost entirely negative CD over the spectral range studied (Figure 3.5a,b, red traces), in striking contrast to CD spectra of WC duplexes or quadruplexes. We formed linear combinations of these Ag^+-paired homobase strand's spectra with weights chosen to match the G,C content in the palindromic mixed-base sequences (Figure 3.3e). Using 33% spectral weighting of the Ag^+-paired cytosine homobase strands and 66% spectral weighting of the Ag^+-paired guanine homobase strands (green curve, Figure 3.3e) gives good agreement with the measured CD signal for Ag^+-paired $G_4C_4G_4$ (green curve, Figure 3.3d). Similarly, using 66% spectral weighting of the cytosine component and 33% spectral weighting of the guanine

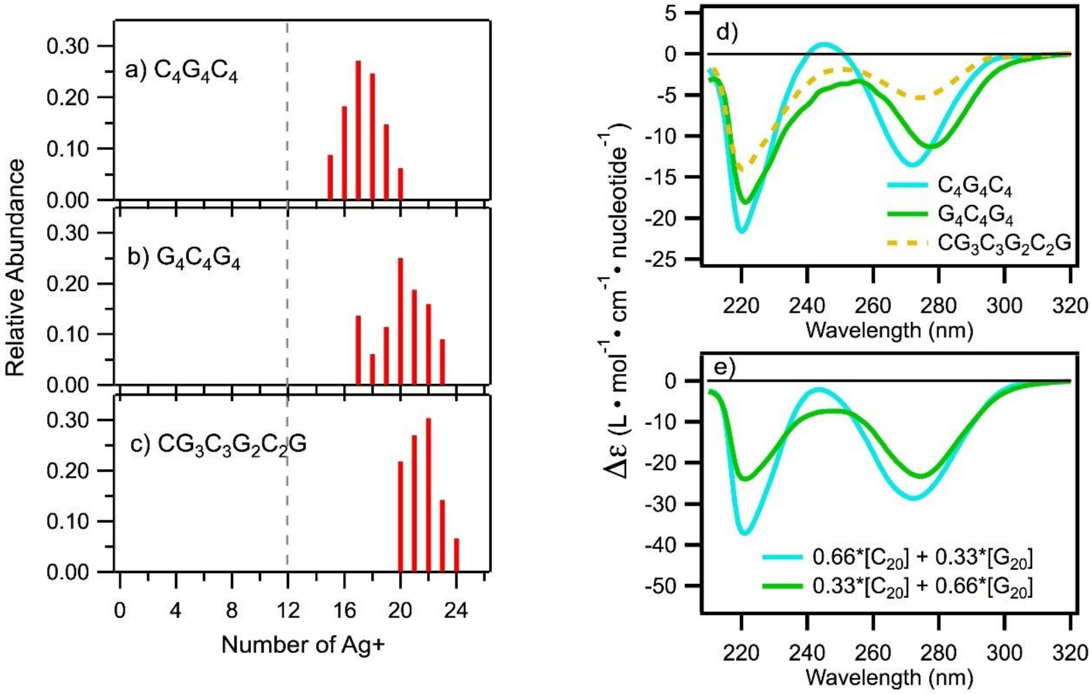

Figure 3.3) Distribution of Ag^+ binding stoichiometry in Ag^+-paired strands of 12 base C,G strands, and corresponding CD spectra. a) $C_4G_4C_4$, b) $G_4C_4G_4$, and c) $CG_3C_3G_2C_2G$ at 80 μM DNA, 1 Ag^+ / base and in 10 mM ammonium acetate. Abundance-weighted Ag^+ per paired strand is 17.4, 20.1 and 22.6 for $C_4G_4C_4$, $G_4C_4G_4$ and $CG_3C_3G_2C_2G$ respectively. Overall binding is much higher than expected for 1 Ag^+ per C-Ag^+-C or G-Ag^+-G base pair (dashed gray line). d) Circular dichroism spectra of the strands at 7.5 μM and 1 Ag^+ / base exhibit signals similar to e) linear combinations of normalized C_{20} and G_{20} spectra at 1 Ag^+ per base.

component (blue curve, Figure 3.3e) gives good agreement with the measured CD signal for Ag^+-paired $C_4G_4G_4$ (blue curve, Figure 3.3d). The agreement of the spectral shapes from these linear combinations of Ag^+-paired homobase strands' spectra (Figure 3.3e) with the measured CD spectra for the palindromic strands $C_4G_4G_4$ and $G_4C_4G_4$ (Figure 3.3d, blue and green curves) indicates that the underlying secondary structure is preserved, despite the presence of additional bound silver associated with the heterobase crossovers. This agreement also suggests that the strand orientations favored by homobase runs of C-Ag^+-C and G-Ag^+-G pairings may be the same. If the Ag^+-paired $C_4G_4C_4$ and $G_4C_4G_4$ strands instead had different secondary structures, we would not expect both CD spectra (Figure 3.3d) to agree with the weighted linear combinations of homobase Ag^+-paired components in Figure 3.3e.

It appears that the major effects of the heterobase crossovers in these palindromic sequences is incorporation of additional Ag^+, without major disruption to the underlying Ag^+-paired structures of the constituent G homobase and C homobase components. To test the effects of increasing the number of heterobase crossovers we use the strand $CG_3C_3G_2C_2G$ (5 heterobase crossovers). Consistent with the expectation that base crossovers incorporate additional Ag^+, the abundance weighted Ag^+ stoichiometry rose further, to 22.6 Ag^+ per paired strand (Figure 3.3c), or 1.88 Ag^+ per paired base. (Full mass spectra are shown in Appendix B.4). The CD spectrum for $CG_3C_3G_2C_2G$ shows the same overall peak structure as for $C_4G_4G_4$ and $G_4C_4G_4$, albeit with reduced amplitude (Figure 3.3d, orange dashed curve). This is consistent with preservation of the same underlying Ag^+-paired structure, given that heterogeneous dipolar couplings introduced by base crossovers can also affect CD amplitudes.

Overall, results from CD spectra and silver binding stoichiometries suggest a fairly simple structural picture in which the underlying Ag^+-paired strand motifs from Ag^+ base pairings are stable in the presence of heterobase crossovers between C homobase motifs with lengths of up to 5 or more bases, and G homobase motifs with lengths of up to 4 bases. In all cases, heterobase inclusion within C,G rich strands appears to be stabilizing, as indicated by the increase in numbers of incorporated Ag^+.

In order to create high yields of larger nanostructures from smaller subunits, the subunits should form with minimal polydispersity. In particular, it is important to minimize Ag^+-bearing strand monomer products, such as those identified previously for cytosine homobase strands in Chapter 2. These prior studies were made in low ionic conditions. Investigating whether increased ionic strength could improve Ag^+-paired product homogeneity, as is the case for Watson-Crick mediated assemblies, requires an alternative assay to ESI-MS, which is incompatible with solutions of high ionic strength. Therefore we turn to high performance liquid chromatography (HPLC) with inline absorbance detection to monitor the retention times of the various Ag^+-DNA products formed in the presence of additional salts. To test this approach we focus on the strand $T_2C_{20}T_2$. We select the 24 base length because suitable solvent gradients in HPLC produce well-separated peaks for strand monomer versus strand dimer products. This is because for the ion-pair reverse-phase HPLC with a C18 column used in this study, the retention time of the DNA products depends most strongly on the amount of column-accessible phosphate backbone, and to a lesser extent the hydrophobicity of the nucleobases.[119,120] Therefore more rigid, compact structures with less exposed backbone will elute earlier.

The HPLC chromatogram for $T_2C_{20}T_2$ annealed in low ionic conditions (10 mM ammonium acetate) displays a high degree of heterogeneity in peak location and amplitude (Figure 3.4a). The two dominant peaks (Figure 3.4a) have large separation in retention time.

The aliquots corresponding to these dominant peaks were collected and identified through ESI-MS (full mass spectra are shown in Appendix B.5). The early-eluting peak is comprised of strand monomers with 8 and 9 attached Ag^+ (left inset, Figure 3.4a). The late eluting peak is comprised of Ag^+-paired strands with 19 and 20 attached Ag^+ (right inset, Figure 3.4a). That the Ag^+-paired strands elute last is expected because the length of column-exposed backbone is greater than for strand monomer products.

Annealing at higher ionic conditions, 500mM ammonium acetate (Figure 3.4b) or 60 mM $MgSO_4$ (Figure 3.4c) produced a much cleaner chromatogram with one dominant

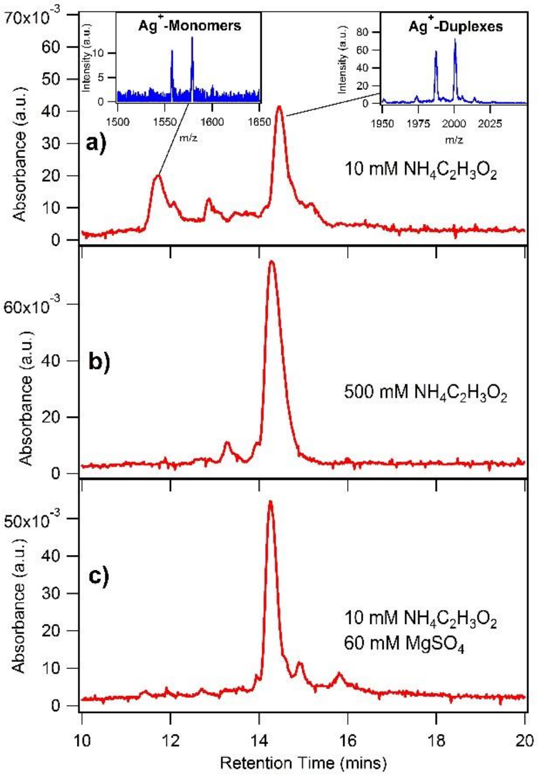

Figure 3.4) HPLC chromatograms of Ag^+- $T_2C_{20}T_2$ solutions monitored at 260 nm for solutions prepared at 5 µM DNA and 1 Ag^+/base in a) 10 mM ammonium acetate, b) 500 mM ammonium acetate and c) 10 mM ammonium acetate and 60 mM magnesium sulfate. The extra two thymine bases on each end were used to increase chromatogram resolution of monomer and Ag^+-paired products. The insets in a) display mass spectra of the marked peaks in the HPLC chromatogram, which were caught and injected in to an ESI-MS in negative ion mode. The lower retention time peak in a) consists of Ag^+-strand monomer products containing 8 and 9 Ag^+ while the higher retention time peak consists of Ag^+-paired strands containing 19 and 20 Ag^+. For labelled, full range mass spectra of these chromatogram peaks please see Appendix B.5. Higher ionic conditions in the chromatograms for b) and c) produce one narrow peak with a retention time corresponding to the Ag^+-paired strand in a).

absorbance peak. The running HPLC buffer remained constant at 10 mM ammonium acetate and 35 mM triethylamine acetate in all cases. This single dominant peak has a nearly identical elution time to that of the Ag^+-paired strands in low ionic conditions. Therefore we conclude that they are the Ag^+-paired strand structure. Full mass spectra for solutions synthesized across a wider range of ionic conditions, then solvent exchanged into 10 mM ammonium acetate, are shown in Appendix B.6. In particular, because 10 mM Mg^{2+} is commonly used to create Watson-Crick paired DNA nanostructures by assembly techniques such as origami, we tested relative yields of Ag^+-paired strand and monomer products for annealing at 10 mM magnesium sulfate with 10 mM ammonium acetate (Appendix B.6c). We found that this lower Mg^{2+} concentration is sufficient to produce high yields of Ag^+-paired strands with almost no contamination by monomer byproducts. Thus formation of double-stranded regions paired by Ag^+ appears consistent with DNA nanotechnology conditions for stable Watson-Crick pairings.

The CD spectrum for $T_2C_{20}T_2$ in 60 mM $MgSO_4$ has the same overall shape as the CD with no $MgSO_4$, but with slightly higher magnitude peaks (Appendix B.7), indicating that the structure of the Ag^+-paired strands do not vary significantly with ionic strength. Given the apparent removal of the strand monomer products by the use of higher ionic conditions (Figure 3.4b,c), it appears that charge screening from the additional ions promotes monodisperse paired strand formation, an important finding for developing protocols for Ag^+-assembly of more elaborate structures. With the bound Ag^+ alone, insufficient screening of the phosphate backbone at low ionic strength may be responsible for the presence of monomer products.

Ag^+-mediated pairings of C base mismatches have been shown to provide surprising thermal robustness compared to otherwise canonical, Watson-Crick paired DNA duplexes,[30,39]

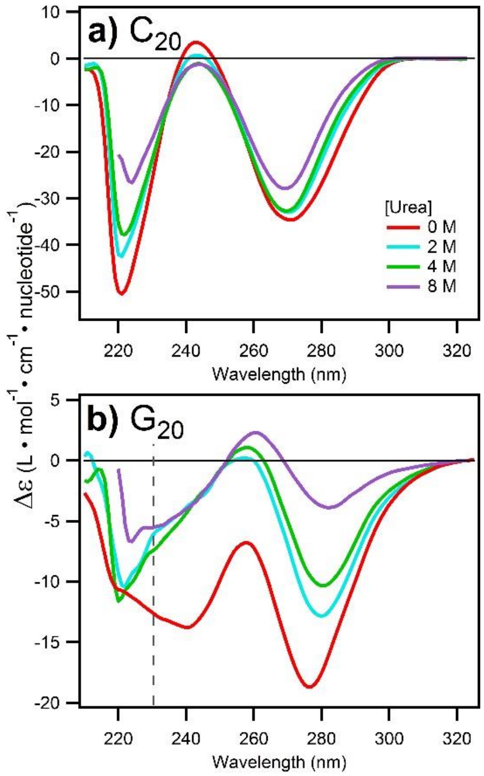

Figure 3.5) CD spectra for solutions of strands a) C_{20} and b) G_{20} at 1 Ag^+ per base in varying concentrations of urea: 0 M (red traces), 2 M (blue traces), 4 M (green traces) and 8 M (purple traces). The DNA concentrations were 4 μM and the buffer was 10 mM ammonium acetate pH = 7. Data to the left of the dashed line in b) for solutions with urea has a large degree of instrumental uncertainty due to high absorbance from high urea concentrations.

and in Chapter 2 we found Ag^+-paired C_6 and G_6 homobase strands displayed very little change in CD signal even at 90 ºC. Apparently thermal stability is excellent, at least for these tested base motifs. To determine how resistant these Ag^+-mediated base pairings are to chemical perturbation, we use urea because it is a common additive for denaturing DNA.[121] The stability of Ag^+-paired C_{20} and G_{20} homobase strands in varying concentrations of urea, at low ionic conditions, was tested by CD spectroscopy (Figure 3.5). The Ag^+-C_{20} solution showed high resistance to urea, with CD magnitude dropping by only 20% at 270 nm in 8M urea (Figure 3.5a), while retaining overall spectral shape. Conversely, for the Ag^+-G_{20} solution the CD magnitude dropped by 76% at 282 nm in 8M urea (Figure 3.5b), though the spectral shape remained similar. It is not clear whether the reduction in CD signal for G_{20} relates to a loss of

Ag^+-mediated base pairing or an alteration in the structure of the Ag^+-paired strands. The surprising resistance of Ag^+-paired C_{20} strands to denaturation by urea suggests that structure designs which incorporate abundant C-Ag^+-C base pairs could be highly resistant to denaturing.

The high thermal stabilities of strands stabilized by G-Ag^+-G and C-Ag^+-C base pairs and the high chemical stabilities of C-rich Ag^+-mediated pairings suggest that two-stage assemblies for incorporating both Ag^+ and WC pairings may be achievable. For example, an Ag^+-mediated assembly stage could be made under thermal or chemically denaturing conditions to suppress WC pairings that might impede Ag^+ assembly. A subsequent, lower temperature (or denaturant-free) assembly stage could then be made to form WC pairings. Any such a two-stage assembly will require the Ag^+-assembled strands to remain stable in the presence of Na^+ or Mg^{2+} cations, which are used to stabilize WC-based DNA nanotechnology. To examine the stability of Ag^+-mediated pairings in the presence of additional salts, we measured CD spectra of C_{20} and G_{20} with 100 mM NaCl (Figure 3.6a,c) at 1 Ag^+/base and with 60 mM $MgSO_4$ (Figure 3.6b,d), also at 1 Ag^+/base. A control spectrum for each strand at 1 Ag^+/base, but no additional salt is included for reference in every graph (Figure 3.6, red curves). For C_{20} with 1 Ag^+ per base (Figure 3.6a,b), 100 mM NaCl and 60 mM $MgSO_4$ had similar effects, reducing the magnitude of the CD spectrum while retaining similar spectral shapes. This surprising resistance of C-Ag^+-C base pairing to AgCl precipitation is very promising for DNA nanotechnology. For G_{20} with 1 Ag^+ per base and 100 mM NaCl (Figure 3.6c, green curve) the Ag^+-paired structure appears to be completely disrupted, as evidenced by similarity in dichroic signal to the bare G_{20} strand in 100 mM NaCl (Figure 3.6c, blue curve). Apparently G-Ag^+-G base pairs do not persist in high amounts of NaCl. However the CD signal

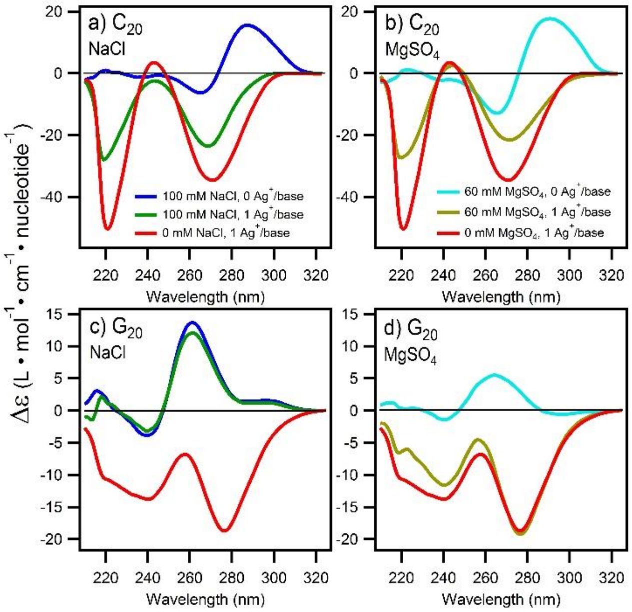

Figure 3.6) CD spectra of C_{20} with a) NaCl and b) $MgSO_4$ and G_{20} in c) NaCl and d) $MgSO_4$. CD curves for a) and c) were measured on solutions in 100 mM NaCl with no Ag^+ (blue) and 100 mM NaCl with 1 Ag^+/base (green). CD curves for b) and d) were measured on solutions in 60 mM $MgSO_4$ with no Ag^+ (teal) and 60 mM $MgSO_4$ with 1 Ag^+/base (gold). The corresponding controls with 1 Ag^+/base but without NaCl or $MgSO_4$ are represented by the red curves. For NaCl, the salt was added after annealing to check for precipitate formation, while for $MgSO_4$ the salt was added prior to annealing. No precipitates were observed for Ag^+-G_{20} or Ag^+-C_{20} solutions with 100 mM NaCl or 60 mM $MgSO_4$.

for G_{20} in 60 mM $MgSO_4$ with Ag^+ (Figure 3.6d, gold curve) remained spectrally similar in magnitude and shape to the control with no additional salt (Figure 3.6d, red curve). Thus it seems both C-Ag^+-C and G-Ag^+-G base parings would be compatible with DNA nanostructures stabilized by Mg^{2+} cations.

3.3) Towards Ag^+-stabilized DNA Nanotechnology

Success in any 2-stage assembly, with an Ag^+-pairing stage followed by a WC pairing stage, will require that the 1st step not introduce a significant amount of disruptive Ag^+ pairings in the regions for planned WC pairing in the 2nd step. The notion that this 2-stage assembly may be achievable for diverse WC pairing motifs is suggested by the recent success in using pre-formed Ag_N-DNA, synthesized on strands with mixed base hybridization tails, to decorate DNA nanotubes.[122] The hybridization tails were designed using recent advances in machine learning of “bright” multi-base motifs that promote formation of fluorescent silver clusters, and “dark” motifs that do not.[53] To achieve dense decoration of the DNA nanotube, the tails appended to the silver cluster template had to include C and G bases in order to be short enough to hybridize the Ag_N-DNA onto closely spaced sites along the nanotube.[122] The successful decoration of the DNA nanotubes with Ag_N-DNA designed with select 10-base tails with significant (40%) G,C content indicates that if any silver was attached to these mixed-base tails, it did not significantly interfere with WC hybridization.

We conclude that it is reasonable to expect properly designed strands with up to ~ 40% G and C bases to form duplexes primarily through WC pairing after a prior, Ag^+ mediated assembly stage. This is consistent with the preservation of an overall WC geometry after addition of Ag^+ to canonical mixed-base WC duplexes with individual C-C mismatches,[31] and with recent quantum chemical calculations which found diverse, geometrically distinct but energetically similar Ag^+-mediated base pairings in Chapter 2. The small differences found in calculated binding energies for differently configured Ag^+ pairings imply that geometries of Ag^+-mediated pairs that are embedded within a background of WC pairs may be strongly influenced by steric constraints from neighboring regions.

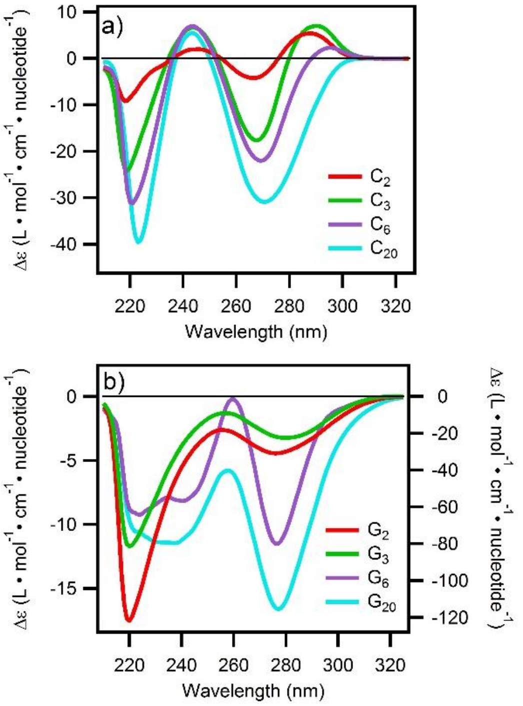

Figure 3.7) CD spectra of varying lengths of a) G and b) C homobase oligonucleotides in 7.5 mM MOPS at 1 Ag^+ per base. CD spectra correspond to sequences of length 2 (red), 3 (green), 6 (purple) and 20 (teal). The trace for C_2 in a) was reproduced with permission from.[114]

The critical issue of strand orientation for Ag^+-paired strands was not yet established at the time of the work discussed in this chapter, though early studies of Ag^+-paired $d(C_8)$ strands, and our results above, provide some evidence for a parallel orientation.[91] Parallel orientations are also suggested by the most stable configurations found in theoretical calculations for C-Ag^+-C and G-Ag^+-G pairings (Chapter 2 and Appendix A). In Chapter 4 we present very recent experimental studies that indicate parallel strand orientations for C and G of homobase strands.

Detailed structural information on structures formed by Ag^+-mediated base pairs has yet to be elucidated. However trends in CD spectra for C and G homopolymer strands of increasing length (Figure 3.7) suggest simple helical duplex structures. For Ag^+-paired C_N strands, this is indicated by the similarity of CD spectra for strand lengths, N, ranging from 2 to 20 (Figure 3.7a). The increase in the per-base CD signal with increasing N (Figure 3.7a) is qualitatively as expected for increasingly ordered helices in which the relative contributions from less conformationally constrained end bases decrease with strand length. Also suggestive of simple helical structures is the agreement between strand length, N, and the numbers of Ag^+ in the dominant Ag^+-paired C homobase product for lengths N of 2-20 bases (Chapter 2 and other works).[114] For the longer Ag^+-paired G_N strands, the number of Ag^+ in the dominant Ag^+-paired product also agrees with strand length (6 Ag^+ for N=6 and 20 Ag^+ for N=20), again suggestive of a simple helical structure (Chapter 2). However for N=2 and 3, the CD spectrum changes dramatically (Figure 3.7b, right axis), with a large increase in normalized CD magnitude that suggests Ag^+-induced strand aggregation.[123,124] We conclude that for both C and G homobase strands, the CD spectra show high amplitudes indicative of Ag^+-assembled pairings at lengths of just 2 bases. Thus it appears that Ag^+-mediated pairings may enable much shorter base motifs to be used for "sticky ends" than is the case for WC pairings, which typically require runs of 6 or more bases for adequate stability at room temperature.

Based on the above results, we anticipate that it may be possible to exploit the high stability of Ag^+ pairings in new types of dynamic DNA nanostructures. Figure 3.8a proposes a simple prototype structure, assuming parallel strand orientations of Ag^+-paired motifs. The

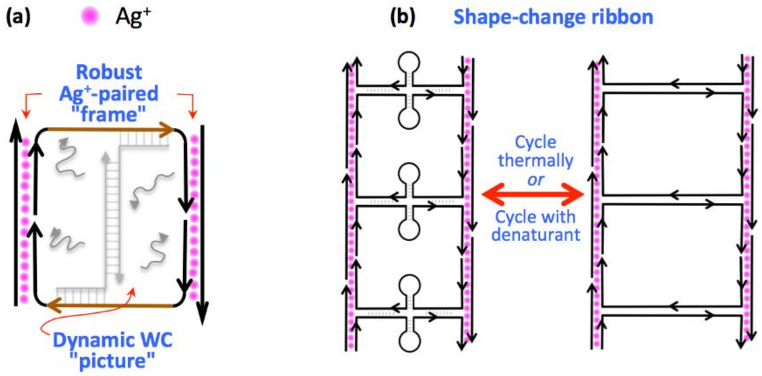

Figure 3.8) (a) Simple 4-strand scheme for a robust structure that employs Ag^+-pairing to form a stable "frame" around a central, dynamic "picture". The outer strands have different (C_n,G_n) motifs that Ag^+-pair to the black segments of the upper and lower strands. The brown segments of the upper and lower strands are comprised of motifs that do not Ag^+ pair. Instead they anchor subsequent formation of the WC-paired "picture" (gray). **(b)** A ribbon variant would reversibly change width and stiffness on thermal or denaturant melting of the WC-paired

brown segments of the upper and lower strands contain base motifs that do not Ag^+-pair. These are flanked by segments containing different G_N- and C_N–rich motifs that Ag^+-pair with the two outer strands. This would form sturdy side "frames" supporting a WC-paired "picture" formed by subsequent WC hybridization (gray strands). We expect that the WC "picture" could be both thermally and chemically manipulated without disturbing the "frame." For example in an extended, ribbon-type structure (Figure 3.8b), disruption of WC paired stem-loop structures in the "picture" would alter the ribbon width and rigidity, but the strands would be retained by the frame. Such a change in structure, without loss of strands, could be very useful (for example, the change in width could be used to alter flow through nanoconstrictions without any loss of strands).

3.4) Conclusions

We have shown that Ag^+-base pairing holds promise for DNA nanotechnology through surprising thermal and chemical robustness of Ag^+-base pairing, the formation of monodisperse Ag^+-paired strands, and the consistent structures of Ag^+-paired strands with both mixed base and homobase motifs, as indicated by CD spectroscopy. The examples in Figure 3.8 are intended only to convey that new DNA nanostructure function with improved robustness could arise from Ag^+ pairing of select DNA strands. There are important issues that must be resolved before such structures can be made a reality. These include the issue of strand orientation for Ag^+-paired motifs, how best to design strands that engage in both Ag^+ and WC pairing, and the structural regularity of mixed base Ag^+-pairing motifs. We are continuing to investigate these questions and are optimistic about the inclusion of Ag^+-base pairing in DNA nanotechnology.

3.5) Methods

All DNA oligonucleotides were synthesized by Integrated DNA Technologies with standard desalting and additionally desalted by spin filtration. Strand G_{20} contains the longest series of guanine bases provided at this time by at Integrated DNA Technologies as a standard order. All mass spectra show 90+% purity. All solutions were prepared with nuclease free water (Integrated DNA Technologies) except for the HPLC running buffers which used 18 MΩ MilliQ water. The $AgNO_3$ was analytical grade, 99.999% purity (Sigma-Aldrich). For preparation of any solution containing DNA for instrumental analysis, the solution was annealed at 90^{o}C for 5 minutes and cooled slowly to room temperature.

Circular dichroism spectra were measured on an Aviv 202 circular dichrometer. Multiple sample spectra and multiple buffer blank spectra were separately averaged to enable accurate background subtraction. All spectra were measured on pH 7 solutions, buffered by the concentrations of ammonium acetate specified below.

High-performance liquid chromatography (HPLC) was performed on a Hitachi L-6200A pump and L-4200 UV/Vis detector using a pH 7 water-methanol gradient from 15-40% methanol at 1% per minute, with 35 mM triethylamine acetate as the ion-pairing agent to the C18 column (50 x 4.6 mm Kinetex EVO with 2.6 μm particle size and 100 Å pore size).

Solutions for mass spectrometry were injected into a Waters QTOF2 mass spectrometer at 10 μL/min in negative ion mode with a 2kV capillary voltage, 45V cone voltage and 14V collision energy. All solutions were injected with 10 mM or 50 mM ammonium acetate buffer as specified (pH 7). Prior to injection, samples collected from HPLC were solvent exchanged into 10 mM ammonium acetate by spin filtration.

Chapter 4) Structural insights into Ag^+-paired DNA from fluorescence resonance energy transfer studies and ion mobility mass spectrometry

Adapted with permission from: S. M. Swasey, F. Rosu, V. Gabelica, S. M. Copp and E. G. Gwinn. Structural insights into Ag^+-paired DNA from fluorescence resonance energy transfer studies and ion mobility mass spectrometry. *In preparation*.

4.1) Introduction

DNA functions not only as a pivotal biological molecule but also as a versatile structural material capable of self-assembly into intricate nanostructures. An area of research that makes contact with both the biological and structural material aspects of DNA is metal-base interactions. While many metal cations interact with various parts of DNA, only Hg^{2+}, Ag^+ and Pt^{2+} are known to specifically interact with the bases as opposed to the negatively charged phosphate backbone.[59] Base specificity gives these metals the capability to target specific base motifs within DNA to alter its biological function or to form potentially functional metallic DNA.[57,58,125,126] Pt^{2+} complexes have been extensively studied for their potent anti-cancer activity and are believed to bind preferentially to guanine bases which may form crosslinks in duplex DNA and interfere with cell replication.[10,11,127–132] More recently, it has been discovered that Hg^{2+} can serve as a bridge stabilizing the formation of thymine homobase pairs,[29] and that Ag^+ can mediate the formation of cytosine and guanine homobase pairs in DNA (Chapter 2 and other work).[30]

While Hg^{2+} and Ag^+ are both capable of base pairing, Ag^+ has little known toxicity in humans and is commonly used as a potent antimicrobial agent, making it better suited for applications in biotechnology and nanotechnology.[13] Ag^+-mediated base pairs show particular promise for potential applications such as gene regulation through the interaction of Ag^+ with G-quadruplexes,[133] gating of enzyme activity behind an Ag^+-pairable base mismatch,[134] better understanding of the underlying mechanism behind silver's antimicrobial activity,[135] and controlling the size and optical properties of fluorescent DNA templated silver nanoclusters.[47,136]

Ag^+-mediated base pairs have been shown to form chemically and thermally robust dimeric DNA structures comprised of homobase guanine and cytosine Ag^+-bridged pairs (Chapters 2-3 and other work).[91] The thermal stabilities of these Ag^+-paired strands significantly eclipse Watson-Crick (WC) paired duplexes of similar length (Chapter 2). Due to the ease of formation, stability and low dispersity of products observed for short homobase oligomers (Chapter 3), Ag^+-mediated base pairing holds particular promise for formation of more robust and thermodynamically tunable metal-DNA nanostructures, without the inherent toxicity of Hg^{2+}. Practical applications of DNA nanostructures can require conditions which lead to degradation from a variety of factors including enzymes and denaturation.[137] Incorporation of Ag^+-mediated base pairing with WC base pairing may be an interesting avenue to counter these effects. However, the development of design protocols for self-assembling DNA nanostructures using Ag^+-paired building blocks has been hindered by lack of knowledge of fundamental structural properties. This is in part due to issues of aggregation as observed in Chapter 3 at the high concentrations required by many analytic techniques.

Current DNA nanotechnology is built on decades of research into the structure and thermodynamics of canonical duplex DNA and hydrogen (H) bonded non-canonical forms. This knowledge base has been essential to development of techniques for efficient and ordered hybridization of single-stranded DNA into nanostructures formed by H-bonds. Here we focus on elucidating the strand orientations and overall shapes that result from Ag^+-mediated pairings, in the simplest sequence context of DNA homobase strands. The importance of this understanding for use of Ag^+ pairings is underlined by the wide variety of structures that DNA forms under native conditions, including G-quadruplexes[6] and C i-motifs[9] that may include one, two or four DNA strands, as well as folded hairpins,[138] triplex structures[139] and a variety of duplex forms in which the helicity of the overall linear, dimeric molecule depends on salt conditions and sequence.[1–3] Recent studies suggest that the formation of Ag^+-mediated base pairs in canonical B-DNA with artificial base mismatches, or in complementary DNA strands with sparse insertions of C-C mismatches, may in certain solution conditions produce duplex structures that are qualitatively similar to WC-paired DNA.[62,140] However for non-complementary strands, the issue of structure resulting from Ag^+-mediated pairings is mostly unexplored.

Recent DFT-based quantum mechanics/molecular mechanics calculations for Ag^+-mediated pairings of DNA considered two base long cytosine DNA strands, 5´-C_2-3´, in water. For the hydrated Ag^+-bridged strand dimer, designated here as $(C_2)_2(Ag^+)_2$, calculations found a simple duplex structure formed by parallel Ag^+-paired strands that also contained unique planar and inter-planar H-bonds between bases.[114] Later, a crystal structure of Ag^+-mediated N^1-hexylcytosine pairs displayed a linear chain of N^1-hexylcytosine pairs stabilized by πstacking, argentophilic interactions between silver atoms as well as the unique hydrogen bonding patterns which agreed with the calculations for the $(C_2)_2(Ag^+)_2$ DNA.[114,141]

Here we use FRET to experimentally investigate the strand orientation that results from consecutive G-Ag^+-G and C-Ag^+-C pairings in DNA. To elucidate overall shape, we turn to electrospray-ionization ion-mobility spectrometry-mass spectrometry (IMS-MS) of Ag^+-assembled guanine and cytosine homobase strands, 6-30 bases in length, and compare results to H-bonded DNA motifs with similar numbers of bases. The data indicate that linear duplex structures are the predominant form produced by runs of up to 20 sequential G-Ag^+-G pairs, while for up to 30 sequential C-Ag^+-C pairs the data suggest a more compact duplex form at low magnitude charge states and a more extended form at high magnitude charge states, possibly reflecting the presence of the special H-bond patterns that were found in calculations for low charge states of canonical duplex DNA and the disruption of these H bonds at high charge states. (However, ESI-IMS-MS cannot establish which gas phase form more closely correlates to solution structure for the Ag^+-paired cytosine strands).

4.2) Results and Discussion

4.2.1) Investigation of strand orientation in Ag^+-paired DNA by FRET

Prior work on DNA duplexes used indirect techniques to infer strand orientation, including UV absorbance, circular dichroism (CD), and the incorporation of dye intercalators.[142,143] NMR has also been used,[143,144] but requires large amounts of pure material at high concentrations that can induce structural rearrangements. Changes in CD upon addition of Ag^+ to solutions of 5´-C_8-3´DNA were used to indirectly support the idea of a parallel stranded duplex arising from C-Ag^+-C pairs.[91] However, unambiguous determination of structure from CD spectra remains out of reach at the present time for two reasons. First, CD is quite sensitive to relative base orientations, but the changes in structure that result from Ag^+-mediated pairings are largely unknown. And second, although significant progress has been made towards obtaining reliable quantum mechanical/molecular mechanics (QM/MM) calculations for biomolecular CD spectra in aqueous solution, such calculations can only be applied to small systems, such as $(C\text{-}Ag^+\text{-}C)_2$,[114] due to the high computational costs associated with realistic hydration and to the lack of experimentally tested Ag^+-base bonding parameters.

Here we directly probe strand orientation through use of fluorescence resonance energy transfer (FRET) studies of Ag^+-paired, dye-labelled guanine and cytosine DNA. In FRET, an excited donor dye, *d*, transfers energy non-radiatively to an acceptor dye, *a*, with an efficiency

$$E = 1/(1+(R/R_0)^6) \qquad \text{Eq. 4.1}$$

where R is the *d*-a separation and R_0, the Förster radius, is set by the properties of the dyes used in the *d-a* pair. FRET reduces donor emission and turns on acceptor emission upon excitation of the donor, providing a valuable structural probe for dye-labelled biological molecules due to the steep R-dependence of the efficiency, *E* (Eq. 4.1). Structural changes that decrease *d-a* separations lead to increased acceptor emission for excitation *via* the donor, together with decreased donor emission. We selected the *d-a* dye pair Alexa 488-Alexa 647 because excitation near 450 nm directly excites only the Alexa 488 donor, so that emission from the Alexa 647 acceptor is due to FRET alone (rather than to direct excitation of the acceptor). For this *d-a* pair, R_0 = 5.2 nm (Appendix C.1). We infer strand orientations by examining relative FRET efficiencies for different dye labelled strand pairings and use the accepted quantum yields for the acceptor and donor dyes to normalize emission spectra of different products *via* ratiometric FRET analysis between the donor and acceptor dye channels (see Appendix C for details). Due to length variability introduced by the flexible thymine strand extensions we use to reduce effects of dye-base interactions and to promote HPLC separation of different paired products, we do not provide a detailed analysis involving calculated lengths between dyes.[145]

4.2.2) Sequential C-Ag$^+$-C pairings prefer a parallel strand orientation

Figure 4.1a sketches the 3-strand FRET scheme used here. Green circles represent the Alexa 488 donor dye, "*d*", and red circles represent the Alexa 647 acceptor dye, "*a*". Strand $\mathbf{A_{3'C}}$ (5´-T$_5$C$_{20}$T$_5$-3´-*a*) has the acceptor dye on the 3' end. Strand $\mathbf{D_{3'C}}$ (5´-T$_2$C$_{20}$T$_2$-3´-*d*) has the donor dye on the 3´ end. The third strand, $\mathbf{D_{5'C}}$ (*d*-5´-T$_2$C$_{20}$T$_2$-3´), has the donor dye at the 5´ end. The T base extensions, which interact minimally with Ag$^+$ (Chapter 2), are included to allow free rotation of dye molecules and to promote HPLC separation of different silver-DNA products.

To test strand orientations produced by silver pairing, we compare FRET signals from two samples containing strand mixtures with silver nitrate added at one Ag$^+$ per C base, per strand. (This choice of silver concentration ensures high yields of Ag$^+$-paired strands). Sample C(3´-3´) contained equimolar quantities of $\mathbf{A_{3'C}}$ and $\mathbf{D_{3'C}}$**,** while sample C(5´-3´) contained equimolar quantities of $\mathbf{A_{3'C}}$ dye and $\mathbf{D_{5'C}}$. These solutions contained the desired $\mathbf{D_{5'C}}$**-**$\mathbf{A_{3'C}}$ and $\mathbf{A_{3'C}}$**-**$\mathbf{D_{3'C}}$ Ag$^+$-paired products (here, we reverse order for A and D designations simply to provide easier visual distinction of $\mathbf{D_{5'C}}$**-**$\mathbf{A_{3'C}}$ from $\mathbf{A_{3'C}}$**-**$\mathbf{D_{3'C}}$ in the text), together with co-formed **A-A** and **D-D** Ag$^+$-paired byproducts. We removed these byproducts using high performance liquid chromatography (HPLC) to isolate the Ag$^+$-paired $\mathbf{A_{3'C}}$**-**$\mathbf{D_{3'C}}$ and $\mathbf{D_{5'C}}$**-**$\mathbf{A_{3'C}}$ products of interest here. All FRET data shown here are for these purified products.

The DNA in the initially prepared samples (prior to HPLC) was buffered at a fairly high ammonium acetate concentration, 500 mM, to aid in formation of **A**-**D** Ag$^+$-duplexes by reducing the amounts of co-formed **A**-**A** and **D**-**D** Ag$^+$-duplexes, which predominate at low buffer concentrations. HPLC separation of the residual **A**-**A** and **D**-**D** products was facilitated by the difference in numbers of terminal thymine bases in the **A** and **D** strands. During HPLC, we used UV excitation to identify the **A**-**D** pairs by their simultaneous donor and acceptor emissions. (Due to the single-stranded regions of thymine bases, no product is expected have a FRET efficiency approaching unity; thus a donor signal is present for all products containing the donor dye). Absorbance and emission chromatograms can be found in Appendix C.2.

Sample C(3´-3´) exhibited one major HPLC peak with simultaneous acceptor and donor emission, corresponding to $\mathbf{A_{3'C}}$-$\mathbf{D_{3'C}}$ Ag$^+$-paired products. The irregular peak shape indicated the presence of unresolved substructures from minor structural variants (Appendix C.2a,b). For this eluent peak, the major product detected in ESI-MS was a strand dimer containing 19 Ag$^+$, an $\mathbf{A_{3'C}}$ strand and a $\mathbf{D_{3'C}}$ strand, as expected for a duplex with an Ag$^+$ bridging each pair of C bases. For sample C(5´-3´) we find two, closely spaced product peaks in HPLC that exhibit simultaneous acceptor and donor emission (Appendix C.2c,d). The similar elution times indicate similar structures, and both had nearly the same ratios of donor to acceptor emission. One of these product peaks also contained detectable quantities of residual **D**-**D** Ag$^+$-paired strands in ESI-MS, which we believe had fortuitously similar retention times due to shape perturbations from donor dye interactions. Here we focus on the $\mathbf{D_{5'C}}$-$\mathbf{A_{3'C}}$ Ag$^+$-paired product peak that did not have detectable byproduct residues, and further discuss the other peak in Appendix C.

The purified Ag$^+$-paired **A**-**D** products were solvent-exchanged into 10 mM ammonium acetate for further FRET analysis and mass spectrometry. Electrospray-ionization mass-spectrometry of the **A**-**D** solutions showed narrow Ag$^+$ distributions (Appendix C.3) centered at 18 Ag$^+$ for **D**$_{\mathbf{5'C}}$-**A**$_{\mathbf{3'C}}$ and 19 Ag$^+$ for **A**$_{\mathbf{3'C}}$-**D**$_{\mathbf{3'C}}$, with a spread of roughly 2-3 Ag$^+$ in both cases.

The sizes of the red and green "haloes" in Figure 4.1a qualitatively indicate the relative intensities in the donor and acceptor channels for the parallel and antiparallel strand

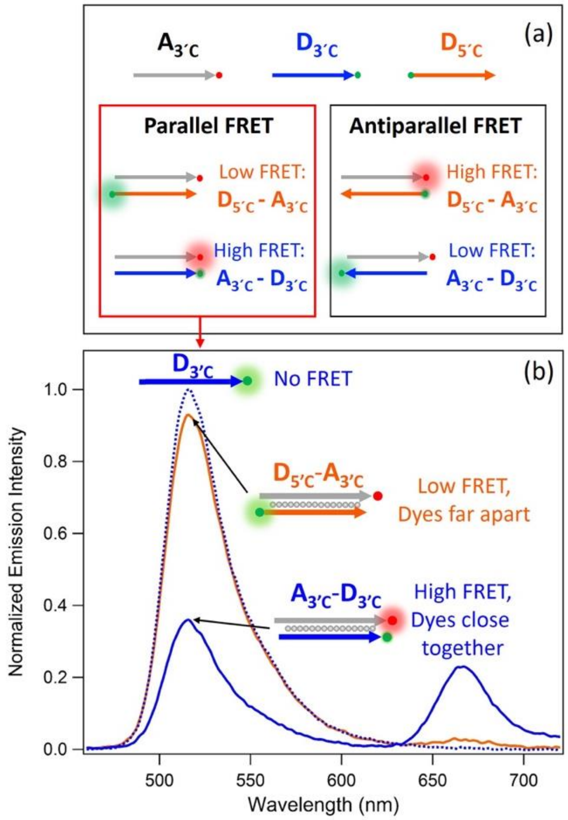

Figure 4.1) (a) Schematic for the FRET experiment. Strand $A_{3'C}$ (gray) is labelled at its 3´end with an acceptor dye (red dot). Strand $D_{3'C}$ (blue) is labelled at its 3´end with a donor dye (green dot). Strand $D_{5'C}$ (orange) is labelled at its 5´end with a donor dye (green dot). Arrows point in the 5' to 3' direction. Whether FRET is high or low for a given pairing, $A_{3'C}$-$D_{3'C}$ or $D_{5'C}$-$A_{3'C}$, depends on whether the strand orientation is parallel (left, red box) or antiparallel (right, black box). (b) Unsmoothed emission spectra of $D_{3'C}$ DNA, without Ag$^+$ (dotted blue curve) and of the purified Ag$^+$-paired $A_{3'C}$-$D_{3'C}$ (solid blue curve) and $D_{5'C}$-$A_{3'C}$ (solid orange curve). The high FRET signal for $A_{3'C}$-$D_{3'C}$ and low FRET signal for $D_{5'C}$-$A_{3'C}$ suggests a parallel strand orientation, as indicated in the cartoons. In all cases excitation is at 450 nm, which excites the donor but does not directly excite the acceptor. Emission spectra are normalized to their relative FRET efficiencies calculated ratiometrically from the donor and acceptor channels (see Appendix C for details).

possibilities, depicted as linear structures for simplicity. If Ag^+-pairing resulted in a *parallel* strand orientation, the *d* and *a* dyes would be held closer in $\mathbf{A_{3'C}}$-$\mathbf{D_{3'C}}$, resulting in stronger donor quenching and greater acceptor emission than for $\mathbf{D_{5'C}}$-$\mathbf{A_{3'C}}$. If Ag^+-pairing instead produced an *anti*parallel strand orientation, as for canonical H-bonded duplexes, the *d* and *a* dyes would be held farther apart in $\mathbf{A_{3'C}}$-$\mathbf{D_{3'C}}$ resulting in weaker donor quenching and less acceptor emission than for $\mathbf{D_{5'C}}$-$\mathbf{A_{3'C}}$.

Figure 4.1b displays the measured emission spectra of the Ag^+-paired $\mathbf{D_{5'C}}$-$\mathbf{A_{3'C}}$ and $\mathbf{A_{3'C}}$-$\mathbf{D_{3'C}}$ and of the $\mathbf{D_{3'C}}$ control strand with no Ag^+ (green curve, Figure 4.1b). The spectra in Figure 4.1b are normalized to the ratiometrically calculated FRET efficiencies using the donor and acceptor emission channels (Appendix C). Strand $\mathbf{D_{3'C}}$ exhibits no FRET since there is no acceptor dye present. Donor excitation was at 450 nm, which does not directly excite the acceptor (Appendix C.1). $\mathbf{A_{3'C}}$-$\mathbf{D_{3'C}}$ (blue curve, Figure 4.1b) exhibits strong quenching of donor emission and enhancement of acceptor emission. This is expected if the $\mathbf{A_{3'C}}$ and $\mathbf{D_{3'C}}$ strands are oriented parallel by Ag^+ pairing, resulting in high FRET efficiency because *a* and *d* are held close together (schematic, Figure 4.1b). In contrast, the acceptor emission from the $\mathbf{D_{5'C}}$-$\mathbf{A_{3'C}}$ Ag^+-duplex is weak (orange curve, Figure 4.1b). This is also as expected for parallel pairing to place *d* and *a* on opposite ends of $\mathbf{D_{5'C}}$-$\mathbf{A_{3'C}}$ (schematic, Figure 4.1b). Due to the considerable variation in the dye separation, R, that is permitted by the T extensions and the alkyl linkers to the dyes, a quantitative estimate of the length of the Ag^+-paired segments is beyond the reach of these FRET experiments. We defer further discussion of overall shape to the section on results of collision cross-section measurements.

We conclude that the FRET data indicate parallel strand pairing of cytosine strands by Ag^+, as was suggested indirectly by prior circular dichroism measurements on much shorter

(8-base) C strands[91] and by prior calculations.[114] The combination of high FRET for $\mathbf{A_{3'C}}$-$\mathbf{D_{3'C}}$ with low FRET for $\mathbf{D_{5'C}}$-$\mathbf{A_{3'C}}$ makes an i-motif-like (internally folded), dimeric Ag$^+$-paired structure unlikely, because folding near the center of the paired strands would result in similar FRET signals for $\mathbf{D_{5'C}}$-$\mathbf{A_{3'C}}$ and $\mathbf{A_{3'C}}$-$\mathbf{D_{3'C}}$ regardless of strand orientation.

Just as DNA structure is sensitive to sequence in the absence of Ag$^+$, the structures that arise from Ag$^+$-mediated pairings can be expected to be sensitive to sequence context. We note that prior studies that combined Ag$^+$ with 5´-(TAACCC)$_4$-3´ suggested the formation of an i-motif-like duplex folded by Ag$^+$, perhaps due to the addition of the (A,T) base motifs between the short runs of C bases.[146] We also must acknowledge the possibility that an unknown, unusual folded conformation might offer an alternative explanation for the FRET data in Figure 4.1b.

4.2.3) Sequential G-Ag$^+$-G pairings prefer a parallel strand orientation

To investigate the strand orientation in Ag$^+$-paired guanine DNA, we again used the three types of dye labelled DNA strands indicated in Figure 4.1a, with G instead of C bases. Because guanine DNA exhibited a much more pronounced tendency than cytosine DNA to form Ag$^+$-paired **A**-**A** and **D**-**D**, we modified the strand structure and solution conditions in order to obtain sufficient yields of the **D**-**A** pairs necessary for these FRET experiments (Methods). The strands each contain 15 consecutive G bases with T overhangs to promote separation by HPLC and random dye orientations. Strand $\mathbf{A_{3'G}}$ (5´-$T_4G_{15}T_4$-3´-*a*) has an acceptor dye on the 3´ end, strand $\mathbf{D_{3'G}}$ (5´-$T_2G_{15}T_2$-3´-*d*) has a donor dye on the 3´ end, and strand $\mathbf{D_{5'G}}$ (*d*-5´-$T_2G_{15}T_2$-3´) has a donor dye on the 5´ end. The dye locations are indicated by the red (*a*) and green (*d*) circles at the ends of the strand cartoons in Figure 4.2a, with $\mathbf{D_{3'G}}$ shown as blue, $\mathbf{D_{5'G}}$ as orange, and $\mathbf{A_{3'G}}$ as gray.

The DNA strands received from the manufacturer were polydisperse in length and in attachment of dye labels due to the difficulty in synthesizing poly-guanine DNA strands. We therefore used reversed-phase ion-pairing HPLC (Methods) to twice purify $\mathbf{A}_{\mathbf{3'G}}$. This additional purification eliminates products without acceptor dyes in further experiments, which otherwise would result in acceptorless pairings with donor-labelled strands and contribute spurious background donor emission. We prepared the Ag$^+$-paired $\mathbf{A}_{\mathbf{3'G}}$**-**$\mathbf{D}_{\mathbf{3'G}}$ and $\mathbf{D}_{\mathbf{5'G}}$**-**$\mathbf{A}_{\mathbf{3'G}}$ products with silver concentrations of 1 Ag$^+$ per G base, per strand, as in the above section for cytosine strands. The products with *d*-*a* pairs were isolated using HPLC and identified by monitoring the fluorescence chromatograms for simultaneous emission from both *d* and *a* under UV excitation (Appendix C.4). The composition of these purified *d*-*a* samples was examined by electrospray ionization mass spectrometry (ESI-MS) (Appendix C.5) after solvent exchange into 50 mM NH$_4$OAc and 10 μM AgNO$_3$ to prevent leaching of Ag$^+$ from repeated solvent exchange steps (Methods). This was a necessary step since the Ag$^+$-paired guanine strands were more fragile during the solvent exchange process than the Ag$^+$-paired cytosine strands, likely either due to the shorter lengths or different stabilities.

The HPLC chromatogram of the Sample G(3´-3´) solution, prepared by combining $\mathbf{A}_{\mathbf{3'G}}$, $\mathbf{D}_{\mathbf{3'G}}$ and Ag$^+$, exhibited only one $\mathbf{A}_{\mathbf{3'G}}$**-**$\mathbf{D}_{\mathbf{3'G}}$ product peak with emission from both *d* and *a*. For this eluent peak, the major product detected in ESI-MS was a strand dimer containing 15 Ag$^+$, an $\mathbf{A}_{\mathbf{3'G}}$ strand and a $\mathbf{D}_{\mathbf{3'G}}$ strand, as expected for a duplex with an Ag$^+$ bridging each pair of G bases. Rather than the single peak with simultaneous emission from *d* and *a* found for $\mathbf{A}_{\mathbf{3'G}}$**-**$\mathbf{D}_{\mathbf{3'G}}$**,** the HPLC chromatogram of the Sample G(5´-3´) solution, prepared by combining $\mathbf{A}_{\mathbf{3'G}}$, $\mathbf{D}_{\mathbf{5'G}}$ and Ag$^+$, exhibited two closely spaced $\mathbf{D}_{\mathbf{5'G}}$**-**$\mathbf{A}_{\mathbf{3'G}}$ eluent peaks. For both of peaks, the major product detected in ESI-MS was a strand dimer with 15 Ag$^+$, one $\mathbf{A}_{\mathbf{3'G}}$ and

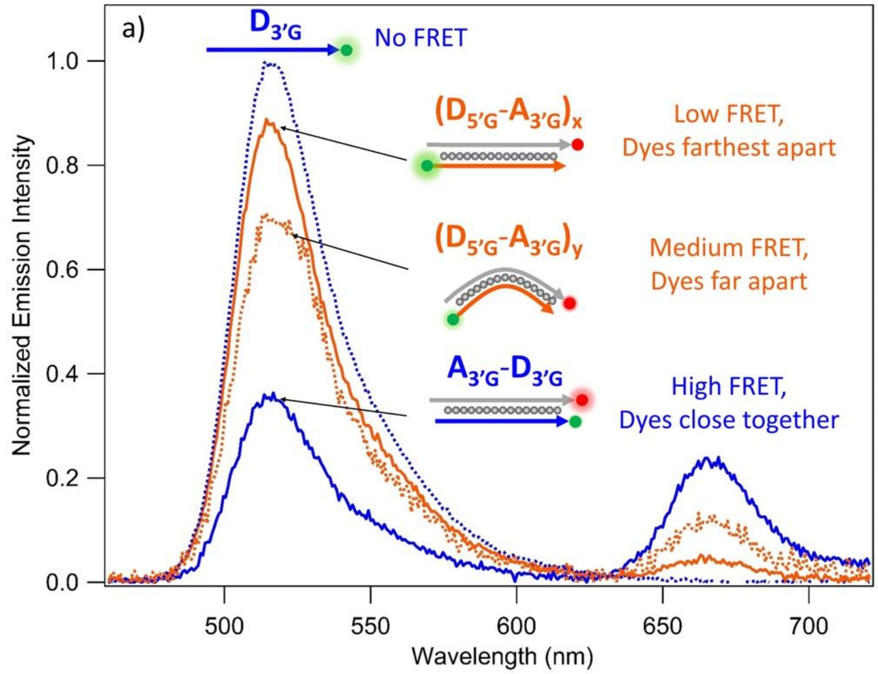

Figure 4.2) Unsmoothed emission spectra of $D_{3'G}$ bare DNA (dotted blue curve) and of the purified Ag^+-paired $A_{3'G}$-$D_{3'G}$ (solid blue curve), $(D_{5'G}\text{-}A_{3'G})_x$ (solid orange curve) and $(D_{5'G}\text{-}A_{3'G})_y$ (dotted orange curve). Arrows point in the 5' to 3' direction. In all cases excitation is at 450 nm, which excites the donor but does not directly excite the acceptor. The high FRET signal from $A_{3'G}$-$D_{3'G}$ and low to medium FRET signals for $(D_{5'G}\text{-}A_{3'G})_x$ and $(D_{5'G}\text{-}A_{3'G})_y$ respectively suggest a parallel strand orientation. Emission spectra are normalized to their relative FRET efficiencies calculated ratiometrically from the donor and acceptor channels (see Appendix C for details).

one **$D_{5'G}$** strand. We will refer to the faster-eluting, major product as (**$D_{5'G}$-$A_{3'G}$**)$_x$ and the slightly slower eluting minor product as (**$D_{5'G}$-$A_{3'G}$**)$_y$. This is similar to the case with the cytosine strands, where **$D_{5'C}$-$A_{3'C}$** also showed a doublet peak structure in the HPLC chromatogram, with similar ratios of donor and acceptor emission. It seems plausible that structural perturbations are caused by the donor dye, A488, being on the 5' end for both cytosine and guanine DNA.

Figure 4.2 plots emission spectra of the purified solutions of **$A_{3'G}$-$D_{3'G}$**, (**$D_{5'G}$-$A_{3'G}$**)$_x$ and (**$D_{5'G}$-$A_{3'G}$**)$_y$ excited at 450 nm along with the emission spectrum for the control **$D_{3'G}$** strand (no Ag^+). The spectra are normalized to their relative FRET efficiencies calculated ratiometrically from the donor and acceptor channels (Appendix C). **$A_{3'G}$-$D_{3'G}$** exhibits strong

FRET (Figure 4.2, solid blue curve), with a large decrease in emission intensity at the donor emission peak compared to the bare $\mathbf{D_{3'G}}$ strand, which has no FRET, (Figure 4.2, dotted blue curve) and a large increase in acceptor emission. Both of the products formed with the $\mathbf{A_{3'G}}$ strand, $(\mathbf{D_{5'G}\text{-}A_{3'G}})_x$ (Figure 4.2, solid orange curve) and $(\mathbf{D_{5'G}\text{-}A_{3'G}})_y$ (Figure 4.2, dotted orange curve), show weaker FRET with less donor quenching and a smaller increase in acceptor emission. Despite similar retention times during HPLC, which is sensitive to DNA secondary structure in reversed-phase ion-pairing HPLC,[147,148] $(\mathbf{D_{5'G}\text{-}A_{3'G}})_y$ displays somewhat more FRET than $(\mathbf{D_{5'G}\text{-}A_{3'G}})_x$. The differences may arise from dye-DNA interactions that produce a perturbed structural form with slightly reduced *d-a* separation in $(\mathbf{D_{5'G}\text{-}A_{3'G}})_y$, as indicated schematically in the inset of Figure 4.2. For example, a tendency to partial dye intercalation into Ag^+-paired G bases could produce structural deformation that might be suppressed by dye proximity in the "same end" case of $\mathbf{A_{3'G}\text{-}D_{3'G}}$, for which we detect just one *d-a* product. In any case, it appears that moving the donor dye from the 3' to the 5' is sufficient to introduce an additional slightly modified structure. Overall, the data is strongly suggestive for a preferential parallel strand orientation from runs of sequential G-Ag^+-G pairs.

Given the rather short Ag^+-paired regions in these FRET studies (15 base pairs), it is also conceivable that Ag^+ might be assembling the strands into folded dimers with different proximities of dye labels for attachment to the different strand ends. For example, H-bondings of G-rich strands are known to produce dimeric quadruplex structures, depending on sequence details.[6] The possibility that Ag^+-pairing produces dimeric forms that are internally folded rather than extended, unfolded duplexes could in principle be tested using of longer runs of G-Ag^+-G pairs. However, such an approach is challenged by the pronounced tendency of $d(G_N)$ strands to self-dimerize with Ag^+ as well as by the difficulty of synthesizing long poly G sequences. In addition for the guanine case, simply combining equimolar mixtures of *d* and *a* labelled strands with Ag^+, as we did for the cytosine case, produced abundant *a-a* and *d-d* guanine Ag^+-duplexes, but only barely detectable quantities of the desired *d-a* pairs that were insufficient for FRET measurements. The multi-step assembly discussed in the Methods section was used to overcome this difficulty, which likely arises from the tendency of G-rich strands to self-associate *via* non-canonical H-bondings, leading to multi-strand guanine quadruplexes or super stable guanine aggregates[149] in the absence of Ag^+. This would lock the hydrated *a*-labelled strands together, and similarly for the *d*-labelled strands, thus favoring formation of self-dimers upon addition of Ag^+. HPLC chromatograms for strands used in this study do suggest that the bare guanine DNA is aggregated, but after the addition of Ag^+ the strong association of silver with the G-Ag^+-G base pairs favors unaggregated Ag^+-dimers (see Appendix C.6).

This strong preference for Ag^+ assembly of guanine self-dimers is interesting for biologically relevant DNA, where introduction of Ag^+ may locally disrupt G-G hydrogen bonds in G-quadruplexes by forming G-Ag^+-G pairs between proximate G bases. This has the potential for future applications in regulating formation of G-quadruplexes, which are thought to be important in aspects of cellular regulatory functions, gene expression and control over telomere length.[150] The ion mobility structural studies of unlabeled, Ag^+-paired homodimers discussed in the next section further address the issue of whether Ag^+-pairings favor duplex or folded dimeric forms. Here we use "duplex" to refer to any unfolded, essentially linear strand dimer structure.

4.2.4) Probing the shapes of $(G_N)_2(Ag^+)_N$ and $(C_N)_2(Ag^+)_N$ by ion mobility measurements

To gain insight into the overall shapes of Ag^+-paired DNA, we turn to ion-mobility spectrometry-mass spectroscopy (IMS-MS). IMS-MS with electrospray ionization has become a powerful tool for gathering structural information on biological molecules.[151–156] This gentle technique is capable of studying even some native forms of DNA, as shown in studies on ligand binding,[157,158] unfolding intermediates,[153,159] and structure.[117,160] IMS-MS determines the drift time of the gas phase ion, which is the amount of time taken by the ion to travel in an applied electric field through a chamber containing a carrier gas. The drift time depends on factors including the ion shape, charge and mass as well as instrumental parameters. As the ion travels, its movement is slowed by collisions with the carrier gas causing larger molecules to have a longer drift time. The drift time data from IMS-MS can be used to extract the shape of the ion, as parameterized by its collision cross-section (CCS). The CCS is the orientationally averaged surface area of the ion that is accessible to carrier gas collisions. CCS measurements are often sensitive enough to resolve different ion shapes of the same molecular composition.

Here we probe structure by comparing CCS of Ag^+-paired strand dimers with lengths of $N = 6$ to $N = 30$ pairs (20 for guanine DNA) to CCS values obtained for canonical DNA duplexes and for G-quadruplexes that are known to preserve memory of their structure upon transfer from solution to gas phase.[161,162] This comparison provides structural insight without the need for accurate molecular dynamics calculations, which remain a serious computational challenge even f or well-studied H-bonded DNA duplexes due to issues with proper simulation of long-range phosphate group hydrogen bonding in gas phase, the distribution of charge on gas phase ions, and the structural consequences of realistic desolvation.[154,163] The measured CCS values are tabulated in Appendix C, Tables C.1-4.

The experiments were carried out using an Agilent 6560 IMS-Q-TOF instrument with helium carrier gas in the drift tube using methods detailed in a recent study of WC duplexes.[163] Representative IMS-ESI-MS spectra of Ag^+-cytosine homopolymer solutions and Ag^+-guanine homopolymer solutions, prepared as discussed in the methods section, showed that Ag^+-paired dimers $(G_N)_2(Ag^+)_N$ and $(C_N)_2(Ag^+)_N$ with numbers of Ag^+ equal to the strand length are the major products across wide-ranging strand lengths (Appendix C.7). Higher order products (containing, e.g., 3 and 4 strands) were either undetectable, or present in much lower abundance. Thus, for even for quite long homopolymer segments (N of at least 20 pairs for guanine and N of at least 30 for cytosine), the Ag^+-paired dimer is the favored product. This is an important consideration for incorporation of Ag^+-mediated pairings into larger DNA constructs. We believe that this predominance in gas phase reproduces the predominance of Ag^+-paired dimers in solution, because the Ag^+-mediated pairings are significantly more robust

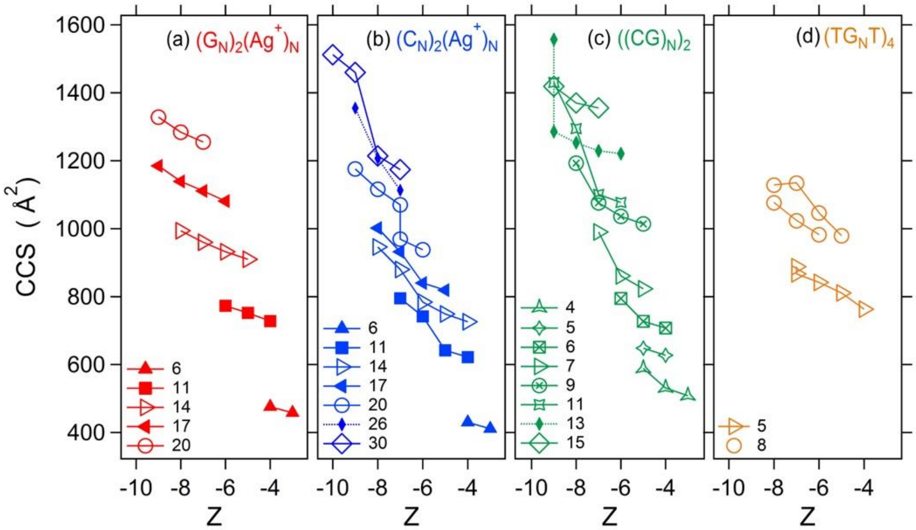

Figure 4.3) Collision cross-sections (CCS) from IMS-MS of a) $(G_N)_2(Ag^+)_N$ for N=6-20, b) $(C_N)_2(Ag^+)_N$ for N=6-30, c) WC-paired duplexes $((CG)_N)_2$ for N=4-15 and d) G-quadruplexes $(TG_NT)_4$ for N=5,8 *versus* charge state (Z). Changes in CCS with Z are more pronounced and less regular for the $(C_N)_2(Ag^+)_N$ and $((CG)_N)_2$ than for $(G_N)_2(Ag^+)_N$ and G-quadruplexes. The CCS were obtained using the step-field method from the slope of the linear regression of arrival time as a function of the inverse drift voltage. The arrival times were obtained from Gaussian fits of the arrival time distributions. When more than one peak was distinguishable, two collision cross section values were extracted (see Appendix C). Fit errors (not shown) are smaller than the plot symbols. Multiple CCS values for the same Z are derived from multi-peaked CCS distributions, indicative of the coexistence of different well-defined conformations.

than H-bonded pairings (Chapter 2 and other work)[39] which persist into gas phase under the gentle ionization conditions used here.

Figure 4.3 displays CCS values for Ag^+-paired DNA $(G_N)_2(Ag^+)_N$ (Figure 4.3a) and $(C_N)_2(Ag^+)_N$ (Figure 4.3b), WC paired $((CG)_N)_2$ duplexes (Figure 4.3c) and G-quadruplexes (Figure 4.3d) at various strand lengths and observed charge states. Since it is currently debated what charge state, Z, most faithfully reflects solution phase data for nucleic acids, we show the data for all values of Z detected in sufficient abundance.[163] The CCS values in Figure 4.3 are the peak locations obtained from Gaussian fits to the full arrival time distributions at each value of Z, which are reconstructed by taking each ESI-IMS-MS measurement at several different voltages using the step-field method. In some cases the presence of two or more structural forms at intermediate values of Z, discussed further below, required the reconstruction of a separate CCS distribution for each peak. Each CCS distribution was then deconvoluted with Gaussian fits.

The charge dependences of the CCS for $(G_N)_2(Ag^+)_N$ and $(C_N)_2(Ag^+)_N$ are qualitatively different (Figure 4.3a,b). For $(G_N)_2(Ag^+)_N$ at all lengths, N, the CCS increases linearly with Z indicating a regular expansion in size with increasing average charge per base (Figure 4.3a). In contrast, for $(C_N)_2(Ag^+)_N$ the CCS displays a nonlinear dependence on Z (Figure 4.3b) with a larger increase in CCS at intermediate Z than at low and high |Z|, corresponding to a transition between distinct forms at low and high average charge per base. The transition from more compact to less compact form is demonstrated by a double peak structure in the CCS distributions for N=20 at Z = -7, for which the CCS distributions showed two resolved peaks of comparable magnitude (both CCS values are plotted in Figure 4.3b, its full CCS distribution can be seen in Appendix C.8). A qualitatively similar transition from compact to less compact form with increasing |Z| occurs in the $((CG)_N)_2$ duplexes (Figure 4.3c), while G-quadruplexes show less dependence of CCS on Z (Figure 4.3d), consistent with prior work.[163] The Z-dependences of the CCS for $(C_N)_2(Ag^+)_N$ and the WC duplexes, $((CG)_N)_2$, is reminiscent of recent IMS-MS studies that used similarly wide ranges of Z to probe gas-phase ions derived from a variety of WC duplexes.[163] In those studies of duplexes with B-form DNA structure in solution, the gas phase transition from a compact to an extended form with increasing |Z| was found to arise from the formation, at low |Z|, of gas-phase hydrogen bonds between the deprotonated phosphate groups that carry the ion charge. These inter-phosphate gas-phase H-bonds had the effect of "zipping" the gas-phase duplexes into more compact double-stranded forms at low |Z|. With increasing |Z| these gas-phase H-bonds opened, resulting in transitions to elongated duplex structures.

Changes in gas-phase hydrogen bonding may also contribute to the sudden changes in CCS at intermediate Z for $(C_N)_2(Ag^+)_N$. Computational studies of $(C_2)_2(Ag^+)_2$ found that in solution, H-bonds between Ag^+-paired C bases and H-bonds between adjacent C-Ag^+-C pairs help stabilize the duplex.[114] It is possible that changes in Z alter the degree of inter-phosphate hydrogen bonding in gas phase, which could then sterically affect the H-bonding between adjacent C-Ag^+-C pairs. For example, a compact gas phase $(C_N)_2(Ag^+)_N$ could favor H-bonds between Ag^+-paired C bases while an expanded form for $(C_N)_2(Ag^+)_N$ could make the C-Ag^+-C pairs too far apart for this type of H-bonding. An interesting difference between the gas-phase ions of Ag^+-paired strands and the H-bonded duplexes is the higher deprotonation in the Ag^+-paired case at the same Z. For the H-bonded duplexes, removal of Z protons accounts for the full (negative) Z of the gas phase ion. For $(C_N)_2(Ag^+)_N$ (and $(G_N)_2(Ag^+)_N$), a total of Z+N protons must be removed to achieve the same negative Z charge state. Thus the specific patterns of H-bonding in the gas-phase ions of Ag^+-paired duplexes are likely different from those in their H-bonded counterparts. We also note the possibility that ionic interactions between the deprotonated, negatively charged phosphate backbone and the positively charged C-Ag^+-C and G-Ag^+-G pairs may contribute to changes in the gas phase structure.

To infer whether the overall structure of the Ag^+-paired dimers may be similar to a duplex or to a folded dimeric structure, we compare CCS of the Ag^+-paired $(G_N)_2(Ag^+)_N$ and $(C_N)_2(Ag^+)_N$ to compact G-quadruplexes that are known to retain memory of their overall solution structure upon transfer to gas phase. We additionally compare to the CCS of WC paired duplexes, for which the relation between solution and gas phase structure is more complex.[163] We normalize the data to the same average charge per base, Z/N_{total}, where N_{total} is the total number of bases, by extrapolating the CCS data (Figure 4.3a-d) from the two nearest data points to the values $Z/N_{total} = -0.15$ and $Z/N_{total} = -0.20$ (Figure 4.4a,b). We selected these values of Z/N_{total} because they fall close to measured data points, and are different enough to illustrate effects of increasing charge density.

Figure 4.4 shows that for both values of Z/N_{total}, the CCS for $(G_N)_2(Ag^+)_N$ exhibit a highly linear dependence on N_{total} (red points). This is the expected behavior for any essentially linear structure formed by stacking well-defined structural units, such as a duplex made from regularly stacked base pairs. The CCS of the $((CG)_N)_2$ duplexes (green points) has a nonlinear dependence on N_{tot} at $Z/N_{total} = -0.15$ and a nonlinear rising trend at high N_{total} at $Z/N_{total} = -0.20$, likely corresponding to size and charge dependent variations in structure that prior work found to arise from changes in gas-phase H-bonding.[163] For $(C_N)_2(Ag^+)_N$ (blue points) the dependence of CCS on N_{total} is closer to linear than for the WC case, and somewhat less linear than for $(G_N)_2(Ag^+)_N$.

Because previous work established that certain G quadruplexes have similar gas and solution phase shapes,[151,163] here we include them as structural benchmarks. We verified that the solution circular dichroism spectra of the $(TG_NT)_4$ used here exhibit the distinctive UV peak structure characteristic of the expected tetrameric quadruplex form (Appendix C.7). G-quadruplexes are very compact and rigid structures with four guanine bases that H-bond to form a planar tetrad, with successive tetrads stacked at a rise per tetrad of approximately 3.2 Å (with some sequence dependent variations).[164] Conversely, in solution WC paired DNA is much more elongated and less rigid than a G-quadruplex, with a rise per base pair of 3.3 Å in B-form DNA. For G-C rich cases, WC DNA retains memory of its duplex structure in gas phase, albeit with considerable compaction at low $|Z|$ due the interphosphate H-bonding mentioned above, and with expansion at high $|Z|$ due to breakage of these interphosphate H-bonds and charge repulsion.[163] As shown in Figure 4.4, the $(TG_NT)_4$ G-quadruplexes (orange points) are more compact than the $((CG)_N)_2$ duplexes with the same total base numbers, N_{total} (Figure 4.4, orange points), despite the larger size of G than C bases.

Because the G-quadruplexes and $(G_N)_2(Ag^+)_N$ have very similar base compositions, the much larger CCS for $(G_N)_2(Ag^+)_N$ at the same N_{total} (Figure 4.4) is strong evidence for a much less compact structure than the G-quadruplex, again pointing to a duplex form for $(G_N)_2(Ag^+)_N$. The $(G_N)_2(Ag^+)_N$ are also larger than the $((CG)_N)_2$ duplexes, which in turn have larger CCS than $(C_N)_2(Ag^+)_N$ (Figure 4.4). Presumably this size ordering is in part due to the larger size of G than C bases; however a detailed understanding of the relative effects of overall structural form and of base size must await the development of CCS modeling that realistically incorporates silver-mediated base pairing.

Peak widths of CCS distributions provide additional information on the distribution of conformational states, where a narrower distribution of molecular shapes would result in a narrower CCS distribution. We examine the peak widths of the CCS distributions for the Ag^+-paired cytosine and guanine strands as compared to the control WC-paired duplexes and G-quadruplexe~~s~~. Figure 4.5a displays the peak widths at different Z for products with a total of 28 bases, while Figure 4.5b is for products with 36-40 bases. The peak widths for the G-quadruplexes (Figure 4.5, gold stars) are narrowest, and the peak widths for the WC duplexes

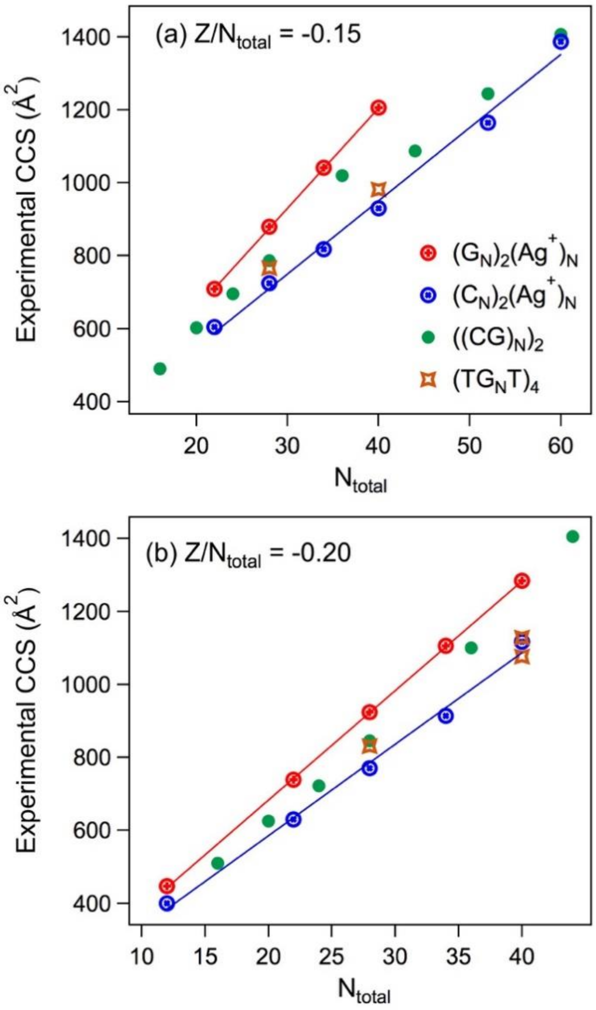

Figure 4.4) (a) Experimental CCS plotted versus the total number of bases in a product, N_{total}, at fixed charge to base ratios, Z/N_{total}. (a) Z/N_{total} = 0.15 and (b) Z/N_{total} = -0.2. Experimental CCS points are from linear interpolation of the measured CCS (Figure 4.3).

(Figure 4.5, green circles) are widest, across all Z. The broader CCS distributions for the WC duplexes than the quadruplexes are expected because the duplex is a more flexible, less tightly H-bonded structure in solution, that produces more conformationally diverse ions on transfer to gas phase. In addition, unlike the quadruplex, the WC duplex exhibits significant changes in H bonding in gas phase, distributed over many different sites on the ion.[163]

The Ag^+-paired $(C_{14})_2(Ag^+)_{14}$ (Figure 4.5a, blue circles) and $(G_{14})_2(Ag^+)_{14}$ (Figure 4.5a, red circles) display peak widths that fall in between those of the $(TG_5T)_4$ G-quadruplex and $((CG)_7)_2$ WC paired DNA. The Ag^+-paired strands have peak widths approximately 3-6 times

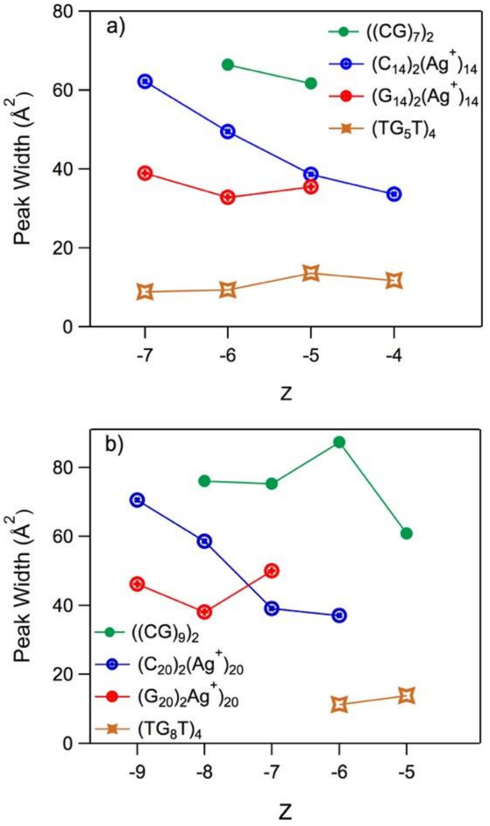

Figure 4.5) Peak widths of major features in CCS distributions at various charge states, Z, for a) $((CG)_7)_2$, $(C_{14})_2(Ag^+)_{14}$, $(G_{14})_2(Ag^+)_{14}$ and $(TG_5T)_4$ and b) $((CG)_9)_2$, $(C_{20})_2(Ag^+)_{20}$, $(G_{20})_2(Ag^+)_{20}$ and $(TG_8T)_4$. For comparison of peak widths, all products in a) have 28 bases and b) have 36-40 bases. In a) the G-quadruplex $(TG_5T)_4$ (gold stars) has the lowest peak width, suggesting a rigid and compact structure, as expected; while the WC paired $((CG)_7)_2$ (green circles) has the highest peak widths, suggesting an extended and flexible structure as expected for ions derived from duplex B-DNA. The $(C_{14})_2(Ag^+)_{14}$ (blue circles) and $(G_{14})_2(Ag^+)_{14}$ (red circles) have intermediate peak widths, indicating that the Ag^+-paired strands are more rigid than their WC counterparts, but less so than the G-quadruplexes. All products are fairly consistent in peak width across Z except $(C_{14})_2(Ag^+)_{14}$, which shows a rapid increases in width at high |Z| coincident with the sharp increase in CCS in Figure 4.3.

wider than their G-quadruplex counterpart at the same length, which makes any similarly folded structures unlikely. In the gas phase, argentophilic (Ag^+-Ag^+) interactions[165] could reduce the degree of flexibility in the Ag^+-paired structures, and partly account for the smaller peak widths of the Ag^+-paired strands compared to WC paired duplexes. The same trends in Figure 4.5a with 28 base DNA structures are well reproduced at 36-40 bases as seen in Figure 4.5b. Thus these trends in peak width can be attributed to the conformational diversity of each type of structure, rather than to specific length effects.

The width of the CCS distribution for Ag^+-paired $(C_{14})_2(Ag^+)_{14}$ is strongly dependent on charge state (Figure 4.5a), mirroring the strong CCS dependence on charge state (Figure 4.3b). This further suggests the transition from a compact structure at low magnitude charge state, perhaps akin to that of the WC duplexes, to a more elongated form at high magnitude charge state. It is interesting to note that the peak widths for Ag^+-paired cytosine strands at both length scales (Figure 4.5a,b) quickly approach the peak widths for the B-DNA strands, suggesting that at high magnitude charge states the Ag^+-paired cytosine strands may be elongated linear duplexes similar to B-DNA.

In summary, IMS-MS experiments indicate simple unfolded duplex shapes for $(G_N)_2(Ag^+)_N$, with no evidence for significant charge-dependent changes in overall structure in gas phase. Simple unfolded duplex shapes are also indicated for $(C_N)_2(Ag^+)_N$, but the irregular dependences of CCS on charge state suggest changes between two distinct gas phase structures with different compactness.

4.3) Conclusions

We find evidence from FRET experiments that strands with many consecutive guanine bases, or many consecutive cytosine bases, are paired by Ag^+ in a parallel orientation. This is indicated by a high FRET signal when the donor and acceptor dyes are both on the 3’ end of the Ag^+-paired strands, and a low FRET signal when the donor dye is on the 5’ end and the acceptor dye is on the 3’ end. We find two isolatable conformations with very similar retention times in HPLC for both the cytosine and guanine Ag^+-paired strands when the 5’ donor dye strand is paired with the 3’ acceptor dye strand, indicating some degree of dye influence on conformation. While we cannot rule out the possibility that the dyes affect the preferred strand orientation, we believe that our observation of higher FRET for dyes on the same ends of the strands and lower FRET for dyes on opposite strand ends provides strong evidence for a preferred parallel orientation, with or without the dye labels.

We use IMS-MS to discover shape information for Ag^+-paired structures consisting of long series of G-Ag^+-G and C-Ag^+-C base pairs. The large CCS values of Ag^+-paired G_N strands, relative to G-quadruplexes with the same number of bases, and the highly linear dependence of the CCS for $(G_N)_2(Ag^+)_N$ on N both indicate that Ag^+ pairs the G_N strands into a simple duplex form rather than a folded dimer structure. The strong contrast in FRET signal for different donor dye locations on both $(C_N)_2(Ag^+)_N$ and $(G_N)_2(Ag^+)_N$ also suggests unfolded duplex forms. The Ag^+-paired C_N strands show a transition from a less compact to more extended form with increasingly negative Z, qualitatively similar to the changes in CCS due to gas phase changes in H bonding in WC duplexes. The CCS distributions for $(C_N)_2(Ag^+)_N$ and $(G_N)_2(Ag^+)_N$ are wider than for the rigid G quadruplexes, corresponding to a broader range of conformational states, but are narrower than for the WC-paired $(CG)_N$ duplexes. We expect that these CCS results will be useful for future development of structural calculations that incorporate Ag^+-mediated base pairings.

4.4) Methods

4.4.1) General FRET Experimental Methods:

The dye-labelled DNA strands were synthesized and HPLC purified by ChemGenes Corporation. RNAse/DNAse free water (Integrated DNA Technologies) or HPLC/MS grade water was used in all of the experiments. The DNA strands were additionally desalted upon receipt by centrifugal solvent exchange with 3k MWCO filters. All DNA solutions were annealed at 90^{o}C for 5 minutes, and then allowed to cool to room temperature over 30 minutes prior to HPLC.

To separate DNA products we used a Hitachi L-6200A pump and L-4200 UV-Vis detector with a 50 x 4.6 mm Kinetex EVO C18 column (2.6 μm particle size, 100 Å pore size) and a methanol and water gradient in 35 mM triethylamine ammonium acetate pH = 7. The DNA solutions were concentrated 3-fold prior to injection into the HPLC using 3k MWCO centrifugal filters. Both absorbance signal and emission signal with excitation at 270 nm were monitored to determine which dyes were on each DNA product eluting from the HPLC. After catching the separated peaks in HPLC corresponding to Ag^+-paired strands with both *a* and *d* dyes, the solutions were solvent-exchanged by centrifugal filtration into 10 mM (for C Ag^+-duplexes) or 50 mM (G Ag^+-duplexes) ammonium acetate again using 3k MWCO centrifugal filters, unless otherwise noted. We used a 15-35% (for C Ag^+-paired strands) and 20-40% (for G Ag^+-paired strands) methanol gradient at 1% per minute with a 1 μL/min flow rate for purification of each sample.

Spectral measurements at ambient temperature were performed for FRET studies. Samples were excited by Micropack's high power xenon light source (HPX-2000) at 450 nm wavelength selected by a monochromator (Monoscan 2000). Emission signal was detected by a thermo-electrically cooled QC6500 Ocean Optics detector. The purified cytosine Ag$^+$-paired strand solutions were injected into a Waters QTOF2 negative-ion mode electrospray-ionization (ESI) mass-spectrometer at 10 μL/min with a 2 kV capillary voltage, 30V cone voltage and 10V collision energy for product verification (Appendix C.2). The purified guanine Ag$^+$-paired strand solutions were injected into a Xevo G2-XS QToF ESI mass spectrometer in negative-ion mode at 5 μL/min with a 2kV capillary voltage, 10V cone voltage and 6V collision energy for product verification.

4.4.2) Cytosine Ag$^+$-paired strands FRET experiments:

The cytosine Ag$^+$-paired strands were synthesized by separately combining strands $\mathbf{A_{3'C}}$ with $\mathbf{D_{5'C}}$, and $\mathbf{A_{3'C}}$ with $\mathbf{D_{3'C}}$, at a final concentration of 2.5 μM for each DNA strand in a solution of 500 mM ammonium acetate at pH = 7. After mixing, $AgNO_3$ was added to the solutions for a final concentration of 100 μM $AgNO_3$ (Sigma-Aldrich analytical grade). The samples were purified with HPLC and FRET and MS measurements proceeded on the $\mathbf{A_{3'C}}$-$\mathbf{D_{3'C}}$ and $\mathbf{D_{5'C}}$-$\mathbf{A_{3'C}}$ duplexes as per the previous section.

4.4.3) Guanine Ag$^+$-paired strands FRET experiments:

Due to the difficulties with the guanine strands presented for obtaining Ag$^+$-paired strands that contained both the acceptor dye and donor dye, we modified the preparation steps from the cytosine case as needed to obtain suffivient D-A product yield for FRET experiments. The $\mathbf{A_{3'G}}$ strand received from the supplier had a polydisperse set of products and the bare strand was not isolatable with our standard HPLC experimental conditions due to aggregation (Appendix C.6). Thus we additionally purified the $\mathbf{A_{3'G}}$ strand by first adding Ag$^+$ to form high yields of unaggregated Ag$^+$-paired strands. The solution consisting of 25 μM $\mathbf{A_{3'G}}$ DNA, 50 mM NH_4OAc pH = 7, and 375 μM $AgNO_3$ was then injected into the HPLC and all resolvable major peaks were collected. The products were examined by electrospray-ionization mass-spectrometry (ESI-MS). The product which was determined to be an Ag^+-paired **$A_{3'G}$-$A_{3'G}$** was then (see Appendix C.5a) incubated in 50 mM cysteine for 1 hour to chelate out the Ag^+ and the twice purified product determined as strand **$A_{3'G}$** was used for all further experiments.

Initial attempts to create Ag^+-paired strands with both an acceptor and donor dye labels proved difficult due to self-pairing and/or aggregation of the bare dye-labelled strands: upon addition of $AgNO_3$ to solutions containing strands with donor and acceptor dyes, Ag^+-paired acceptor-acceptor and donor-donor homodimers predominated. To obtain sufficient yields of the donor-acceptor pairs required for FRET studies, we first synthesized the Ag^+-paired homodimers in a solution consisting of 2.5 μM **$D_{3'G}$** or **$D_{5'G}$**, 2.5 μM **$A_{3'G}$**, 50 mM NH_4OAc pH = 7 and 75 μM $AgNO_3$ and annealed them. After cooling, aqueous cysteine was then added to each solution to a final concentration of 50 mM cysteine. Each solution was then solvent exchanged to 50 mM NH_4OAc by centrifugal filtration with 3k MWCO filters to remove excess cysteine (approximately 0.001% of original solvent remained). Aqueous $AgNO_3$ was then added to a final concentration of 75 μM $AgNO_3$. After annealing each solution again, they were injected into the HPLC. The Ag^+-dimers with both an acceptor and donor dye were then caught during elution from the HPLC and solvent exchanged with spin centrifugation (3k MWCO filters) into 50 mM NH_4OAc and 10 μM $AgNO_3$. The guanine Ag^+-duplexes required a slight addition of $AgNO_3$ post HPLC to retain a majority of duplex product in MS, as opposed to the cytosine Ag^+-duplexes which had a majority of duplex product post-HPLC with no additional $AgNO_3$. After solvent exchanging, the samples were immediately spectrally analyzed for FRET signals and then injected into the ESI-MS.

4.4.4) Ion-mobility experiments:

Ag^+-DNA samples for IMS experiments were prepared at 80 μM DNA, 1 equivalent $AgNO_3$ per base and 50 mM NH_4OAc at pH = 7 and injected into the MS as prepared. The G-quadruplex $(TG_NT)_4$ DNA samples were prepared at 80 μM DNA in 100 mM NH_4OAc at pH = 7 and injected into the MS as prepared. The WC paired $((CG)_N)_2$ duplex samples were prepared at 50 μM DNA in 100 mM 100 mM NH_4OAc at pH = 7 and diluted to 10 μM DNA in the same buffer conditions prior to injection into the MS. All samples were annealed at 90^{o}C for 5 minutes then cooled slowly over 30 minutes. The samples were then shipped on ice overnight to IECB for IMS-MS analysis, except for the $((CG)_N)_2$ samples which were prepared at IECB. Upon receipt the samples were refrigerated at 4^{o}C and stored until analysis. The samples were ionized under soft conditions with the same procedure found in prior work,[163] and the procedure will only briefly be discussed here. The experiments were completed on an Agilent 6560 DTIMS-Q-TOF in negative ion mode. The source temperature was 200^{o}C, the drift tube helium pressure was 3.89 ± 0.01 Torr and the trapping funnel pressure was 3.67 ± 0.01 Torr. The samples were injected into the mass spectrometer at 3 µL/min.

Chapter 5) Chiral Electronic Transitions in Fluorescent Silver Clusters Stabilized by DNA

Adapted with permission from: S. M. Swasey, N. Karimova, C. M. Aikens, D. E. Schultz, A. J. Simon and E. G. Gwinn. Chiral Electronic Transitions in Fluorescent Silver Clusters Stabilized by DNA. *ACS Nano* **2015**, 8 (7), 6883-6892.[166] *Copyright 2015 American Chemical Society.*

5.1) Introduction

In Chapter 5 we depart from the focus on Ag^+-mediated base pairings in DNA for use in creating more robust DNA nanotechnology in Chapters 2-4, and move on to the topic of fluorescent silver clusters templated by DNA (Ag_N-DNA). Ag_N-DNA are an emerging new class of fluorophore with promising optical properties such as the potential to have high quantum yields and wide-ranging emission wavelengths from the visible into the near-infrared.[47] The optical properties of Ag_N-DNA are determined by the templating DNA sequence, which selects for cluster size.[47] The details of Ag_N-DNA structure and how the DNA sequence selects the cluster's size and optical properties are still unknown. Ag_N-DNA also contain both cationic and neutral silver,[50] possibly hinting at the involvement of Ag^+-mediated base pairings in these unique fluorophores.

Non-disruptive structural probes of these delicate materials are needed to elucidate the connection between DNA sequence and the formation of fluorescent silver clusters with specific optical properties. Here we focus on CD spectroscopy as a tool to infer aspects of AgN-DNA struc-ture. At the much larger size scale of metal nanoparticles, advances in chemical control over the shape, as well as size, of metal nanoparticles are resulting in remarkable optical signatures of chirality.[167–174] Recent studies found that decorating 50 nm metal nanoparticles with DNA could lead to circular dichroism (CD) signals at visible wavelengths spanning the plasmonic response of the metal particles.[167] This visible signature of induced chirality occurred at energies 1-2 eV below the ultraviolet (UV) CD of DNA itself, which arises in the 4-6 eV range (200-300 nm) from differences in the absorption of left and right circularly polarized light that characterize the specific chiral arrangement of the bases. The visible CD enhancement *via* coupling of plasmonic absorption to UV transitions of DNA was greatly enhanced by use of non-spheroidal metal nanoparticles, pointing to the crucial role of metal particle shape.

At the much smaller (~1 nm) size scale of metal clusters, optical signatures of chirality are also evident and are particularly exciting due to the emergence of strong fluorescence in the cluster size regime. Gold and silver clusters protected by chiral ligand monolayers exhibit circular dichroism near wavelengths of metal-based transitions.[168,169] Intrinsically chiral ligands are not even necessary for cluster chirality. $Au_{38}(SR)_{24}$ clusters with achiral thiol ligands displayed pronounced CD signals,[170,171] reflecting a chiral pattern of ligand attachment that shapes a chiral metal cluster.[169]

While a chiral twist in cluster shape, and thereby on free electron currents, should be easier to impress on elongated rather than spherical clusters, effects of the shape of gold clusters on chirality of electronic transitions are not well understood. Interpretation of the chiroptical properties is complicated by the broad band of transitions arising from d-orbitals of gold, which spread across the range of the shape-dependent cluster excitations and into the UV. Although silver nanoparticles[172,175] and clusters[176–182] are less studied than their gold counterparts, silver has the advantage of weaker, higher energy d-band transitions. Thus silver-based particles have potential for strong chiral signatures with a transparent relation to cluster structure, and associated promise for use in chiral sensing applications.

ID	Template Strand	Exc.[(a)] Energy	Emission Energy[(a)]	Ag^0 (b)	Ag^+ (b)
S1	CCCACCCA- CCCGCCCA	1.74 eV (711 nm)	1.60 eV (776 nm)	12	8 or 9
S2	GGCAGGTTGG GGTGACTAAA AACCCTTAAT CCCC	2.06 eV (601 nm)	1.83 eV (677 nm)	6	9
S3	CACCGCTTTT GCCTTTTGGG GACGGATA	2.07 eV (600 nm)	1.85 eV (670 nm)	6 or 7	8 or 9
S4	TGCCTTTTGG GGACGGATA	2.55 eV (487 nm)	2.19 eV (566 nm)	4	6

Table 5.1) Ag_N-DNA properties. (a) Aqueous visible fluorescence excitation maxima and emission maxima. (b) Numbers of neutral silver atoms (Ag^0) and numbers of silver cations (Ag^+) in the AgN-DNA templated by the indicated strand. Reported values[49,50] were determined by mass spectrometry of the pure AgN-DNA in ~ 30% methanol solvent.

Recently it was shown that silver clusters with sizes of 10-20 silver atoms stabilized by DNA can be isolated with compositional purity.[50,183] Optical studies of pure, fluorescent Ag_N-DNA, which contain cationic as well as neutral silver atoms, suggested a rod-like structure for a neutral silver cluster core, with core length governing color.[49,51] If chiral, such elongated clusters might be expected to exhibit particularly rich CD signatures.

Here we investigate the chirality of the optical transitions in pure Ag_N-DNA with cluster emission colors ranging from blue-green through the near infrared (Table 1). Samples S2 and S3 are stabilized by different DNA template strands but hold silver clusters with similar absorbance and emission spectra. Previous studies[49,50] identified the composition of S2[184] and

S3 as 6-7 silver atoms in the neutral cluster core, with 8-9 silver cations also incorporated into the Ag_N-DNAs. The redshifted emitter S1[48] contains 12 neutral silver atoms in the cluster core and 8-9 silver cations,[49,50] while the blueshifted emitter S4 holds 4 neutral silver atoms in the core and 6 silver cations. This selection of Ag_N-DNA probes the chirality of visible through IR absorbance transitions that correspond to peak excitation of fluorescence. In the UV, changes in CD relative to the bare DNA template strands indicate nucleobase rearrangement by cluster-DNA interactions. While early studies of DNA-stabilized silver clusters also investigated UV chirality using CD spectroscopy, these investigations used unpurified solutions,[63,185,186] which typically contain mixtures of many different silver-DNA products and consequently cannot address chirality of specific DNA-stabilized silver clusters.

5.2) Results and Discussion

5.2.1) Reshaping of UV Circular Dichroism in Ag_N-DNA

In native DNA, chiroptical activity in the 4.1-6.2 eV range (200-300 nm) arises largely from the relative orientations of transition dipoles of the chromophoric bases, and therefore is extremely sensitive to conformational changes. To investigate the effects of the strand-embedded silver clusters on the shaping of the DNA itself, we compare the UV circular dichroism of the bare DNA strands, the non-fluorescent solutions of the DNA strands incubated with unreduced silver ions (Ag^+-DNA), and the purified fluorescent Ag_N-DNA solutions (Figure 5.1). The Ag^+-DNA solutions had the same $[Ag^+]/[DNA]$ as used in synthesis of the pure Ag_N-DNA (Appendix D).

The bare DNA strands (black curves, Figure 5.1a-d) show a positive CD peak near 4.5 eV (270-280 nm) and negative peak near 5.0 eV (250 nm), as expected for random coil DNA.[187–189] The attachment of Ag^+ (Ag(I) cations) to the DNA produces large negative CD features (red curves, Figure 5.1a-d). In contrast to the large changes in CD spectra, the UV absorbance spectra are similar in the absence/presence of either Ag^+ or the pure clusters (Figure 5.1e). We attribute the Ag^+-induced reorganization of the UV CD to the known ability of silver cations to mediate artificial base pairing (Chapters 2-4 and other works),[30,78,190,191] which should alter relative orientations of base transition moments and change UV CD relative to the bare DNA. Interestingly, the largely negative CD spectra for the DNA with Ag^+ (red curves,

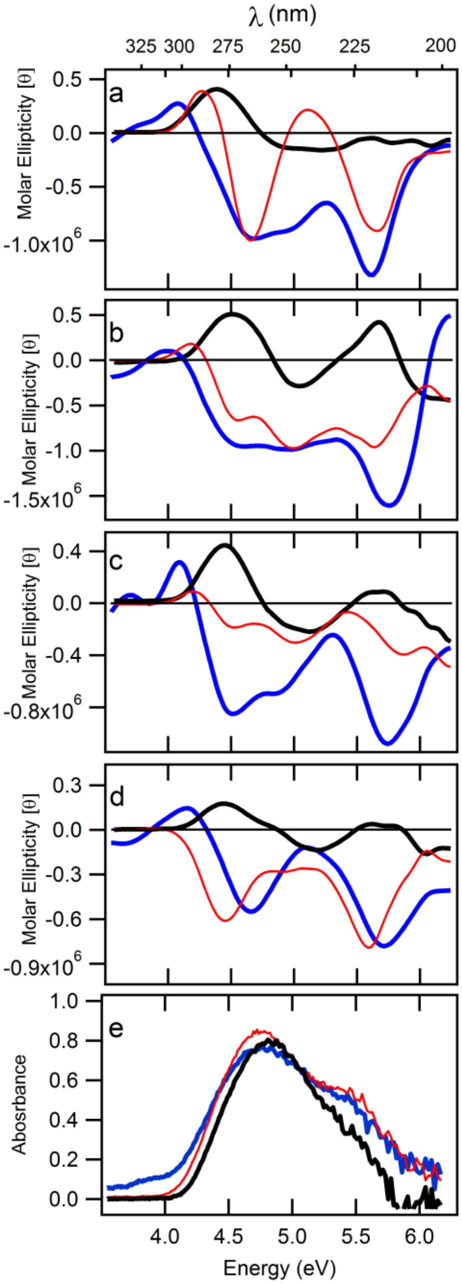

Figure 5.1) UV CD spectra for templates S1-S4 in (a) – (d), respectively. Black curves are bare DNA template solutions, red curves are DNA-Ag^+ solutions, and blue curves are the pure cluster solutions. In all cases, DNA-Ag^+ interactions produce negative-going CD which is further enhanced in the pure cluster solutions. (e) Absorbance spectra of the S3 template strand (black), S3 template with Ag^+ (red), and for the pure S3 Ag_N-DNA (blue).

Figure 5.1a-d) are similar to the largely negative CD spectra of Ag^+-paired homobase cytosine and guanine strands (Chapter 3, Figure 3.7). The DNA template strand for S1 is comprised largely of cytosine bases (Table 5.1). Strikingly, the CD spectrum for S1 with Ag^+ (red curve, Figure 5.1a) matches closely with the CD spectra of Ag^+-paired cytosine strands (Chapter 3, Figure 3.7a) with negative peaks at approximately 5.6 eV (221 nm) and 4.5 eV (275 nm).

The blue curves in Figure 5.1a-d show the UV CD spectra of the pure, fluorescent cluster solutions. In all cases the striking, negative CD bands are quite distinct from the bare DNA spectra, and overall more similar to the UV CD spectra of the DNA-Ag^+ solutions. It seems likely the formation of the Ag^+-mediated base pairings are an important precursor to the formation of Ag_N-DNA. For the *im*pure reduced solutions, which contain many different species of Ag-bearing DNA, CD amplitudes are reduced and additional weak peaks appear (Appendix D).

The CD anisotropy, or dissymmetry, $g = (A_L - A_R)/A = \Delta\varepsilon/\varepsilon$, provides a useful dimensionless measure of the chirality of electronic transitions[192] (A_L and A_R are absorbances for left and right circularly polarized light). All of the pure Ag_N-DNA samples show prominent, negative CD peaks near 4.7 eV, with g of -1×10^{-3} to -2.3×10^{-3}; and near 5.7 eV, with g of -3×10^{-3} to -5.7×10^{-3} (Table 5.2 gives experimental g values at the energies of individual fitted Gaussian CD peaks, discussed below). These values are up to ~30 times larger than for the bare DNA and point to the persistence of silver-mediated base-pairing in the pure Ag_N-DNA. Such pairing should constrain relative nucleobase orientations more than in random coil DNA, enhancing CD by reducing fluctuational averaging. Apparently the formation of the neutral silver clusters leaves intact much of the DNA structuring produced by Ag^+-mediated base interactions in the Ag^+-DNA solutions. This is consistent with the simultaneous presence of silver cations and neutral silver atoms in the pure Ag_N-DNA (Table 5.1) and with incorporation of silver clusters *via* base-Ag^+-silver cluster bonding, as previously suggested.[49]

The UV peaks in the Ag_N-DNA CD spectra might instead arise from high energy transitions of the clusters themselves, rather than from the base chromophores. However, the overall similarity of the pure Ag_N-DNA CD spectra and the CD spectra of the unreduced Ag^+-DNA solutions, which cannot contain clusters of metallically bonded silver atoms, suggest that the DNA plays the dominant role in the UV chirality.

5.2.2) Low Energy, Cluster-Dominated CD

We now turn to the CD features induced at low energies by the incorporation of silver clusters into the templating DNA strands (black curves, Figure 5.2). Comparison to absorbance spectra of the pure cluster solutions (blue curves, Figure 5.2) shows that in all cases, a positive dichroic peak overlies the low energy cluster absorbance transition, which itself lies at energies well below the d-band transitions in silver. Because the absorbance peak coincides with peak fluorescence excitation,[193] we tested the possibility that the CD signal might be spurious polarized light emission by using a short-pass filter to block the fluorescence from entering the detector. The negligible change in the CD signal confirmed that it originates from differential absorbance of left and right circularly polarized light.

This striking *mono*signate CD signal (Figure 5.2, red stars) differs qualitatively from the *bi*signate excitonic splittings characteristic of macromolecular CD spectra, which arise in the UV from dipolar couplings of the transition moments of the chromophores. Bisignate CD also results from coupling of the plasmonic dipole moments of disconnected, spherical metal nanoparticles that are arranged in chiral patterns. In such multi-nanoparticle assemblies, the positive-negative bisignate peaks lie near the plasmon energy of the individual particles.[173] If an Ag_N-DNA contained multiple smaller clusters, rather than a single connected cluster, dipolar inter-cluster couplings would also be expected to produce bisignate CD, though such effects should be greatly weakened relative to the case of ~ 10 nm coupled nanoparticles due to the much smaller number of free electrons in the cluster limit.

The monosignate form of the CD signal in Figure 5.2 and its transparent association with a cluster-centered absorbance transition also differs strikingly from the chiroptical

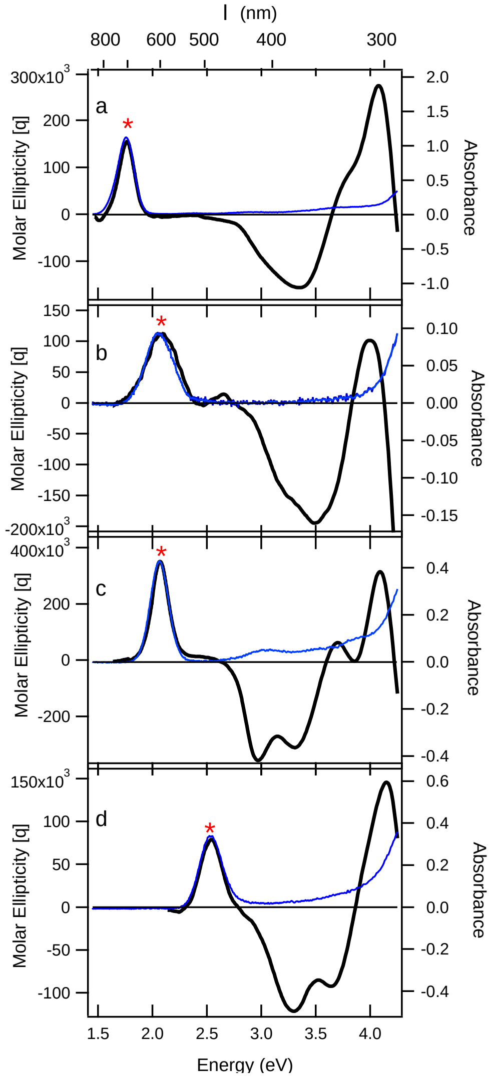

Figure 5.2) CD (black) and absorption (blue) spectra of pure cluster solutions S1 (a), S2 (b), S3 (c) (aqueous solution) and S4 (d; 50% MeOH). A positive CD peak overlies the collective longitudinal cluster absorbance peak (red stars).

signatures of ligand-protected gold clusters with similar numbers of metal atoms.[171] In such Au clusters, there is no well resolved absorbance peak that can be identified with a collective excitation of delocalized electrons in the cluster. Instead the broad absorbance spectrum extends from the UV through ~ 800 nm and the corresponding CD signal oscillates rapidly in sign. Here, in contrast, the absorbance shows a distinct low energy peak and the CD signal exhibits the same shape (Figure 5.2, red stars). These features strongly suggest that electronic chirality of this transition reflects a continuous, chiral metal path for free electrons.

5.2.3) Giant Anisotropies at Intermediate Energies

Below 4 eV, neither the bare DNA nor the Ag^+-DNA solutions show a CD signal. Thus all CD features at energies below 4 eV are due to the free electrons from the neutral silver atoms in Ag_N-DNA, which are also responsible for fluorescence. Figure 5.2 shows that although the absorbance between the low energy peak and the UV region is quite weak, the presence of clusters induces very pronounced CD features with negative anisotropies and high g, reaching ~ -10×10^{-3} (Table 5.2), similar to the largest magnitudes of g reported for chiral, thiol-protected gold clusters.[171]

5.2.4) Fits to CD Spectra

Across the entire spectral range, fits to the superposition of seven dichroic peaks with Gaussian lineshapes give consistent results for signs and strengths of the CD spectra of the pure Ag$_N$-DNA (Figure 5.3). The similar energies and amplitudes of the fitted peaks (Appendix D; Table 5.2 gives peak energies) again indicate that the silver-silver and cluster-base bonding is similar for all four cluster species, despite their quite different DNA template strands (Table 5.1). Thus the geometry of the silver cluster is the primary determinant of the optical response,

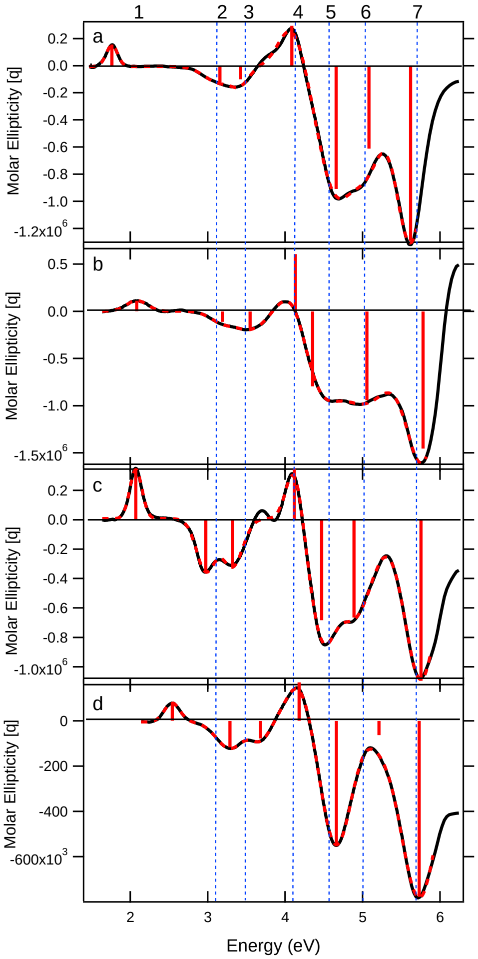

Figure 5.3) Fits (red dashed curves) of experimental CD spectra (black curves) to the superposition of seven Gaussian peaks for S1 (a), S2 (b), S3 (c) (aqueous solution) and S4 (d) (50% MeOH). Peaks are numbered; 1 represents the lowest energy peak for each spectrum (no guideline shown). Red bars: fitted amplitudes, at fitted energies (fit parameters are tabulated in Appendix D).

Peak	S1	S2	S3	S4
1	0.305±0.001 (1.76 eV)	0.37±0.01 (2.09 eV)	0.753±0.002 (2.07 eV)	0.389±0.001 (2.54 eV)
2	-9.2±0.3 (3.16 eV)	-29±13 (3.19 eV)	-6.7±0.1 (2.98 eV)	-6.4±0.2 (3.29 eV)
3	-5.9±0.1 (3.42 eV)	-11±2 (3.55 eV)	-6.3±0.1 (3.32 eV)	-2.33±0.04 (3.68 eV)
4	3.84±0.02 (4.09 eV)	0.045±0.005 (4.13 eV)	1.50±0.01 (4.12 eV)	0.849±0.004 (4.18 eV)
5 (UV)	-2.33±0.01 (4.66 eV)	-1.30±0.06 (4.35 eV)	-1.268±0.002 (4.47 eV)	-0.986±0.001 (4.66 eV)
6 (UV)	-2.12±0.01 (5.08 eV)	-1.04±0.02 (5.06 eV)	-0.850±0.001 (4.89 eV)	-0.364±0.001 (5.21 eV)
7 (UV)	-5.9±0.01 (5.62 eV)	-3.3±0.2 (5.78 eV)	-3.47±0.01 (5.75 eV)	-3.000±0.008 (5.73 eV)

Table 5.2) Experimental anisotropy values (*g* x 10_3) at energies of individual fitted Gaussian CD peaks (eV).

rather than detailed strand composition. It appears that particular base motifs are selecting the cluster geometry, and that distinct base motifs can produce the same cluster structure.

5.2.5) Quantum chemical calculations

Previous experimental studies of pure Ag_N-DNA found evidence for an elongated, rod-like cluster structure in which the low energy absorbance resonance arises from the longitudinal collective response of the cluster's free electrons.[49] Non-planar curvature of such a filamentary cluster would result in chiral currents and circular dichroism. The consistently positive sign of the lowest energy CD peak would then be associated with the flow of free electrons along clusters with consistent helicity across the 4-12 atom neutral cluster sizes in samples S1-S4, in qualitative agreement with their similar anisotropy values, $g = 0.3\times10^{-3}$ to $g = 0.75\times10^{-3}$.

To investigate whether chiral, filamentary silver clusters in the several atom size range could exhibit chiroptical properties similar to Ag_N-DNA, we used time-dependent density functional theory to calculate absorbance and CD spectra of 6-atom neutral silver cluster chains with non-planar curvature (Figure 5.4). Cluster shapes were selected to have a simple chiral form, a filamentary shape with 170º, 160º and 150º Ag-Ag-Ag bond angles, 2.7 Å bond length, and a torsional (dihedral) Ag-Ag-Ag-Ag angle of 10º. We focus on this filamentary shape since

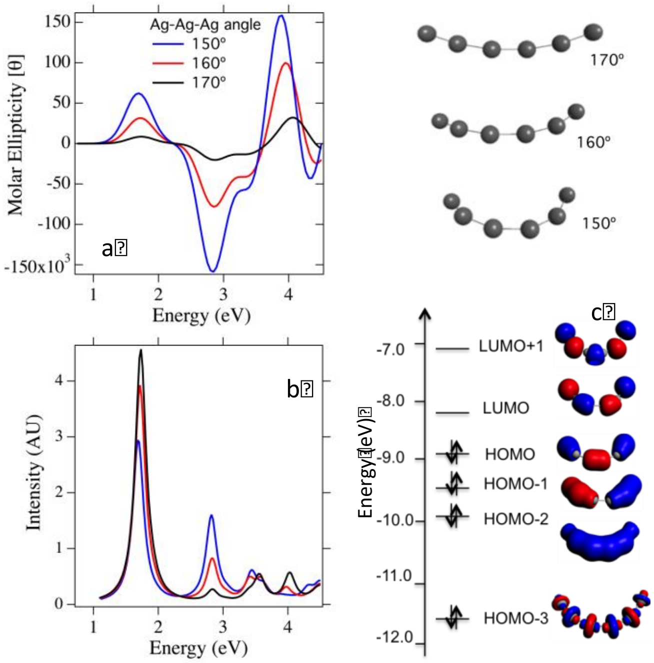

Figure 5.4) Calculated circular dichroism spectra (a) and optical absorption spectra (b) for neutral, filamentary Ag6 clusters shown at the top right. Calculations using the SAOP functional with TZP basis set. (c) Kohn-Sham orbitals and energies for 150º Ag-Ag-Ag angle and 10º torsional angle.

globular silver clusters and their less globular isomers do not reproduce the experimental absorption spectra well.[194] For a torsional angle of 0º, the clusters are achiral, with increasing planar curvature for decreasing Ag-Ag-Ag angles below 180º.

Overall, the calculated spectra in Figure 5.4 are strikingly similar to the data (Figure 5.2 and Figure 5.3 below ~ 4.5 eV; DNA transitions dominate at higher energy). The lowest energy calculated CD peak is positive (Figure 5.4a) and overlies the lowest energy absorbance transition (Figure 5.4b). In terms of molecular orbitals (Figure 5.4c), this is a HOMO-LUMO transition, corresponding to the collective, phased oscillation of all the cluster electrons. At higher energies, the calculated CD exhibits pronounced negative peaks, as in the data. These arise from HOMO → LUMO+1, HOMO-1 → LUMO and HOMO-3 → LUMO transitions that are forbidden in perfectly straight wires. (The HOMO-LUMO gap for all structures is 0.7 eV).

The lowest energy, positive CD peak for all calculated structures appears near 1.7 eV, with negative dichroic peaks near 2.8 and 3.3 eV (Figure 5.4a). This is in good agreement with the data for sample S2, which has the same neutral silver content (6 atoms), a positive CD peak at 2.0 eV and first and second negative CD peaks at 3.0 and 3.3 eV. While peak energies agree rather well between calculation and experiment (within ~ 0.3 eV), this may be partly fortuitous for the lowest energy transition. The energy of these longitudinal plasmon-like excitations is expected to increase with decreasing Ag-Ag-Ag angle within the cluster[195] and to decrease with increasing refractive index of the medium (vacuum for the calculations). To the extent that these effects do not cancel, the lowest energy peak will shift.

In the calculated CD, peak energies and relative peak amplitudes depend only weakly on the Ag-Ag-Ag angle, but the CD intensity rises rapidly as decreasing Ag-Ag-Ag angle increases chirality (Figure 5.4a). Below 4 eV, the integrated CD peak intensities for sample S2 are similar to the calculated CD for 150º Ag-Ag-Ag angle and 10º torsional angle. (Above ~ 4eV, bare cluster calculations are incomparable to data because the DNA dominates the high energy CD spectra of Ag_N-DNA). The ratio of integrated spectral weights in calculation *versus* experiment is ~ 0.8 for the positive dichroic peak as well as for the negative dichroic peaks.

In contrast to the insensitivity of the spectral shapes in calculated CD spectra to the Ag-Ag-Ag angle, the calculated absorbance spectra show a marked increase in the relative intensity of the peak near 3 eV as the Ag-Ag-Ag angle decreases from 170º to 150º (Figure 5.4b). The rise of this absorbance peak corresponds to a large increase in the overall CD intensity (Figure 5.4a). The behavior in calculated CD and absorbance is consistent with the differences in CD and absorbance spectra of sample S3 relative to sample S2. Sample S3 has larger absorbance near 3 eV than sample S2 (Figure 5.2b,c, blue traces), which according to the calculations implies higher chirality in S3 than in S2. Consistent with this expectation, the integrated CD peak strengths in sample S3 are 2 times larger than in sample S2 (Figure 5.2b,c, black curves). While only sample S3 exhibits a resolved absorbance peak near 3 eV, the similar pronounced, negative features in the CD of samples S1, S2 and S4 indicate that such an absorbance transition is weakly present but obscured by the noise in the absorbance signal.

In order to understand how peak locations and peak amplitudes depend on the torsional angle, as opposed to the Ag-Ag-Ag angle investigated in Figure 5.4, we calculated structures with a fixed Ag-Ag-Ag angle of 160º and different torsional angles from 10º to 60º. The calculated CD spectra show that the absolute peak locations are insensitive to the torsional angle, whereas the peak amplitudes initially rise rapidly with increasing torsional angle and saturate at a torsional (Ag-Ag-Ag-Ag) angle of ~ 50º. The low energy, positive dichroic peak and the negative dichroic peak at 2.8 eV are roughly 3 times more intense at a helical angle of 50º than 10º. Apparently differences in torsional angle could account for the difference in CD intensities for same-size clusters measured in experiment.

To examine the length dependence of the optical absorption and CD of these filamentary wires, TDDFT calculations were performed on Ag_n (n = 4, 6, 8, 10, 12) clusters with 170° Ag-Ag-Ag bond angles and a 10º torsional (dihedral) Ag-Ag-Ag-Ag angle. For *n* values from 4 to 8, the absorption shows only one strong peak, which linearly shifts to lower energy with increasing *n*, while the longer systems exhibit an additional, weaker but significant peak at ~ 1 eV higher energy than the dominant low energy transition (Appendix D.3A). CD spectra (Appendix D3.B) also become stronger and redshift as *n* increases. For all *n* the CD exhibits a strong, monosignate, positive first peak coinciding with the main absorbance peak (the HOMO- LUMO transition), as in the data. For all *n* the second dichroic peak has a negative sign, also in qualitative agreement with the data. As discussed for Ag_6, this peak arises from the HOMO → LUMO+1 and HOMO-1 → LUMO transitions that are forbidden for perfectly linear wires. In all cases this second peak is strong in the CD spectrum even if it is weak in the optical absorption spectrum.

The good agreement between the bare cluster calculations and our data, in both overall spectral shapes and peak intensities, suggests that the low energy experimental CD may be dominated by free electron transitions of a chiral, filamentary cluster. The positive, monosignate CD that overlies the primary absorbance resonance (Figure 5.4) arises from the filamentary cluster shape and is in marked contrast to the bisignate CD characteristic of quasi-spherical metal nanoparticles with chiral shape distortions.[196]

An alternative mechanism that has been calculated[197] and observed[198–200] for much larger metal nanoparticles is induced CD (ICD) at the plasmon energy, arising from nonresonant Coulomb coupling to the UV transitions of chiral molecules. This produces a monosignate CD peak overlying the plasmon absorbance. The ICD sign can be negative or positive, depending on the orientation of the chiral molecule relative to the nanoparticle surface, and the magnitude is proportional to the number of metal atoms and inversely proportional to the cube of the separation between the metal particle and the chiral molecule. While size scaling suggests that such an effect may be weak in the cluster regime,[201] the theory was developed for much larger particles without discrete transitions, for which the chiral molecules could be treated as point-like. (We also note that molecular mechanisms for nonresonant ICD can produce a monosignate ICD signal at the absorbance transitions of small, achiral molecules bound in the DNA groove,[202] with sign and magnitude dependent on the relative orientation of the groove binder and DNA.) Although the main features in the low energy, cluster-dominated CD of Ag_N-DNA are captured by a chiral, filamentary Ag cluster, ICD may also contribute in our experiments.

5.2.6) A Solvent-driven Conformational Shift

For sample S4, the blue-green fluorescent Ag_N-DNA, we found that changes in solvent composition alone could induce dramatic changes in both absorbance and CD spectra that are indicative of a solvent-mediated equilibrium between two distinct species: a fluorescent silver cluster and a conformationally distinct, non-fluorescent form. In aqueous solution, the pure S4 Ag_N-DNA absorbance spectrum shows low-energy peaks at both 2.54 and 3.04 eV, with the higher energy peak more intense (blue curve, Figure 5.5b). Increasing methanol concentration strengthens the 2.54 eV absorbance and weakens the 3.04 eV absorbance peak, which can no longer be detected at 50% methanol by volume (black curve, Figure 5.5b). The fluorescence excitation spectra (Figure 5.5c), measured by detecting at the peak emission energy (2.19 eV) while scanning the excitation wavelength, show that only the 2.54 eV absorbing form is fluorescent. A dramatic increase in fluorescence intensity with increasing methanol fraction (a factor of 5 at 50% methanol, relative to aqueous solution), accompanies the disappearance of the 3.04 eV absorbance peak, again confirming that it is associated with a non-fluorescent form.

These solvent-driven changes in optical spectra are reversible, as determined by use of spin filtration to change solvent composition while retaining the DNA. Cycling the solvent between 0% and 50% MeOH shifted the absorbance spectra between the blue (0% MeOH) and black (50% MeOH) traces in Figure 5.5b. Silver cations or small clusters released into the solvent would be removed by filtration and produce irreversible changes, contrary to the reversible behavior we find. Thus, overall silver content is conserved between fluorescent and

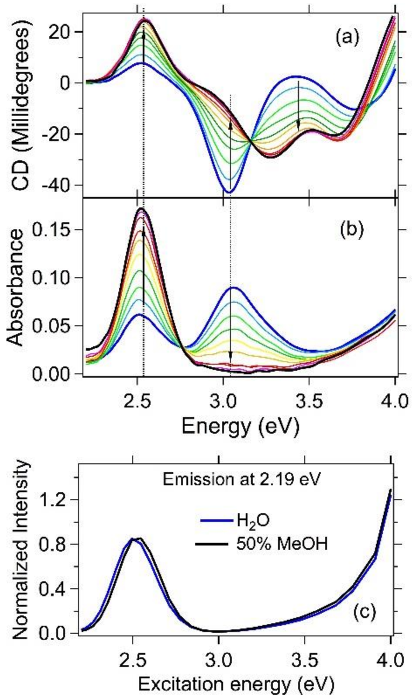

Figure 5.5) (a) CD and (b) absorbance spectra for the titration of sample S4 from 0-50% methanol by volume in 5% increments. Direction of arrows indicate increasing methanol concentration. (c) Fluorescence excitation spectrum of sample S4 in water and in 50% methanol. Detection at emission peak (2.19 eV).

dark forms. The well-defined isodichroic point at 3.16 eV (Figure 5.5a) further indicates an equilibrium between two distinct species having the same overall silver content but different structure.

Apparently the titration of S4 with methanol produces structural changes that strongly influence electronic structure. Increasing methanol concentration favors the fluorescent form, with dichroic bands similar to the other pure, fluorescent Ag_N-DNA in aqueous solution. Titration with sucrose, rather than methanol, produces similar enhancement of the fluorescent form. Apparently solvent composition can be manipulated to activate the DNA structural motifs most conducive to the structure that maximizes fluorescence quantum yield.

Since higher transition energies correspond to shorter silver cluster chains,[181] changes in Ag-Ag bonding may be responsible for the 0.5 eV increase in peak absorbance energy between the fluorescent and dark forms, which have significantly different CD spectra. The fluorescent form has a positive CD peak that overlies the main cluster absorbance peak (Figure 5.5a-b, black curves), the same as for the other fluorescent clusters. In contrast, the dark form exhibits a negative dichroic peak near the 3.04 eV absorbance maximum and a pronounced positive shift in CD amplitude at higher energy (Figure 5.5a,b, blue curves).

An equilibrium between dark and fluorescent forms of silver-decorated DNA with different absorbance energies and the same total silver content was found previously in studies of the hybridization of complementary strands to silver-bearing DNA.[203] Thus, changes in the DNA environment can produce similar behavior to altering solvent composition.

The addition of alcohols and sucrose as cosolvents is known to alter DNA conformation through changes in hydration.[204,205] Thus it appears that cosolvent-mediated alterations of DNA conformation induce structural changes in the embedded silver clusters.

5.3) Conclusions

The chiral structure of four different species of pure Ag_N-DNA has been investigated using circular dichroism and absorbance spectroscopy and compared to quantum chemical calculations for bare silver cluster chains with non-planar curvature. In all cases, the data show a monosignate, positive CD peak that overlies the lowest energy absorbance transition and highly anisotropic, negative dichroic peaks well below the UV transitions of the bases. Thus despite their different colors, all of the DNA-stabilized silver clusters studied here appear to belong to the same structural family. Agreement in spectral shapes and overall CD magnitudes between experiment and theory suggests that helical, filamentary silver clusters are present experimentally.

In the UV, the similar CD structure across all pure Ag_N-DNA and the much higher CD amplitudes than for the bare strands indicate that nucleobases near the clusters are held in similar, compactified geometries. The similarities in the UV CD spectra of Ag^+-paired guanine and cytosine homobase strands, Ag^+-DNA templates and Ag_N-DNA suggest that Ag^+-mediated base pairings are important in the formation and structure of Ag_N-DNA. The smallest cluster, S4, exhibits a solvent-tuned equilibrium between fluorescent and dark conformations, suggesting new sensing possibilities for solvent-induced changes in the immediate environment of the cluster. Our work provides new perspective on chirality of ligand-protected metal clusters, in an entirely different size regime from the many previous studies of chirality in much larger metal nanoparticles and nanoparticle assemblies. These studies of silver clusters make possible a more transparent connection between CD spectra and cluster structure than for their more frequently studied gold cluster counterparts, due to the larger energetic separation of localized *d* orbitals from delocalized cluster states.

5.4) Methods

5.4.1) Synthesis and Purification of Ag_N-DNA

DNA oligomers were obtained from Integrated DNA Technologies with standard desalting. All solutions, except HPLC running buffers, were made with RNase/DNase free distilled water from Life Technologies. All other chemicals used were analytical grade or higher. DNA strands were selected from previously reported sequences known to form silver cluster emitters of varying wavelengths.[48,49,184,206] The Ag_N-DNAs were synthesized by annealing solutions of bare DNA oligomers in 7.5mM ammonium acetate buffer with optimized silver nitrate (75-250μM) and DNA (5-20μM) concentrations at 90°C for 5 minutes and allowing them to cool slowly to ambient temperature. Solutions were reduced with sodium borohydride in a ratio of half that to silver nitrate and allowed to react in optimized temperature (4-40°C) conditions for each sample.

Samples were purified using reverse-phase high performance liquid chromatography (HPLC), with water-methanol solvent mixtures in 35mM triethylamine acetate (TEAA) as the ion pairing agent to the C18 column (Phenomenex). The gradient was optimized for each sample, and in each case started between 5%-20% methanol by volume and ended between 20-40% methanol, with a 1% per minute gradient. To estimate purity we compared absorbance chromatograms measured at the peak visible excitation wavelength of the fluorescent Ag_N-DNA to the 260 nm absorbance chromatograms, which provided a conservative estimate of 80% purity in all samples. Following collection of the pure samples, they were solvent exchanged back to 7.5mM ammonium acetate by spin filtration which ensured that less than 0.5% of the running buffer remained.

5.4.2) Optical Characterization

All absorption and fluorescence spectra were measured using a thermoelectrically cooled array detector (Ocean Optics QE65000). The CD data was collected using a circular dichrometer (Aviv 202) at ambient temperature. The instrument's wavelength accuracy was calibrated with a 40 g/L holmium oxide in 10% perchloric acid standard solution (Agilent Technologies). The samples were run at concentrations required to reach the ideal 0.87 absorbance for dichroic measurements.[207] Purified S2 did not achieve this ideal absorbance due to low chemical yields, however it was still within allowable analytical range. Blanks with appropriate concentrations of buffer were run before and after each sample and averaged for the blank subtraction. The spectra were normalized to molar ellipticity by their absorbances at 4.77 eV (260 nm) using the nearest neighbor calculated molar extinction coefficients for the DNA oligomers.

For methanol titrations of sample S4, a blank with pure water was taken before the titration and a blank with 50% methanol was taken after the titration. The data was corrected by applying a linear background subtraction to account for drift, and the data was corrected for the DNA concentration dilution from added methanol. The solution equilibrated for 20 minutes after each addition of methanol before collecting the spectra. This was shown to be sufficient time by conducting a titration while monitoring fluorescence intensities.

5.4.3) Calculation Techniques

The Amsterdam Density Functional (ADF) program[208] was used for calculation of optical absorption and circular dichroism spectra. In the ADF calculations, scalar relativistic effects are included by utilizing the zero-order regular approximation (ZORA).[209] Time-dependent density functional theory (TDDFT) is employed to calculate excited states. For these calculations we used the asymptotically correct SAOP functional.[210] This functional was combined with a triple-ζ plus polarization (TZP) Slater type basis set. The SCF convergence is tightened to 10^{-8}, the tolerance was set to 10^{-8} and the orthonormality was set to 10^{-10}. The first 200 dipole-allowed transitions were evaluated for the optical absorption and CD spectrum.

The simulation of the CD spectra is based on the relations[169,211,212]

$$\Delta\varepsilon = 4\alpha \sum_m R_m E_m \sigma_m(E)$$

$$\alpha = \frac{4\pi N_A}{3ln(10)10^3}\frac{2\pi}{hc}$$

$$\sigma_m(E) = \frac{1}{\sigma\sqrt{2\pi}}\exp(-\frac{1}{2\sigma^2}(E - E_m)^2)$$

where Δε is molar circular dichroism or molar differential dichroic absorptivity in units of L•mole^{-1}•cm^{-1}, α is a set of constants, N_A is Avogadro's number in units of mole^{-1}, h is the Planck constant in units of J•s, c is the speed light in units of cm/s, R_m is rotatory strength in units of esu^2•cm^2, E is the energy of the incident light in eV, E_m is the excitation energy to state M in eV, $\sigma_m(E)$ is the Gaussian band shape factor, and σ is the exponential half-width (we used $\sigma = 0.2$ eV). Molar circular dichroism is related to molar ellipticity by the following equation[213]

$$[Q] = 3298.2D\epsilon$$

where [Θ] is molar ellipticity, expressed in deg•cm^2•dmole^{-1}.

Chapter 6) Concluding remarks

We hope to have provided a meaningful analysis of the potential for using Ag^+ towards more robust and functional DNA nanotechnology. While we investigated only the simplest structures formed by Ag^+-mediated base pairings, we believe to have provided important basic information on the types of Ag^+-base pairs in Chapter 2, their stability and behavior with heterogeneous base motifs in Chapter 3 and their strand orientations and overall shapes in Chapter 4 required to achieve such a goal. This information may inform future use of Ag^+-mediated pairings in more elaborate DNA nanotechnology schemes. Beyond Ag^+-mediated pairings use in DNA nanotechnology, we hope this information provided in this dissertation will also be useful from a biomedical standpoint. Preliminary titration experiments using Ag^+ with a pre-folded G-quadruplex structure (Appendix E) suggest that Ag^+ is able to easily modulate the structure of a G-quadruplex, possibly through the formation of the G-Ag^+-G base pairs described in Chapters 2-4. This discovery warrants further research for the potential use of Ag^+ complexes to inhibit telomerase activity through binding to the G-rich telomeric regions, which could lead to potential anti-cancer drugs.

In Chapter 5 we explored the structure of fluorescent silver clusters templated by DNA (Ag_N-DNA) and discovered a chiral, rod-like shape for the silver cluster core. Inadvertently, we may have already realized the incorporation of Ag^+-mediated base pairs in DNA nanotechnology with Ag_N-DNA. Due to the similarity in CD spectral shapes of unreduced Ag^+-paired homobase cytosine and guanine strands (Chapter 3, Figure 3.7) to Ag_N-DNA and their Ag^+-DNA precursors (Chapter 5, Figure 5.1) it seems likely that Ag^+-mediated base pairs form a structural foundation to form the silver cluster on in Ag_N-DNA. Ag_N-DNAs are fluorophores whose amazing potential are mainly limited by the difficulty in discovering template sequences which lead to Ag_N-DNA with promising optical properties such as high chemical yields, high quantum yields and desired wavelength of emission. This difficulty is primarily due to the large sequence space that 10-30 base-long DNA strands have. Better understanding how heterobase motifs, as are common in Ag_N-DNA template strands, incorporate Ag^+ could be the key to controlling cluster formation to achieve desired optical properties. While Chapter 4 scratched the surface on Ag^+-incorporation into heterobase motifs, more research is required into understanding their intricacies.

The future of Ag_N-DNA is looking brighter as more research is done on these unique fluorophores. A current project we are working on is the discovery of Ag_N-DNA with wavelengths further into the near-infrared (NIR). This is particularly promising due to the NIR tissue transparency windows (650-950 nm and 1000-1350 nm) which are useful for biological imaging.[214] Unfortunately, NIR instrumentation is fairly underdeveloped especially for microplate readers which can process many samples at once. This required us to modify an existing microplate reader to function into the NIR, which we achieved with detection capabilities up to 1400 nm.[215] Current efforts scanning 384-well plates with designed sequences to produce Ag_N-DNA has lead to the discovery of Ag_N-DNA with detectable emission all the way out to 1200 nm, further into the NIR than any Ag_N-DNA has currently been reported. We are currently in the process of characterizing these novel NIR Ag_N-DNAs.[216]

Appendix A) Supporting Information for Chapter 2

A.1) Experimental mass spectra

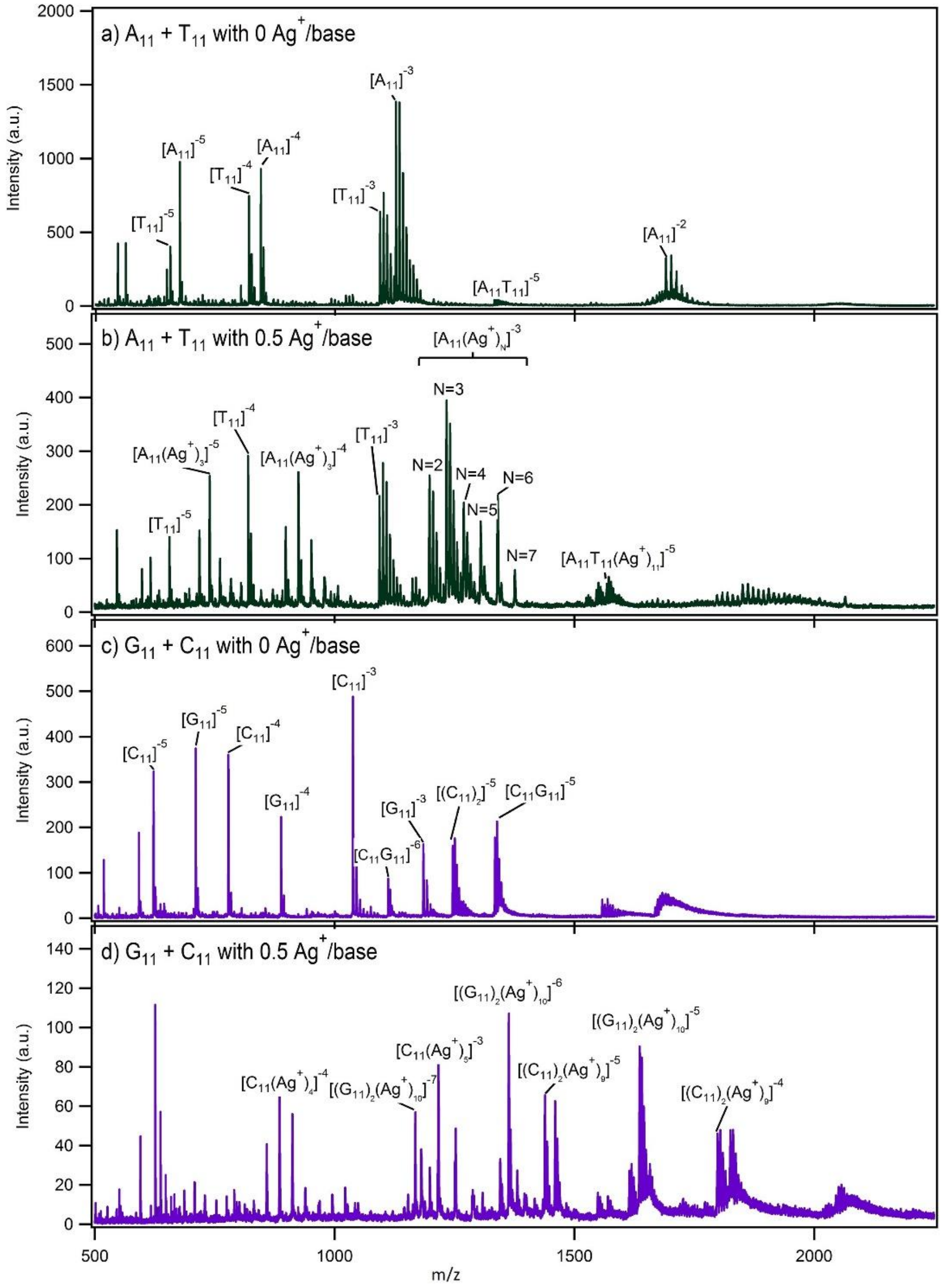

Figure A.1) Full range mass spectra of solutions containing A_{11} and T_{11} with a) no Ag^+ and b) $0.5Ag^+$/base as well as G_{11} and C_{11} with c) no Ag^+ and d) 0.5 Ag^+/base. The products are labeled in the format $[(X_{11})_y(Ag^+)_N]^Z$ where X is the base of the homobase strand, y is the number of homobase strands in the product, N is the number of cationic silver atoms, and z is the charge state. z is negative, and is given by $z = N_{Ag}^+ - n_{pr}$, where n_{pr} is the number of protons removed from the DNA, and N_{Ag+} is the number of attached silver cations.

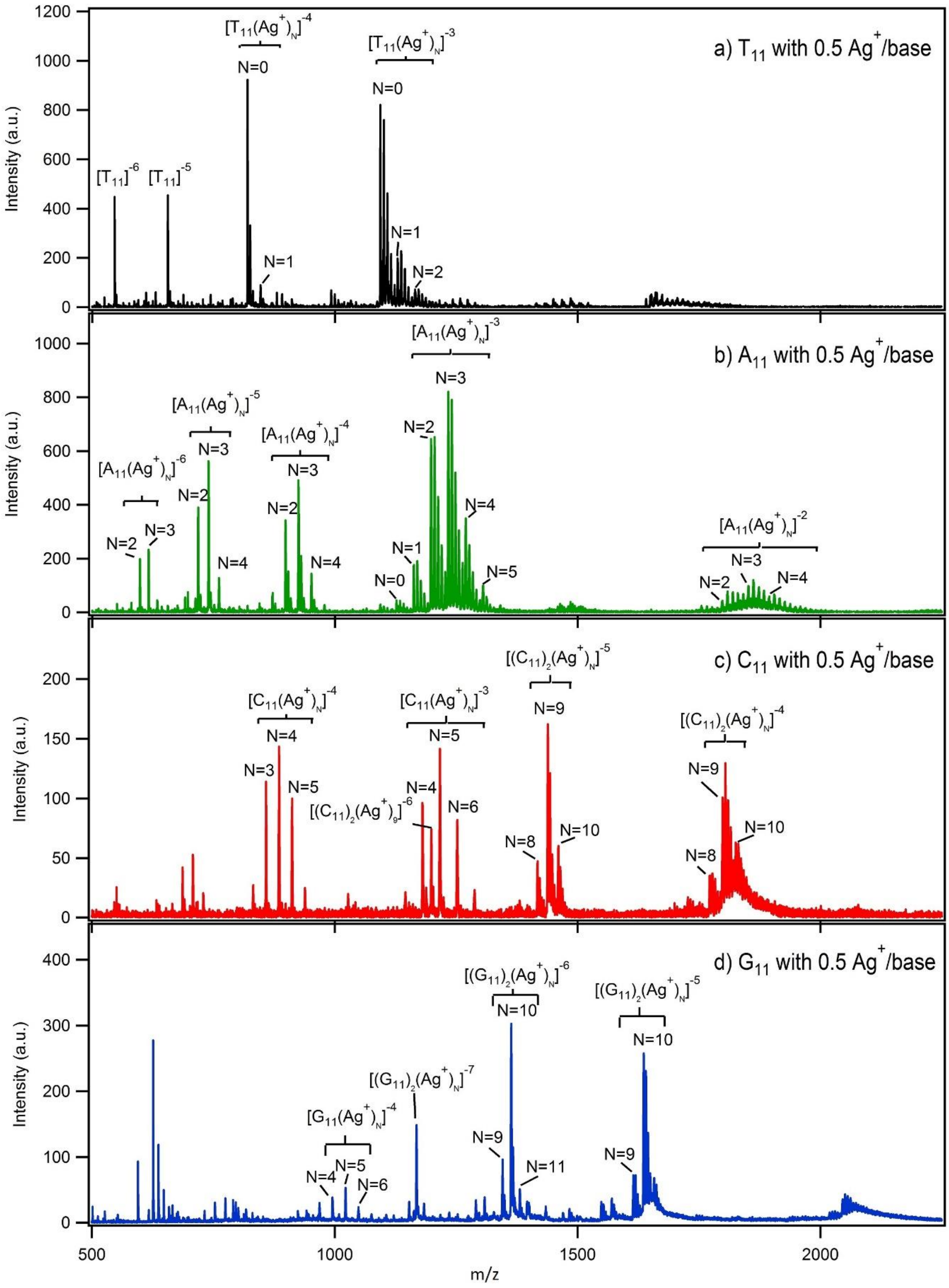

Figure A.2) Full range mass spectra of a) T_{11} b) A_{11} c) C_{11} and d) G_{11} at 80μM DNA concentration and 0.5 Ag^+/base ratio taken in ESI negative mode.

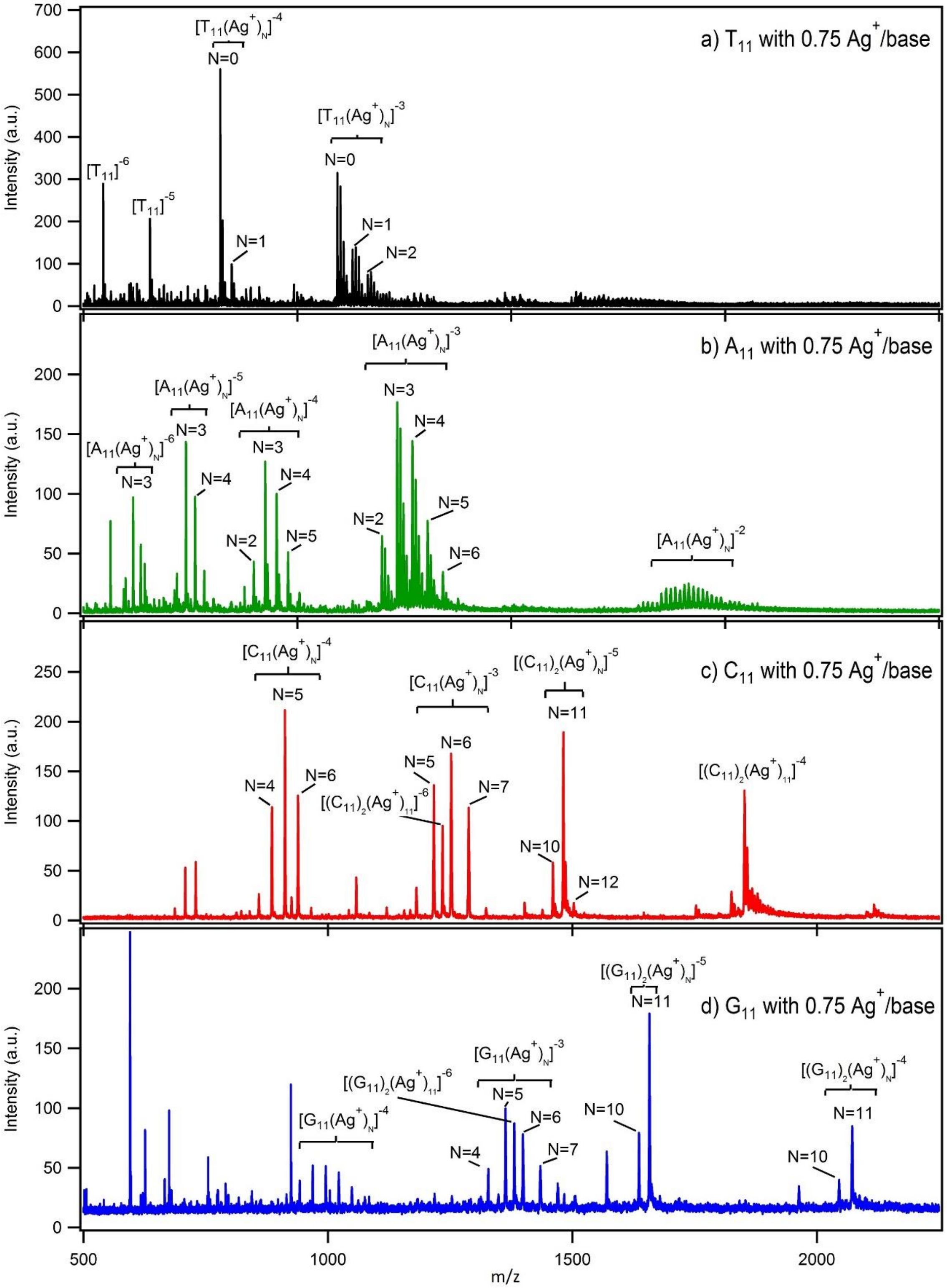

Figure A.3) Full range mass spectra of a) T_{11} b) A_{11} c) C_{11} and d) G_{11} at 80μM DNA concentration and 0.75 Ag^+/base ratio taken in ESI negative mode.

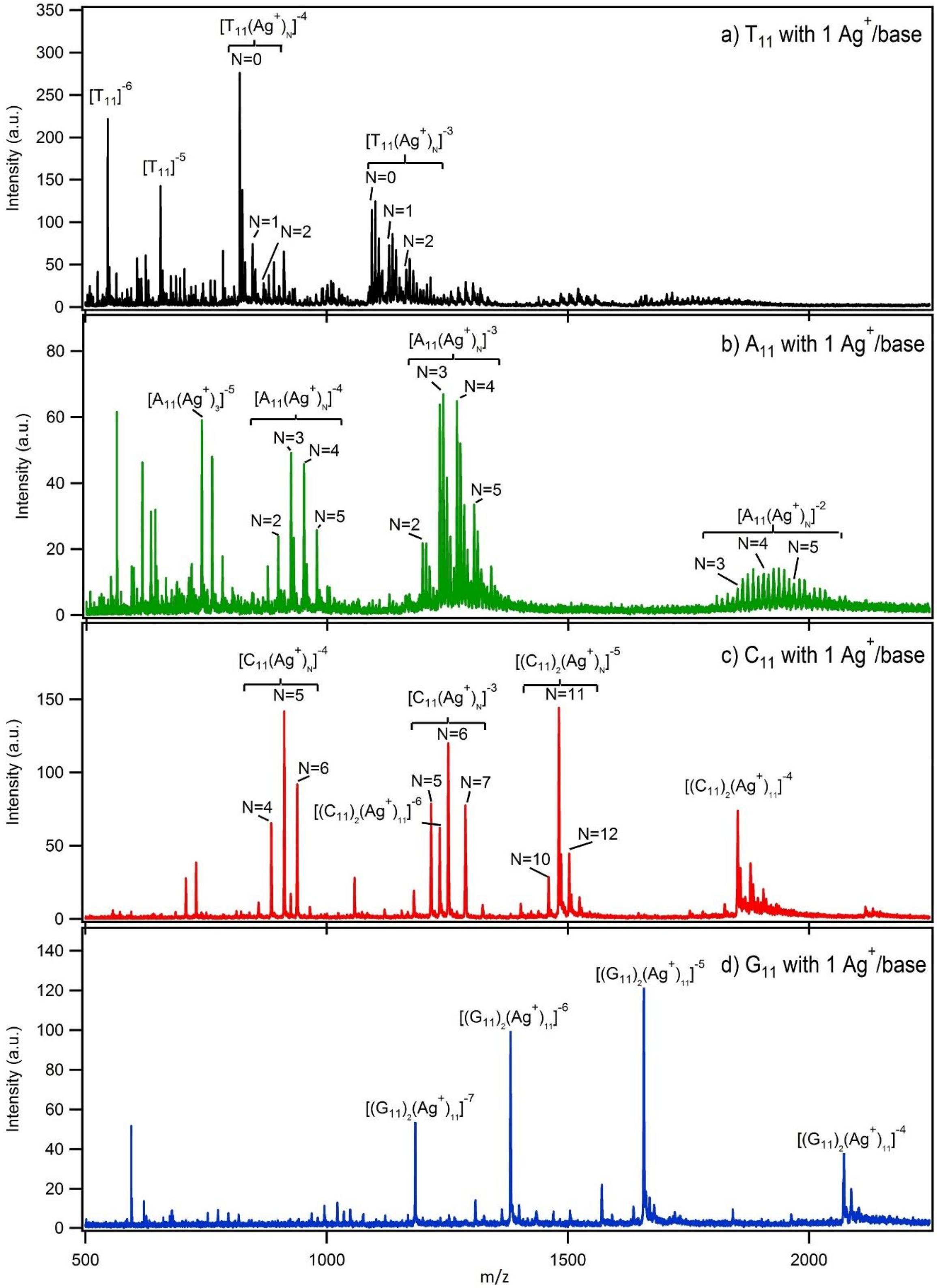

Figure A.4) Full range mass spectra of a) T_{11} b) A_{11} c) C_{11} and d) G_{11} at 80μM DNA concentration and 1 Ag^{+}/base ratio taken in ESI negative mode.

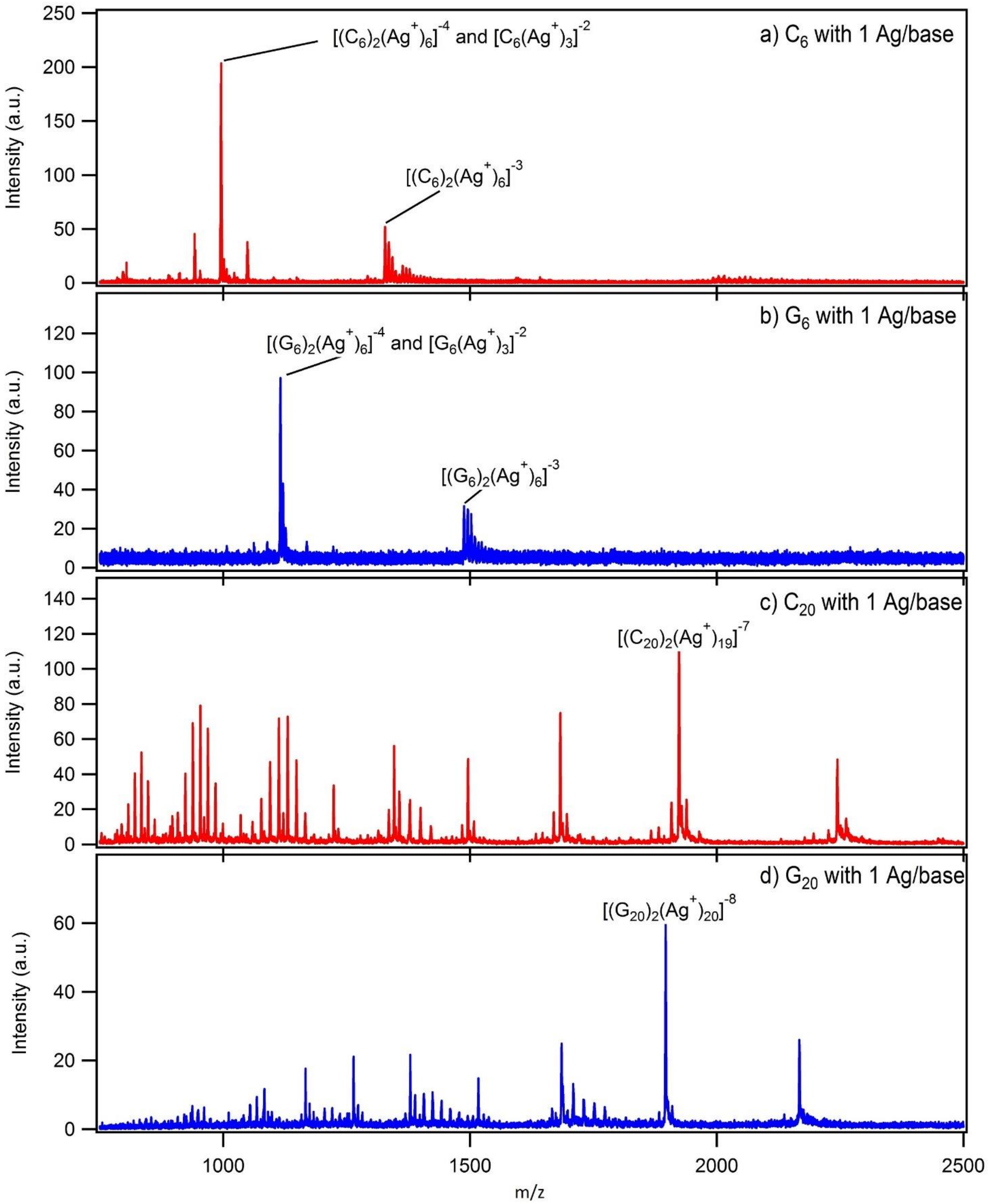

Figure A.5) Mass spectra of a) C_6, b)G_6, c) C_{20} and d) G_{20} at 80μM DNA concentration and 1 Ag^+/base ratio taken in ESI negative mode. Certain peaks have multiple assignments due to overlapping charge states of dimer and monomer products.

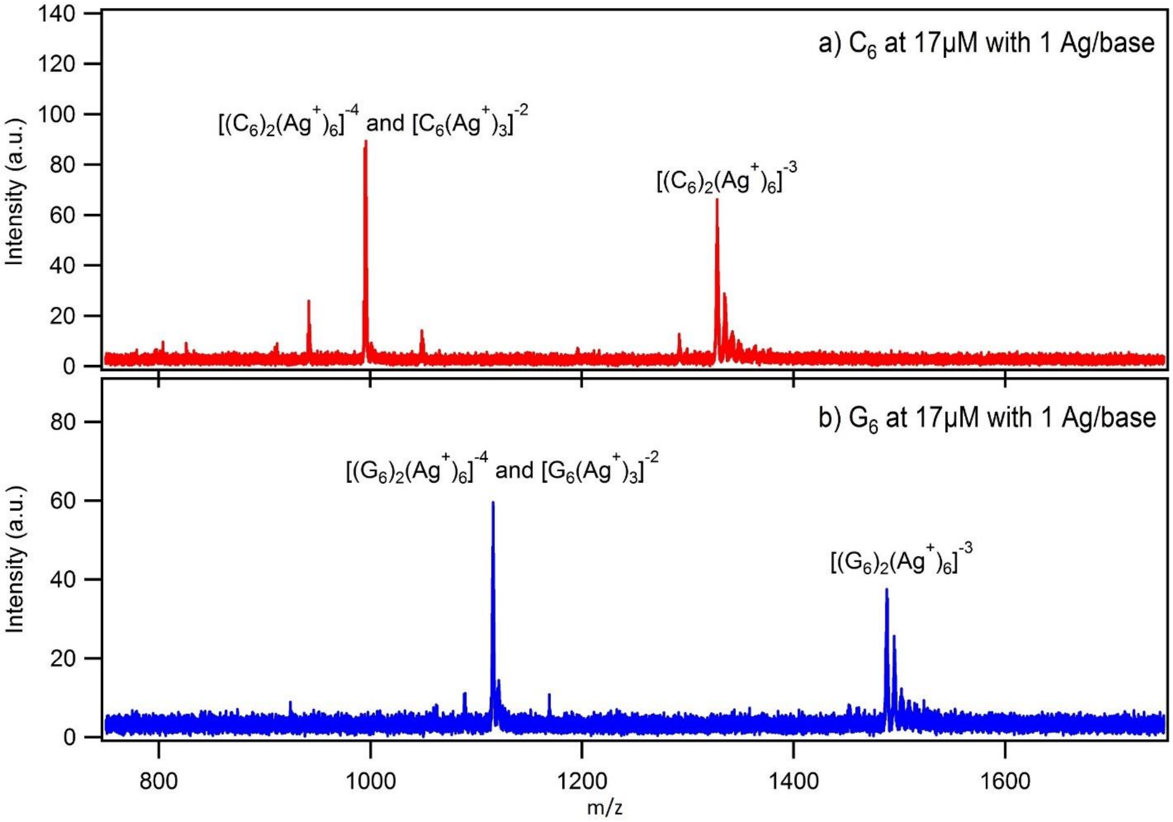

Figure A.6) Mass spectra of a) C_6 and b) G_6 at strand concentrations used for circular dichroism experiments (17 μM) and 1 Ag^+/base ratio taken in ESI negative mode. Certain peaks have multiple assignments due to overlapping charge states of dimer and monomer products.

Product	N	m/z
$[T_{11}(Ag^+)_N]^{-4}$	0	819.89
	1 (0.99)	846.60
	2 (1.99)	873.32
$[A_{11}(Ag^+)_N]^{-3}$	0	1126.60
	1 (1.00)	1162.15
	2 (2.00)	1197.80
	3 (3.00)	1233.43
	4 (4.00)	1269.07
	5 (5.00)	1304.70
	6 (6.00)	1340.33
	7 (7.01)	1376.31
$[A_{11}T_{11}(Ag^+)_N]^{-5}$	0	1332.48
	9 (9.00)	1524.91
	10 (10.01)	1546.44
	11 (11.00)	1567.68
	12 (12.00)	1589.00
$[(C_{11})_2(Ag^+)_N]^{-5}$	9 (9.00)	1438.93
	10 (10.00)	1460.34
	11 (10.99)	1481.53
	12 (12.00)	1503.11
	13 (12.99)	1524.31

Product	N	m/z
$[C_{11}]^{-3}$	N/A	1038.54
$[C_{11}(Ag^+)_N]^{-4}$	3 (2.99)	858.77
	4 (4.00)	885.50
	5 (5.00)	912.23
	6 (6.01)	939.20
	7 (6.99)	965.64
$[(C_{11})_2]^{-5}$	N/A	1246.60
$[G_{11}(Ag^+)_N]^{-4}$	2 (2.00)	942.30
	3 (3.00)	969.03
	4 (3.99)	995.51
	5 (4.99)	1022.23
	6 (6.00)	1049.18
	7 (7.00)	1075.66
	8 (8.00)	1102.63
$[G_{11}]^{-5}$	N/A	710.71
$[(G_{11})_2(Ag^+)_N]^{-5}$	10 (10.00)	1636.34
	11 (11.00)	1657.75
	12 (12.00)	1679.34
$[C_{11}G_{11}]^{-5}$	N/A	1334.61

Table A.1) m/z values for highly abundant charge state products obtained from the mass spectra in Figures A.1-2 and the corresponding numbers of attached silver cations, N, rounded to an integer from the experimental value in parentheses. The small difference is due to experimental uncertainty in the calibration of the m/z axis.

The masses of A_{11}, C_{11}, G_{11} and T_{11} are 3383.3, 3119.1, 3559.3, and 3284.2 g/mol respectively. We use the separately determined ion mass, m, and charge state, z, from the isotope peak envelope (as exemplified in Chapter 2, Figure 2.1b) to obtain the silver cation composition. The measured charge state, z, depends on the difference in the number of protons removed from the DNA and the number of attached Ag^+.

The number of silver cations, N, is given by $N = [m-(X_{11}+zm_p)]/(m_{Ag}-m_p)$ where X_{11} is the molecular weight of the (unionized) homobase strand (or the mass of two strands, in the case of a dimer product); $m_{Ag} = 107.868$ g/mol is the atomic weight of silver and $m_p = 1.007$

g/mol is the mass of a proton. This calculation assumes all silver is cationic, verified through calculated isotope peak fitting to the high resolution mass spectra as described in Chapter 2. (The presence of any neutral silver atoms would shift the isotope peak pattern by reducing the number of protons that must be removed to reach the measured charge state, z).

A.2) Computational details

A high number of incorporated silver ions per duplex means that we can expect high symmetry. Indeed, the model proposed experimentally for a silver mediated cytosine duplex contains repeated C-Ag$^+$-C units, each in a trans configuration. The trans C-Ag$^+$-C is also the ground-state structure we obtained at DFT level in vacuum.[100] In those simulations, including an implicit solvent decreased the binding energy but did change the relative ordering of the binding energies of the various base-Ag$^+$ and base-Ag$^+$-base complexes considered. In this computational section, we consider as a model of the metal-mediated duplex the trans C-Ag$^+$-C that would be repeated along the backbone axis. This trimer is comprised of a base homodimer and a silver atom in vacuum, and the overall charge is set to +1. Starting from various initial conditions, comprising WC-type and not WC-type, we first apply a global optimization followed by a final force optimization.

The binding strengths from this the metal mediated dimer model agree with quantitative results obtained in the mass spectroscopy experiment. From calculation of binding energies, the ordering G ~ C > A > T is obtained. Respectively in kcal/mol the binding energies, defined as sum of energy of fragments minus the energy of the complex, are 129.72 ~ 126.17 > 111.90 > 91.53 for the PBE-TS09 calculations, which used a real-space basis and the projector-augmented wave method (PAW). The values obtained with the real-space PAW method does not give inaccuracies due to basis set superposition errors (BSSE) (See explanation below).

The same ordering with binding energies of 116.15 ~ 115.26 > 94.78 > 78.28 kcal/mol is obtained with CAM-B3LYP/6-311+G(d,p), an average shift of 13.7 kcal/mol but with a much smaller standard deviation of the shifts, 2.6 kcal/mol, reflecting the general feature that DFT methods give good *relative* energies. Here the BSSE energy subtracted to find the total binding energy is 1.27, 1.54, 1.29 and 1.07 kcal/mol, respectively. Using instead the Minnesota functional M06-L, the results are 112.57 ~ 112.22 > 91.80 > 74.54 kcal/mol, with BSSE energy correction of 1.29, 1.19, 1.03 and 0.98 kcal/mol. This is in excellent agreement with our other Gaussian basis calculations (CAM-B3LYP), with an average shift of 3.3 kcal/mol and a quite small standard deviation of the shift, 0.4 kcal/mol. With the M06-L there is a switch in the order of the binding energies for C-Ag^+-C and G-Ag^+-G, from G~C>A>T to C ~ G > A > T. However, the values are very close to each other.

As the measure of co-planarity of the bases in the trimer complexes, we use a dihedral angle. C-Ag^+-C and G-Ag^+-G are nearly planar while T-Ag^+-T and A-Ag^+-A are significantly non-planar. This agrees with the experimental findings of a metal mediated duplex of G DNA oligomers and C DNA oligomers, but no metal mediated duplex of T DNA oligomers or A DNA oligomers. The G-Ag^+-G ground state is non WC type and the silver binds through the N7 atom in each base. In contrast, the C-Ag^+-C ground state is WC type and the silver bridges the N3 atom of each base. In both cases a hydrogen bond helps stabilize the complexes. T-Ag^+-T binding energy is much lower and the ground state is non planar with no local minima close to planar configuration. This qualitatively accounts for the experimental results that at most 2 silver cations to attach to T_{11} DNA strands, with the bare T_{11} strand the dominant product even at 1 Ag^+ added per base (Chapter 2, Figure 2.1a-c). In contrast to the other bases, A-Ag^+-A has many configurations close in energy, with 14 in an energy interval of 8 kcal/mol

(0.35 eV). The many equivalent binding sites of adenine may explain the higher numbers of silver cations (up to 6) attached to individual A_{11} DNA strands in the data (Chapter 2, Figure 2.3 d-f).

For completeness, we also explored CG and AT dimers mediated by silver cations. The C-Ag^+-G complex's ground state is non-WC type and planar. This bonding configuration has been reported earlier in silver mediated GCG triplexes.[81] The metal-AT dimer's ground state is non WC-type and non-planar.

A.2.1) Planarity of metal mediated homodimers

The dihedral angles (see Figure A.7 for the labeling in all bases) are C8-N7-N7-C8 = 181.2º (180º with CAM-B3LYP) for G-Ag^+-G and C2-N3-N3-C3 = 172º (180º with CAM-B3LYP) for C-Ag^+-C. A quite different configuration is obtained for A-Ag^+-A and T-Ag^+-T where the ground state is non-planar. For A-Ag^+-A, C2-N3-N3-C2 has an angle of 101.6º (84.70º for C2-N1-N1-C2 with CAM-B3LYP). The binding site of A-Ag^+-A depends then on the functional used. This is the only ground state where PBE+TS09 and CAM-B3LYP disagree. With PBE+TS09 functional it was found that there is a large rotational freedom for the ground state for the A-Ag^+-A dimer. The difference in energy for the perpendicular dimer and a dimer in a local minimum close to planar is around 0.7 kcal/mol (0.03 eV). For T-Ag^+-T, the C2-N3-N3-C2 dihedral angle was -140º degrees (-129.26º with CAM-B3LYP).

A.2.2) Metal bound to single bases

In the lowest energy Ag^+-G structure, the silver binds to N7-O atoms in the G base with binding energy of 77.08 kcal/mol (70.39 with CAM-B3LYP). In the Ag^+-C case, the silver binds to the central nitrogen with 71.16 kcal/mol of binding energy (64.73 using CAM-B3LYP).

A.2.3) Metal mediated GC and AT dimers

The most stable non-WC G-Ag$^+$-C geometry has a binding energy of 130.95 kcal/mol (120.16 with CAM-B3LYP) and a dihedral angle, defined by G[C2]-C[N3]-G[N7]-G[C5], of 183º (180º with CAM-B3LYP). Non-WC A-Ag$^+$-T has a binding energy of 102.08 kcal/mol (87.63 with CAM-B3LYP) and the dihedral angle for T[C4]-T[O4]-A[N3]-A[C4] is 129.8º (126.3º with CAM-B3LYP). For the WC G-Ag$^+$-C geometry the binding energy is 116.64 kcal/mol (104.96 with CAM-B3LYP) and the dihedral angle of C[C2]-C[N3]-G[O6]-G[C6] is 3.7º (0.0 º with CAM-B3LYP). For the WC A-Ag$^+$-T geometry the binding energy is 101.22 kcal/mol (87.81 with CAM-B3LYP) and the angle defined by T[C4]-T[O4]-A[N1]-A[C6] is 155.6º (125.7º with CAM-B3LYP). For the deprotonated (denoted with a *) silver mediated WC base pairs the binding energy is defined differently to include the change in electrons and protons from final structure and components. The binding energy is computed as the difference between the system composed of a trimer and a water ion and the energy of the separated bases, silver ion and water molecule: E(T*-Ag$^+$-A)+E(H_3O^+)- E(T)-E(A)-E(Ag$^+$)-E(H_2O). An equivalent definition is used for G*C. For T*-Ag$^+$-A the binding energy is 30.01 kcal/mol (15.72 with CAM-B3LYP) and for G*-Ag$^+$-C is 37.07 kcal/mol (24.62 with CAM-B3LYP). Both T*-Ag$^+$-A and G*-Ag$^+$-C are fully planar.

A-Ag$^+$-A (see Figure A.8)

str	Binding (kcal/mol)	dihedral angle (degrees)	bond length (Å) (angle -degrees)
WC			
1	109.60	C2-N1-N1-C2: 342.4	2.108-2.109 (174.6)
2	110.10	C2-N1-N1-C2: 179.1	2.097-2.097 (176.6)
3	110.96	C2-N1-N1-C2: 265.0	2.107-2.104 (178.3)
4	**111.90 (96.07)**	**C2-N3-N3-C2: 101.6**	**2.087-2.087 (178.8)**
non-WC			
1	110.51	C2-N1-N3-C2: 174.3	2.099- 2.088 (178.5)
2	109.45	C2-N1-N3-C2: 353.2	2.108-2.101 (173.8)
3	106.94	C2-N1-N7-C9: 178.5	2.097-2.083 (177.3)

4	106.80	C2-N1-N7-C9: 9.0	2.104-2.093 (171.0)
5	109.51	C9-N7-N7-C9: 357.5	2.098-2.094 (168.7)
6	111.23	C2-N3-N3-C2: 175.6	2.093-2.093 (178.4)
7	106.44	C8-N7-N3-C2: 359.5	2.085-2.090 (177.7)
8	107.52	C8-N7-N3-C2: 174.8	2.089-2.093 (177.8)
9	106.12	C8-N7-N7-C8: 14.2	2.081-2.080 (177.2)
10	103.88	C8-N7-N7-C8: 180.6	2.086-2.086 (176.5)

C-Ag$^+$-C (see Figure A.9)

str	Binding (kcal/mol)	dihedral angle (degrees)	bond length (Å) (angle -degrees)
WC			
1	121.40	C2-N3-N3-C2: 311.1	2.124-2.123 (178.4)
2	**126.18 (116.08)**	**C2-N3-N3-C2: 171.9**	**2.104-2.114 (169.2)**
non-WC			
1	121.19	C2-O2-N3-C2: 3.3	2.133-2.121 (170.7)
2	119.29	C2-O2-N3-C2: 157.6	2.100-2.108 (177.9)
3	117.15	C2-O2-O2-C2: 173.3	2.124-2.133 (179.4)
4	95.23	O2-C2-O2-C2: 176.4	2.228-2.492 (57.4)
5	97.49	O2-C2-O2-C2: 8.1	2.241-2.439 (58.0)

G-Ag$^+$-G (see Figure A.10)

str	Binding (kcal/mol)	dihedral angle (degrees)	bond length Å) (angle -degrees)
WC			
1	104.12	O6-C6-C6-O6: 158	2.369-2.247 (81.6)
2	102.67	C8-N7-N6-C6: 192.5	2.107- 2.171 (172.5)
3	97.74	C6-O6-O6-C6: 17.5	2.069- 2.070 (177.4)
4	71.50	C2-N2-N2-C2: 340.7	2.162- 2.167 (173.6)
non-WC			
1	110.52	C6-O6-N3-C4: 176.3	2.099- 2.084 (179.2)
2	110.69	C6-O6-N3-C4: 358.7	2.089- 2.081 (177.6)
3	125.32	C5-N7-N7-C5: 22.5	2.105- 2.107 (166.2)
4	128.57	C8-N7-N7-C8: 186.8	2.100- 2.091 (166.2)
5	118.67	C8-N7-O6-C6: 159.6	2.106- 2.125 (157.8)
6	129.56	C8-N7-N7-C8: 179.0	2.091- 2.097 (175.0)
7	**129.72 (117.77)**	**C8-N7-N7-C8: 181.2**	**2.094- 2.094 (176.9)**
8	108.53	C6-O6-O6-C6: 358.9	2.082- 2.111 (166.8)

T-Ag$^+$-T (see Figure A.11)

str	Binding (kcal/mol)	dihedral angle (degrees)	bond length (Å) (angle -degrees)
WC			
1	90.88	C4-O4-O4-C4: 351.1	2.086-2.086 (174.4)
2	88.58	C4-O4-O2-C2: 357.3	2.078-2.086 (173.0)
3	85.45	C2-O2-O2-C2: 348.1	2.088-2.088 (179.6)
4	**91.53 (79.35)**	**C4-O4-O4-C4: -140.0**	**2.088-2.087 (173.9)**

A-Ag$^+$-T (see Figure A.12)

str	Binding (kcal/mol)	dihedral angle (degrees)	bond length (Å) (angle -degrees)

WC			
1	76.30	A[C2]-A[N1]-T[N3]-T[C2]: 177	2.113 A(N7)*
2	91.39	A[C6]-A[N6]-T[O4]-T[C4]: 339.7	2.107-2.159 (165.7)
3	**101.22 (87.81)**	**A[C6]-A[N1]-T[O4]-T[C4]: 155.6**	**2.093-2.085 (179)**
4	98.57	A[C2]-A[N1]-T[O2]-T[C2]: 125.7	2.099-2.100 (178.6)
5	73.90	A[C2]-A[N1]-T[N3]-T[C2]: 349.2	2.136- 2.804 T(73.1)*
6	80.65	A[C2]-A[N1]-T[N3]-T[C2]: 359.3	2.122 A(N3)*
7	98.80	A[C2]-A[N1]-T[O2]-T[C2]: 67.1	2.095-2.090 (174.5)
non-WC			
1	98.90	A[C2]-A[N1]-T[O2]-T[C2]: 358.8	2.092- 2.093 (178.4)
2	99.00	A[C2]-A[N3]-T[O2]-T[C2]: 337.5	2.082- 2.090 (171.4)
3	97.35	A[C2]-A[N3]-T[O2]-T[C2]: 155.6	2.094-2.094 (164.8)
4	95.55	A[C8]-A[N7]-T[O2]-T[C2]: 350.4	2.077- 2.089 (167.3)
5	95.09	A[C8]-A[N7]-T[O2]-T[C2]: 170.6	2.083 -2.087 (169.9)
6	95.84	A[C8]-A[N7]-T[O4]-T[C4]: 241.7	2.074 – 2.066 (175.1)
7	98.61	A[C8]-A[N7]-T[O4]-T[C4]: 31.3	2.075-2.083 (166.1)
8	101.32	A[C2]-A[N3]-T[O4]-T[C4]: 355.4	2.084- 2.087 (169.2)
9	98.86	A[C2]-A[N3]-T[O4]-T[C4]: 19.0	2.071- 2.082 (178.4)
10	98.57	A[C2]-A[N3]-T[O4]-T[C4]: 116.8	2.071- 2.091 (179.5)
11	98.29	A[C2]-A[N1]-T[O4]-T[C4]: 251.1	2.080 – 2.099 (167.5)
12	**102.08 (87.63)**	**A[C4]-A[N3]-T[O4]-T[C4]: 129.8**	**2.076- 2.074 (173.5)**

G-Ag$^+$-C (see Figure A.13)

str	Binding (kcal/mol)	dihedral angle (degrees)	bond length (Å) (angle -degrees)
WC			
1	112.82	G[C2]-G[N1]-C[N3]-C[C2]: 177.3	2.431- 2.211 G(80.6)*
2	**116.64 (104.96)**	**G[C6]-G[O6]-C[N3]-C[C2]: 3.7**	**2.118- 2.086 (163.2)**
3	106.59	G[C2]-G[N2]-C[O2]-C[C2]: 12.9	2.149- 2.083 (170.5)
4	81.13	G[C2]-G[N1]-C[N3]-C[C2]: 352.8	2.150 C(O2)*
5	92.02	G[C2]-G[N1]-C[N3]-C[C2]: 352.7	2.115 G(N3)*
non-WC			
1	130.67	G[C8]-G[N7]-C[N3]-C[C2]: 355.5	2.094-2.102 (170.5)
2	120.22	G[C6]-G[O6]-C[N3]-C[C2]: 192.0	2.107-2.105 (176.4)
3	111.89	G[C2]-G[N3]-C[N3]-C[C2]: 185.0	2.095-2.118 (168.0)
4	110.62	G[C2]-G[N3]-C[N3]-C[C2]: 3.2	2.092-2.112 (171.4)
5	114.84	G[C6]-G[O6]-C[N3]-C[C2]: 355.8	2.073-2.103 (178.3)
6	107.60	G[C6]-G[O6]-C[O2]-C[C2]: 358.1	2.091-2.102 (175.0)
7	106.25	G[C2]-G[N2]-C[O2]-C[C2]: 0.5	2.150-2.088 (172.3)
8	122.11	G[C6]-G[O6]-C[N3]-C[C2]: 171.5	2.116-2.100 (173.2)
9	**130.95 (120.16)**	**G[C8]-G[N7]-C[N3]-C[C2]: 358.8**	**2.092-2.102 (167.5)**
10	106.90	G[C2]-G[N3]-C[O2]-C[C2]: 9.7	2.095-2.093 (177.4)
11	106.60	G[C2]-G[N3]-C[O2]-C[C2]: 183.7	2.087- 2.089 (174.4)

Deprotonated (see Figure A.14)

str	Binding (kcal/mol)	dihedral angle (degrees)	bond length (Å) (angle -degrees)
T*-Ag$^+$-A	30.09 (15.72)	A[C2]-A[N1]-T[N3]-C[C2]:355.0	2.116-2.079 (160.3)

G*-Ag$^+$-C	37.07 (24.62)	G[C2]-G[N1]-C[N3]-C[C2]:353.0	2.097-2.121 (157.4)

Table A.2) Summary of all structures including: structure label (str), binding energies obtained with PBE+vdW, dihedral angles and atom-metal-atom bond lengths and angles. The notation “WC” means that Ag$^+$ binds at base sites for Watson-Crick pairing. The boldface entries are for the most stable structure. For reference the values of the binding energies obtained with the Gaussian code are in parentheses. The values marked with asterisk (*) in the fourth column corresponds to structures where the Ag$^+$ binds to only one nucleobase in the pair. The labeling of the figures on the following pages follows the labeling convention in this table.

A.2.4) The PAW method

The computational results in the main text were calculated with a grid based code (GPAW) that does not present the problem of superposition errors of atomic basis. GPAW could present a similar type of superposition error if the bond distances between two atoms where smaller than the sum of cutoff radius where the PAW transformation is applied. Cutoff values are chosen small enough to avoid this problem, as shown in Table A.3.

The dataset used in the stable release of GPAW uses a variable named rcut that determines the size of the sphere around each atom where the PAW transformation is applied. We are providing here the maximum rcut (there is one per valence atomic orbital) in the setups released on Mar 27 2014 version 0.9 revision 11271.

atom	rcut	vdW
H	0.9	2.27
C	1.2	3.21
O	1.3	2.87
N	1.14	2.93
Ag	2.51	3.25

Table A.3) Values of rcut (in Bohr) for the different atoms in the studied molecular structures of this work. The van der Waals radius is giving for comparison.

A.2.5) Images of calculated ground state geometries

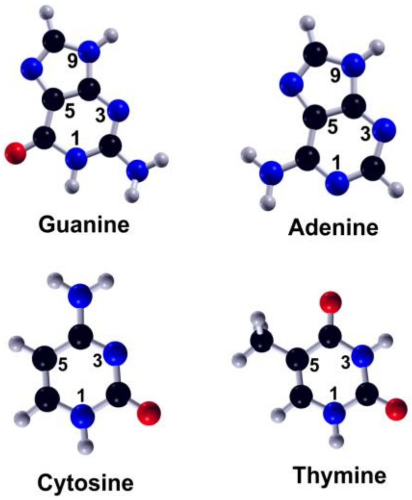

Figure A.7) Labels used in this work for the definition of the dihedral angles in the four DNA bases

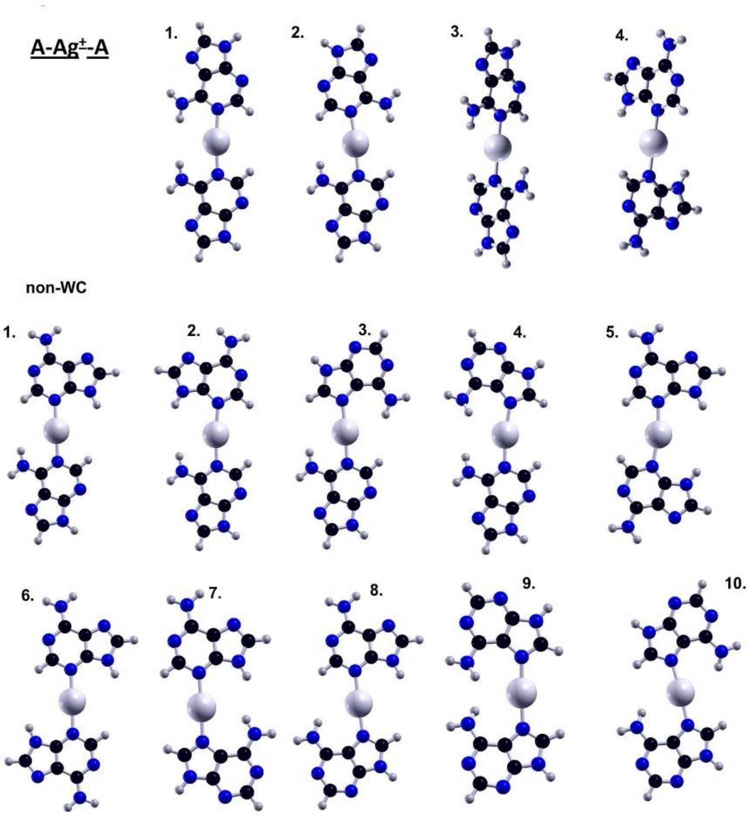

Figure A.8) Representation of the optimized geometries for the A-Ag$^+$-A pairs (see Table A.2) obtained by means of Density Functional theory (DFT) at PBE+vdW level.

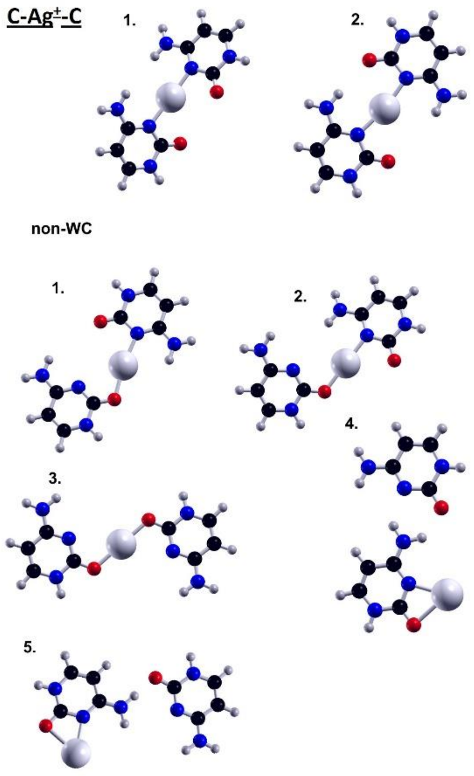

Figure A.9) Representation of the optimized geometries for the C-Ag$^+$-C pairs (see Table A.2) obtained by means of Density Functional theory (DFT) at PBE+vdW level.

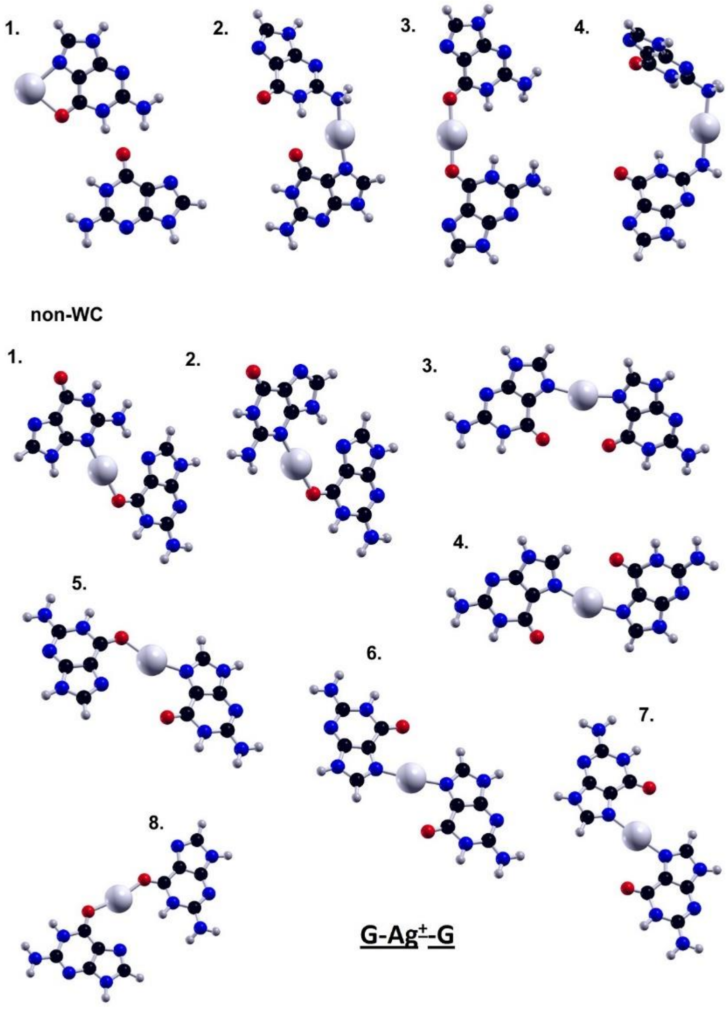

Figure A.10) Representation of the optimized geometries for the G-Ag^{+}-G pairs (see Table A.2) obtained by means of Density Functional theory (DFT) at PBE+vdW level.

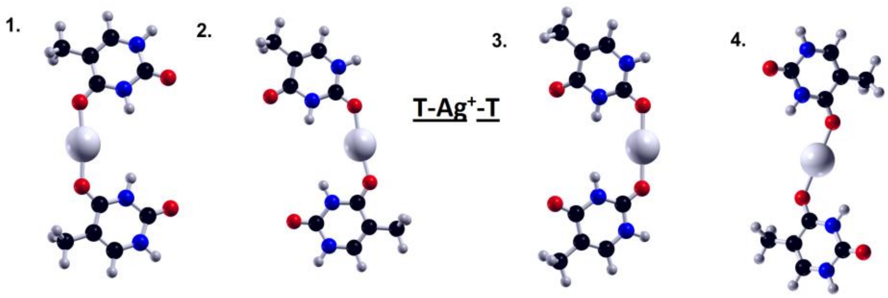

Figure A.11) Representation of the optimized geometries for the T-Ag^{+}-T pairs (see Table A.2) obtained by means of Density Functional theory (DFT) at PBE+vdW level.

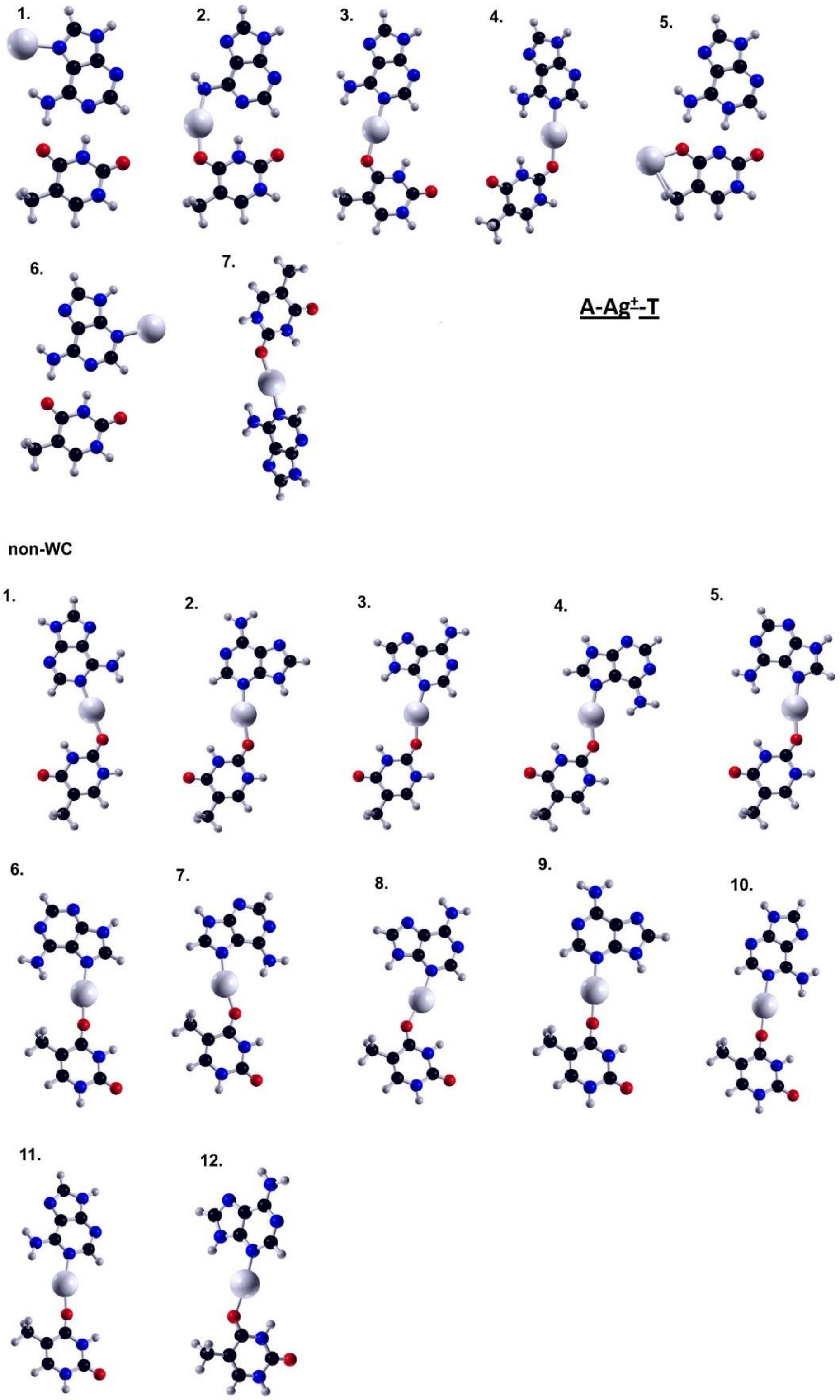

Figure A.12) Representation of the optimized geometries for the A-Ag^{+}-T pairs (see Table A.2) obtained by means of Density Functional theory (DFT) at PBE+vdW level.

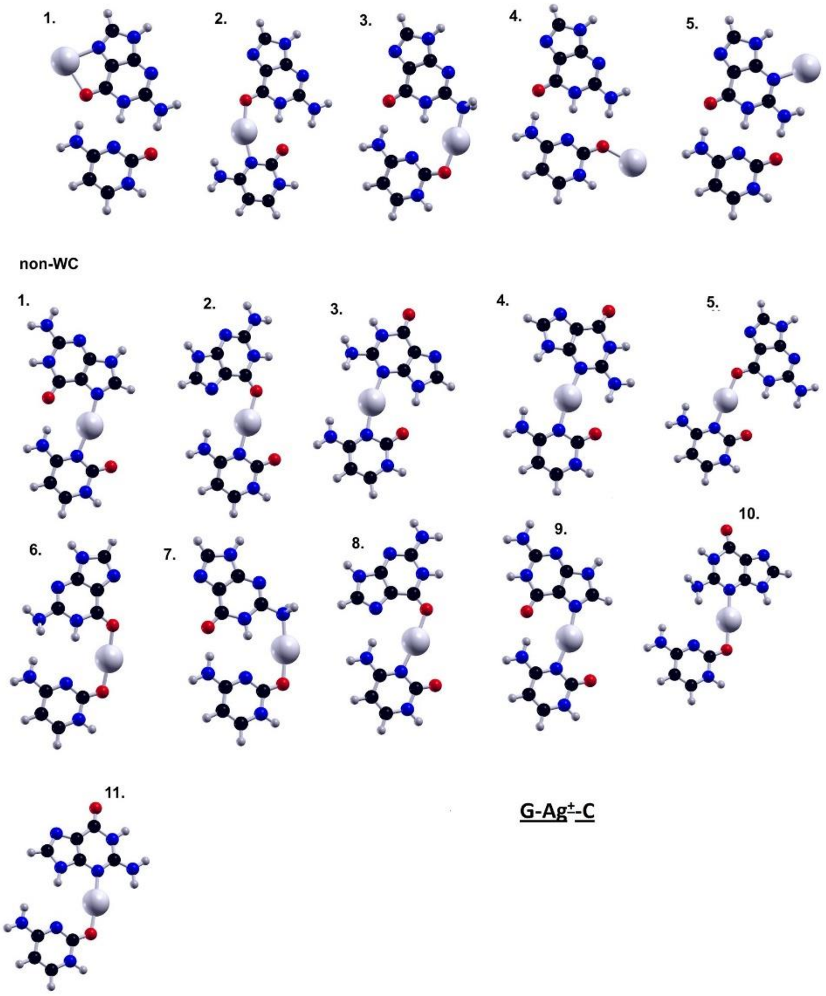

Figure A.13) Representation of the optimized geometries for the G-Ag^{+}-C pairs (see Table A.2) obtained by means of Density Functional theory (DFT) at PBE+vdW level.

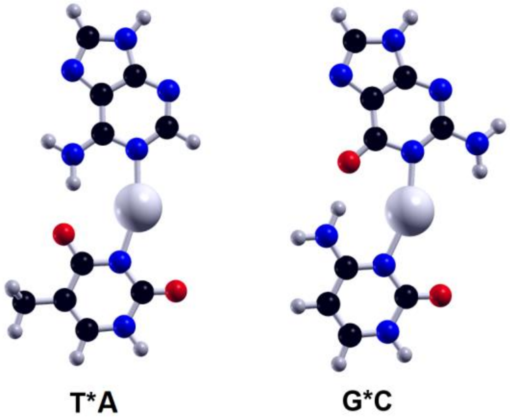

Figure A.14) Representation of the optimized geometries for the deprotonated T*-Ag^{+}-A and G*-Ag^{+}-C pairs (see Table A.2) obtained by means of Density Functional theory (DFT) at PBE+vdW level.

A.2.6) Initial configurations

The initial configurations were chosen to sample all possible combinations of the Watson-Crick and Hoogsteen region of the bases. For every configuration we have placed the cation in the region in between the bases. Representations of such configurations are shown in Figure A.15 for the case of the Guanine homo-duplex. If the repulsive forces in the initial configuration are too high large distortions can occur quickly; This problem is typically solved with a very small step size that increments the total time of simulation. Instead, we have performed small translations or rotations on the initial configurations around the indicated position in Figure A.15 that decrease the positive repulsion before the optimization, which moves the cation closer to a bonding configuration. For example, in the first configuration in Figure A.15, the complex with the Ag^+ cation placed in the middle of the region optimizes very quickly to the ground state of the bridged Guanine homo-duplex. More interesting is the case when the Ag^+ cation is placed nearest the Oxygen (for the right base), where the left base shifted downwards to decrease the repulsion with the Hydrogen atom, then an optimization with the BFGS algorithm finds the global minimum after only 206 steps.

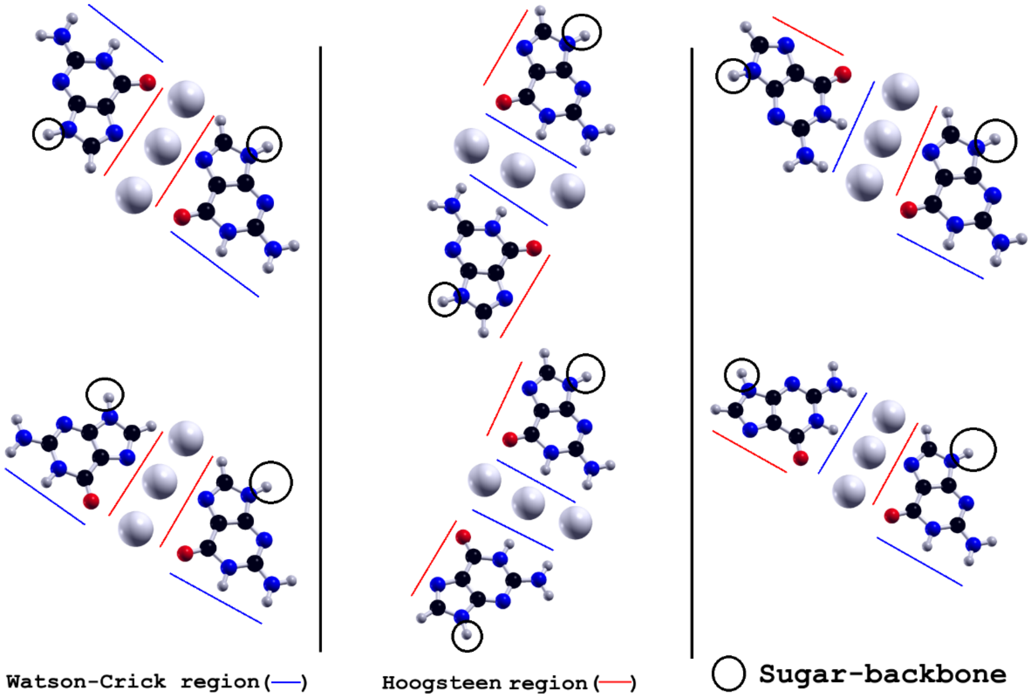

Figure A.15) Schematic representation of the initial configurations used for the search algorithm in the case of the Ag^{+} homo-duplex with Guanine. The bases are facing their Watson-Crick and Hoogsteen regions and the cation is placed in positions sampling the available bonding space. A small rotation or translation of the bases to decrease high positive repulsions was performed in every case.

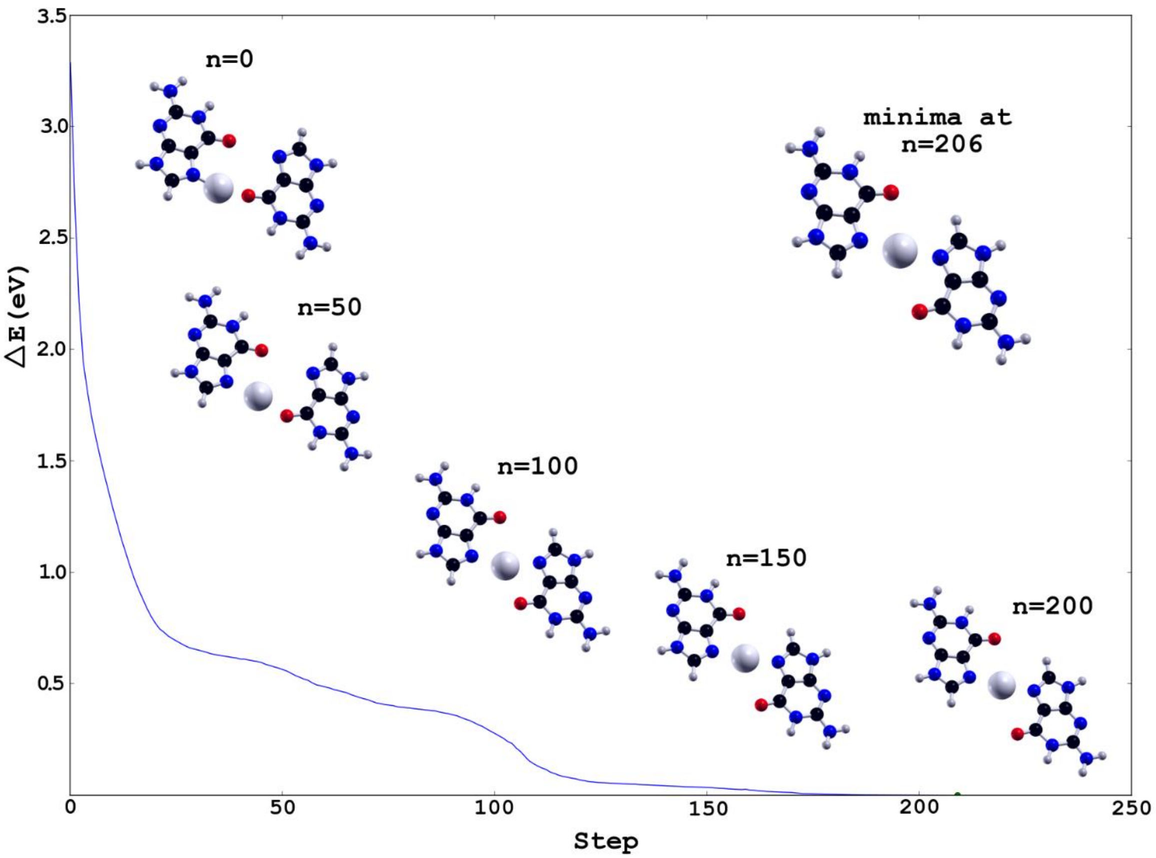

Figure A.16) Example of a single force optimization leading to the bridged Guanine homo-duplex ground state.

Appendix B) Supporting Information for Chapter 3

B.1) Determining the number of Ag^+ cations in Ag^+-paired DNA from Electrospray-Ionization Mass Spectrometry (ESI-MS)

Below we display the full mass spectra of samples injected into the Waters QTOF2 mass spectrometer in negative ion mode. Product compositions were determined by Gaussian fits of the isotope peak envelopes to locate the center of the envelope, $|m/z|_{fit}$. (For certain mass products with asymmetric isotope peak envelopes this procedure is less accurate; However, for the fairly symmetric Ag^+-DNA mass isotope peak envelopes relevant here, we have found that the systematic errors introduced by the Gaussian envelope approximation are small). We assume that ionization by the ESI process proceeds exclusively by deprotonating the DNA in Ag^+-DNA complexes, creating a negatively charged gas phase ion which migrates towards the detector in negative ion mode. In DNA studies with no attached Ag^+ cations, the magnitude of the charge state, z, of the detected ion equals the number of protons removed. When Ag^+ are embedded in the DNA, the additional positive charges from the metal cations require removal of additional protons to achieve the same negative charge state, z. We know from our previous studies there is no detectable reduction of Ag^+ under the ESI conditions we employ here; thus one additional proton is removed for each attached Ag^+ to realize a given charge state, z.[55]

To determine the number N_{Ag+} of attached Ag^+, we relate the mass $m_{product}$ of the fully protonated product to the (negative) charge state, z, of the detected ion:

$$m_{product} = [|\frac{m}{z}|_{fit} * |z| + (|z| * m_{proton})] + [N_{Ag^+} * m_{proton}] \qquad \text{Eq. B.1)}$$

where m_{proton} is the mass of a proton. Since the products must contain an integer number of DNA strands, N_{DNA}, we know that:

$$m_{product} = m_{DNA} * N_{DNA} + m_{Ag^+} * N_{Ag^+}$$ Eq. B.2)

where m_{DNA} is the mass of the fully protonated DNA strand and m_{Ag^+} is the mass of Ag^+. Then, by substitution:

$$m_{DNA} * N_{DNA} + m_{Ag^+} * N_{Ag^+} = \left[\left| \frac{m}{z} \right|_{fit} * |z| + \left(|z| * m_{proton} \right) \right] + \left[N_{Ag^+} * m_{proton} \right]$$

Eq. B.3)

and solving for N_{Ag+}:

$$N_{Ag^+} = \frac{\left[\left| \frac{m}{z} \right|_{fit} * |z| + |z| * m_{proton} \right] - m_{DNA} * N_{DNA}}{\left[m_{Ag^+} - m_{proton} \right]}$$ Eq. B.4)

In the case where $m_{product} < m_{DNA}*2$, Eq. B.4 can be easily solved since there can only be one DNA strand in the product. In the case where $m_{product} > m_{DNA}*2$, Eq. B.4 is solved for all strand numbers N_{DNA} consistent with the requirement $m_{product} > m_{DNA}*N_{DNA}$. Since we have an experimentally determined mass accuracy of approximately $0.3*m_{proton}$ or better, any case where an assumed number of DNA strands results in an N_{Ag}^+ value that is offset from an integer value of more than $0.3*m_{proton}/m_{Ag}^+$, or ~ 0.01, is discarded. We have not encountered any cases where multiple N_{DNA} values have resulted in unambiguous values of N_{Ag}^+.

B.2) Mass spectra for centrally mutated Ag^+-paired strands

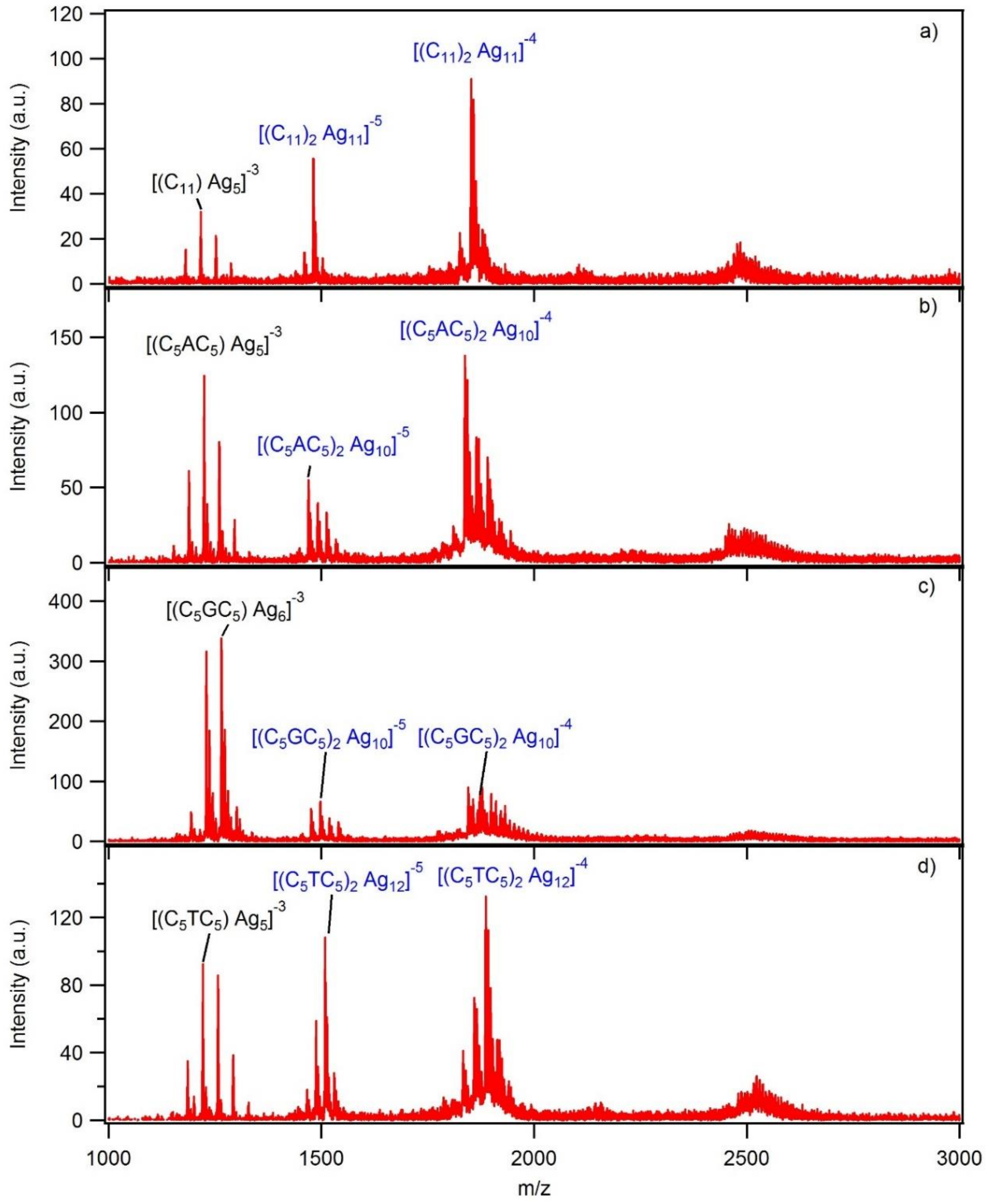

Figure B.1) Mass spectra for solutions of 80 µM DNA, 880 µM $AgNO_3$ and 50 mM $NH_4C_2H_3O_2$ (pH = 7) injected into the mass spectrometer in negative ion mode for DNA strands a) C_{11}, b) C_5AC_5, c) C_5GC_5 and d) C_5TC_5. Monomeric products are labelled in black while duplex products are labelled in blue. From left to right in each mass spectrum the labelled products are a) 1216.75, 1481.68 and 1852.34 m/z, b) 1224.70, 1469.86 and 1837.64 m/z, c) 1265.70, 1497.69 and 1872.38 m/z, d) 1221.69, 1509.05 and 1886.58 m/z. Additional products located around the main, labelled peaks represent distributions in the number of Ag^+, which is discussed in greater detail for Ag^+-duplex products in Chapter 3 (Figure 3.2).

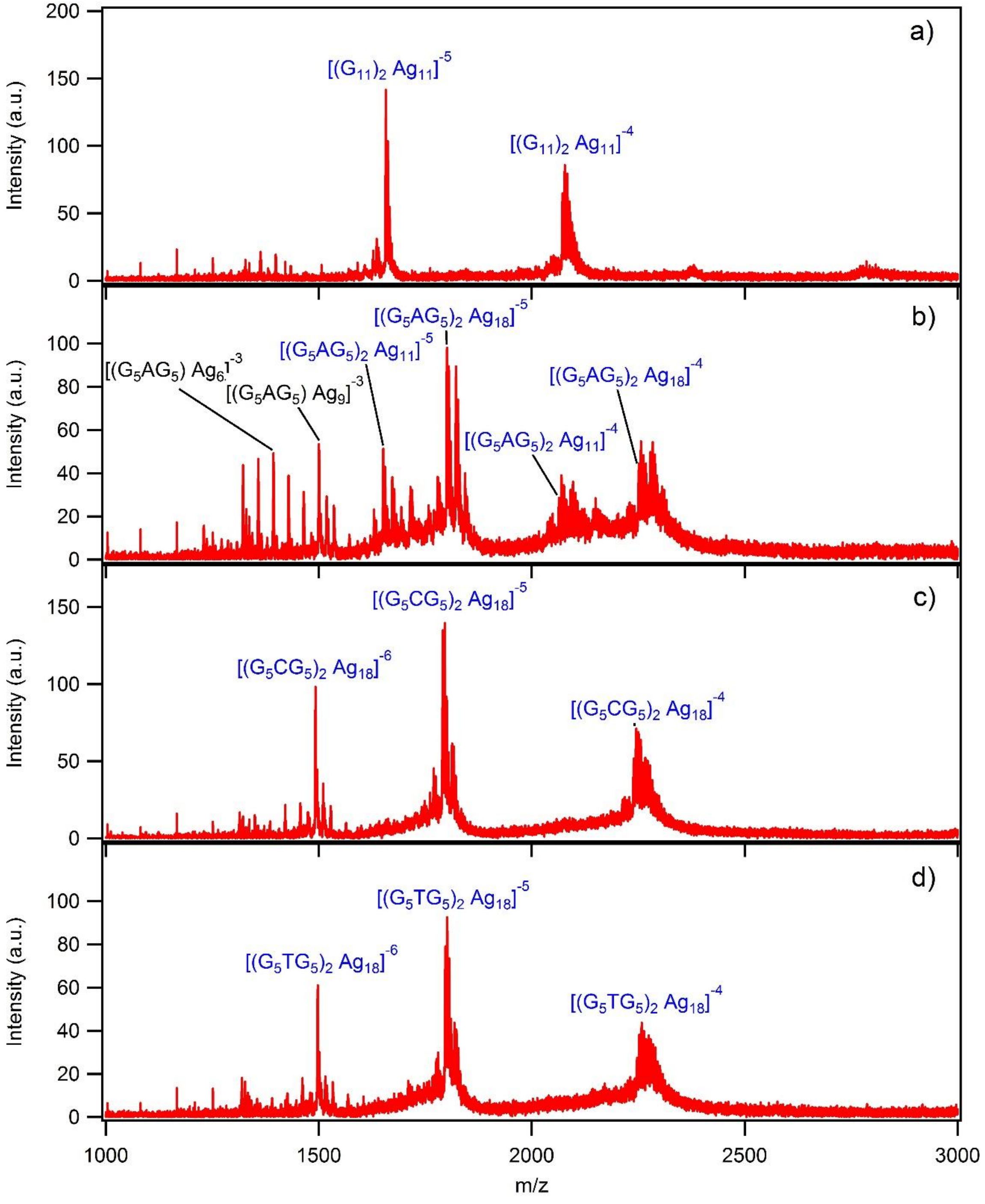

Figure B.2) Mass spectra for solutions of 80 µM DNA, 880 µM $AgNO_3$ and 50 mM $NH_4C_2H_3O_2$ (pH = 7) injected into the mass spectrometer in negative ion mode for DNA strands a) G_{11}, b) G_5AG_5, c) G_5GG_5 and d) G_5TG_5. Monomeric products are labelled in black while duplex products are labelled in blue. From left to right in each mass spectrum the labelled products are a) 1657.76 and 2072.48 m/z, b) 1393.81, 1500.66, 1651.39, 1800.98, 2064.48 and 2251.55 m/z, c) 1492.65, 1791.40, and 2239.59 m/z, d) 1497.66, 1797.43 and 2247.04 m/z. Additional products located around the main, labelled peaks represent distributions in the number of Ag+, which is discussed in greater detail for Ag^+-duplex products in Chapter 3 (Figure 3.2).

B.3) CD spectra for centrally mutated Ag$^+$-paired strands

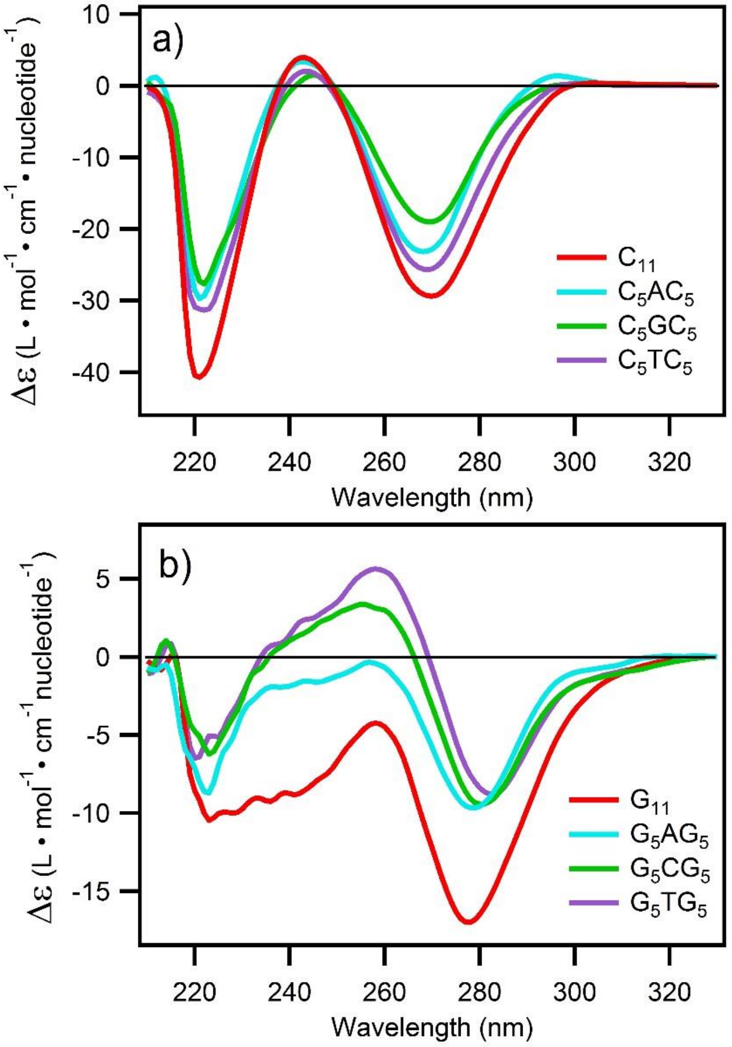

Figure B.3) Circular dichroism spectra for solutions of 7.5 μM DNA, 82.5 μM $AgNO_3$ and 50 mM $NH_4C_2H_3O_2$ (pH = 7) for strands a) C_{11} (red curve), C_5AC_5 (teal curve), C_5GC_5 (green curve) and C_5TC_5 (purple curve) and b) G_{11} (red curve), G_5AG_5 (teal curve), G_5CG_5 (green curve) and G_5TG_5 (purple curve). All solutions with strands that have a central mutation in C_{11} in a) show the same spectral shape and similar CD magnitudes suggesting the mutated strands produce Ag$^+$-duplexes with a secondary structure that is very similar to the control C_{11} Ag$^+$-duplex. Solutions with strands that have a central mutation in G_{11} in b) deviate more significantly in both CD magnitude and shape to the control G_{11} Ag$^+$-duplex solution; however wavelengths of spectral features are similar. Thus the structure of duplexes formed by the mutated G-rich strands appears to be perturbed.

B.4) Mass spectra for Ag^+-paired heterobase strands

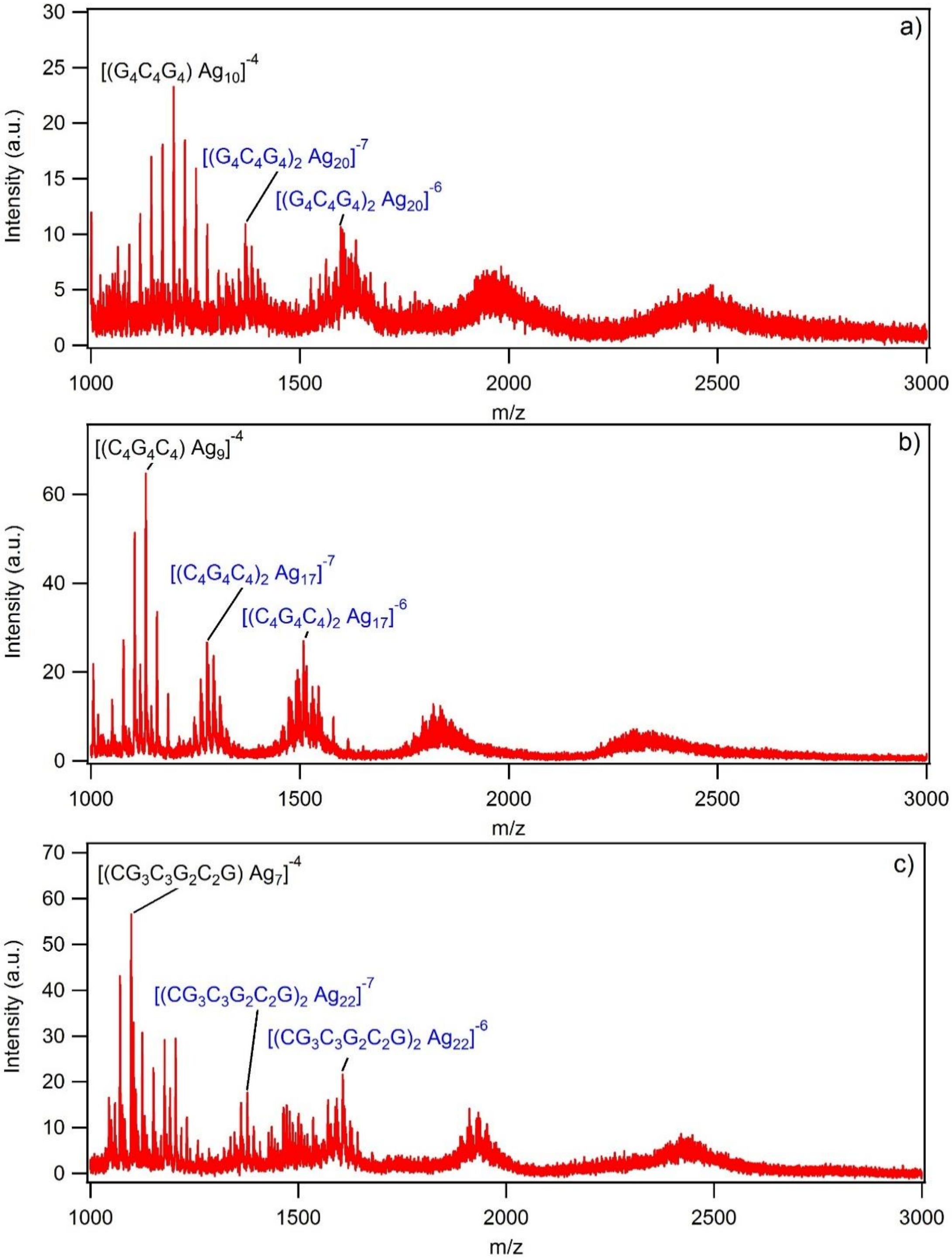

Figure B.4) Mass spectra for solutions of 80 μM DNA, 960 μM $AgNO_3$ and 10 mM $NH_4C_2H_3O_2$ (pH = 7) injected into the mass spectrometer in negative ion mode for DNA strands a) $G_4C_4G_4$, b) $C_4G_4C_4$ and c) $CG_3C_3G_2C_2G$. Monomeric products are labelled in black while duplex products are labelled in blue. From left to right in each mass spectrum the labelled products are a) 1198.19, 1369.58 and 1598.01 m/z, b) 1131.47, 1277.00 and 1509.98 m/z, c) 1098.04, 1377.21 and 1606.90 m/z. Additional products located around the main, labelled peaks represent distributions in the number of Ag+, as discussed in greater detail for Ag^+-duplex products in Chapter 3 (Figure 3.3).

B.5) Mass spectra for Ag^+-paired $T_2C_{20}T_2$

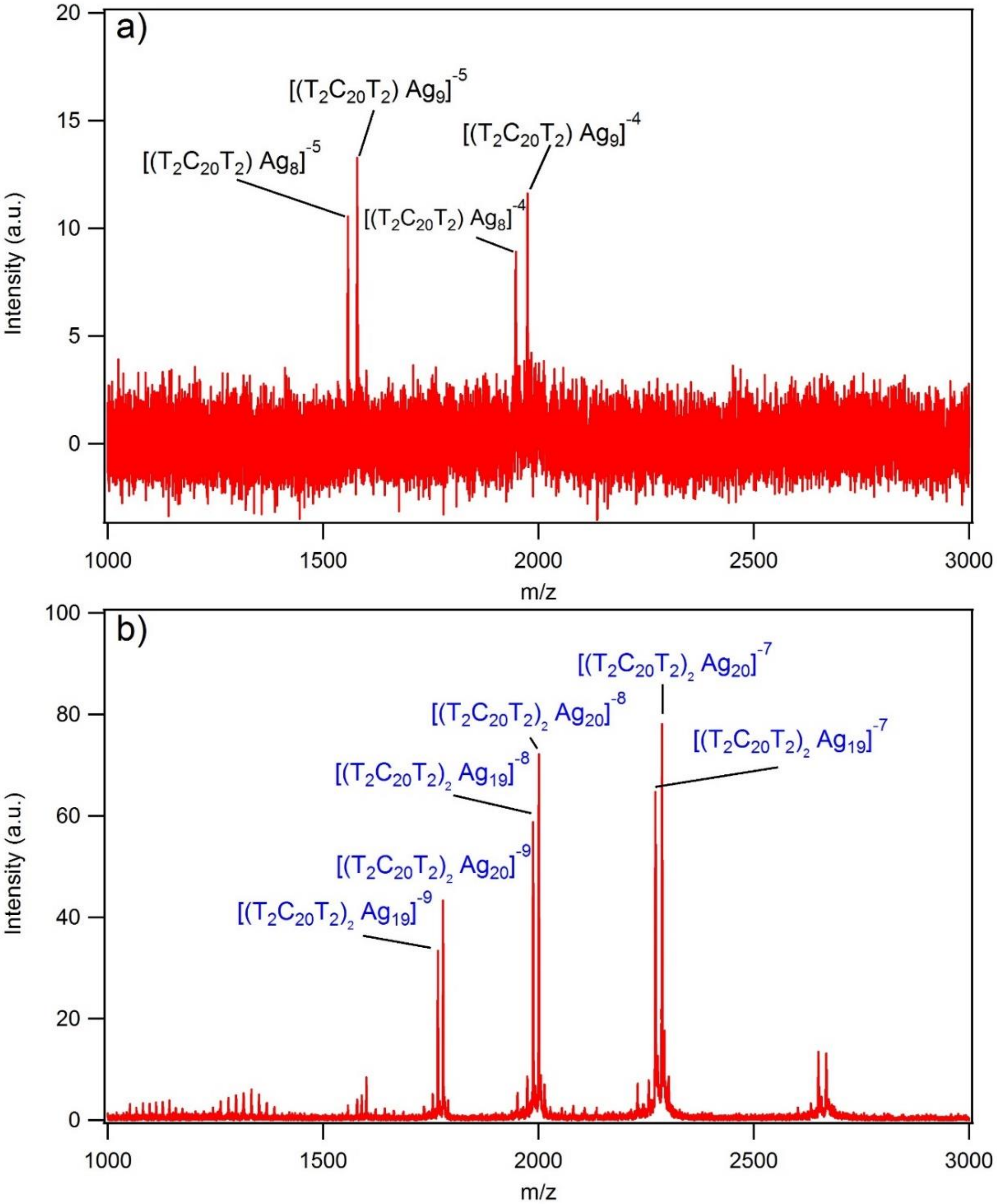

Figure B.5) Mass spectra of the HPLC aliquots collected from the two dominant chromatogram peaks of a solution prepared at 5 μM $T_2C_{20}T_2$, 100 uM $AgNO_3$ and 10 mM $NH_4C_2H_3O_2$ pH = 7. These plots are enlarged versions of the insets in Chapter 3, Figure 3.4a. The eluted samples were solvent exchanged by spin filtration to 10 mM $C_2H_3O_2NH_4$ before injection into the mass spectrometer. Monomeric products are labelled in black while duplex products are labelled in blue. a) The mass spectrum for the first eluted dominant HPLC chromatogram peak consists entirely of Ag^+-monomers, with peaks at 1557.6 and 1579.02 m/z for products $[(T_2C_{20}T_2)\ Ag_8]^{-5}$ and $[(T_2C_{20}T_2)\ Ag_9]^{-5}$ respectively. b) The mass spectrum for the second eluted dominant HPLC chromatogram peak consists entirely of Ag^+-duplexes, with peaks at 2271.50 and 2286.79 m/z for products $[(T_2C_{20}T_2)_2\ Ag_{19}]^{-7}$ and $[(T_2C_{20}T_2)_2\ Ag_{20}]^{-7}$, respectively.

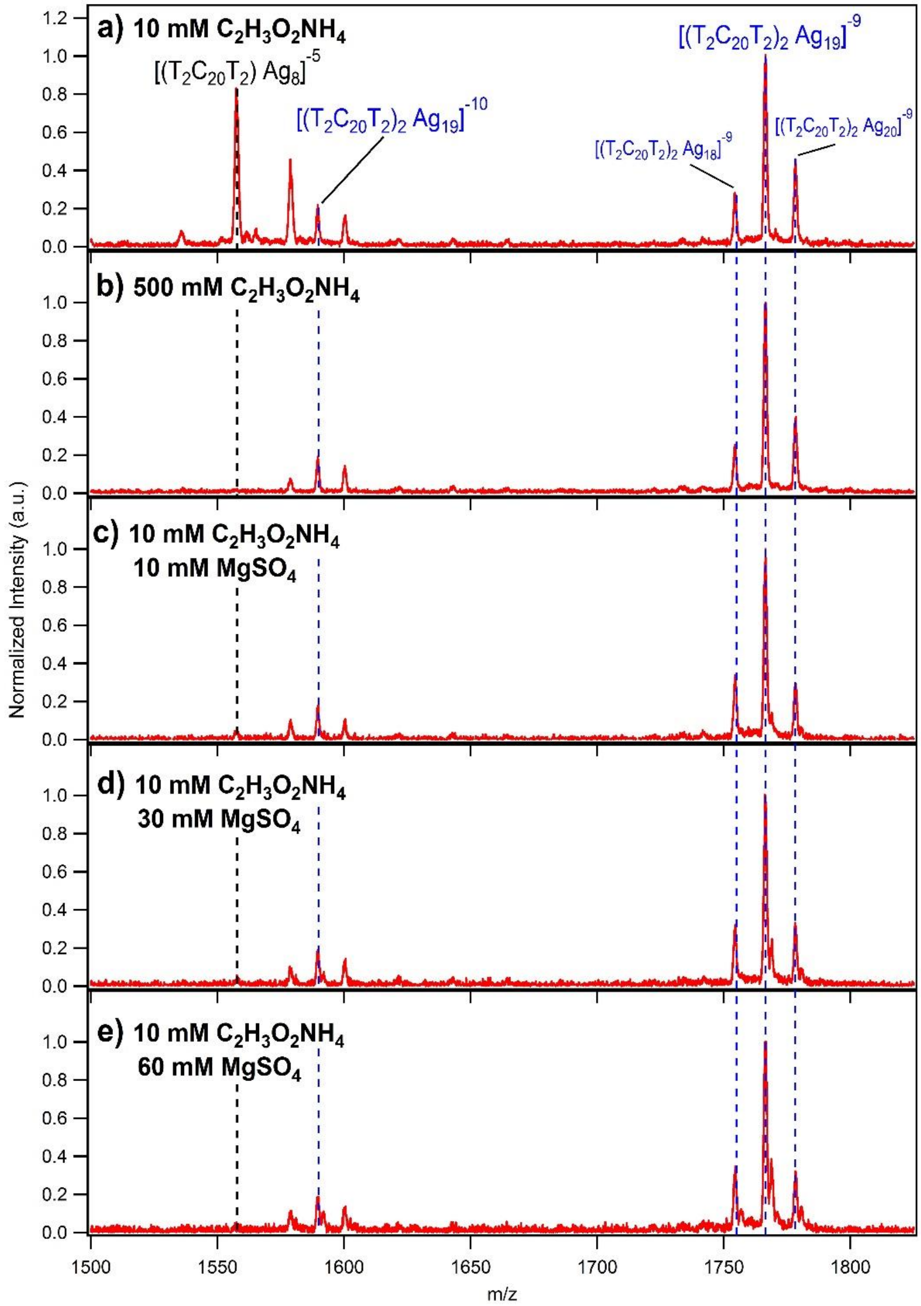

Figure B.6) Mass spectra of samples prepared by annealing strand $T_2C_{20}T_2$ with 1 Ag^+/base in a) 10 mM $C_2H_3O_2NH_4$, b) 500 mM $C_2H_3O_2NH_4$, c) 10mM $C_2H_3O_2NH_4$ and 10mM $MgSO_4$, d) 10mM $C_2H_3O_2NH_4$ and 30 mM $MgSO_4$ and e) 10mM $C_2H_3O_2NH_4$ and 60 mM $MgSO_4$. Since high concentrations of salts, especially non-volatile ones, are incompatible with ESI-MS the samples were solvent exchanged into 10 mM $C_2H_3O_2NH_4$ by spin filtration with a 3k MWCO filter before injection into the ESI-MS. Major products in a) consisted of Ag^+-mediated duplex products, labelled in blue, and Ag^+-strand monomer products, labelled in black. Higher ionic conditions during the annealing process results in negligible amounts of Ag^+-strand monomer products compared to Ag^+-mediated duplex products, as seen in b), c), d), and e). Black dashed lines represent expected locations for Ag^+-strand monomer products while blue dashed lines represent expected locations for Ag^+-mediated duplex products as found in a). For comparison, the signal intensity for product $[(T_2C_{20}T_2)_2Ag_{19}]^{-9}$ is normalized to 1 for each mass spectrum and the same x-scaling and y-scaling is used throughout this figure.

B.6) CD spectra for T_2C20T_2 with and without $MgSO_4$

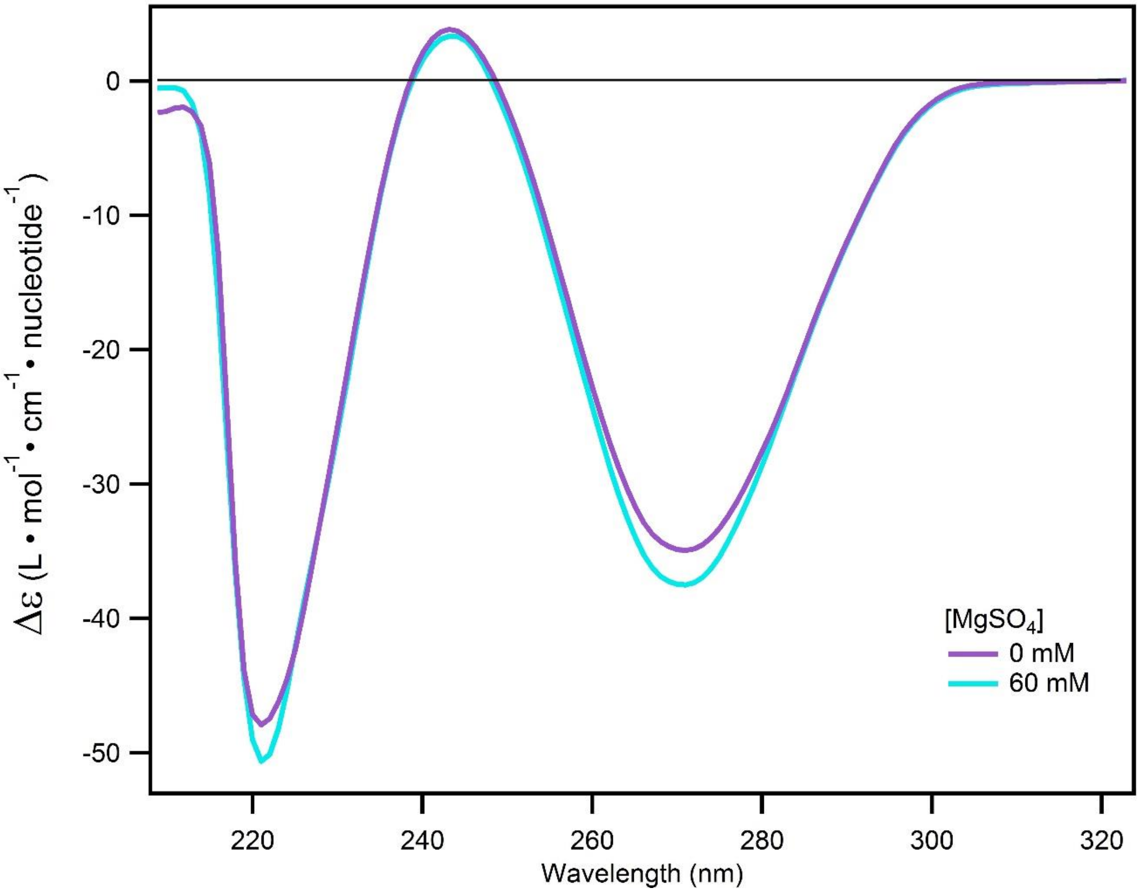

Figure B.7) CD spectra of solutions of 5 μM $T_2C_{20}T_2$ and 10 mM $NH_4C_2H_3O_2$ (pH = 7) in 0 mM (purple) and 60 mM (teal) $MgSO_4$. The very slight changes in CD spectrum after addition of MgSO4 shows that the Ag^+-mediated duplex structure is essentially unchanged.

B.7) Absorbance spectra of C20 and T2C20T2 with and without $MgSO_4$ and NaCl

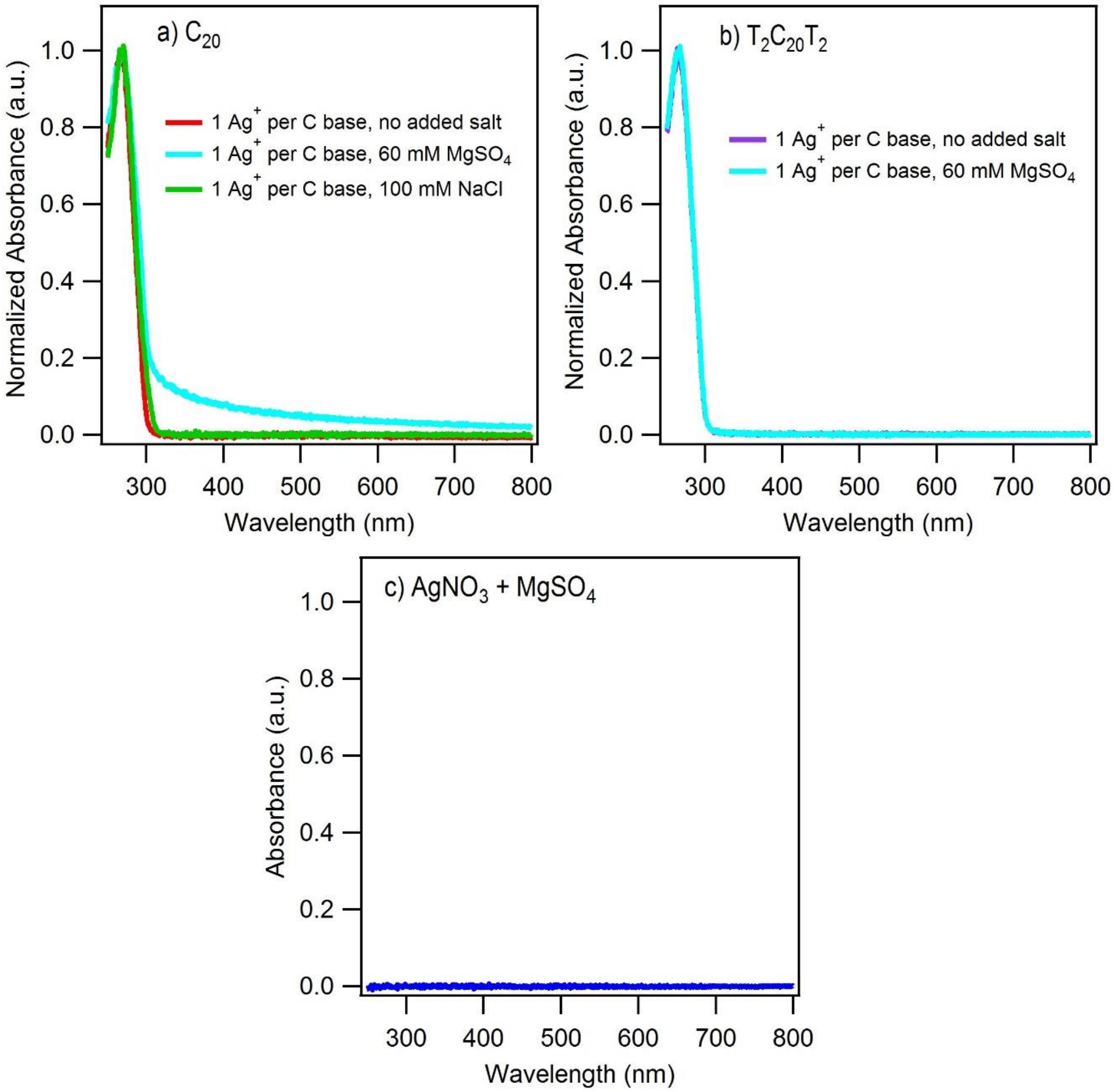

Figure B.8) Absorbance spectra of solutions with a) 4 µM C_{20} and b) 5 µM $T_2C_{20}T_2$ in 10mM $NH_4C_2H_3O_2$ (pH = 7) at 1 Ag^+ per cytosine base, as used for CD experiments. a) Absorbance spectra for solutions with strand C_{20} with no added salt (red), 60 mM $MgSO_4$ (teal) and 100 mM NaCl (green). b) Absorbance spectra for solutions with strand $T_2C_{20}T_2$ with no added salt (purple) and 60 mM $MgSO_4$ (teal). Rise of visible absorbance in the spectrum of a) 60 mM $MgSO_4$ for strand C_{20} may suggest the presence of some aggregates, which could be the cause of reduced CD signal compared to the control with no $MgSO_4$ (Chapter 3, Figure 3.6b). No such visible absorbance increase is detected in the absorbance spectrum for b) strand $T_2C_{20}T_2$ with 60 mM $MgSO_4$. The additional thymine bases at the beginning and end of the $T_2C_{20}T_2$ strand appear to prevent this aggregation interaction. No such increase in visible absorbance is observed in solutions with a) 100 mM NaCl either, suggesting that the decrease in CD (Chapter 3, Figure 3.6a) signal compared to the control may be the result of destabilizing Cl^- interactions with C-Ag^+-C base pairs. c) Solution of 10 mM $NH_4C_2H_3O_2$ (pH = 7), 800 µM $AgNO_3$ and 60 mM $MgSO_4$ displays no visible absorbance when blanked against a solution of 10 mM $NH_4C_2H_3O_2$, ruling out the possibility of Ag_2SO_4 contributing to visible absorbance. No precipitates were observed in any solution.

Appendix C) Supporting Information for Chapter 4

C.1) FRET experiments

C.1.1) Experimental Design

Ag^+-paired strands were formed from strands labeled with Alexa 488 donors (*"d"*) and Alexa 647 acceptors (*"a"*). For the cytosine strand experiments: strand $\mathbf{A_{3'C}}$ is 5'-$T_5C_{20}T_5$-3'-*a* (9814.0 g/mol), strand $\mathbf{D_{5'C}}$ is *d*-5'-$T_2C_{20}T_2$-3' (7633.3 g/mol) and strand $\mathbf{D_{3'C}}$ is 5'-$T_2C_{20}T_2$-3'-*d* (7665.3 g/mol). For the guanine strand experiments: strand $\mathbf{A_{3'G}}$ is 5'-$T_4G_{15}T_4$-3'-*a* (8360.5 g/), strand $\mathbf{D_{3'G}}$ is 5'-$T_2G_{15}T_2$-3'-*d* (6818.8 g/mol) and strand $\mathbf{D_{5'G}}$ is *d*-5'-$T_2G_{15}T_2$-3' (6818.7 g/mol). All masses were the reported values from the supplier Chemgenes, as confirmed by ESI-MS. The donor emission and acceptor absorbance spectra correspond to a R_0 = 5.2 nm Förster radius, assuming randomized dye orientations. The dye spectra used to calculate R_0 are plotted in Figure C.1. We measured these spectra in 10 mM NH_4OAc pH = 7 for strands $\mathbf{A_{3'C}}$ at 1.7 μM and $\mathbf{D_{5'C}}$ at 1.6 μM. To calculate R_0 we used the equation:[217–219]

$$R_0^6 = \frac{9\ln(10)\phi_{\mathrm{D}}\kappa^2\left(\int f_D(\lambda)\varepsilon_A(\lambda)\lambda^4 d\lambda\right)}{128\pi^5 n^4 N_A} \qquad (\mathrm{Eq. C. 1})$$

Here ϕ_{D} is the donor dye's fluorescence quantum yield (0.92 for *d*), κ^2 is the relative dipole orientation factor between the donor and acceptor dye (here we assume 0.66, corresponding to random orientation), *n* is the medium's refractive index (1.33 for water), N_A is Avagadro's number, and $\int f_D(\lambda)\varepsilon_A(\lambda)\lambda^4 d\lambda$ is the spectral overlap integral. In this integral, f_D is the donor's emission spectrum normalized to an area of 1, and ε_A is the acceptor's molar extinction coefficient spectrum.

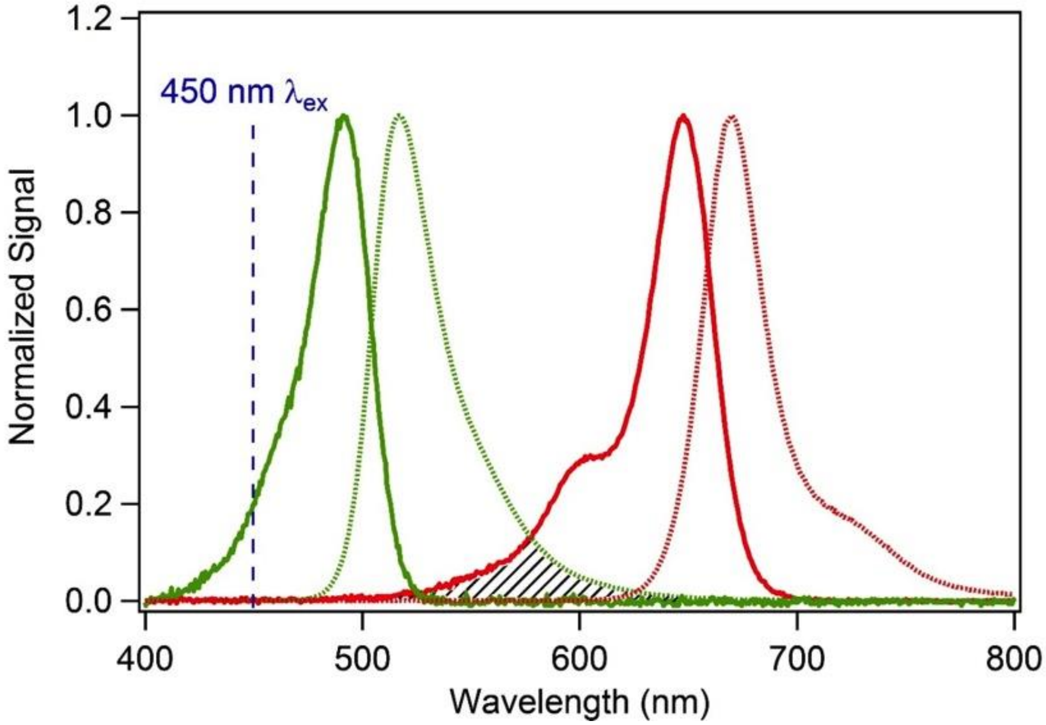

Figure C.1) Experimental absorbance (solid curves) and emission (dashed curves) spectra for donor dye Alexa 488 "*d*" (green curves) and acceptor dye Alexa 647 "*a*" (red curves) used in this study. Emission was excited at the visible absorbance peak. The 450 nm excitation wavelength used for all FRET experiments (blue dashed line) negligibly excites the acceptor. The spectral overlap of the normalized emission spectrum of the donor and the normalized absorbance spectrum of the acceptor is represented by solid black slashed lines.

C.1.2) Purification and mass spectral characterization

We used HPLC to isolate the Ag$^+$-paired **A$_{3'C}$-D$_{3'C}$** and **D$_{5'C}$-A$_{3'C}$** from the mixture of A-A, D-D and A-D products formed by Ag$^+$-mediated assembly. Figure C.2 shows the HPLC absorbance and emission chromatograms for the prepared solutions. Figure C.3 shows the corresponding mass spectra for the purified products. We identify the A-D products using uv excitation and monitoring for simultaneous emission from *d* and *a*. (Figure C.2) The data for **A$_{3'C}$-D$_{3'C}$**, which is the high FRET Ag$^+$-paired duplex in Figure 4.1 of Chapter 4, exhibits one HPLC peak with emission from both *d* and *a* (Figure C.2 a). The unresolved substructure of this "bumpy" peak indicates that it contains a mixture of silver-paired **A$_{3'C}$-D$_{3'C}$** with slightly different conformations. The dominant product detected in MS of this eluent peak contains 19

Ag^+ (Figure C.3a). In addition, the MS for $\mathbf{A_{3'C}\text{-}D_{3'C}}$ contains lower abundance peaks with the same silver content, but missing one T base from the $\mathbf{D_{5'C}}$ strand, consistent with the manufacturer's purity report. The missing T base is likely responsible for part of the HPLC peak substructure, and structural perturbation due to the donor dye may contribute the additional substructure (Figure C.2a,b). We estimate that the presence of $\mathbf{D_{3'C}}$ strands containing such single T base deletions does not significantly affect the measured FRET efficiencies due to the large separations of the donor and acceptor which is supported by the consistent ratio of acceptor to donor dye emission across the entire peak structure in Figure C.2b. For $\mathbf{D_{5'C}\text{-}A_{3'C}}$, which is the low FRET Ag^+-paired duplex in Figure 4.1 of Chapter 4, the dominant product detected in MS contains 18 Ag^+ (Figure C.3b). We find an additional peak in the HPLC chromatogram (Figure C.2c,d) which is the same $\mathbf{D_{5'C}\text{-}A_{3'C}}$ product with 18 Ag^+ (Figure C.3c for ESI-MS) which we name $\mathbf{(D_{5'C}\text{-}A_{3'C})_y}$. $\mathbf{(D_{5'C}\text{-}A_{3'C})_y}$ also has an impurity product of $\mathbf{D_{5'C}\text{-}D_{5'C}}$ in the ESI-MS which would contribute to FRET background signal from the donor dye excitation and makes accurate FRET estimation difficult. However, since the ratio in donor and acceptor intensities from the HPLC chromatogram are close both for the $\mathbf{D_{5'C}\text{-}A_{3'C}}$ and $\mathbf{(D_{5'C}\text{-}A_{3'C})_y}$ peaks (Figure C.2d) we believe the structures to be very similar. Furthermore, since the peaks in the HPLC chromatograms which only have emission from the acceptor dyes in Figure C.2 are always singular, while the peaks with only emission from the donor dyes have 2-4 peaks we believe the two separate peaks for $\mathbf{D_{5'C}\text{-}A_{3'C}}$ and $\mathbf{(D_{5'C}\text{-}A_{3'C})_y}$ are likely due to structural perturbations caused by the donor dye possibly due to intercalation or some other mechanism. We do not believe we are missing any products exhibiting FRET due to masking of donor emission since the single-stranded thymine base extensions give sufficient length that a FRET efficiency near unity is unlikely.

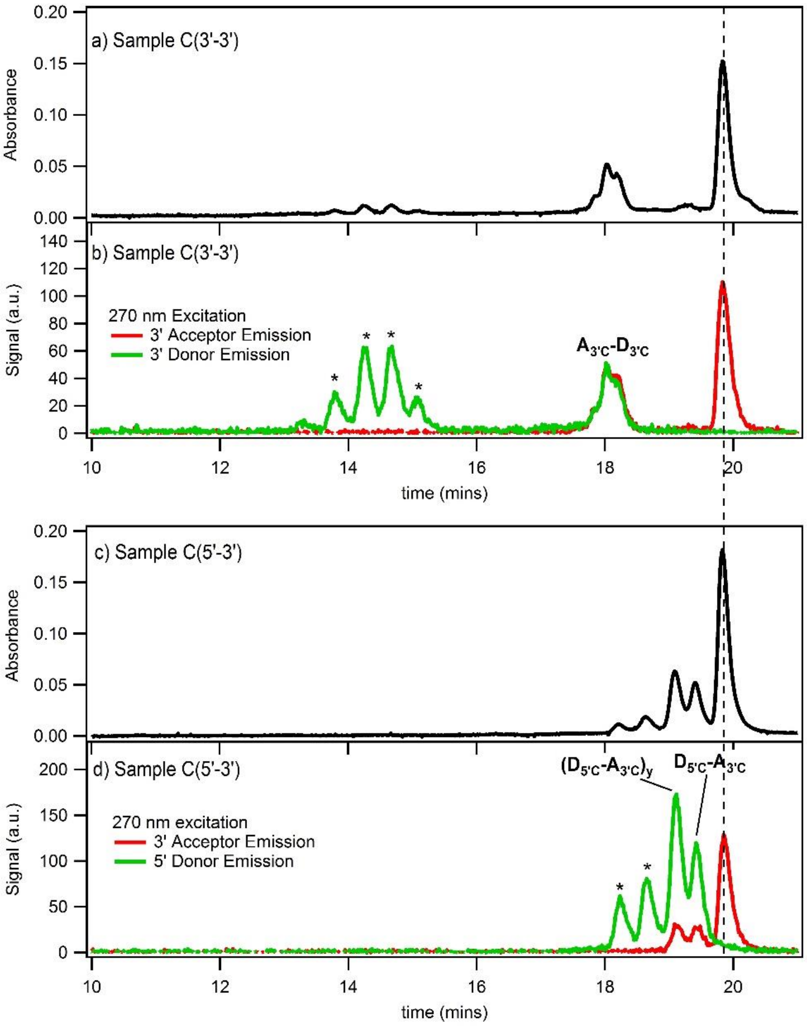

Figure C.2) HPLC chromatograms for sample C(3'-3') (solutions containing strands $A_{3'C}$ and $D_{3'C}$ with Ag^+) for a) absorbance and b) emission. HPLC chromatograms for sample C(5'-3') (solutions containing strands $A_{3'C}$ and $D_{5'C}$ with Ag^+) for c) absorbance and d) emission. We used 270 nm excitation to simultaneously excite both the donor (green curves, b and d) and acceptor (red curves, b and d) dyes. Peaks where there is signal for both the donor and acceptor dyes in the emission chromatograms in b) and d) are products which contain both the acceptor and donor dye-labelled strands. The peaks marked by black, dashed lines are the product which contains only acceptor dyes, likely a Ag^+-paired $A_{3'C}$-$A_{3'C}$. Peaks marked by "*" are products which contain only a donor dye, likely a Ag^+-paired $D_{3'C}$-$D_{3'C}$ or $D_{5'C}$-$D_{5'C}$. It is interesting to note there is only one peak for the Ag^+-paired $A_{3'C}$-$A_{3'C}$ product while the Ag^+-paired $D_{3'C}$-$D_{3'C}$ and $D_{5'C}$-$D_{5'C}$ products each have multiple peaks associated with them. It seems likely that the donor dye, A488, is causing minor structural perturbations resulting in the coexistence of similar conformations. The $A_{3'C}$-$D_{3'C}$ peak in b) with concurrent acceptor and donor dye emission appears to be convoluted with smaller peaks. However, the ratio of acceptor to donor dye emission remains constant across the entire peak structure suggesting these represent very minor structural variations. The additional peak structure is likely related to a combination of the missing thymine nucleotides from the corresponding mass spectra (Figure C.3a) and donor dye structural perturbations. For solutions of $A_{3'C}$ and $D_{5'C}$ with Ag^+ in d) there are two observable peaks with concurrent donor and emission and the ratio of acceptor to donor dye emission remains very similar. The peak on the right is the Ag^+-paired $D_{5'C}$-$A_{3'C}$ product referred to in the main text, while the peak on the left (labelled $(D_{5'C}$-$A_{3'C})_y$) was difficult to separate and had a non-negligible amount of Ag^+-paired $D_{5'C}$-$D_{5'C}$ which convolutes FRET analysis. The ratios between emission and donor dye appear very similar in the chromatogram and we believe these minor conformational changes to be attributed to the inclusion of the donor dye.

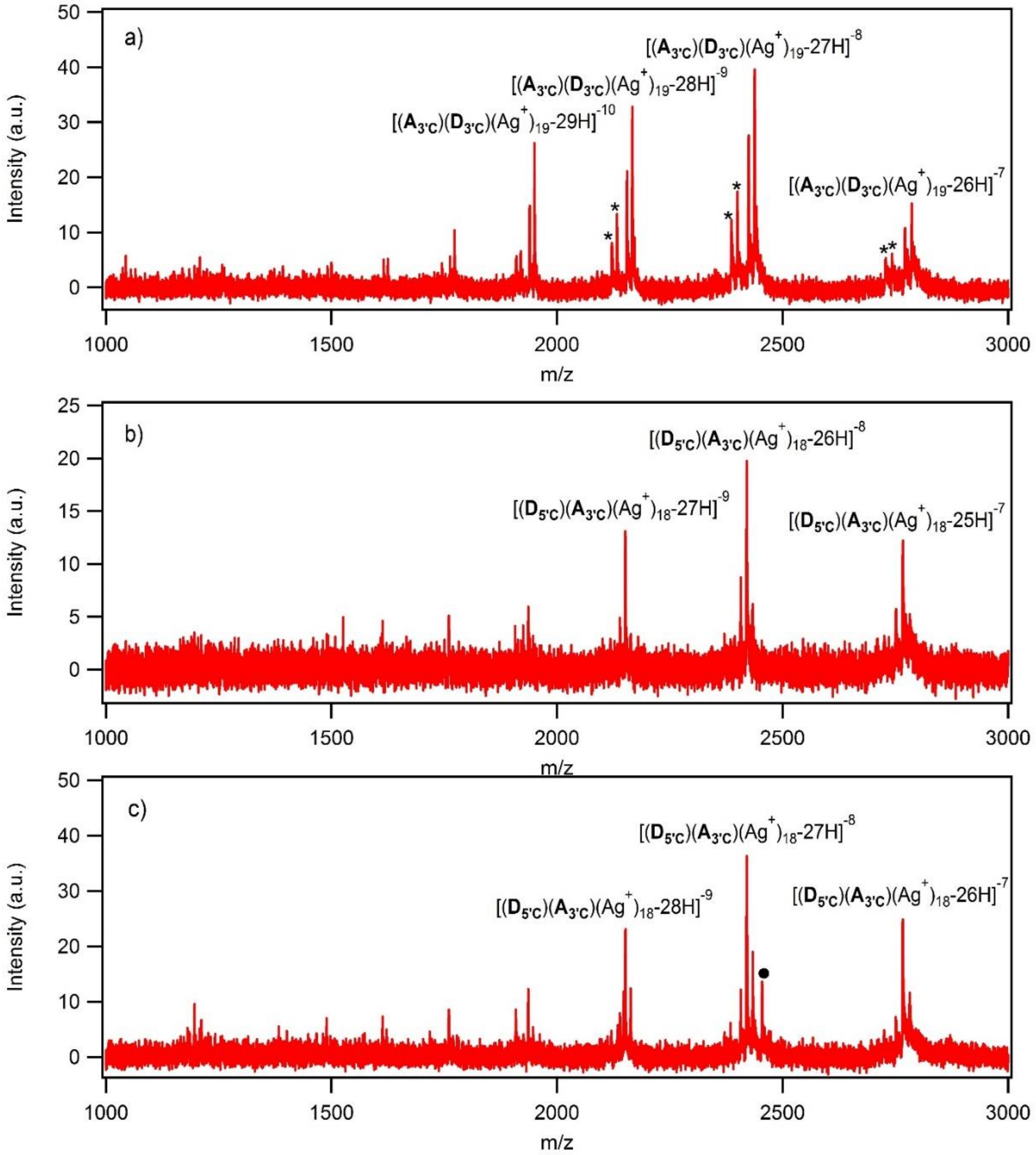

Figure C.3) Mass spectra of the HPLC-isolated duplex solutions of a) **A**$_{3'C}$-**D**$_{3'C}$ and b) **D**$_{5'C}$-**A**$_{3'C}$ and c) (**D**$_{5'C}$-**A**$_{3'C}$)$_y$. The dominant product in (a) consists of a 19 Ag$^+$ **A**$_{3'C}$-**D**$_{3'C}$ (product [(**A**$_{3'C}$)(**D**$_{3'C}$)(Ag$^+$)$_{19}$-26H]$^{-8}$ is at 2438.01 m/z). The lower abundance peak immediately to the left of the dominant product peak is the 18 Ag$^+$ **A**$_{3'C}$-**D**$_{3'C}$. We also note the existence of 18 and 19 Ag$^+$ **A**$_{3'C}$-**D**$_{3'C}$ that are likely missing one 304.5 g/mol thymine nucleotide (peaks denoted by *), which was expected based on the manufacturer's purity estimate; and a reported, unresolvable impurity from the manufacturer for strand **D**$_{3'C}$. The dominant product in (b) consists of a 18 Ag$^+$ **D**$_{5'C}$-**A**$_{3'C}$ (product [(**D**$_{5'C}$)(**A**$_{3'C}$)](Ag$^+$)$_{18}$-27H]$^{-8}$ is at 2420.70 m/z). The dominant product in c) is a Ag$^+$-paired **D**$_{5'C}$-**A**$_{3'C}$ with 18 Ag$^+$ (product [(**D**$_{5'C}$)(**A**$_{3'C}$)](Ag$^+$)$_{18}$-27H]$^{-8}$ is at 2420.72 m/z). We also find an impurity product of an Ag$^+$-paired **D**$_{5'C}$-**D**$_{5'C}$ with 18 Ag$^+$ at 2454.89 m/z (marked with a closed circle). Minor products correspond to **D**$_{5'C}$-**A**$_{3'C}$ Ag$^+$-paired strands with 18 Ag$^+$. No other products are detected at significant abundance for **A**$_{3'C}$-**D**$_{3'C}$ or **D**$_{5'C}$-**A**$_{3'C}$. Thus the number of strands without dye molecule labels appears to be negligible.

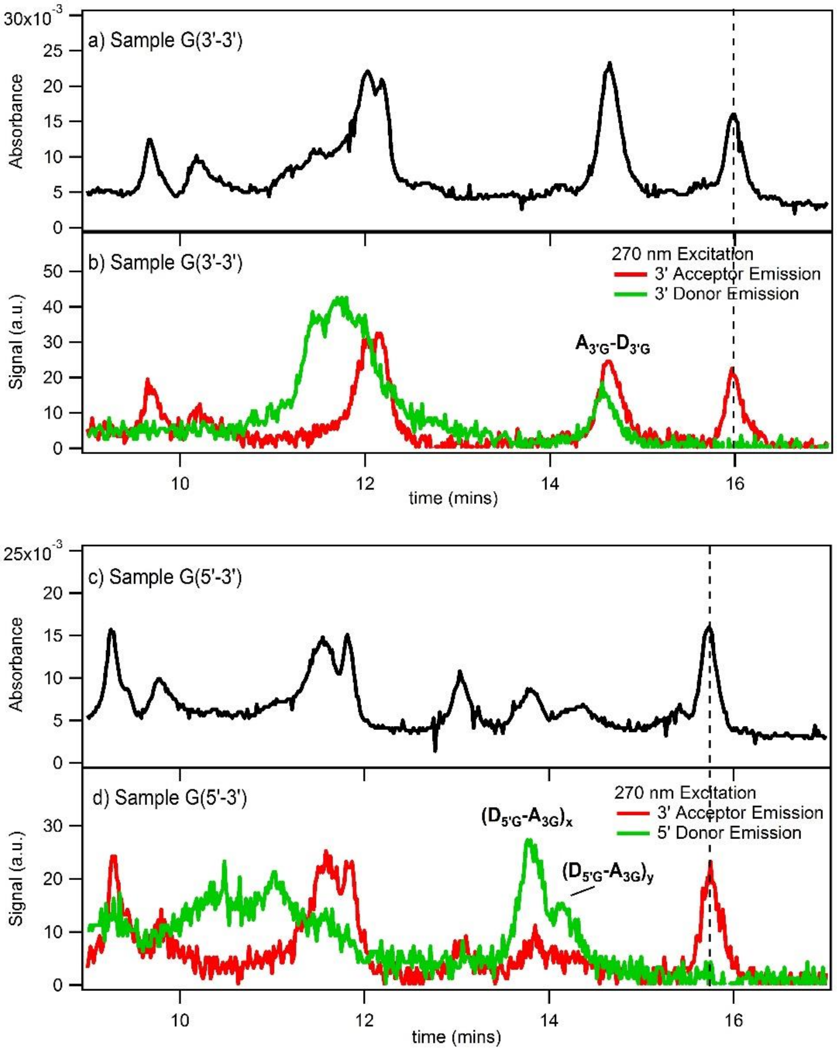

Figure C.4) HPLC chromatograms for sample G(3'-3') (solutions containing strands $A_{3'G}$ and $D_{3'G}$ with Ag^+) for a) absorbance and b) emission as well as for sample G(5'-3') (solutions containing strands $A_{3'G}$ and $D_{5'G}$ with Ag^+) for c) absorbance and d) emission. We used 270 nm excitation to simultaneously excite both the donor (green curves, b and d) and acceptor (red curves, b and d) dyes. Due to the fairly heterogeneous solutions containing both strand dimers and monomers with Ag^+ there are many places where both the donor and acceptor emission overlap. However, many of the overlapping signals are not similar in shape and were likely Ag^+ paired $A_{3'G}$-$A_{3'G}$ (black dashed line, which matches closely to the expected retention time as determined from Figure C.6), $D_{3'G}$-$D_{3'G}$, $D_{5'G}$-$D_{5'G}$, or monomeric strands with Ag^+. Additionally many of the peak patterns for acceptor emission in b) are reproduced in d) with slightly lower retention times except for the labelled Ag^+-paired products. Peaks where there is signal for both the donor and acceptor dyes and good overlap in the emission chromatograms in b) and d) are Ag^+-paired products which contain both the acceptor and donor dye as confirmed with ESI-MS (see Figure C.5b-d for mass spectra).

As described in the main text the guanine Ag^+-paired strands required a modified procedure to achieve Ag^+-paired strands with both a donor and acceptor dye. In order to achieve high yields of Ag$^+$-paired $\mathbf{A_{3'G}}$**-**$\mathbf{D_{3'G}}$ and $\mathbf{D_{5'G}}$**-**$\mathbf{A_{3'G}}$, we HPLC purified strand $\mathbf{A_{3'G}}$ a second time (the first HPLC purification was performed by the supplier). Due to the problems with aggregation for the bare $\mathrm{A_{3'G}}$ strand, we added Ag$^+$ to form unaggregated, Ag$^+$-paired $\mathbf{A_{3'G}}$**-**$\mathbf{A_{3'G}}$ (see Figure C.6a,b for HPLC chromatograms) which we were able to isolate from the Ag$^+$-paired, shorter strands (which terminated early during manufacturer's synthesis) and verify with ESI-MS (Figure C.5a). During the HPLC runs for a solution containing strands $\mathbf{A_{3'G}}$ and $\mathbf{D_{3'G}}$ with Ag$^+$ we found one product peak containing both the acceptor and donor dye, product $\mathbf{A_{3'G}}$**-**$\mathbf{D_{3'G}}$, while for a solution of $\mathbf{A_{3'G}}$ and $\mathbf{D_{5'G}}$ with Ag$^+$ we found two peaks corresponding to products with both an acceptor and donor dye, $\mathbf{(D_{5'G}\text{-}A_{3'G})_1}$ is the faster eluting product and $\mathbf{(D_{5'G}\text{-}A_{3'G})_2}$ is the slower. The products were analyzed with ESI-MS and $\mathbf{A_{3'G}}$**-**$\mathbf{D_{3'G}}$ was found to contain a dominant product with 1 $\mathbf{A_{3'G}}$ strand, 1 $\mathbf{D_{3'G}}$ strand and 15 Ag$^+$ as well as a similar product with a missing donor dye (Figure C.5b). $\mathbf{(D_{5'G}\text{-}A_{3'G})_1}$ had a dominant product with 1 $\mathbf{A_{3'G}}$ strand, 1 $\mathbf{D_{5'G}}$ strand and 15 Ag$^+$ (Figure C.5c). While $\mathbf{(D_{5'G}\text{-}A_{3'G})_1}$ had a dominant product with 1 $\mathbf{A_{3'G}}$ strand, 1 $\mathbf{D_{5'G}}$ strand and 15 Ag$^+$ as well as a similar product with a donor dye missing (Figure C.5d).

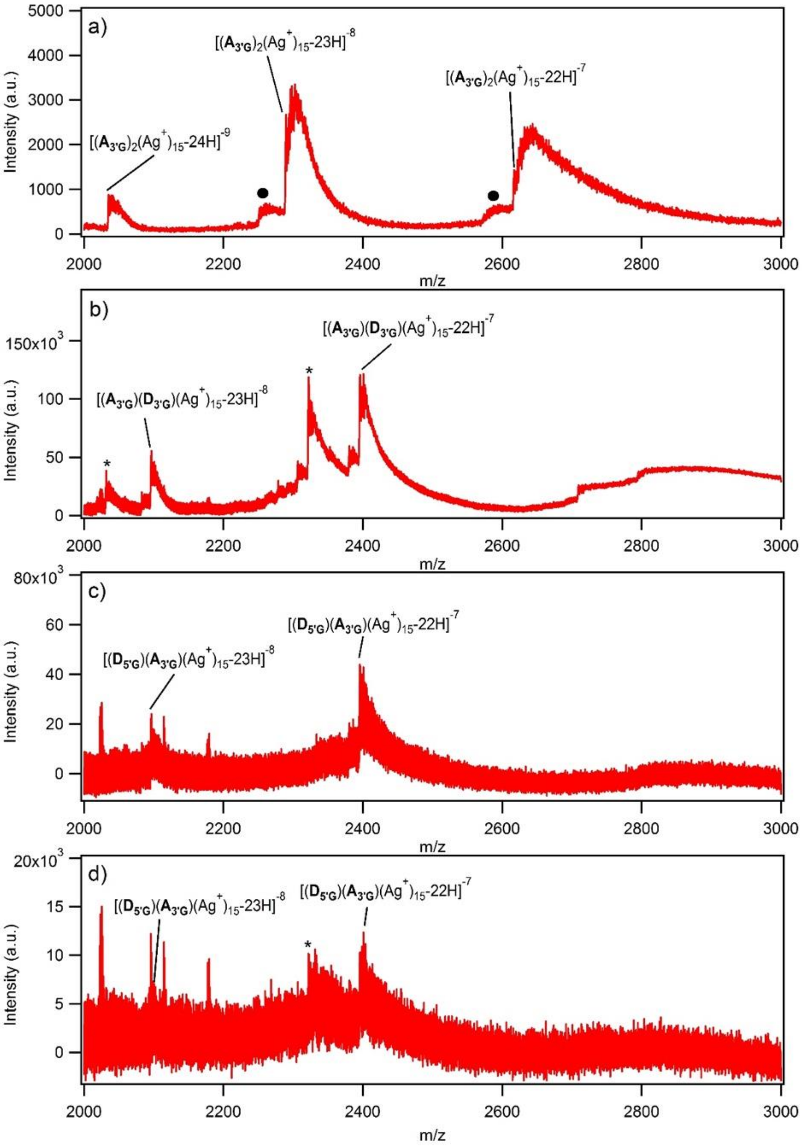

Figure C.5) Mass spectra of HPLC isolated solutions of a) $A_{3'G}$-$A_{3'G}$, b) $A_{3'G}$-$D_{3'G}$, c) $(D_{5'G}$-$A_{3'G})_1$ and d) $(D_{5'G}$-$A_{3'G})_2$. The dominant product in (a) consists of a 15 Ag^+ $A_{3'G}$-$A_{3'G}$ duplex ($[(A_{3'G})_2(Ag^+)_{15}\text{-}23H]^{-8}$ is at 2289.80 m/z with a trail salt peaks at higher m/z). Impurity products are marked by black circles in (a). These impurity products are the same composition as the 15 Ag^+ $A_{3'G}$-$A_{3'G}$ product but are missing one thymine nucleotide, 304.0 g/mol, and are in much lower quantities (the charge state -8 impurity product is at 2251.80 m/z). One of the dominant products in (b) consists of a 15 Ag^+ $A_{3'G}$-$D_{3'G}$ duplex ($[(A_{3'G})(D_{3'G})(Ag^+)_{15}\text{-}22H]^{-7}$ is at 2396.14 m/z with a trail salt peaks at higher m/z and a much lower intensity 14 Ag^+ product can be found immediately to the left at 2380.83 m/z). Peaks marked with a "*" in (b) represent products missing 516.32 g/mol from the expected 15 Ag^+ $A_{3'G}$-$D_{3'G}$ duplex product (dominant "*" product peak is charge state -7 at 2322.38 m/z). 516.32 g/mol is approximately the same mass as the donor dye Alexa 488, which may have come off during the ESI process. Since the 450 nm excitation wavelength used in the FRET experiments does not excite the acceptor dye, these Ag^+-paired strands missing a donor dye should not impact the FRET results. The dominant product in (c) consists of a 15 Ag^+ $(D_{5'G}$-$A_{3'G})_1$ product ($[(D_{5'G})(A_{3'G})(Ag^+)_{15}\text{-}22H]^{-7}$ is at 2396.11 m/z). The dominant product in (d) consists of a 15 Ag^+ $(D_{5'G}$-$A_{3'G})_2$ product ($[(D_{5'G})(A_{3'G})(Ag^+)_{15}\text{-}22H]^{-7}$ is at 2396.12 m/z). Peaks marked with a "*" in (d) represent products missing 516.53 g/mol from the expected 15 Ag^+ $(D_{5'G}$-$A_{3'G})_2$ duplex product (dominant "*" product peak is charge state -7 at 2322.33 m/z) which is likely a missing Alexa 488 dye. Additional peaks in c) and d) are chemical background noise.

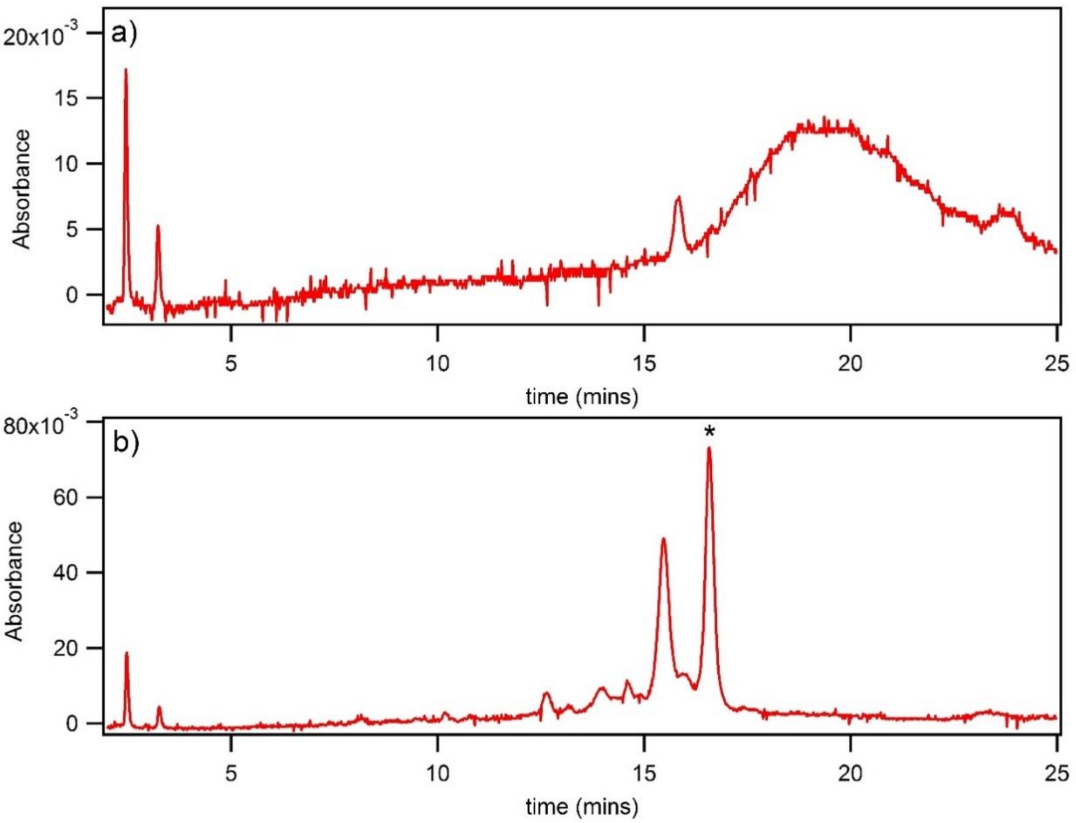

Figure C.6) HPLC absorbance chromatograms monitored at 260 nm for strand $A_{3'G}$ at 2.5 µM with a) 10 mM NH_4OAc and b) 50 mM NH_4OAc and 37.5 µM $AgNO_3$. The broad and relatively featureless chromatogram in a) with no added $AgNO_3$ suggests aggregation. Conversely, by adding $AgNO_3$ as in b) well defined peaks a ppear (the peak denoted with a "*" was identified as a Ag^+-paired $A_{3'G}$-$A_{3'G}$, see above in Figure C.5a). Apparently, adding $AgNO_3$ breaks up the bare aggregated guanine strands to form unaggregated Ag^+-paired guanine strands.

C.1.3) FRET efficiency calculation and spectral normalization

We estimate FRET efficiencies using the ratiometric method. This method uses the ratio of emission intensities from the donor and acceptor dye channels for each sample. Mathematically this is represented as:

$$E = \frac{1}{(\frac{\phi_A I_D}{\phi_A I_D}+1)} \qquad \text{Eq. C. 2}$$

Where E is the FRET efficiency, ϕ_A and ϕ_D are the acceptor and donor dye quantum yields respectively and I_A and I_D are the acceptor and donor dye integrated emission intensities respectively. We use the standard quantum yield values of 0.92 for the donor dye, Alexa 488, and 0.33 for the acceptor dye, Alexa 647. We then normalize the sample emission spectra by their relative FRET efficiencies.

C.2) IMS-MS Experiments

C.2.1) Tabular CCS values

Product	Charge State (Z)	CCS (Å^2)
$((CG)_4)_2$	-3	505
$((CG)_4)_2$	-4	528
$((CG)_4)_2$	-5	586
$((CG)_5)_2$	-4	625
$((CG)_5)_2$	-5	646
$((CG)_6)_2$	-4	705.4
$((CG)_6)_2$	-5	725.3
$((CG)_6)_2$	-6	793.1
$((CG)_7)_2$	-5	822
$((CG)_7)_2$	-6	860
$((CG)_7)_2$	-7	990
$((CG)_9)_2$	-5	1014
$((CG)_9)_2$	-6	1036
$((CG)_9)_2$	-7	1076
$((CG)_9)_2$	-8	1193.6
$((CG)_{11})_2$	-6	1077.2
$((CG)_{11})_2$	-7	1101
$((CG)_{11})_2$	-8	1296
$((CG)_{11})_2$	-9	1432.6
$((CG)_{13})_2$	-6	1221.8
$((CG)_{13})_2$	-7	1230.2
$((CG)_{13})_2$	-8	1254.3
$((CG)_{13})_2$	-9	1287
$((CG)_{13})_2$	-9	1560
$((CG)_{15})_2$	-7	1357
$((CG)_{15})_2$	-8	1372
$((CG)_{15})_2$	-9	1420.9

Table C.1) Tabular CCS values for WC-paired ($((CG_N)_2)$) duplexes.

Product	Charge State (Z)	CCS (Å^2)
$(TG_5T)_4(NH_4)_4$	-4	763
$(TG_5T)_4(NH_4)_4$	-5	811
$(TG_5T)_4(NH_4)_4$	-6	842
$(TG_5T)_4(NH_4)_4$	-7	867
$(TG_5T)_4(NH_4)_4$	-7	888
$(TG_8T)_4(NH_4)_7$	-5	979
$(TG_8T)_4(NH_4)_7$	-6	982
$(TG_8T)_4(NH_4)_7$	-6	1046
$(TG_8T)_4(NH_4)_7$	-7	1023
$(TG_8T)_4(NH_4)_7$	-7	1134
$(TG_8T)_4(NH_4)_7$	-8	1076
$(TG_8T)_4(NH_4)_7$	-8	1128

Table C.2) Tabular CCS values for $(TG_NT)_4$ G-quadruplexes.

Product	Charge State (Z)	CCS (Å^2)
$(C_6)_2(Ag^+)_6$	-3	411
$(C_6)_2(Ag^+)_6$	-4	430
$(C_{11})_2(Ag^+)_{11}$	-4	622
$(C_{11})_2(Ag^+)_{11}$	-5	642
$(C_{11})_2(Ag^+)_{11}$	-6	742
$(C_{11})_2(Ag^+)_{11}$	-7	795
$(C_{14})_2(Ag^+)_{14}$	-4	726
$(C_{14})_2(Ag^+)_{14}$	-5	749
$(C_{14})_2(Ag^+)_{14}$	-6	784
$(C_{14})_2(Ag^+)_{14}$	-7	880
$(C_{14})_2(Ag^+)_{14}$	-8	946
$(C_{17})_2(Ag^+)_{17}$	-5	819
$(C_{17})_2(Ag^+)_{17}$	-6	840
$(C_{17})_2(Ag^+)_{17}$	-7	932
$(C_{17})_2(Ag^+)_{17}$	-8	1002
$(C_{20})_2(Ag^+)_{20}$	-6	938
$(C_{20})_2(Ag^+)_{20}$	-7	969
$(C_{20})_2(Ag^+)_{20}$	-7	1070
$(C_{20})_2(Ag^+)_{20}$	-8	1116
$(C_{20})_2(Ag^+)_{20}$	-9	1176
$(C_{26})_2(Ag^+)_{26}$	-7	1113
$(C_{26})_2(Ag^+)_{26}$	-8	1207
$(C_{26})_2(Ag^+)_{26}$	-9	1355
$(C_{30})_2(Ag^+)_{30}$	-7	1174
$(C_{30})_2(Ag^+)_{30}$	-8	1214
$(C_{30})_2(Ag^+)_{30}$	-9	1460
$(C_{30})_2(Ag^+)_{30}$	-10	1512

Table C.3) Tabular CCS values for Ag^+-paired $(C_N)_2(Ag^+)_N$.

Product	Charge State (Z)	CCS (Å^2)
$(G_6)_2(Ag^+)_6$	-3	458
$(G_6)_2(Ag^+)_6$	-4	476
$(G_{11})_2(Ag^+)_{11}$	-4	728
$(G_{11})_2(Ag^+)_{11}$	-5	752
$(G_{11})_2(Ag^+)_{11}$	-6	773
$(G_{14})_2(Ag^+)_{14}$	-5	910
$(G_{14})_2(Ag^+)_{14}$	-6	932
$(G_{14})_2(Ag^+)_{14}$	-7	960
$(G_{14})_2(Ag^+)_{14}$	-8	994
$(G_{17})_2(Ag^+)_{14}$	-6	1081
$(G_{17})_2(Ag^+)_{14}$	-7	1111
$(G_{17})_2(Ag^+)_{14}$	-8	1139
$(G_{17})_2(Ag^+)_{14}$	-9	1185
$(G_{20})_2(Ag^+)_{14}$	-7	1255
$(G_{20})_2(Ag^+)_{14}$	-8	1284
$(G_{20})_2(Ag^+)_{14}$	-9	1328

Table C.4) Tabular CCS values for Ag^+-paired $(G_N)_2(Ag^+)_N$.

C.2.2) Representative mass spectra and CCS distributions

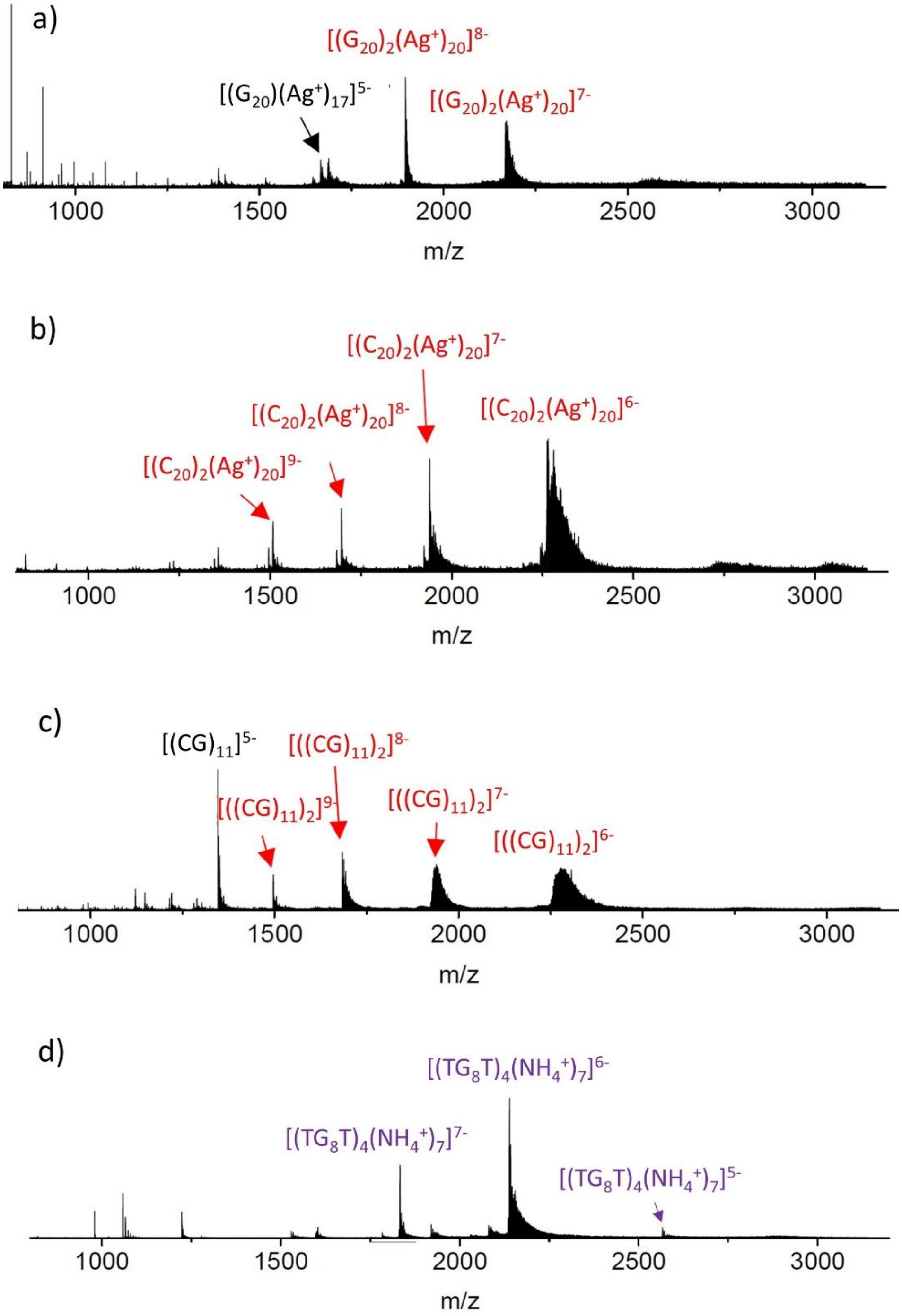

Figure C.7) Representative mass spectra for solutions containing the DNA species explored in the IMS-MS studies in Chapter 4. Solutions injected into the MS consisted of a) 80 µM strand G_{20} and 1.6 mM $AgNO_3$ in 50 mM NH_4OAc pH = 7, b) 80 µM strand C_{20} and 1.6 mM $AgNO_3$ in 50 mM NH_4OAc pH = 7, c) 10 µM strand $(CG)_{11}$ in 100 mM NH_4OAc pH = 7 and d) 80 µM strand TG_8T in 100 mM NH_4OAc pH = 7.

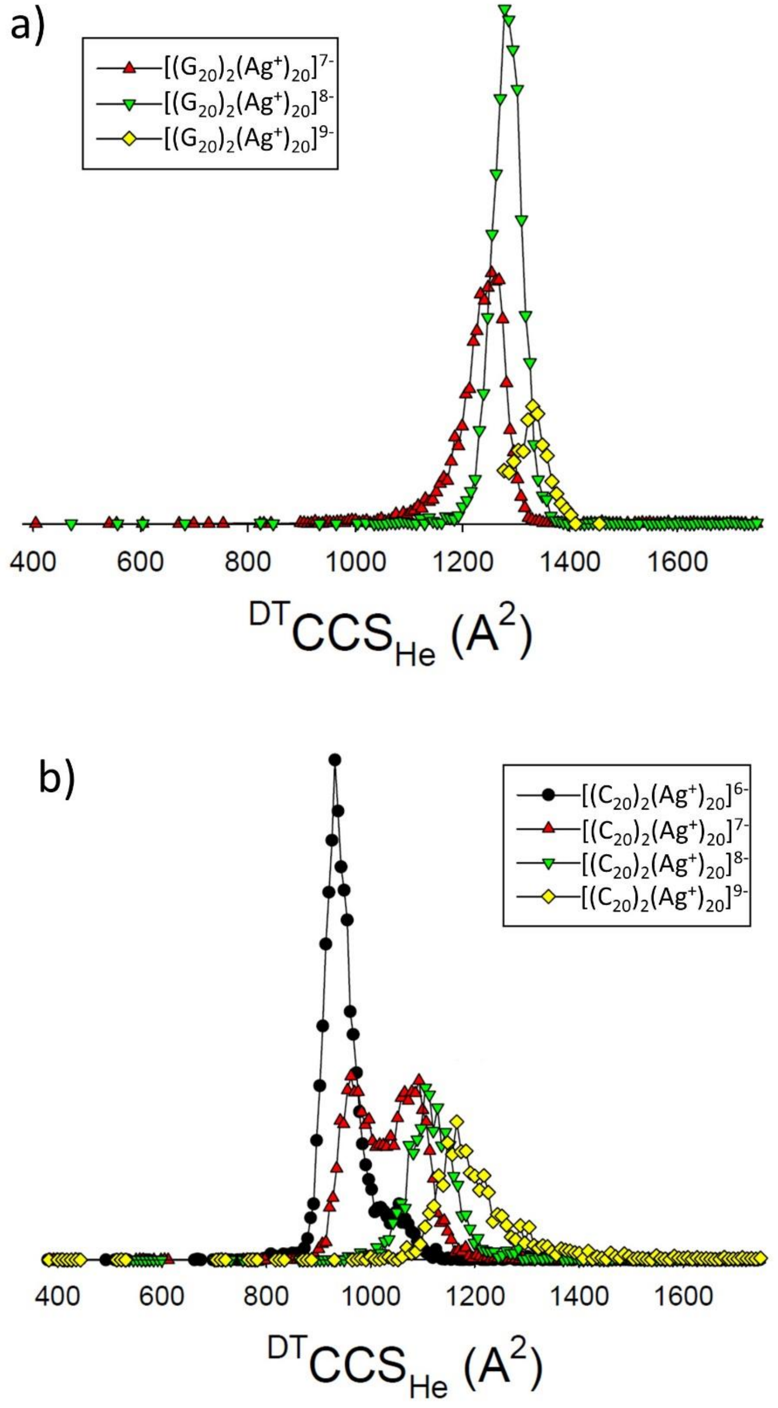

Figure C.8) Representative CCS distributions for various charge states of a) $(G_{20})_2(Ag^+)_{20}$ and b) $(C_{20})_2(Ag^+)_{20}$.

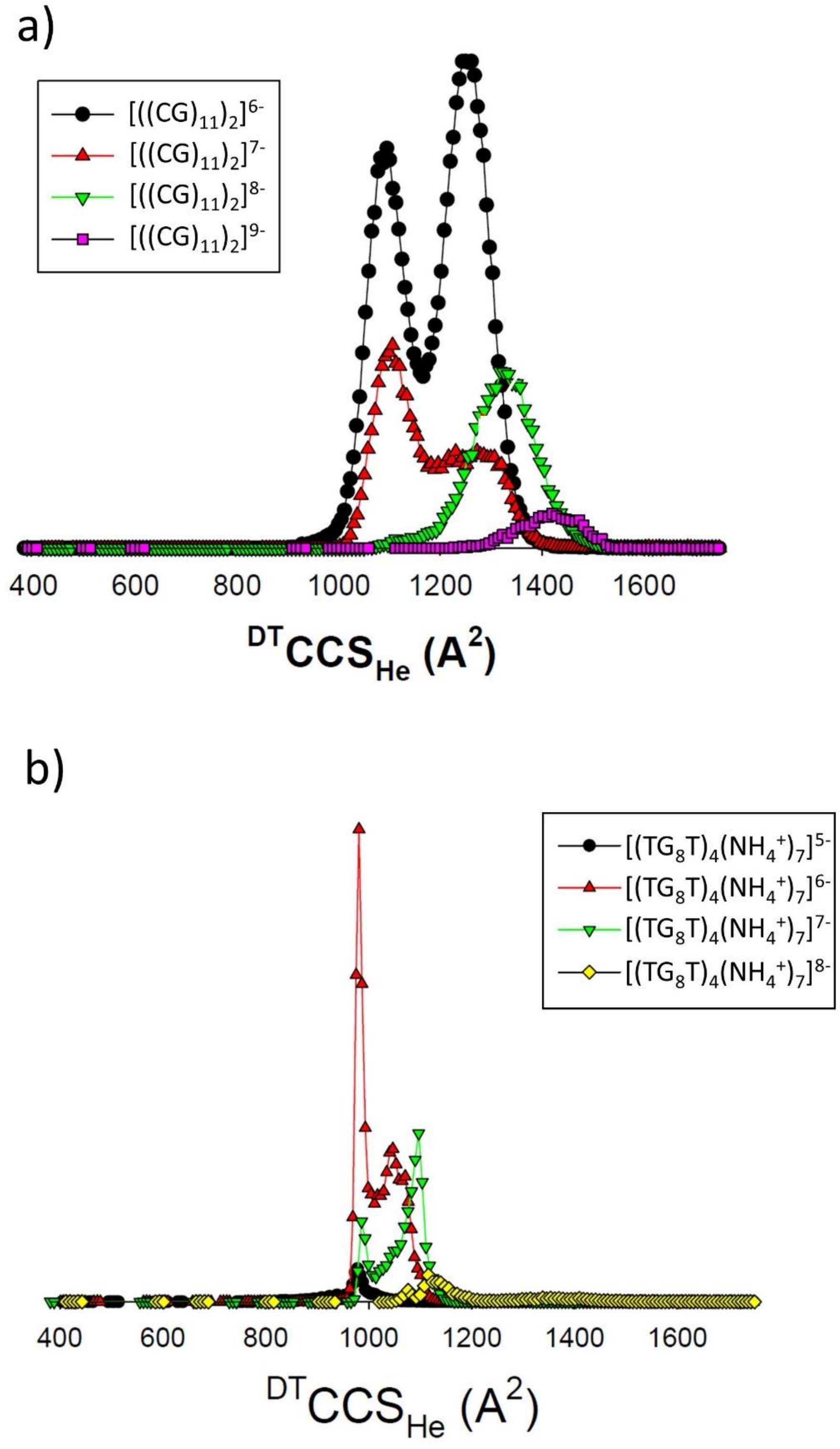

Figure C.9) Representative CCS distributions for various charge states of a) $(CG_{11})_2$ and b) $(TG_8T)_4(NH_4^+)_7$.

C.2.3) CD spectra for G-quadruplexes used in IMS

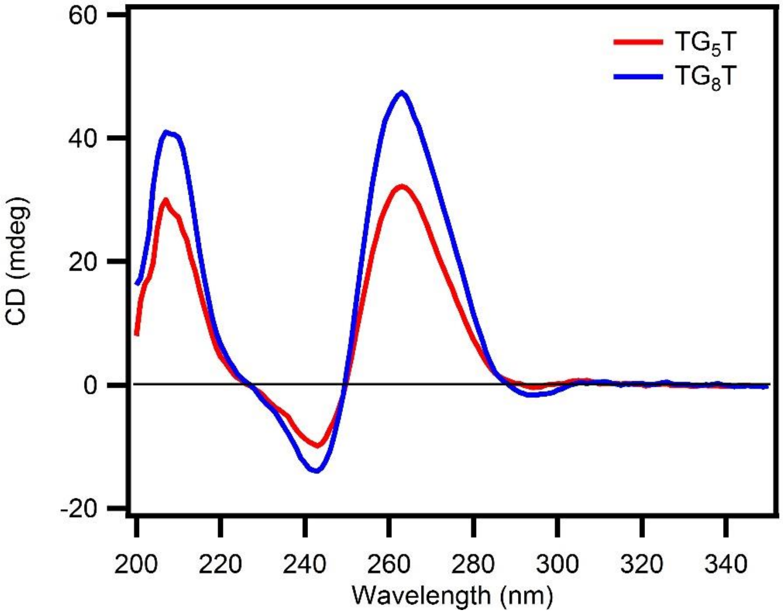

Figure C.10) CD spectra for solutions of 80 μM DNA in 100 mM NH_4OAc pH = 7. The spectral signature is as expected for a parallel four-stranded G-quadruplex.[187]

Appendix D) Supporting Information for Chapter 5

D.1) Ag_N-DNA Synthesis

Sample	DNA (μM)	Buffer (mM)	$AgNO_3$ (μM)	$NaBH_4$ (μM)	T (ºC)	Time Incubated (hrs)	HPLC Gradient (%MeOH)
S1	20	7.5	250	125	4	24	5-22
S2	5	7.5	75	38	4	24	12-27
S3	15	7.5	188	94	40	4	5-20
S4	15	7.5	188	94	4	24	25-40

Table D.1) Synthesis and Purification Parameters for Ag_N-DNA. This table contains the optimized synthesis and purification conditions for each Ag_N-DNA used in the Circular Dichroism (CD) experiments. The buffer was ammonium acetate (pH ~7). The samples were incubated at the temperature and length of time specified for each sample. The solutions were refrigerated at 4ºC after incubation for no longer than two days before being HPLC purified with the gradient specified for each sample.

The templates used in this work are listed in Chapter 5 in Table 5.1 and reproduced here for convenience:

S1 = CCCACCCACCCGCCCA

S2 = GGCAGGTTGGGGTGACTAAAAACCCTTAATCCCC

S3 = CACCGCTTTTGCCTTTTGGGGACGGATA

S4 = TGCCTTTTGGGGACGGATA

We note that monomeric templates S2-S4 lack the special G-rich or C-rich motifs required to form G-quadruplex or i-motif structures, as confirmed by the bare strand CD spectra. S1 is C-rich but again the bare CD spectra lack characteristic i-motif features.[92]

D.2) Sample Purity Estimates

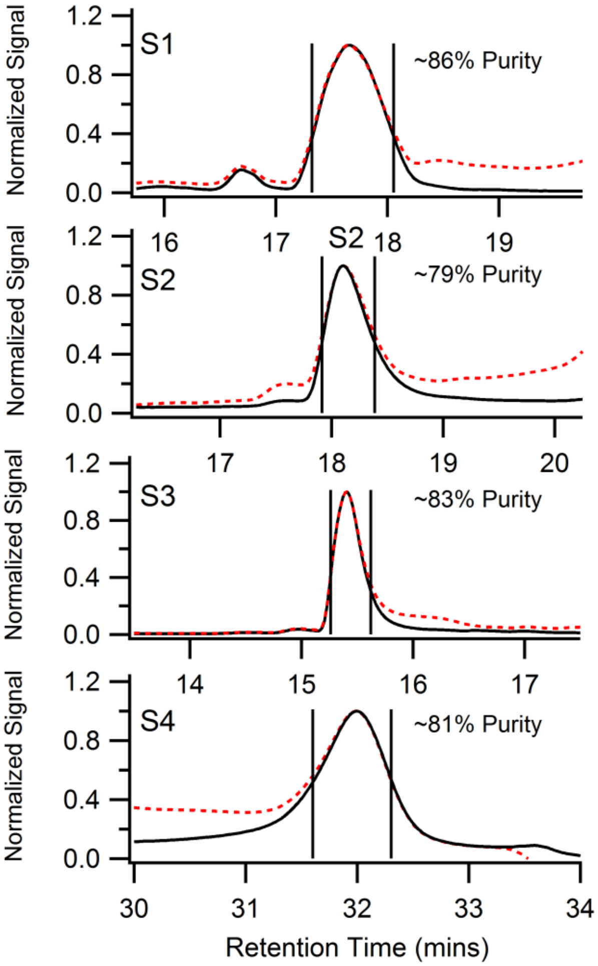

Figure D.1) Purity estimates based on the overlaid 4.77 eV (260 nm) (dashed red) chromatograms, which peak when any DNA-containing species elutes from the column, and the chromatograms measured at the peak visible absorbance energy specific to each sample (solid black; detection at 1.74 eV, 2.06 eV, 2.07 eV and 2.55 eV for samples S1-S4, respectively). Black bars represent the time span for collection of the purified samples.

Figure D.1 shows the absorbance chromatograms measured during HPLC. The conditions used, as specified in Chapter 5 (Materials and Methods), produced good separation of the fluorescent Ag_N-DNA from other silver-DNA products that formed during synthesis. The absorbance at 4.77 eV (260 nm) (red trace, Figure A.1) peaks at times corresponding to elution of any DNA-containing product from the column. Typically many distinct silver-bearing DNA products elute during the 30-60 minute HPLC separation. The times in Figure A.1 cover a narrow span centered on elution of the fluorescent Ag_N-DNA.

Comparison of the absorbance chromatogram measured at the peak visible excitation wavelength of the fluorescent Ag_N-DNA (black trace, Figure A.1) to the 4.77 eV (260 nm) absorbance chromatogram provides an estimate of ~80% purity for the samples used in CD measurements.

D.3) Quantum Chemical Calculations

Optical absorption and CD spectra of the neutral helix Ag_6 nanoparticle were calculated by TDDFT methods, as discussed in the main text. Three "gently curved" structures S(170), S(160) and S(150) with helical angles 170º, 160º and 150º were considered. Table A.2 shows the calculated peak energies, molar ellipticity, rotatory strength and oscillator strength of the lowest two CD peaks.

Structure	First peak				Second peak			
	E, eV	$[\Theta]^a$	R_m^b	f^c	E, eV	$[\Theta]^a$	R_m^b	f^c
S(170)	1.73	8501	17.3	1.46	2.84	-20245	-24.1	0.06
S(160)	1.72	31467	64.4	1.22	2.83	-78215	-94.9	0.24
S(150)	1.69	62280	129.3	0.96	2.82	-158837	-198.6	0.48

Table D.2) Calculated Parameters of the Two Lowest CD Peaks. ^{a} Molar ellipticity deg·cm^2·dmole^{-1}; ^{b} rotatory strength 10^{-40} esu^2 ·cm^2; ^{c} oscillator strength.

To examine the length dependence of the optical absorption and CD of these filamentary wires, TDDFT calculations have also been performed on Ag_n (n = 4, 6, 8, 10, 12) clusters with 170° Ag-Ag-Ag bond angles, 2.7 Å bond length, and a torsional (dihedral) Ag-Ag-Ag-Ag angle of 10°. As shown in Figure D.3A, absorption spectra for helical systems Ag_4, Ag_6, and Ag_8 show only one strong peak at 2.19, 1.73, and 1.44 eV, respectively, whereas longer systems exhibit two strong peaks (1.24 and 2.12 eV in the case of Ag_{10} and 1.09 and 1.89 eV for Ag_{12}). As the number of silver atoms in the chain increases, the excitation spectrum redshifts.

Circular dichroism spectra (Figure D.2) also become stronger and redshift as the particle size increases. The strongest spectrum is observed for Ag_{12} and the weakest for Ag_4. All systems exhibit a strong positive first peak. This peak arises from HOMO to LUMO orbital transition. The HOMO-LUMO gap is decreased in the order $Ag_4 > Ag_6 > Ag_8 > Ag_{10} > Ag_{12}$ and is equivalent to 1.01, 0.70, 0.54, 0.43, and 0.37 eV, respectively. The second dichroic peak has a negative sign. As discussed for Ag_6, this peak arises from the HOMO $\rightarrow$ LUMO+1 and HOMO-1 $\rightarrow$ LUMO transitions that are forbidden for perfectly linear wires. This second peak appears to be strong in the CD spectrum even if it is not noticeable in the optical absorption spectrum.

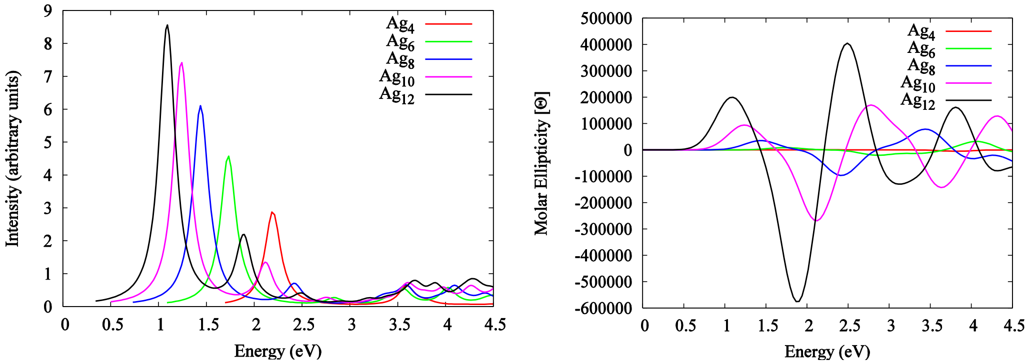

Figure D.2) TDDFT A) optical absorption and B) circular dichroism spectra for Ag_n (n = 4, 6, 8, 10, 12) with 170° Ag-Ag-Ag bond angles and 10° Ag-Ag-Ag-Ag torsional angles.

Structure	First peak				Second peak			
	E, eV	$[\Theta]^a$	R_m^b	f^c	E, eV	$[\Theta]^a$	R_m^b	f^c
Ag_4	2.19	617	0.9	0.91	3.80	-5289	-5.8	0.03
Ag_6	1.73	8501	17.3	1.46	2.84	-20245	-24.1	0.06
Ag_8	1.44	34733	84.3	1.88	2.40	-97043	-92.5	0.12
Ag_{10}	1.24	94106	257.5	2.23	2.12	-268957	-435.0	0.39
Ag_{12}	1.09	199489	588.2	2.39	1.89	-575845	-1073.7	0.64

Table D.3) Calculated Parameters of the Two Lowest CD Peaks for Silver Wires Ag_n (n = 4, 6, 8, 10, 12) with 170° Bond Angles and 10° Torsional Angles. ^{a} Molar ellipticity deg·cm^2·dmole^{-1}; ^{b} rotatory strength 10^{-40} esu^2 ·cm^2; ^{c} oscillator strength.

D.4) Pure *versus* Impure Spectra

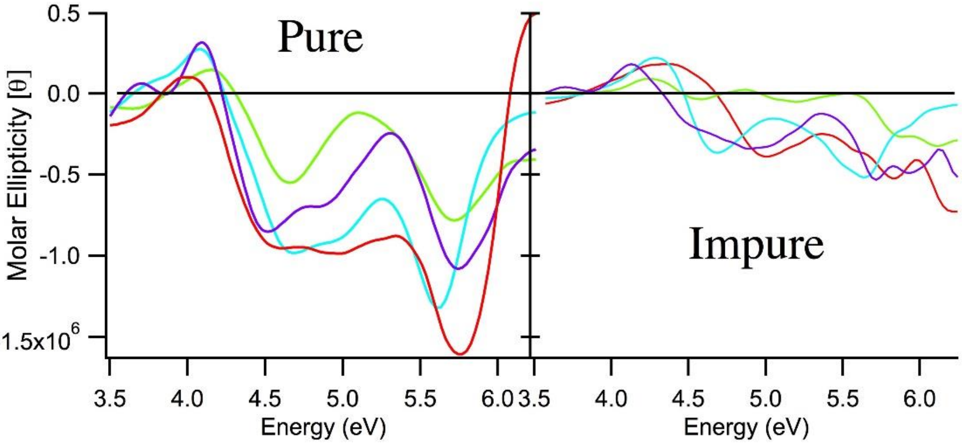

Figure D.3) UV CD spectra of purified (A) and unpurified (B) solutions of S1 (teal), S2 (red), S3 (purple) and S4 (green).

Figure D.3 compares the UV CD spectra of the pure Ag_N-DNA with the corresponding as-synthesized solutions, without purification. Spectra for the impure samples show additional unordered peaks with lower magnitudes compared to the characteristic peaks in the UV region of the pure samples. The reduced CD signal in the unpurified Ag_N-DNA solutions reflects averaging over many different forms of silver-bearing DNA. The fluorescent Ag_N-DNAs are typically synthesized in chemical yields of 2-10%.

D.5) Gaussian Fits to CD Spectra

The experimental CD spectra in Chapter 5 Figure 5.3 were each fit to the superposition of seven Gaussian peaks. This was the minimum number of individual peaks required for consistent fits across all spectra. The fits will not capture individual transitions in the data that are weak and/or closely spaced.

The red, dashed lines in Chapter 5 Figure 5.3 represent the overall fit: the superposition of all of the Gaussian peaks. The vertical, red bars in Chapter 5 Figure 5.3 represent the individual peak energies and magnitudes. Where successive individual peaks have opposite amplitudes, extrema in the overall fit need not coincide with the individual peak energies.

The blue, vertical lines are guides to the eye that identify the peak numbering scheme for peaks 2-7. Peak 1, the lowest energy peak, has no corresponding guideline. The table below gives the peak amplitudes, A, energies, E, and widths, σ_E, for each of the seven individual Gaussian components, where σ_E corresponds to the full width of the Gaussian at half maximum amplitude. Uncertainties are standard errors of the fits.

	S1			S2			S3			S4		
	A /10^5 (Mol. Ellip)	*E* (eV)	σ_E (eV)	*A* /10^5 (Mol. Ellip.)	*E* (eV)	σ_E (eV)	*A* /10^5 (Mol. Ellip.)	*E* (eV)	σ_E (eV)	*A* /10^5 (Mol. Ellip.)	*E* (eV)	σ_E (eV)
1	**1.56** ±0.02	1.762 ±0.001	0.103 ±0.001	**1.119** ±0.001	2.084 ±0.001	0.192 ±0.002	**3.36** ±0.02	2.0715 ±0.0006	0.1105 ± 0.0009	**0.835** ±0.006	2.5403 ±0.0008	0.143 ±0.002
2	**-1.21** ±0.05	3.16 ±0.02	0.27 ±0.02	**-1.12** ±0.03	3.19 ±0.03	0.23 ±0.01	**-3.53** ±0.03	2.975 ±0.002	0.173 ±0.003	**-1.165** ±0.007	3.288 ±0.002	0.249 ±0.003
3	**-1.0** ±0.1	3.423 ±0.007	0.16 ±0.01	**-1.8** ±0.1	3.55 ±0.02	0.26 ±0.01	**-3.24** ±0.03	3.32 ±0.02	0.188 ±0.01	**-0.77** ±0.01	3.681 ±0.003	0.169 ±0.004
4	**2.95** ±0.08	4.087 ±0.007	0.243 ±0.006	**6** ± 3	4.13 ±0.01	0.27 ±0.02	**3.48** ± 0.08	4.118 ±0.003	0.150 ±0.004	**1.70** ± 0.02	4.180 ±0.003	0.237 ±0.004
5	**-9.1** ±0.3	4.66 ±0.01	0.33 ±0.02	**-8** ± 2	4.35 ±0.08	0.39 ±0.04	**-6.8** ± 0.3	4.472 ±0.004	0.225 ±0.007	**-5.45** ± 0.1	4.660 ±0.001	0.283 ±0.002
6	**-6.1** ±0.5	5.08 ±0.01	0.27 ±0.02	**-9.4** ±0.09	5.056 ±0.009	0.53 ±0.01	**-6.65** ±0.08	4.89 ±0.01	0.34 ±0.01	**-0.62** ±0.03	5.210 ±0.007	0.21 ±0.01
7	**-12.9** ±0.05	5.620 ±0.001	0.269 ±0.006	**-14.55** ±0.06	5.780 ±0.002	0.295 ±0.004	**-10.95** ±0.04	5.754 ±0.002	0.296 ± 0.003	**-7.76** ±0.01	5.731 ±0.001	0.338 ±0.002

Table D.4) Table for the parameters of the Gaussian peaks fitted to the experimental CD spectra in Chapter 5, Figure 5.3.

Appendix E) Ag$^+$ disrupts folding in a human telomeric G-quadruplex structure

E.1) Introduction

The human telomeres are regions of DNA with repeating TTAGGG units at the end of chromosomes. The telomeric region is an important buffer region during DNA replication to protect coding regions of DNA, as DNA truncation is an inevitable part of the replication process. Telomerase is an enzyme that regenerates the length of telomeres. In most normally functioning human cells telomerase is not expressed to any significant degree, with some notable exceptions including epidermal cells.[220] However, telomerase is overexpressed in the majority of human cancer cells and contributes to their immortality, making the telomeric region of DNA an attractive region for cancer drug research.[221]

There is growing evidence that the G-rich telomeric region forms structural units known as G-quadruplexes *in vivo*.[222] G-quadruplexes are comprised of repeating units of four guanine bases hydrogen bonded together in a planar configuration, known as G-tetrads, which can then stack successively.[6] There is evidence that G-quadruplexes in the telomeric region could inhibit telomerase activity,[222] making the stabilization of G-quadruplexes an interesting prospect for cancer research. G-rich DNA, which can form G-quadruplexes, in other regions of DNA are also suggested to play a possible role in gene regulation.[222] Learning how to manipulate G-quadruplex structures could have important biological significance.

Here we attempt to manipulate G-quadruplex structure by the addition of Ag$^+$, which from Chapters 2-4 is shown to have strong affinity for G-rich strands resulting in the formation of G-Ag$^+$-G base pairs. We perform Ag$^+$ titrations on the human telomeric DNA sequence $(T_2AG_3)_6$ to determine whether Ag$^+$ can modulate the structure of a pre-folded G-quadruplex. We analyze the change in DNA structure with circular dichroism (CD) spectroscopy.

E.2) Results and Discussion

Figure E.1 displays the titration of strand $(T_2AG_3)_6$ with $AgNO_3$ in 4.5 µM increments. The CD spectrum with no $AgNO_3$ for strand $(T_2AG_3)_6$ suggests a folded structure and is representative of a hybrid type G-quadruplex.[223] Upon the first titration of $AgNO_3$ the CD spectral shape immediately begins to change, becoming more negative. This change continues up to 90 µm $AgNO_3$, where the CD spectrum becomes negative at all wavelengths with detectable signal. Apparently even without proper temperature protocols, the binding of Ag^+ is strong enough to disrupt G-quadruplex structure as displayed by the significant spectral changes between 0 and 90 µM AgNO3 (Figure E.1).

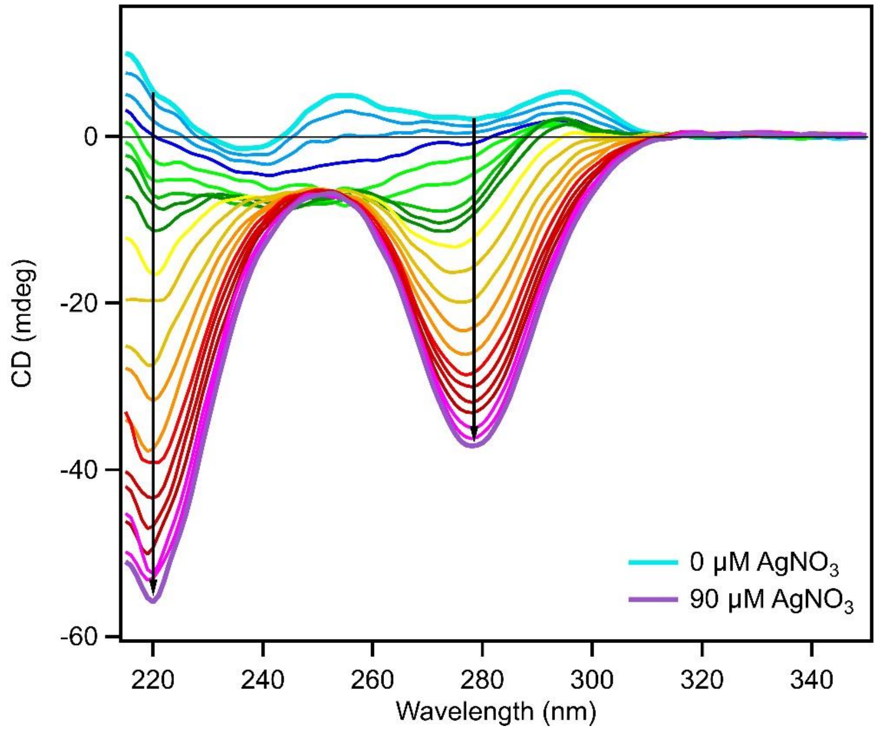

Figure E.1) CD spectra for the titration of human telomeric sequence $(T_2AG_3)_6$ with $AgNO_3$. Titrations were in increments of 4.5 µM $AgNO_3$ from 0 µM (teal, top-most curve) to 90 µM (purple, bottom-most curve) $AgNO_3$ at 25 °C. The black arrows point in the direction of increasing $AgNO_3$ concentration. The initial DNA concentration was 2 µM with a 100 mM NH_4OAc pH = 7 buffer. The teal, top-most curve with no $AgNO_3$ is representative of hybrid type G-quadruplex structure.[223]

The CD spectra show negative peaks at 220 nm and 275-280 nm from 27-90 µM $AgNO_3$ (Figure E.1). These negative peak locations agree with CD spectra of Ag^+-paired guanine homobase strands from 6-20 bases in length formed from G-Ag^+-G base pairs (Chapters 2-3). This seems to suggest that the formation of G-Ag^+-G base pairs are driving the change in G-quadruplex structure.

E.3) Conclusion

This experiment is a proof-of-principle that G-quadruplexes can be modulated with Ag^+. The $AgNO_3$ titration with G-quadruplex forming strand $(T_2AG_3)_6$ showed a significant change in DNA structure as displayed by the strong contrast in CD spectral shapes at low and high $AgNO_3$ concentrations. This study warrants further research into how Ag^+ affects different types of folded G-quadruplexes such as parallel and anti-parallel G-quadruplexes, how competitive binding with thiols affects binding of Ag^+ to G-quadruplexes and if Ag^+-complexes can specifically bind to G-quadruplexes.

E.4) Methods

The DNA strand $(T_2AG_3)_6$ was received from IDT and additionally desalted with centrifugal filtration upon receipt. All water was HPLC/MS grade and the $AgNO_3$ was analytical grade, 99.999% (Sigma-Aldrich).

The CD titration was performed on a Jasco J-1000 series CD spectrophotometer. The titration was performed with an initial DNA concentration of 2 µM and ended with a final DNA concentration of 1.3 µM. The buffer concentration was held constant throughout the titration at 100 mM NH4OAc pH = 7. $AgNO_3$ was added in 4.5 µM increments and the solution was equilibrated for 5 minutes after each titration before the spectra were collected. The solution was constantly stirred with a magnetic stir bar throughout the experiment.

References

(1) Tan, Z.-J.; Chen, S.-J. Nucleic Acid Helix Stability: Effects of Salt Concentration, Cation Valence and Size, and Chain Length. *Biophys. J.* **2006**, *90*, 1175–1190.

(2) Lu, X.-J.; Shakked, Z.; Olson, W. K. A-Form Conformational Motifs in Ligand-Bound DNA Structures. *J. Mol. Biol.* **2000**, *300*, 819–840.

(3) Herbert, A.; Rich, A. Left-Handed Z-DNA : Structure and Function. *Genetica* **1999**, *106*, 37–47.

(4) Jain, A.; Wang, G.; Vasquez, K. M. DNA Triple Helices: Biological Consequences and Therapeutic Potential. *Biochemie* **2008**, *90*, 1117–1130.

(5) Bacolla, A.; Wang, G.; Vasquez, K. M. New Perspectives on DNA and RNA Triplexes As Effectors of Biological Activity. *PLoS Genet.* **2015**, *11*, 1–12.

(6) Bochman, M. L.; Paeschke, K.; Zakian, V. A. DNA Secondary Structures: Stability and Function of G-Quadruplex Structures. *Nat Rev Genet* **2012**, *13*, 770–780.

(7) Moye, A. L.; Porter, K. C.; Cohen, S. B.; Phan, T.; Zyner, K. G.; Sasaki, N.; Lovrecz, G. O.; Beck, J. L.; Bryan, T. M. Telomeric G-Quadruplexes Are a Substrate and Site of Localization for Human Telomerase. *Nat. Commun.* **2015**, *6*, 7643.

(8) Hänsel-Hertsch, R.; Di Antonio, M.; Balasubramanian, S. DNA G-Quadruplexes in the Human Genome: Detection, Functions and Therapeutic Potential. *Nat. Rev. Mol. Cell Biol.* **2017**, *18*, 279–284.

(9) Day, H. A.; Pavlou, P.; Waller, Z. A. E. I-Motif DNA: Structure, Stability and Targeting with Ligands. *Bioorganic Med. Chem.* **2014**, *22*, 4407–4418.

(10) Dilruba, S.; Kalayda, G. V. Platinum-Based Drugs: Past, Present and Future. *Cancer Chemother. Pharmacol.* **2016**, *77*, 1103–1124.

(11) Hambley, T. W. Platinum Binding to DNA: Structural Controls and Consequences. *J. Chem. Soc. Dalt. Trans.* **2001**, 2711–2718.

(12) Zaki, M.; Arjmand, F.; Tabassum, S. Current and Future Potential of Metallo Drugs: Revisiting DNA-Binding of Metal Containing Molecules and Their Diverse Mechanism of Action. *Inorganica Chim. Acta* **2016**, *444*, 1–22.

(13) Lansdown, A. B. Silver in Health Care: Antimicrobial Effects and Safety in Use. *Curr. Probl. Dermatol.* **2006**, *33*, 17–34.

(14) Medvetz, D. A.; Hindi, K. M.; Panzner, M. J.; Ditto, A. J.; Yun, Y. H.; Youngs, W. J. Anticancer Activity of Ag(I) N-Heterocyclic Carbene Complexes Derived from 4,5-Dichloro-1H-Imidazole. *Met. Based. Drugs* **2008**, *2008*, 1–7.

(15) Li, Y.; Liu, G.-F.; Tan, C.-P.; Ji, L.-N.; Mao, Z.-W. Antitumor Properties and Mechanisms of Mitochondria-Targeted Ag(I) and Au(I) Complexes Containing N-Heterocyclic Carbenes Derived from Cyclophanes. *Metallomics* **2014**, *6*, 1460.

(16) Zhu, H. L.; Zhang, X. M.; Liu, X. Y.; Wang, X. J.; Liu, G. F.; Usman, A.; Fun, H. K.

Clear Ag-Ag Bonds in Three silver(I) Carboxylate Complexes with High Cytotoxicity Properties. *Inorg. Chem. Commun.* **2003**, *6*, 1113–1116.

(17) Etaiw, S. E. H.; Sultan, A. S.; Badr El-din, A. S. A Novel Hydrogen Bonded Bimetallic Supramolecular Coordination Polymer {[SnMe3(bpe)][Ag(CN)2]·2H2O} as Anticancer Drug. *Eur. J. Med. Chem.* **2011**, *46*, 5370–5378.

(18) Liu, J. J.; Galettis, P.; Farr, A.; Maharaj, L.; Samarasinha, H.; McGechan, A. C.; Baguley, B. C.; Bowen, R. J.; Berners-Price, S. J.; McKeage, M. J. In Vitro Antitumour and Hepatotoxicity Profiles of Au(I) and Ag(I) Bidentate Pyridyl Phosphine Complexes and Relationships to Cellular Uptake. *J. Inorg. Biochem.* **2008**, *102*, 303–310.

(19) Seeman, N. C. Nucleic Acid Junctions and Lattices. *J. Theor. Biol.* **1982**, *99*, 237–247.

(20) Chen, J.; Seeman, N. C. Synthesis from DNA of a Molecule with the Connectivity of a Cube. *Nature* **1991**, *350*, 631–633.

(21) Okholm, A. H.; Kjems, J. The Utility of DNA Nanostructures for Drug Delivery in Vivo. *Expert Opin. Drug Deliv.* **2017**, *14*, 137–139.

(22) Schlichthaerle, T.; Strauss, M. T.; Schueder, F.; Woehrstein, J. B.; Jungmann, R. DNA Nanotechnology and Fluorescence Applications. *Curr. Opin. Biotechnol.* **2016**, *39*, 41–47.

(23) Chao, J.; Zhu, D.; Zhang, Y.; Wang, L.; Fan, C. DNA Nanotechnology-Enabled Biosensors. *Biosens. Bioelectron.* **2016**, *76*, 68–79.

(24) Abendroth, J. M.; Bushuyev, O. S.; Weiss, P. S.; Barrett, C. J. Controlling Motion at the Nanoscale: Rise of the Molecular Machines. *ACS Nano* **2015**, *9*, 7746–7768.

(25) Zhang, D. Y.; Winfree, E. Control of DNA Strand Displacement Kinetics Using Toehold Exchange. *JACS* **2009**, *131*, 17303–17314.

(26) Yurke, B.; Turberfeld, A. J.; Jr, A. P. M.; Laboratories, B.; Technologies, L.; Avenue, M.; Hill, M. A DNA-Fuelled Molecular Machine Made of DNA. *Nature* **2000**, *406*, 605–608.

(27) Tanaka, K.; Shionoya, M. Programmable Metal Assembly on Bio-Inspired Templates. *Coord. Chem. Rev.* **2007**, *251*, 2732–2742.

(28) Clever, G. H.; Shionoya, M. Metal–base Pairing in DNA. *Coord. Chem. Rev.* **2010**, *254*, 2391–2402.

(29) Miyake, Y.; Togashi, H.; Tashiro, M.; Yamaguchi, H.; Oda, S.; Kudo, M.; Tanaka, Y.; Kondo, Y.; Sawa, R.; Fujimoto, T.; *et al.* MercuryII-Mediated Formation of Thymine-HgII-Thymine Base Pairs in DNA Duplexes. *J. Am. Chem. Soc.* **2006**, *128*, 2172–2173.

(30) Ono, A.; Cao, S.; Togashi, H.; Tashiro, M.; Fujimoto, T.; Machinami, T.; Oda, S.; Miyake, Y.; Okamoto, I.; Tanaka, Y. Specific Interactions between silver(I) Ions and Cytosine-Cytosine Pairs in DNA Duplexes. *Chem. Commun.* **2008**, 4825–4827.

(31) Torigoe, H.; Miyakawa, Y.; Ono, A.; Kozasa, T. Thermodynamic Properties of the Specific Binding between Ag+ Ions and C:C Mismatched Base Pairs in Duplex DNA.

Nucleosides. Nucleotides Nucleic Acids **2011**, *30*, 149–167.

(32) Liu, C.; Huang, C.; Chang, H. Highly Selective DNA-Based Sensor for Lead (II) and Mercury (II) Ions. *Anal. Chem.* **2009**, *81*, 6824–6828.

(33) Wang, Z.; Heon Lee, J.; Lu, Y. Highly Sensitive "turn-On" Fluorescent Sensor for Hg2+ in Aqueous Solution Based on Structure-Switching DNA. *Chem. Commun.* **2008**, 6005.

(34) Wu, Y.; Lai, R. Y. A Reagentless DNA-Based Electrochemical silver(I) Sensor for Real Time Detection of Ag(I) - the Effect of Probe Sequence and Orientation on Sensor Response. *Biotechnol. J.* **2016**, *11*, 788–796.

(35) Toomey, E.; Xu, J.; Vecchioni, S.; Rothschild, L.; Wind, S.; Fernandes, G. E. Comparison of Canonical versus Silver(I)-Mediated Base-Pairing on Single Molecule Conductance in Polycytosine dsDNA. *J. Phys. Chem. C* **2016**, *120*, 7804–7809.

(36) Taniguchi, M.; Kawai, T. DNA Electronics. *Phys. E Low-Dimensional Syst. Nanostructures* **2006**, *33*, 1–12.

(37) Porchetta, A.; Vallée-Bélisle, A.; Plaxco, K. W.; Ricci, F. Allosterically Tunable, DNA-Based Switches Triggered by Heavy Metals. *J. Am. Chem. Soc.* **2013**, *135*, 13238–13241.

(38) Park, K. S.; Lee, C. Y.; Park, H. G. Metal Ion Triggers for Reversible Switching of DNA Polymerase. *Chem. Commun.* **2016**, *52*, 4868–4871.

(39) Torigoe, H.; Okamoto, I.; Dairaku, T.; Tanaka, Y.; Ono, A.; Kozasa, T. Thermodynamic and Structural Properties of the Specific Binding between Ag^+ Ion and C:C Mismatched Base Pair in Duplex DNA to Form C-Ag-C Metal-Mediated Base Pair. *Biochimie* **2012**, *94*, 2431–2440.

(40) Loo, K.; Degtyareva, N.; Park, J.; Sengupta, B.; Reddish, M.; Rogers, C. C.; Bryant, A.; Petty, J. T. Ag+-Mediated Assembly of 5 ′-Guanosine Monophosphate. *J. Phys. Chem. B* **2010**, *114*, 4320–4326.

(41) Ma, Y.; Yang, X.; Wei, Y.; Yuan, Q. Applications of DNA Nanotechnology in Synthesis and Assembly of Inorganic Nanomaterials. *Chinese J. Chem.* **2016**, *34*, 291–298.

(42) Russell, C.; Welch, K.; Jarvius, J.; Cai, Y.; Brucas, R.; Nikolajeff, F.; Al, R. E. T. Gold Nanowire Based Electrical DNA Detection Using Rolling Circle Amplification. *ACS Nano* **2014**, *8*, 1147–1153.

(43) Mertig, M.; Ciacchi, L. C.; Seidel, R.; Pompe, W.; De Vita, A. DNA as a Selective Metallization Template. *Nano Lett.* **2002**, *2*, 841–844.

(44) Wang, Z.; Tang, L.; Tan, L. H.; Li, J.; Lu, Y. Discovery of the DNA "genetic Code" for Abiological Gold Nanoparticle Morphologies. *Angew. Chemie - Int. Ed.* **2012**, *51*, 9078–9082.

(45) Schreiber, R.; Kempter, S.; Holler, S.; Schüller, V.; Schiffels, D.; Simmel, S. S.; Nickels, P. C.; Liedl, T. DNA Origami-Templated Growth of Arbitrarily Shaped Metal Nanoparticles. *Small* **2011**, *7*, 1795–1799.

(46) Shang, L.; Dong, S.; Nienhaus, G. U. Ultra-Small Fluorescent Metal Nanoclusters: Synthesis and Biological Applications. *Nano Today* **2011**, *6*, 401–418.

(47) Gwinn, E. G.; Schultz, D. E.; Copp, S. M.; Swasey, S. M. DNA-Protected Silver Clusters for Nanophotonics. *Nanomaterials* **2015**, *5*, 180–207.

(48) Petty, J. T.; Fan, C.; Story, S. P.; Sengupta, B.; Sartin, M.; Hsiang, J.-C.; Perry, J. W.; Dickson, R. M. Optically Enhanced, near-IR, Silver Cluster Emission Altered by Single Base Changes in the DNA Template. *J. Phys. Chem. B* **2011**, *115*, 7996–8003.

(49) Schultz, D.; Gardner, K.; Oemrawsingh, S. S. R. Markešević, N.; Olsson, K.; Debord, M.; Bouwmeester, D.; Gwinn, E.; Oemrawsingh, S. S. R.; Markešević, N.; Olsson, K.; *et al.* Evidence for Rod-Shaped DNA-Stabilized Silver Nanocluster Emitters. *Adv. Mater.* **2013**, *25*, 2797–2803.

(50) Schultz, D.; Gwinn, E. G. Silver Atom and Strand Numbers in Fluorescent and Dark Ag:DNAs. *Chem. Commun.* **2012**, *48*, 5748–5750.

(51) Copp, S. M.; Schultz, D.; Swasey, S.; Pavlovich, J.; Debord, M.; Chiu, A.; Olsson, K.; Gwinn, E. Magic Numbers in DNA-Stabilized Fluorescent Silver Clusters Lead to Magic Colors. *J. Phys. Chem. Lett.* **2014**, *5*, 959–963.

(52) New, S. Y.; Lee, S. T.; Su, X. D. DNA-Templated Silver Nanoclusters: Structural Correlation and Fluorescence Modulation. *Nanoscale* **2016**, *8*, 17729–17746.

(53) Copp, S. M.; Bogdanov, P.; Debord, M.; Singh, A.; Gwinn, E. Base Motif Recognition and Design of DNA Templates for Fluorescent Silver Clusters by Machine Learning. *Adv. Mater.* **2014**, *26*, 5839–5845.

(54) Takezawa, Y.; Shionoya, M. Metal-Mediated DNA Base Pairing: Alternatives to Hydrogen-Bonded Watson-Crick Base Pairs. *Acc. Chem. Res.* **2012**, *45*, 2066–2076.

(55) Swasey, S. M.; Leal, L. E.; Lopez-Acevedo, O.; Pavlovich, J.; Gwinn, E. G. Silver (I) as DNA Glue: Ag+-Mediated Guanine Pairing Revealed by Removing Watson-Crick Constraints. *Sci. Rep.* **2015**, *5*, 10163–101.

(56) Rangnekar, A.; LaBean, T. H. Building DNA Nanostructures for Molecular Computation, Templated Assembly, and Biological Applications. *Acc. Chem. Res.* **2014**, *47*, 1778–1788.

(57) Park, K. S.; Park, H. G. Technological Applications Arising from the Interactions of DNA Bases with Metal Ions. *Curr. Opin. Biotechnol.* **2014**, *28C*, 17–24.

(58) Scharf, P.; Müller, J. Nucleic Acids With Metal-Mediated Base Pairs and Their Applications. *Chempluschem* **2013**, *78*, 20–34.

(59) Berti, L.; Burley, G. A. Nucleic Acid and Nucleotide-Mediated Synthesis of Inorganic Nanoparticles. *Nat. Nanotechnol.* **2008**, *3*, 81–87.

(60) Tanaka, K.; Clever, G. H.; Takezawa, Y.; Yamada, Y.; Kaul, C.; Shionoya, M.; Carell, T. Programmable Self-Assembly of Metal Ions inside Artificial DNA Duplexes. *Nat. Nanotechnol.* **2006**, *1*, 190–194.

(61) Zimmermann, N.; Meggers, E.; Schultz, P. G. A Novel silver(I)-Mediated DNA Base Pair. *J. Am. Chem. Soc.* **2002**, *124*, 13684–13685.

(62) Johannsen, S.; Megger, N.; Böhme, D.; Sigel, R. K. O.; Müller, J. Solution Structure of a DNA Double Helix with Consecutive Metal-Mediated Base Pairs. *Nat. Chem.* **2010**, *2*, 229–234.

(63) Petty, J. T.; Zheng, J.; Hud, N. V; Dickson, R. M. DNA-Templated Ag Nanocluster Formation. *J. Am. Chem. Soc.* **2004**, *126*, 5207–5212.

(64) Gwinn, E. G.; O'Neill, P.; Guerrero, a. J.; Bouwmeester, D.; Fygenson, D. K. Sequence-Dependent Fluorescence of DNA-Hosted Silver Nanoclusters. *Adv. Mater.* **2008**, *20*, 279–283.

(65) Yuan, Z.; Chen, Y.-C.; Li, H.-W.; Chang, H.-T. Fluorescent Silver Nanoclusters Stabilized by DNA Scaffolds. *Chem. Commun.* **2014**.

(66) Pino, G. A. Effect of Ag+ on the Excited-State Properties of a Gas-Phase (Cytosine) 2 Ag+ Complex: Electronic Transition and Estimated Lifetime. *J. Phys. Chem. Lett* **2014**, *6*, 2295–2301.

(67) Schultz, D.; Gwinn, E. Stabilization of Fluorescent Silver Clusters by RNA Homopolymers and Their DNA Analogs : C , G versus A , T (U) Dichotomy. *Chem. Commun.* **2011**, *47*, 4715–4717.

(68) Menzer, S.; Hillgeris, E. C.; Lippert, B. Preparation, X-Ray Structure and Solution Behavior of [Ag(9-EtGH-N7)2]NO3·H2O (9-EtGH=9-Ethylguanine). *Inorganica Chim. Acta* **1993**, *210*, 167–171.

(69) Fichtinger-Schepman, a M.; van der Veer, J. L.; den Hartog, J. H.; Lohman, P. H.; Reedijk, J. Adducts of the Antitumor Drug Cis-diamminedichloroplatinum(II) with DNA: Formation, Identification, and Quantitation. *Biochemistry* **1985**, *24*, 707–713.

(70) K. Garbutcheon-Singh, M. Grant, B. Harper, M. Manohar, A. Krause-Heuer, N. Orkey, J. Aldrich-Wright, J. A.-W. Transition Metal Based Anticancer Drugs. *Curr. Top. Med. Chem.* **2011**, *11*, 521–542.

(71) Lok, C.-N.; Ho, C.-M.; Chen, R.; He, Q.-Y.; Yu, W.-Y.; Sun, H.; Tam, P. K.-H.; Chiu, J.-F.; Che, C.-M. Silver Nanoparticles: Partial Oxidation and Antibacterial Activities. *J. Biol. Inorg. Chem.* **2007**, *12*, 527–534.

(72) Izatt, R. M.; Christensen, J. J.; Rytting, J. H. Sites and Thermodynamic Quantities Associated with Proton and Metal Ion Interaction with Ribonucleic Acid, Deoxyribonucleic Acid, and Their Constituent Bases, Nucleosides, and and Nucleotides. *Chem. Rev.* **1971**, *71*, 439–482.

(73) DiRico, D. E.; Keller, P. B.; Hartman, K. A. The Infrared Spectrum and Structure of the Type I Complex of Silver and DNA. *Nucleic Acids Res.* **1985**, *13*, 251–260.

(74) Dattagupta, N.; Crothers, D. M. Solution Structural Studies of the Ag(I)-DNA Complex. *Nucleic Acids Res.* **1981**, *9*, 2971–2985.

(75) Ding, D.; Allen, F. S. Electric Dichroism and Sedimentation Velocity Studies of DNA-Hg(II) and DNA-Ag(I) Complexes. *Biochim. Biophys. Acta* **1980**, *610*, 64–71.

(76) Arakawa, H.; Neault, J. F.; Tajmir-Riahi, H. A. Silver(I) Complexes with DNA and RNA Studied by Fourier Transform Infrared Spectroscopy and Capillary Electrophoresis. *Biophys. J.* **2001**, *81*, 1580–1587.

(77) Jensen, R. H.; Davidson, N. Spectrophotometric, Potentiometric, and Density Gradient Ultracentrifugation Studies of the Binding of Silver Ion by DNA. *Biopolymers* **1966**, *4*, 17–32.

(78) Nordén, B.; Matsuoka, Y.; Kurucsev, T. Nucleic Acid-Metal Interactions: V. The Effect of silver(I) on the Structures of A- and B-DNA Forms. *Biopolymers* **1986**, *25*, 1531–1545.

(79) Urata, H.; Yamaguchi, E.; Nakamura, Y.; Wada, S. Pyrimidine-Pyrimidine Base Pairs Stabilized by silver(I) Ions. *Chem. Commun.* **2011**, *47*, 941–943.

(80) Funai, T.; Miyazaki, Y.; Aotani, M.; Yamaguchi, E.; Nakagawa, O.; Wada, S.; Torigoe, H.; Ono, A.; Urata, H. Ag(I) Ion Mediated Formation of a C-A Mispair by DNA Polymerases. *Angew. Chemie* **2012**, *51*, 6464–6466.

(81) Ihara, T.; Ishii, T.; Araki, N.; Wilson, A. W.; Jyo, A. Silver Ion Unusually Stabilizes the Structure of a Parallel-Motif DNA Triplex. *J. Am. Chem. Soc.* **2009**, *131*, 3826–3827.

(82) Burda, J. V; Šponer, J.; Leszczynski, J.; Hobza, P. Interaction of DNA Base Pairs with Various Metal Cations: Nonempirical Ab Initio Calculations on Strcutures, Energies, and Nonadditivity of the Interaction. *J. Phys. Chem. B* **1997**, *5647*, 9670–9677.

(83) Brancolini, G.; Di Felice, R. Electronic Properties of Metal-Modified DNA Base Pairs. *J. Phys. Chem. B* **2008**, *112*, 14281–14290.

(84) Marino, T.; Russo, N.; Toscano, M.; Pavelka, M. Theoretical Investigation on DNA/RNA Base Pairs Mediated by Copper, Silver, and Gold Cations. *Dalt. Trans.* **2012**, *41*, 1816–1823.

(85) Metal, B.; Li, C.; Heyro, J. V. Ab Initio Study of the Interaction of Guanine and Adenine with Various Mono- and. *J. Phys. Chem.* **1996**, *100*, 7250–7255.

(86) Megger, D. A.; Fonseca Guerra, C.; Bickelhaupt, F. M.; Müller, J. Silver(I)-Mediated Hoogsteen-Type Base Pairs. *J. Inorg. Biochem.* **2011**, *105*, 1398–1404.

(87) Ganem, B. Detection of Noncovalent Receptor-Ligand Complexes by Mass Spectrometry. *J. Am. Chem. Soc.* **1991**, *113*, 6294–6296.

(88) Rosu, F.; Gabelica, V.; Houssier, C.; De Pauw, E. Determination of Affinity, Stoichiometry and Sequence Selectivity of Minor Groove Binder Complexes with Double-Stranded Oligodeoxynucleotides by Electrospray Ionization Mass Spectrometry. *Nucleic Acids Res.* **2002**, *30*, e82.

(89) Koszinowski, K.; Ballweg, K. A Highly Charged Ag(6)(4+) Core in a DNA-Encapsulated Silver Nanocluster. *Chem. Eur. J.* **2010**, *16*, 3285–3290.

(90) Shukla, S.; Sastry, M. Probing Differential Ag+-Nucleobase Interactions with Isothermal Titration Calorimetry (ITC): Towards Patterned DNA Metallization. *Nanoscale* **2009**, *1*, 122–127.

(91) Megger, D. A.; Müller, J. Silver(I)-Mediated Cytosine Self-Pairing Is Preferred over Hoogsteen-Type Base Pairs with the Artificial Nucleobase 1,3-Dideaza-6-Nitropurine. *Nucleosides. Nucleotides Nucleic Acids* **2010**, *29*, 27–38.

(92) Manzini, G.; Yathindra, N.; Xodo, L. E. Evidence for Intramolecularly Folded I-DNA Structures in Biologically Relevant CCC-Repeat Sequences. *Nucleic Acids Res.* **1994**, *22*, 4634–4640.

(93) Simonsson, T.; Pribylova, M.; Vorlickova, M. A Nuclease Hypersensitive Element in the Human c-Myc Promoter Adopts Several Distinct I-Tetraplex Structures. *Biochem. Biophys. Res. Commun.* **2000**, *278*, 158–166.

(94) Gray, D. M.; Wen, J.-D.; Gray, C. W.; Repges, R.; Repges, C.; Raabe, G.; Fleischhauer, J. Measured and Calculated CD Spectra of G-Quartets Stacked with the Same or Opposite Polarities. *Chirality* **2008**, *20*, 431–440.

(95) Paramasivan, S.; Rujan, I.; Bolton, P. H. Circular Dichroism of Quadruplex DNAs: Applications to Structure, Cation Effects and Ligand Binding. *Methods* **2007**, *43*, 324–331.

(96) Enkovaara, J.; Rostgaard, C.; Mortensen, J. J.; Chen, J.; Dułak, M.; Ferrighi, L.; Gavnholt, J.; Glinsvad, C.; Haikola, V.; Hansen, H. a; *et al.* Electronic Structure Calculations with GPAW: A Real-Space Implementation of the Projector Augmented-Wave Method. *J. Phys. Condens. Matter* **2010**, *22*, 253202.

(97) Perdew, J. P.; Burke, K.; Ernzerhof, M. Generalized Gradient Approximation Made Simple. *Phys. Rev. Lett.* **1996**, *77*, 3865–3868.

(98) Tkatchenko, A.; Scheffler, M. Accurate Molecular Van Der Waals Interactions from Ground-State Electron Density and Free-Atom Reference Data. *Phys. Rev. Lett.* **2009**, *102*, 73005.

(99) Frisch, M. J.; Trucks, G. W.; Schlegel, H. B.; Scuseria, G. E.; Robb, M. A.; Cheeseman, J. R.; Scalmani, G.; Barone, V.; Mennucci, B.; Petersson, G. A.; *et al.* Gaussian 09, Revision D.01, 2009.

(100) Leal, L. A. E.; Lopez-Acevedo, O. On the Interaction between Gold and Silver Metal Atoms and DNA / RNA Nucleobases - a Comprehensive Computational Study of Ground State Properties. *Nanotechnol. Rev.* **2015**, *4*, 173–191.

(101) Breslauer, K. J.; Frank, R.; Blöcker, H.; Marky, L. a. Predicting DNA Duplex Stability from the Base Sequence. *Proc. Natl. Acad. Sci. U. S. A.* **1986**, *83*, 3746–3750.

(102) Petrushka, J.; Goodman, M. F. Enthalpy-Entropy Compensation in DNA Melting Thermodynamics. *J. Biol. Chem.* **1995**, *270*, 746–750.

(103) Dixit, S. B.; Mezei, M.; Beveridge, D. L. Studies of Base Pair Sequence Effects on DNA Solvation Based on All-Atom Molecular Dynamics Simulations. *J. Biosci.* **2012**, *37*,

399–421.

(104) Swasey, S. M.; Gwinn, E. G. Silver-Mediated Base Pairings: Towards Dynamic DNA Nanostructures with Enhanced Chemical and Thermal Stability. *New J. Phys.* **2016**, *18*, 45008.

(105) Sharma, J.; Chhabra, R.; Liu, Y.; Ke, Y.; Yan, H. DNA-Templated Self-Assembly of Two-Dimensional and Periodical Gold Nanoparticle Arrays. *Angew. Chemie Int. Ed.* **2006**, *45*, 730–735.

(106) Pilo-Pais, M.; Goldberg, S.; Samano, E.; Labean, T. H.; Finkelstein, G. Connecting the Nanodots: Programmable Nanofabrication of Fused Metal Shapes on DNA Templates. *Nano Lett.* **2011**, *11*, 3489–3492.

(107) Rothemund, P. W. K.; Ekani-Nkodo, A.; Papadakis, N.; Kumar, A.; Fygenson, D. K.; Winfree, E. Design and Characterization of Programmable DNA Nanotubes. *J. Am. Chem. Soc.* **2004**, *126*, 16344–16352.

(108) Liu, D.; Park, S. H.; Reif, J. H.; LaBean, T. H. DNA Nanotubes Self-Assembled from Triple-Crossover Tiles as Templates for Conductive Nanowires. *Proc. Natl. Acad. Sci. U. S. A.* **2004**, *101*, 717–722.

(109) Biver, T. Stabilisation of Non-Canonical Structures of Nucleic Acids by Metal Ions and Small Molecules. *Coord. Chem. Rev.* **2013**, *257*, 2765–2783.

(110) Braun, E.; Eichen, Y.; Sivan, U.; Ben-Yoseph, G. DNA-Templated Assembly and Electrode Attachment of a Conducting Silver Wire. *Nature* **1998**, *391*, 775–778.

(111) Zinchenko, A. A.; Yoshikawa, K.; Baigl, D. DNA-Templated Silver Nanorings. *Adv. Mater.* **2005**, *17*, 2820–2823.

(112) Sengupta, B.; Ritchie, C. M.; Buckman, J. G.; Johnsen, K. R.; Goodwin, P. M.; Petty, J. T. Base-Directed Formation of Fluorescent Silver Clusters. *J. Phys. Chem. C* **2008**, *112*, 18776–18782.

(113) Sharma, J.; Yeh, H.-C.; Yoo, H.; Werner, J. H.; Martinez, J. S. A Complementary Palette of Fluorescent Silver Nanoclusters. *Chem. Commun. (Camb).* **2010**, *46*, 3280–3282.

(114) Espinosa Leal, L. A. A.; Karpenko, A.; Swasey, S.; Gwinn, E. G. G.; Rojas-Cervellera, V.; Rovira, C.; Lopez-Acevedo, O. The Role of Hydrogen Bonds in the Stabilization of Silver-Mediated Cytosine Tetramers. *J. Phys. Chem. Lett.* **2015**, *6*, 4061–4066.

(115) Li, J.; Zheng, C.; Cansiz, S.; Wu, C.; Xu, J.; Cui, C.; Liu, Y.; Hou, W.; Wang, Y.; Zhang, L.; *et al.* Self-Assembly of DNA Nanohydrogels with Controllable Size and Stimuli-Responsive Property for Targeted Gene Regulation Therapy. *J. Am. Chem. Soc.* **2015**, *137*, 1412–1415.

(116) Rosu, F.; De Pauw, E.; Gabelica, V. Electrospray Mass Spectrometry to Study Drug-Nucleic Acids Interactions. *Biochimie* **2008**, *90*, 1074–1087.

(117) Abi-Ghanem, J.; Gabelica, V. V. Nucleic Acid Ion Structures in the Gas Phase. *Phys. Chem. Chem. Phys.* **2014**, *16*, 21204–21218.

(118) Bayer, E.; Bauer, T.; Schmeer, K.; Bleicher, K.; Maler, M.; Gaus, H. J. Analysis of Double-Stranded Oligonucleotides By Electrospray Mass-Spectrometry. *Anal. Chem.* **1994**, *66*, 3858–3863.

(119) Warren, W. J.; Vella, G. Principles and Methods for the Analysis and Purification of Synthetic Deoxyribonucleotides by High-Performance Liquid Chromatography. *Mol. Biotechnol.* **1995**, *4*, 179–199.

(120) Gilar, M.; Fountain, K. J.; Budman, Y.; Neue, U. D.; Yardley, K. R.; Rainville, P. D.; Russell II, R. J.; Gebler, J. C. Ion-Pair Reversed-Phase High-Performance Liquid Chromatography Analysis of Oligonucleotides: *J. Chromatogr. A* **2002**, *958*, 167–182.

(121) Klump, H.; Burkart, W. Calorimetric Measurements of the Transition Enthalpy of DNA in Aqueous Urea Solutions. *Biochim. Biophys. Acta* **1977**, *475*, 601–604.

(122) Copp, S. M.; Schultz, D. E.; Swasey, S.; Gwinn, E. G. Atomically Precise Arrays of Fluorescent Silver Clusters: A Modular Approach for Metal Cluster Photonics on DNA Nanostructures. *ACS Nano* **2015**, *9*, 2303–2310.

(123) Andrushchenko, V.; Bouř, P. Circular Dichroism Enhancement in Large DNA Aggregates Simulated by a Generalized Oscillator Model. *J. Comput. Chem.* **2008**, *29*, 2963–2703.

(124) Wolf, B.; Berman, S.; Hanlon, S. Structural Transitions of Calf Thymus DNA in Concentrated LiCl Solutions. *Biochemistry* **1977**, *16*, 3655–3662.

(125) Eidelshtein, G.; Fardian-Melamed, N.; Gutkin, V.; Basmanov, D.; Klinov, D.; Rotem, D.; Levi-Kalisman, Y.; Porath, D.; Kotlyar, A. Synthesis and Properties of Novel Silver-Containing DNA Molecules. *Adv. Mater.* **2016**, 4839–4844.

(126) Kelland, L. The Resurgence of Platinum-Based Cancer Chemotherapy. *Nat. Rev. Cancer.* **2007**, *7*, 573–584.

(127) Long, D. F.; Repta, A. J. Review Article Cisplatin: Chemistry, Distribution and Biotransformation. *Biopharm. Drug Dispos.* **1981**, *2*, 1–16.

(128) Hato, S. V.; Khong, A.; De Vries, I. J. M.; Lesterhuis, W. J. Molecular Pathways: The Immunogenic Effects of Platinum-Based Chemotherapeutics. *Clin. Cancer Res.* **2014**, *20*, 2831–2837.

(129) Johnstone, T. C.; Park, G. Y.; Lippard, S. J. Understanding and Improving Platinum Anticancer Drugs--Phenanthriplatin. *Anticancer Res.* **2014**, *34*, 471–476.

(130) Jung, Y.; Lippard, S. J. Direct Cellular Responses to Platinum-Induced DNA Damage. *Chem. Rev.* **2007**, *107*, 1387–1407.

(131) Martin, L. P.; Hamilton, T. C.; Schilder, R. J. Platinum Resistance: The Role of DNA Repair Pathways. *Clin. Cancer Res.* **2008**, *14*, 1291–1295.

(132) Wang, D.; Lippard, S. J. Cellular Processing of Platinum Anticancer Drugs. *Nat. Rev. Drug Discov.* **2005**, *4*, 307–320.

(133) Rhodes, D.; Lipps, H. J. Survey and Summary G-Quadruplexes and Their Regulatory

Roles in Biology. *Nucleic Acids Res.* **2015**, *43*, 8627–8637.

(134) Park, K. S.; Jung, C.; Park, H. G. "Illusionary" Polymerase Activity Triggered by Metal Ions: Use for Molecular Logic-Gate Operations. *Angew. Chemie - Int. Ed.* **2010**, *49*, 9757–9760.

(135) Zhao, G.; Stevens, S. E. Multiple Parameters for the Comprehensive Evaluation of the Susceptibility of Escherichia Coli to the Silver Ion. *BioMetals* **1998**, *11*, 27–32.

(136) Leon, J. C.; Stegemann, L.; Peterlechner, M.; Litau, S.; Wilde, G.; Strassert, C. A.; Müller, J. Formation of Silver Nanoclusters from a DNA Template Containing Ag(I)-Mediated Base Pairs. *Bioinorg. Chem. Appl.* **2016**, *2016*, 1–10.

(137) Linko, V.; Ora, A.; Kostiainen, M. A. Review DNA Nanostructures as Smart Drug-Delivery Vehicles and Molecular Devices. *Trends Biotechnol.* **2015**, *33*, 586–594.

(138) Bikard, D.; Loot, C.; Baharoglu, Z.; Mazel, D. Folded DNA in Action: Hairpin Formation and Biological Functions in Prokaryotes. *Microbiol. Mol. Biol. Rev.* **2010**, *74*, 570–588.

(139) Frank-Kamenetskii, M. D.; Mirkin, S. M. Triplex DNA Structures. *Annu. Rev. Biochem.* **1995**, *64*, 65–95.

(140) Kondo, J.; Tada, Y.; Dairaku, T.; Hattori, Y.; Saneyoshi, H.; Ono, A.; Tanaka, Y. A Metallo-DNA Nanowire with Uninterrupted One-Dimensional Silver Array. *Nat. Chem.* **2017**, 1–5.

(141) Terrón, A.; Moreno-Vachiano, B.; Bauzá, A.; García-Raso, A.; Fiol, J. J.; Barceló-Oliver, M.; Molins, E.; Frontera, A. X-Ray Crystal Structure of a Metalled Double-Helix Generated by Infinite and Consecutive C*-AgI-C* (C*:N1-Hexylcytosine) Base Pairs through Argentophilic and Hydrogen Bond Interactions. *Chem. - A Eur. J.* **2017**, *23*, 2103–2108.

(142) Germann, W. G.; Kalisch, B. W.; van de Sande, J. H. Relative Stability of Parallel- and Antiparallel-Stranded Duplex DNA. *Biochemistry* **1988**, *27*, 8302–8306.

(143) Rippe, K.; Jovin, T. M. Design of Oligonucleotides Strategies for Constructing Parallel-Stranded Duplexes. *Methods Enzymol.* **1992**, *211*, 199–220.

(144) Germann, M. W.; Zhou, N.; Van de Sande, J. H.; Vogel, H. J. Parallel-Stranded Duplex DNA: An NMR Perspective. *Methods Enzymol.* **1995**, *261*, 207–225.

(145) Majumdar, D. S.; Smirnova, I.; Kasho, V.; Nir, E.; Kong, X.; Weiss, S.; Kaback, H. R. Single-Molecule FRET Reveals Sugar-Induced Conformational Dynamics in LacY. *Proc. Natl. Acad. Sci. U. S. A.* **2007**, *104,* 12640–12645.

(146) Day, H. A.; Huguin, C.; Waller, Z. A. E. Silver Cations Fold I-Motif at Neutral pH. *Chem. Commun.* **2013**, *49*, 7696–7698.

(147) Qiao, J.; Liang, C.; Wei, L.; Cao, Z.; Lian, H. Retention of Nucleic Acids in Ion-Pair Reversed-Phase High-Performance Liquid Chromatography Depends Not Only on Base Composition but Also on Base Sequence. *J. Sep. Sci.* **2016**, *39*, 4502–4511.

(148) Sturm, M.; Quinten, S.; Huber, C. G.; Kohlbacher, O. A Statistical Learning Approach to the Modeling of Chromatographic Retention of Oligonucleotides Incorporating Sequence and Secondary Structure Data. *Nucleic Acids Res.* **2007**, *35*, 4195–4202.

(149) Biyani, M.; Nishigaki, K. Structural Characterization of Ultra-Stable Higher-Ordered Aggregates Generated by Novel Guanine-Rich DNA Sequences. *Gene* **2005**, *364*, 130–138.

(150) Dolinnaya, N. G.; Ogloblina, A. M.; Yakubovskaya, M. G. *Structure , Properties , and Biological Relevance of the DNA and RNA G-Quadruplexes : Overview 50 Years after Their Discovery*; 2016; Vol. 4.

(151) Lanucara, F.; Holman, S. W.; Gray, C. J.; Eyers, C. E. The Power of Ion Mobility-Mass Spectrometry for Structural Characterization and the Study of Conformational Dynamics. *Nat. Chem.* **2014**, *6*, 281–294.

(152) Baker, E. S.; Bowers, M. T. B-DNA Helix Stability in a Solvent-Free Environment. *J. Am. Soc. Mass Spectrom.* **2007**, *18*, 1188–1195.

(153) Burmistrova, A.; Gabelica, V.; Duwez, A. S.; De Pauw, E. Ion Mobility Spectrometry Reveals Duplex DNA Dissociation Intermediates. *J. Am. Soc. Mass Spectrom.* **2013**, *24*, 1777–1786.

(154) D'Atri, V.; Porrini, M.; Rosu, F.; Gabelica, V. Linking Molecular Models with Ion Mobility Experiments. Illustration with a Rigid Nucleic Acid Structure. *J. Mass Spectrom.* **2015**, *50*, 711–726.

(155) Ruotolo, B. T.; Benesch, J. L. P.; Sandercock, A. M.; Hyung, S.-J.; Robinson, C. V. Ion Mobility-Mass Spectrometry Analysis of Large Protein Complexes. *Nat. Protoc.* **2008**, *3*, 1139–1152.

(156) Bohrer, B. C.; Merenbloom, S. I.; Koeniger, S. L.; Hilderbrand, A. E.; Clemmer, D. E. Biomolecule Analysis by Ion Mobility Spectrometry. *Annu. Rev. Anal. Chem.* **2008**, *1*, 293–327.

(157) Williams, J. P.; Lough, J. A.; Campuzano, I.; Richardson, K.; Sadler, P. J. Use of Ion Mobility Mass Spectrometry and a Collision Cross-Section Algorithm to Study an Organometallic Ruthenium Anticancer Complex and Its Adducts with a DNA Oligonucleotide. *Rapid Commun. Mass Spectrom.* **2009**, *23*, 3563–3569.

(158) X., M.; S., S.; M., Z.; C.K., P.; V.H., W. Structural Analysis of Activated SgrAI-DNA Oligomers Using Ion Mobility Mass Spectrometry. *Biochemistry* **2013**, *52*, 4373–4381.

(159) Hommersom, B.; Porta, T.; Heeren, R. M. A. Ion Mobility Spectrometry Reveals Intermediate States in Temperature-Resolved DNA Unfolding. *Int. J. Mass Spectrom.* **2017**, *419*, 52–55.

(160) Ferreira, R.; Marchand, A.; Gabelica, V. Mass Spectrometry and Ion Mobility Spectrometry of G-Quadruplexes. A Study of Solvent Effects on Dimer Formation and Structural Transitions in the Telomeric DNA Sequence d(TAGGGTTAGGGT). *Methods* **2012**, *57*, 56–63.

(161) Rosu, F.; Gabelica, V.; Houssier, C.; Colson, P.; De Pauw, E. Triplex and Quadruplex DNA Structures Studied by Electrospray Mass Spectrometry. *Rapid Commun. Mass Spectrom.* **2002**, *16*, 1729–1736.

(162) Rueda, M.; Luque, F. J.; Orozco, M. G-Quadruplexes Can Maintain Their Structure in the Gas Phase. *J. Am. Chem. Soc.* **2006**, *128*, 3608–3619.

(163) Porrini, M.; Rosu, F.; Rabin, C.; Darré, L.; Gómez, H.; Gabelica, V.; Européen, I.; Chimie, D.; Iecb, B. Compaction of Duplex Nucleic Acids upon Native Electrospray Mass Spectrometry. *ACS Cent. Sci.* **2017**, *3*, 454–461.

(164) Neidle, S.; Balasubramanian, S. Fundamentals of Quadruplex Structures. In *Quadruplex Nucleic Acids*; Neidle, S.; Balasubramanian, S., Eds.; The Royal Society of Chemistry, 2006; pp. 1–30.

(165) Schmidbaur, H.; Schier, A. Argentophilic Interactions. *Angew. Chemie - Int. Ed.* **2015**, *54*, 746–784.

(166) Swasey, S. M.; Karimova, N.; Aikens, C. M.; Schultz, D. E.; Simon, A. J.; Gwinn, E. G. Chiral Electronic Transitions in Fluorescent Silver Clusters Stabilized by DNA. *ACS Nano* **2014**, *8*, 6883–6892.

(167) Lu, F.; Tian, Y.; Liu, M.; Su, D.; Zhang, H.; Govorov, A. O.; Gang, O. Discrete Nanocubes as Plasmonic Reporters of Molecular Chirality. *Nano Lett.* **2013**, *13*, 3145–3151.

(168) Farrag, M.; Tschurl, M.; Heiz, U. Chiral Gold and Silver Nanoclusters: Preparation, Size Selection, and Chiroptical Properties. *Chem. Mater.* **2013**, *25*, 862–870.

(169) Lopez-Acevedo, O.; Tsunoyama, H.; Tsukuda, T. Chirality and Electronic Structure of the Thiolate-Protected Au 38 Nanocluster. *J. Am. Chem. Soc.* **2010**, *132*, 8210–8218.

(170) Knoppe, S.; Dolamic, I.; Bürgi, T. Racemization of a Chiral Nanoparticle Evidences the Flexibility of the Gold-Thiolate Interface. *J. Am. Chem. Soc.* **2012**, *134*, 13114–13120.

(171) Dolamic, I.; Knoppe, S.; Dass, A.; Bürgi, T. First Enantioseparation and Circular Dichroism Spectra of Au38 Clusters Protected by Achiral Ligands. *Nat. Commun.* **2012**, *3*, 798.

(172) Ravindran, A.; Chandran, P.; Khan, S. S. Biofunctionalized Silver Nanoparticles: Advances and Prospects. *Colloids Surf. B. Biointerfaces* **2013**, *105*, 342–352.

(173) Kuzyk, A.; Schreiber, R.; Fan, Z.; Pardatscher, G.; Roller, E.-M.; Högele, A.; Simmel, F. C.; Govorov, A. O.; Liedl, T. DNA-Based Self-Assembly of Chiral Plasmonic Nanostructures with Tailored Optical Response. *Nature* **2012**, *483*, 311–314.

(174) Chandra, M.; Dowgiallo, A.-M.; Knappenberger, K. L. Magnetic Dipolar Interactions in Solid Gold Nanosphere Dimers. *J. Am. Chem. Soc.* **2012**, *134*, 4477–4480.

(175) Caro, C.; Castillo, P. M.; Klippstein, R.; Pozo, D.; Zaderenko, A. P. Silver Nanoparticles: Sensing and Imaging Applications. In *Silver Nanoparticles*; Perez, D. P., Ed.; InTech, 2010; pp. 202–223.

(176) Latorre, A.; Somoza, Á. DNA-Mediated Silver Nanoclusters: Synthesis, Properties and Applications. *Chembiochem* **2012**, *13*, 951–958.

(177) Han, B.; Wang, E. DNA-Templated Fluorescent Silver Nanoclusters. *Anal. Bioanal. Chem.* **2012**, *402*, 129–138.

(178) Udayabhaskararao, T.; Pradeep, T. New Protocols for the Synthesis of Stable Ag and Au Nanocluster Molecules. *J. Phys. Chem. Lett.* **2013**, *4*, 1553–1564.

(179) Aikens, C. M. Electronic Structure of Ligand-Passivated Gold and Silver Nanoclusters. *J. Phys. Chem. Lett.* **2011**, *2*, 99–104.

(180) Johnson, H. E.; Aikens, C. M. Electronic Structure and TDDFT Optical Absorption Spectra of Silver Nanorods. *J. Phys. Chem. A* **2009**, *113*, 4445–4450.

(181) Guidez, E. B.; Aikens, C. M. Theoretical Analysis of the Optical Excitation Spectra of Silver and Gold Nanowires. *Nanoscale* **2012**, *4*, 4190–4198.

(182) Yan, J.; Gao, S. Plasmon Resonances in Linear Atomic Chains: Free-Electron Behavior and Anisotropic Screening of D Electrons. *Phys. Rev. B* **2008**, *78*, 235413.

(183) Petty, J. T.; Fan, C.; Story, S. P.; Sengupta, B.; John, A. S.; Prudowsky, Z.; Dickson, R. M. DNA Encapsulation of Ten Silver Atoms. *J. Phys. Chem. Lett.* **2011**, *1*, 2524–2529.

(184) Neidig, M. L.; Sharma, J.; Yeh, H.; Martinez, J. S.; Conradson, S. D.; Shreve, A. P. Ag K-Edge EXAFS Analysis of DNA-Templated Fluorescent Silver by DNA Sequence Variations. *J. Am. Chem. Soc.* **2011**, *133*, 11837–11839.

(185) Sharma, J.; Rocha, R. C.; Phipps, M. L.; Yeh, H.-C.; Balatsky, K. A.; Vu, D. M.; Shreve, A. P.; Werner, J. H.; Martinez, J. S. A DNA-Templated Fluorescent Silver Nanocluster with Enhanced Stability. *Nanoscale* **2012**, *4*, 4107–4110.

(186) Lan, G.-Y.; Chen, W.-Y.; Chang, H.-T. One-Pot Synthesis of Fluorescent Oligonucleotide Ag Nanoclusters for Specific and Sensitive Detection of DNA. *Biosens. Bioelectron.* **2011**, *26*, 2431–2435.

(187) Kypr, J.; Kejnovská, I.; Renciuk, D.; Vorlícková, M. Circular Dichroism and Conformational Polymorphism of DNA. *Nucleic Acids Res.* **2009**, *37*, 1713–1725.

(188) Edwards, E. L.; Ratliff, R. L.; Gray, D. M. Circular Dichroism Spectra of DNA Oligomers Show That Short Interior Stretches of C.C+ Base Pairs Do Not Form in Duplexes with A.T Base Pairs. *Biochemistry* **1988**, *27*, 5166–5174.

(189) Studdert, D. S.; Patroni, M.; Davis, R. C. Circular Dichroism of DNA: Temperature and Salt Dependence. *Biopolymers* **1972**, *11*, 761–779.

(190) Menzer, S.; Sabat, M.; Lippert, B. Ag (I) Modified Base Pairs Involving Complementary (G , C) and Noncomplementary (A , C) Nucleobases . On the Possible Structural Role of Aqua Ligands in Metal-Modified Nucleobase Pairst. *J. Am. Chem. Soc.* **1992**, *114*, 4644–4649.

(191) Zavriev, S. K.; Minchenkova, L. E.; Vorlickova, M.; Kolchinsky, A. M.; Volkenstein, M. W.; Ivanov, V. I. Circular Dichroism Anisotropy of DNA with Different

Modifications at N7 of Guanine. *Biochim. Biophys. Acta* **1979**, *564*, 212–224.

(192) Berova, N.; Di Bari, L.; Pescitelli, G. Application of Electronic Circular Dichroism in Configurational and Conformational Analysis of Organic Compounds. *Chem. Soc. Rev.* **2007**, *36*, 914–931.

(193) O'Neill, P. R.; Gwinn, E. G.; Fygenson, D. K. UV Excitation of DNA Stabilized Ag Cluster Fluorescence via the DNA Bases. *J. Phys. Chem. C* **2011**, *115*, 24061–24066.

(194) Baishya, K.; Idrobo, J.; Öğüt, S.; Yang, M.; Jackson, K.; Jellinek, J. Optical Absorption Spectra of Intermediate-Size Silver Clusters from First Principles. *Phys. Rev. B* **2008**, *78*, 75439.

(195) Ramazanov, R. R. R. R.; Kononov, A. I. A. I. Excitation Spectra Argue for Threadlike Shape of DNA-Stabilized Silver Fluorescent Clusters. *J. Phys. Chem. C* **2013**, *117*, 18681–18687.

(196) Fan, Z.; Govorov, A. O. Chiral Nanocrystals: Plasmonic Spectra and Circular Dichroism. *Nano Lett.* **2012**, *12*, 3283–3289.

(197) Govorov, A. O. Plasmon-Induced Circular Dichroism of a Chiral Molecule in the Vicinity of Metal Nanocrystals. Application to Various Geometries. *J. Phys. Chem. C* **2011**, *115*, 7914–7923.

(198) Maoz, B. M.; van der Weegen, R.; Fan, Z.; Govorov, A. O.; Ellestad, G.; Berova, N.; Meijer, E. W.; Markovich, G. Plasmonic Chiroptical Response of Silver Nanoparticles Interacting with Chiral Supramolecular Assemblies. *J. Am. Chem. Soc.* **2012**, *134*, 17807–17813.

(199) Maoz, B.; Chaikin, Y.; Tesler, A.; Elli, O. B. Amplification of Chiroptical Activity of Chiral Biomolecules by Surface Plasmons. *Nano Lett.* **2013**, *13*, 1203–1209.

(200) Li, Z.; Zhu, Z.; Liu, W.; Zhou, Y.; Han, B. Reversible Plasmonic Circular Dichroism of Au Nanorod and DNA Assemblies. *J. Am. ...* **2012**, *134*, 3322–3325.

(201) Govorov, A. O.; Fan, Z.; Hernandez, P.; Slocik, J. M.; Naik, R. R. Theory of Circular Dichroism of Nanomaterials Comprising Chiral Molecules and Nanocrystals: Plasmon Enhancement, Dipole Interactions, and Dielectric Effects. *Nano Lett.* **2010**, *10*, 1374–1382.

(202) Nordén, B.; Kurucsev, T. Analysing DNA Complexes by Circular and Linear Dichroism. *J. Mol. Recognit.* **1994**, *7*, 141–155.

(203) Petty, J. T.; Sergev, O. O.; Nicholson, D. a; Goodwin, P. M.; Giri, B.; McMullan, D. R. A Silver Cluster-DNA Equilibrium. *Anal. Chem.* **2013**, *85*, 9868–9876.

(204) Spink, C. H.; Garbett, N.; Chaires, J. B. Enthalpies of DNA Melting in the Presence of Osmolytes. *Biophys. Chem.* **2007**, *126*, 176–185.

(205) Son, I.; Shek, Y. L.; Dubins, D. N.; Chalikian, T. V. Hydration Changes Accompanying Helix-to-Coil DNA Transitions. *J. Am. Chem. Soc.* **2014**, *136*, 4040–4047.

(206) Schultz, D.; Copp, S. M.; Markešević, N.; Gardner, K.; Oemrawsingh, S. S. R.;

Bouwmeester, D.; Gwinn, E. Dual-Color Nanoscale Assemblies of Structurally Stable, Few-Atom Silver Clusters, As Reported by Fluorescence Resonance Energy Transfer. *ACS Nano* **2013**, *7*, 9798–9807.

(207) Bishop, G. R.; Chaires, J. B. Characterization of DNA Structures by Circular Dichroism. *Curr. Protoc. Nucleic Acid Chem.* **2003**, *11*, 7.11.1-7.11.8.

(208) te Velde, G.; Bickelhaupt, F. M.; Baerends, E. J.; Fonseca Guerra, C.; van Gisbergen, S. J. A.; Snijders, J. G.; Ziegler, T. Chemistry with ADF. *J. Comput. Chem.* **2001**, *22*, 931–967.

(209) van Lenthe, E.; van Leeuwen, R.; Baerends, E. J.; Snijders, J. G. Relativistic Regular Two-Component Hamiltonians. *Int. J. Quantum Chem.* **1994**, *57*, 281–293.

(210) Schipper, P. R. T.; Grittsenko, O. V.; van Gisbergen, S. J. A.; Baerends, E. J. Molecular Calculations of Excitation Energies and (Hyper) Polarizabilities with a Statistical Average of Orbital Model Exchange-Correlation Potentials. *J. Chem. Phys.* **2000**, *112*, 1344–1352.

(211) Autschbach, J.; Ziegler, T.; van Gisbergen, S. J. A.; Baerends, E. J. Chiroptical Properties from Time-Dependent Density Functional Theory. I. Circular Dichroism Spectra of Organic Molecules. *J. Chem. Phys.* **2002**, *116*, 6930.

(212) Crawford, T. D. Ab Initio Calculation of Molecular Chiroptical Properties. *Theor. Chem. Acc.* **2005**, *115*, 227–245.

(213) Woody, R. Circular Dichroism. *Methods Enzymol.* **1995**, *246*, 34–71.

(214) Smith, A. M.; Mancini, M. C.; Nie, S. Bioimaging: Second Window for in Vivo Imaging. *Nat. Nanotechnol.* **2009**, *4*, 710–711.

(215) Swasey, S. M.; Nicholson, H. C.; Copp, S. M.; Bogdanov, P.; Govoritz, A.; Gwinn, E. G. Low-Cost Adaptation of a Visible Wavelength Fluorescence Microplate Reader for Discovery of near-Infrared Fluorescent Probes. *In Preparation*.

(216) Swasey, S. M.; Nicholson, H. C.; Copp, S. M.; Bogdanov, P.; Govoritz, A.; Gwinn, E. G. Near-Infrared Fluorescent Silver Clusters Templated by DNA. *In Preparation*.

(217) Főrster, T. Energiewanderung Und Fluoreszenz. *Naturwissenschaften* **1946**, *33*, 166–175.

(218) Főrster, T. 10th Spiers Memorial Lecture. Transfer Mechanisms of Electronic Excitation. *Discuss. Faraday Soc.* **1959**, *27*, 7–17.

(219) Clegg, R. M. [18] Fluorescence Resonance Energy Transfer and Nucleic Acids. *Methods Enzymol.* **1992**, *211*, 353–388.

(220) Härle-Bachor, C.; Boukamp, P. Telomerase Activity in the Regenerative Basal Layer of the Epidermis in Human Skin and in Immortal and Carcinoma-Derived Skin Keratinocytes. *Proc. Natl. Acad. Sci. U. S. A.* **1996**, *93*, 6476–6481.

(221) Lu, W.; Zhang, Y.; Liu, D.; Songyang, Z.; Wan, M. Telomeres - Structure, Function, and Regulation. *Exp. Cell Res.* **2013**, *319*, 133–141.

(222) Lipps, H. J.; Rhodes, D. G-Quadruplex Structures: In Vivo Evidence and Function. *Trends Cell Biol.* **2009**, *19*, 414–422.

(223) Ambrus, A.; Chen, D.; Dai, J.; Bialis, T.; Jones, R. A.; Yang, D. Human Telomeric Sequence Forms a Hybrid-Type Intramolecular G-Quadruplex Structure with Mixed Parallel/antiparallel Strands in Potassium Solution. *Nucleic Acids Res.* **2006**, *34*, 2723–2735.